

UPPER MANTLE STRUCTURE FROM LONG-PERIOD SH

by

Shane Foster Ingate

A thesis submitted for the degree of
Doctor of Philosophy
in the
Australian National University

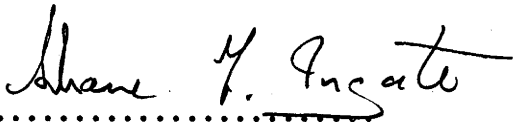
Research School of Earth Sciences
June 1983

STATEMENT

This thesis is a description of a research project undertaken during the period April 1979 to June 1983, while I was a full-time student in the Research School of Earth Sciences at the Australian National University.

The work described in Chapter 1 was performed in collaboration with Drs J.R. Cleary, D.W. King and C.S. Wang, and Chapter 4 with Drs R. Kind and G. Bock. Other than this, the work described in this thesis is entirely my own, except as acknowledged in the text.

This thesis has never been submitted to another university or similar institution.

A handwritten signature in cursive script that reads "Shane F. Ingate". The signature is written in dark ink and is positioned above a horizontal dotted line.

Shane F. Ingate

Canberra

June 1983

PREFACE

In an earlier study, Cleary (1975) recognized that the body-wave train recorded at epicentral distances appropriate to upper mantle studies is composed of a suite of wavelets that have travelled along a variety of paths through the upper mantle. By assuming similarity of the component wavelets, first attempts at identifying individual elements of teleseismic SH records were striking. However, the results obtained from this study were far from compelling. Later research by Cleary, King, Wang and the author attempted to give Cleary's graphical method of analysis a level of respectability and is presented elsewhere in this thesis. Nevertheless, this approach is still largely empirical, and so the current study was initiated to reduce the degree of subjectivity and non-uniqueness inherent in the empirical procedure, and develop a reliable strategy for studying the fine structure of the upper mantle with long-period (LP) body waves.

Contributions by the author can be summarized as follows:

- (i) The identification and assessment of various filtering mechanisms within the Earth, and the degree to which current deconvolution methodologies can reverse their effects on the seismogram.
- (ii) The development and implementation of a deconvolution methodology that requires only that the instrument response be known and that in the absence of noise, the performance of the method is dependent only on the precision with which the wavelet is known and computational round-off errors.
- (iii) The development of a rapid method for the calculation of complete synthetic SH seismograms for a buried source by the Reflectivity method.
- (iv) The reliable identification of later arrivals in the body-wave train by iterative least-squares decomposition, and the demonstration that such later arrivals are a powerful constraint to discriminate between

competing velocity-depth models. To the author's knowledge, this novel processing technique has never before been applied to the problem of identifying arrivals with different travel paths.

- (v) The demonstration that many previously determined models of the upper mantle S-wave (and by implication, P-wave) velocity structure are too simple to adequately explain SH waves propagating below western Europe. A corollary of this exercise was to show that vogue methods of inversion of travel times and waveforms of the first few cycles of the LP body-wave train can result only in oversimplified models.
- (vi) The matching of complete synthetic SH seismograms with data in the distance range 18° to 30° to produce a well-constrained velocity model that exhibits a level of complexity similar to that of many recent studies of short-period data.
- (vii) The development of a method for determining directly and automatically fault-plane solutions from a single 3-component seismic station.

The following papers have resulted from the work described herein:

Cleary, J.R., Ingate, S.F., King, D.W. and Wang, C., 1982. Upper mantle modelling using long-period SH body-wave trains. *Phys.Earth Planet.Inter.*, 30, 36-48.

Ingate, S.F., 1983. An alternative method for focal-plane solutions from a single station. *Geophys.Res.Lett.*, (in press).

Ingate, S.F., Kind, R. and Bock, G., 1983. Synthesis of complete SH seismograms. *Geophys.J.R.astr.Soc.*, (in press).

ACKNOWLEDGEMENTS

I sincerely wish to thank Dr K.J. Muirhead and the late Dr J.R. Cleary for their guidance and encouragement. Appreciation is expressed to Professor A.L. Hales for his interest and support.

I collaborated with or otherwise received advice from several colleagues during the course of this study, in particular, Professor E.S. Husebye, Drs D.W. King, G. Bock and R. Kind. Dr R.A. Wiggins provided source copies of some programmes used in this thesis, and Mr D.R. Christie provided guidance with regard many aspects of computing. I also extend my special thanks to numerous other people for their valued assistance.

I thank Professor Husebye and the University of Sydney for providing a substantial grant enabling me to visit NORSAR where I benefitted from discussions with many seismologists. Financial support provided through the course of this study by the Commonwealth Government and the Australian National University is gratefully acknowledged.

Permission has been obtained from the American Geophysical Union, Geological Society of America, Royal Astronomical Society and Seismological Society of America, to reproduce some of their figures.

CONTENTS

	Page
PREFACE	iii
ACKNOWLEDGEMENTS	v
ABSTRACT	xi
CHAPTER 1. INTRODUCTION	
1.1: Prelude	1
1.2: Upper mantle modelling using long-period SH body-wave trains	4
1.2.1: The NORSAR array and observational data	4
1.2.2: Sequential decomposition	6
1.2.3: Discussion of method	8
1.2.4: Results and interpretation	10
1.3: Scope of this thesis	15
CHAPTER 2. SEQUENTIAL DECOMPOSITION RE-EXAMINED	
2.1: Introduction	17
2.2: Ray-synthetic seismograms of SHMEE	17
2.3: Criticisms of sequential decomposition	24
2.4: Criticisms of SHMEE	27
2.5: Conclusions	28
CHAPTER 3. THE DECONVOLUTION OF TELESEISMIC BODY WAVES	
3.1: Introduction	31
3.2: Seismic wavelet estimation	32
3.2.1: Deterministic methods	33
3.2.2: Wiener-Robinson theory	33
3.2.3: Homomorphic deconvolution seismic wavelet estimation	34

3.2.4:	Wavelet estimation by Minimum Entropy Deconvolution	36
3.2.5:	Instrument response as an estimate of the seismic wavelet	38
3.3:	Deconvolution	38
3.3.1:	Spectral division	39
3.3.2:	Homomorphic deconvolution	43
3.3.3:	Time domain techniques	47
-	Wiener-Robinson deconvolution	
-	Wavelet extraction	
-	Minimum Entropy Deconvolution	
-	Iterative least-squares decomposition	
-	Adaptive deconvolution	
3.4:	Conclusions	71
 CHAPTER 4. COMPLETE SYNTHETIC SH SEISMOGRAMS		
4.1:	Introduction	73
4.2:	SH due to a buried horizontal point force in a layered medium	74
4.3:	SH displacements and stresses for a shear dislocation source in a layered medium	78
4.4:	Numerical considerations	85
4.5:	Examples	86
4.6:	Conclusions	92
 CHAPTER 5. UPPER MANTLE SHEAR WAVE VELOCITY MODELS - PAST AND PRESENT. I: DATA AND PRELIMINARY ANALYSIS		
5.1:	Introduction	93
5.2:	The Mediterranean data	94
5.3:	The North Atlantic data	100
5.4:	<u>A priori</u> assumptions	100
5.5:	Data processing	110
5.6:	Preliminary analysis	114

CHAPTER 6. UPPER MANTLE SHEAR WAVE VELOCITY MODELS - PAST AND PRESENT. II: SYNTHETIC SEISMOGRAMS	
6.1: Introduction	122
6.2: Implementation of the Reflectivity method	123
6.3: The models.	126
6.3.1: JB - Bullen, 1963	127
6.3.2: IN - Ibrahim and Nuttli, 1967	131
6.3.3: US26 - Anderson and Julian, 1969	131
6.3.4: IN2 - Nuttli, 1969	134
6.3.5: STAN 3 - Kovach and Robinson, 1969	136
6.3.6: REDDOG-C - Robinson and Kovach, 1972	138
6.3.7: SW-E - Mayer-Rosa and Muller, 1973	138
6.3.8: SHR14 - Helmberger and Engen, 1974	141
6.3.9: B1 - Jordan and Anderson, 1974	143
6.3.10: B1066 - Gilbert and Dziewonski, 1975	143
6.3.11: PEM-C - Dziewonski et al., 1975	146
6.3.12: MODEL 7 - Nolet, 1977	148
6.3.13: CNNS - Cara et al., 1980	150
6.3.14: PREM - Dziewonski and Anderson, 1981	150
6.3.15: S2 - Hendrajaya, 1981	153
6.3.16: SHMEE - Cleary et al., 1982	155
6.3.17: MA - Massé and Alexander, 1973	158
6.3.18: KCA - King and Calcagnile, 1974	158
6.3.19: EKW - England et al., 1977	161
6.3.20: NAT - England et al. 1978	163
6.3.21: K8 - Given and Helmberger, 1980	163
6.3.22: S8 - Burdick, 1981	166

6.4:	Waveform modelling considerations	168
6.4.1:	The modelling of transitional and first-order discontinuities	168
6.4.2:	Modelling small discontinuities	175
6.4.3:	The modelling of low-velocity zones	177
6.5:	Conclusions	179
CHAPTER 7.	THE APPLICATION OF SYNTHETIC SEISMOGRAMS TO THE INTERPRETATION OF LONG-PERIOD SH	
7.1:	Introduction	181
7.2:	Complete waveform modelling	181
7.3:	Interpretation	187
7.3.1:	The "200-km" discontinuity	187
7.3.2:	The "300-km" discontinuity	189
7.3.3:	The "400-km" discontinuity	189
7.3.4:	The "500-km" discontinuity	190
7.3.5:	The "670-km" discontinuity	191
7.3.6:	Structure below the "670-km" discontinuity	192
7.4:	Discussion	193
7.4.1:	The model SHME	193
7.4.2:	Waveform inversion	195
7.4.3:	Alternative models	196
7.5:	Conclusions	203
CHAPTER 8.	FUTURE RESEARCH	204
BIBLIOGRAPHY		206
APPENDIX 1.	Upper mantle modelling using long-period SH body-wave trains	219
APPENDIX 2.	The calculation of $v(0)/c$	233

- APPENDIX 3. An alternative method for fault-plane solutions from
a single station 237
- APPENDIX 4. Synthetic SH seismograms for a suite of velocity-
depth models. 245

ABSTRACT

Real and synthetic long-period SH data are used to explore the advantages of using as much of the seismic record as possible to delineate the fine structure of the upper mantle. Later arrivals in the teleseismic body-wave train are identified as multiply reflected energy from deep-seated structure. The following strategy for the reliable identification of the travel-time branches of direct and multiple arrivals has been devised. To increase the resolution inherent in recorded long-period data with minimal phase distortion, the effects of the instrument response are first removed by deconvolution. Then comparison of the complete deconvolved body-wave train with complete synthetic seismograms results in better-constrained velocity-depth models.

The success of this strategy is evaluated by using deconvolved long-period SH records from NORSAR of Mediterranean and North Atlantic events, which have dominant periods of less than 15s. Comparison of the deconvolved data with synthetic SH seismograms calculated by the Reflectivity method for a large suite of published velocity-depth models shows that most models are too simple to adequately describe the upper mantle structure below Europe. Travel-time and waveform studies of the first few cycles of long-period data lack the resolution for examination of fine structure. The use of later multiply reflected arrivals acts as a powerful constraint in discriminating between competing velocity-depth models. With the aid of a technique that identifies travel-time branches of the later arrivals, careful waveform modelling with complete synthetic seismograms generates model SHME. This model has first-order velocity discontinuities at depths of 300, 400, 500 and 670 km, with velocity contrasts of 6%, 11%, 2% and 8% respectively. The model is further characterized by low-velocity zones immediately above the "300-km" and "400-km" discontinuities, a steep positive velocity gradient above the "670-km" discontinuity, and uniform velocities elsewhere. There are indications of a deeper discontinuity possibly at a depth of 750 km. The interpretation presented herein is the most detailed yet obtained by a study of long-period SH data.

CHAPTER 1

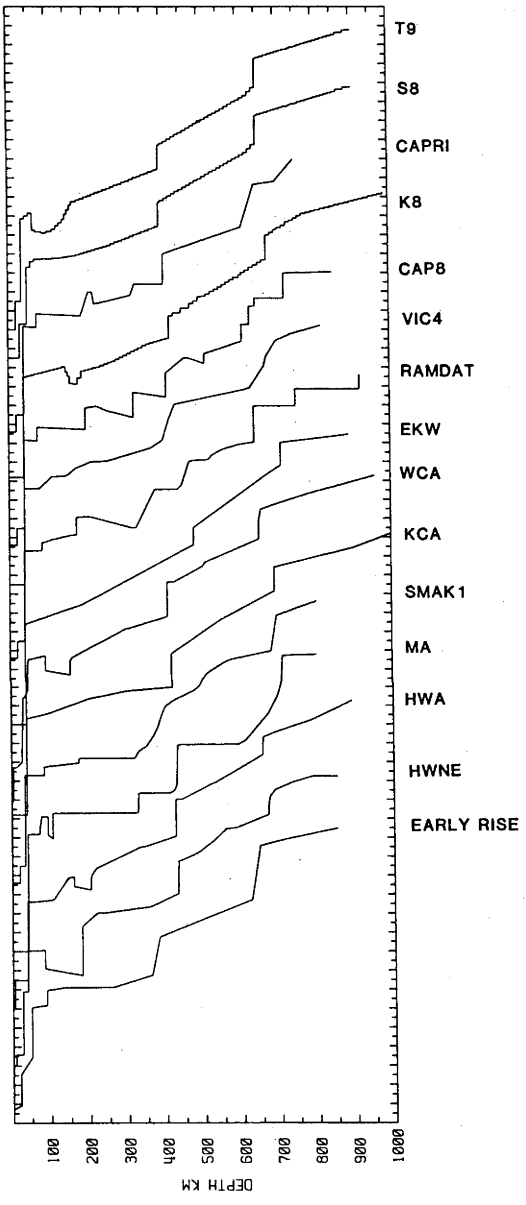
INTRODUCTION

1.1 PRELUDE

There is a consensus that the upper mantle is markedly heterogeneous both vertically and laterally. Such heterogeneity is manifest in the variety of disparate geophysical observations which reflect indirectly the bulk chemistry and state of material in the upper mantle. Indeed, the prevailing concept of a heterogeneous mantle has derived mainly from geophysical observations and investigations. Resolution considerations (and other - see Cleary and Anderssen, 1979) are such that departures from radial and spherical symmetry are most readily inferred from seismological observations and investigations; such studies provide descriptions of the upper mantle in terms of regional velocity-depth and/or specific attenuation-depth distributions.

It has been recognized that the travel-time curve for P waves exhibits significant changes in slope and replication of arrivals at epicentral distances near 20° and 24° , and that arrivals between distances of 5° and 18° are of low amplitude. It is now generally accepted that the former property is the result of two zones of high-velocity gradient (or discontinuities) near 400 and 650 km; these have been attributed by Ringwood and Major (1967) to be the olivine-to-spinel phase change at 400 km, and spinel/garnet to perovskite plus rocksalt-ilmenite phase change at 650 km (Liu, 1979b). The low amplitudes between 5° and 18° are generally associated with low or negative velocity gradients at depths of less than 250 km. Recent attempts at establishing the nature of these and other velocity changes in the upper mantle have led to a variety of models which are similar in gross structure but differ in fine detail; this is evident in the plethora of upper mantle compressional wave velocity-depth models (see Figure 1.1a). Examination of available S-wave models reveals even less conformity (Figure 1.1b). Whether the variations in models are expressions of structural or compositional features which are consistently

a)



b)

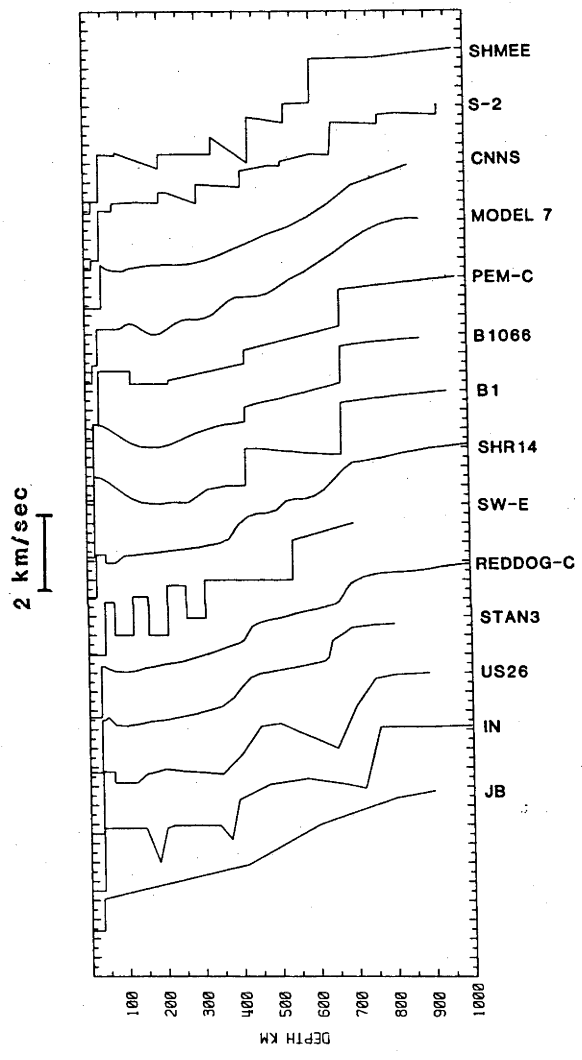


Figure 1.1: Suite of upper mantle (a) compressional wave velocity models, (b) shear wave velocity models. The curves are displaced for clarity.

related to tectonic provinces, is not yet clear. Certainly the data suites, methods of inversion and personal bias of the interpreters, differ significantly; it is the limitations of non-uniqueness which frustrates the qualifications of these differences in terms of model variations.

Non-uniqueness inherent in free-oscillation data (which is relatively insensitive to compressional velocity) shows that changes in shear velocity at depths between 350 and 450 km can be compensated for by changes in density at depths between 50 and 150 km (Dziewonski, 1970). It is important then, to provide independently derived reliable upper mantle shear models to complement existing compressional models (thereby further constraining density models). Unfortunately, the resolution of fine structure in the upper mantle shear velocity distribution is difficult to achieve for a number of reasons:

- (i). The difficulty of recording short-period S waves (masked in P coda) at sufficiently high signal-to-noise ratios (SNR).
- (ii). There are uncertainties associated with the S onset due to precursory P-to-SV and SV-to-P converted arrivals.
- (iii). Coincidence of SV arrivals with PL-coupled shear waves produced by the coupling of P and SV waves in the crustal wave guide (Phinney, 1961; Su and Dorman, 1965; Chander et al., 1968; Helmberger and Engen, 1974).
- (iv). The poor resolving power of long-period (LP) S data as compared with short-period S data.

The resolution obtainable from long-period S data could be improved if a greater proportion of the S body-wave train at distances less than about 30° , presumably comprised of interfering arrivals from a variety of paths through the upper mantle, could be separated into its component signals.

The construction of reliable, well-constrained regional shear-wave velocity models demands the use of the highest quality data, particularly between distances of 10° and 30° where later arrivals are difficult to identify and correlate over an extended distance range. Data of the requisite quality and quantity are most readily available from large aperture seismic arrays equipped with three-component long-period

seismometers and digital recording facilities. Of course, the spatial sampling of arrays has previously been exploited to determine travel-time gradients directly, but the use of such measurements alone is restricted by errors due to local structure near the array. However, the redundancy afforded by arrays is itself an important attribute (see King and Calcagnile, 1976), and enables reliable identification of secondary and possibly later arrivals. An alternative means of improving model resolution is by treating the recorded trace as a superposition of similar time-delayed wavelets, and by means of a deconvolutional filter, to directly decompose the trace into its component body-wave arrivals. Cleary, Ingate, King and Wang (1982) described and applied an empirical method for the sequential decomposition of SH-wave trains; the method appears to provide results that are more readily interpretable than those obtained by automatic least-squares inverse filtering. Travel-time observations of secondary and later arrivals provide valuable constraints for model construction, and may be further supplemented by constraints derived by matching observational data with synthetic seismograms. Notwithstanding the difficulties of accomplishing a reliable decomposition, the decomposition can potentially provide amplitudes and travel times of many arrivals unresolved in the raw data; the inversion of such information would provide tight constraints in modelling upper mantle structure.

The remainder of this chapter describes the preliminary study of Cleary et al. (1982) which attempts to decompose the entire recorded long-period SH body-wave train into its component arrivals. To the authors knowledge, this approach and ensuing inversion for an upper mantle shear-wave velocity model has never before been attempted. This paper is presented in full in Appendix 1.

1.2 UPPER MANTLE MODELLING USING LONG-PERIOD SH BODY-WAVE TRAINS

1.2.1 THE NORSAR ARRAY AND OBSERVATIONAL DATA

During the period May 1971 through to October 1976, the Norwegian Seismic Array (NORSAR), located in south-eastern Norway, comprised 22 subarrays, each containing three long-period (V, NS and EW) and six vertical short-period seismometers distributed over an aperture of about

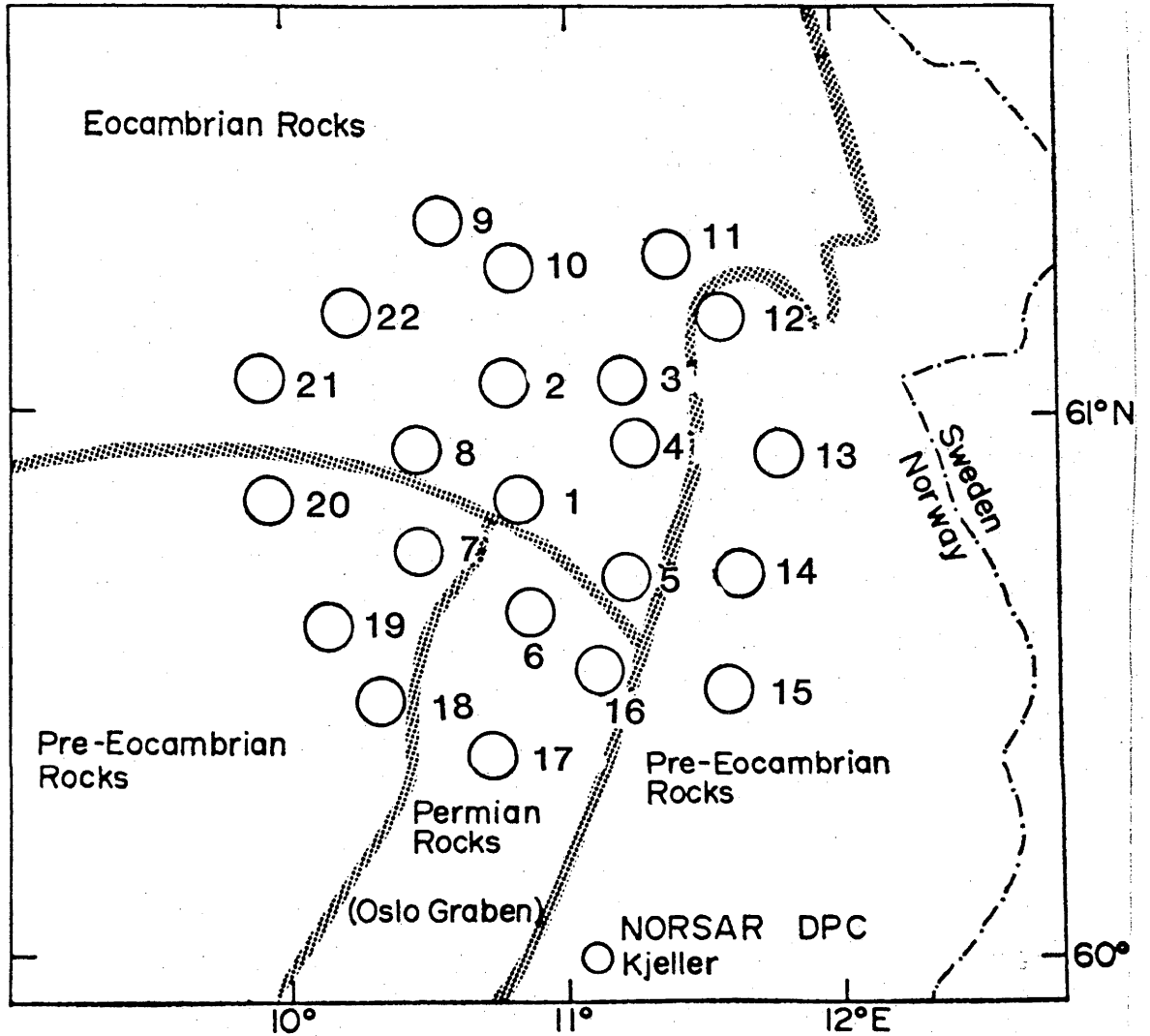


Figure 1.2: NORSAR array configuration. The geological structures in the siting area are briefly outlined.

110 km. The array configuration is shown in Figure 1.2. The long-period instruments used at NORSAR are Geotech models 8700C (horizontal) and 7505B (vertical), which are moving coil, velocity-sensitive seismometers. The outputs of these instruments are continuously sampled at 1 Hz, and are available on digital magnetic tape from the NORSAR Data Processing Centre (DPC). A brief outline of the DPC and the geology beneath the array are to be found in Bungum et al. (1971).

European seismicity is such that the data archive is not well-endowed with events of magnitude 5 and over at distances appropriate to upper mantle investigations, i.e., epicentral distances less than 40° . However, five events from southerly azimuths in the distance range 20° to 28° were well recorded at NORSAR; these events sample the upper mantle beneath eastern Europe. Details of these events can be found in Appendix 1.

In the present study, attention is confined to horizontal transverse (HT) components of LP shear waves, which can be readily obtained from digital data by combination of NS and EW component recordings. HT components are significantly simpler than corresponding recordings of vertical (V) and horizontal radial (HR) components; the relative complexity of V and HR components can be attributed to contamination by shear-coupled PL waves and other P-SV interactions (c.f. Helmberger and Engen, 1974). The HT recordings generally exhibit high coherence across the array (c.f. Figure 3.12), in contrast to the corresponding complex short-period recordings (c.f. Berteussen, 1976). The heterogeneous crust and upper mantle underlying NORSAR is essentially transparent to long-period waves by virtue of the relatively small scale of the inhomogeneities as compared with signal wavelengths (Berteussen, 1976; Haddon and Husebye, 1978).

1.2.2 SEQUENTIAL DECOMPOSITION

A simple procedure for the decomposition of a long-period SH-wave train into its component body-wave arrivals is illustrated in Figure 1.3 using the recorded SH train from NORSAR site 15 of an event in Crete. In essence, the method which is a graphical one, consists of sequential removal of response wavelets from the train, beginning with the first arriving wavelet. The seismic trace then, after subtraction of the suitably scaled wavelet, represents a difference error which is

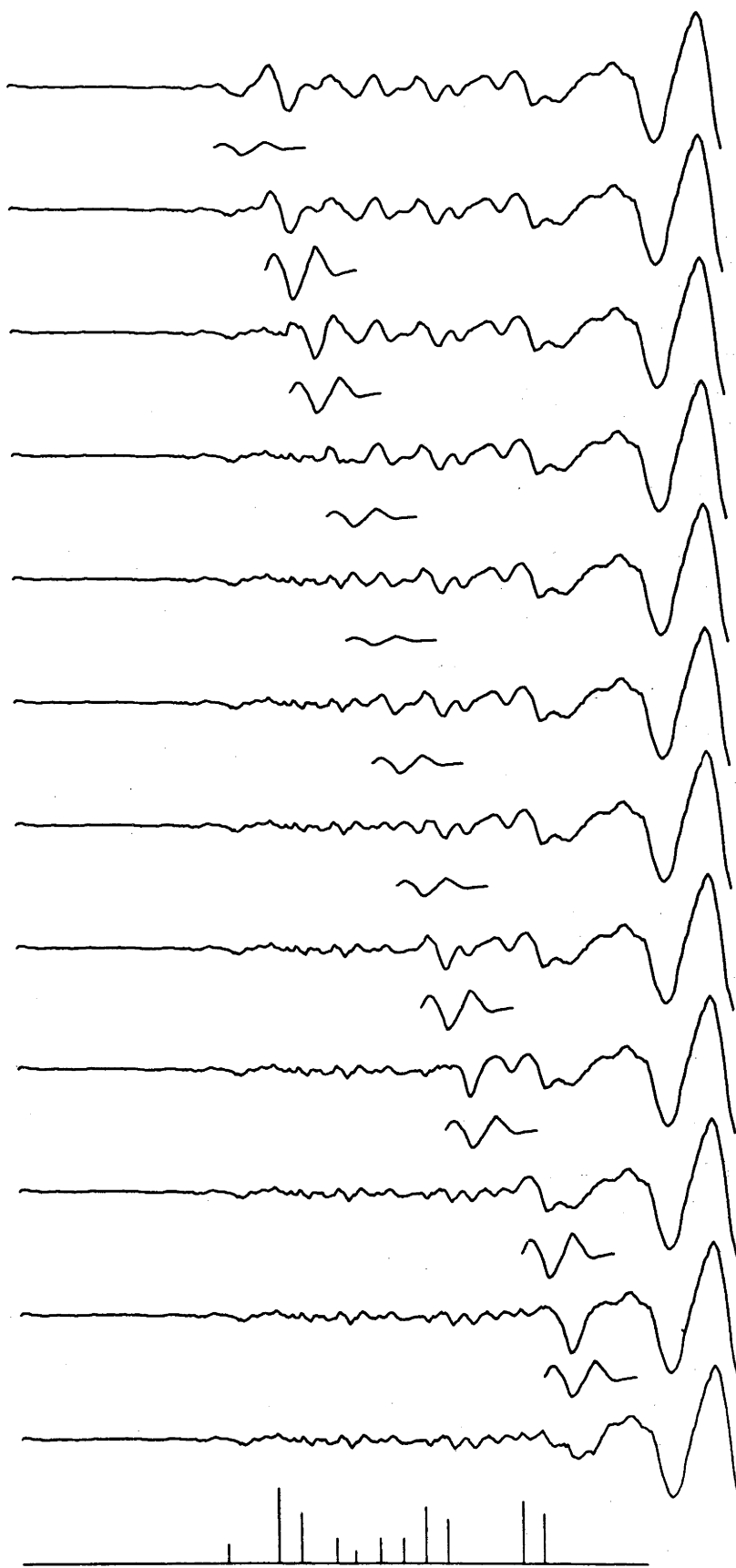


Figure 1.3: An illustration of the method of sequential decomposition, as applied to the SH-wave train recorded from the Crete earthquake at NORSAR site 15. The same wavelet (with only the amplitude changed) is subtracted sequentially from the train up to the arrival of the Love wave. The times and amplitudes of the component wavelets are represented by the spike sequence at the bottom of the figure.

subjectively minimised, and shown after each iteration in Figure 1.3. This process is iterated until the dispersed Love wave is clearly seen near the end of the error train. The response wavelet used in this instance was based on the response of a NORSAR-type long-period horizontal seismometer system to an SH signal from a near-surface strike-slip source, as calculated by Langston and Helmberger (1975), modified slightly to improve the fit to the observed arrivals in the sense of subjectively minimizing the difference error. The times and magnitudes of the component wavelets can be represented by an equivalent spike sequence, as shown at the bottom of the figure.

The solution can be checked by convolving the response wavelet with the derived spike sequence to form a reconstructed (synthetic) wave train, as shown in Figure 1.4. The beginning of the inferred Love-wave train has been "patched in" at the end of the synthetic to complete the picture. Also shown for comparison in Figure 1.4 are automatic deconvolutions of the synthetic and recorded wave trains using an inverse filter derived from the assumed wavelet using programmes published by Robinson (1967). Although the decomposed and deconvolved traces are quite similar, the deconvolved trace is considerably less striking than the decomposed trace indicating that the deconvolution has failed to produce a "spike sequence".

1.2.3 DISCUSSION OF METHOD

The remarkable similarity between the recorded and reconstructed wave trains in Figure 1.4 (and other wave trains, see Appendix 1) appears to vindicate the fundamental assumption underlying sequential decomposition, namely that the recorded SH train can be represented by a wavelet and a spike sequence. Of particular interest in the spike sequence of Figure 1.4 is the succession of paired spikes, suggesting a series of phases accompanied by their near-surface-reflected (i.e., "sS"-type) counterparts. The time separation within each pair is 10 to 11 s, corresponding to a focal depth of 22 to 24 km; a focal depth of 26 km was reported for the event by NEIS (ISC gives 37 km). The reflection coefficient for SH waves incident upon a free surface is always real and unity, meaning that there can be no phase shift or partitioning of energy, i.e. the polarity of the reflected phase is determined solely by the orientation of the source. The

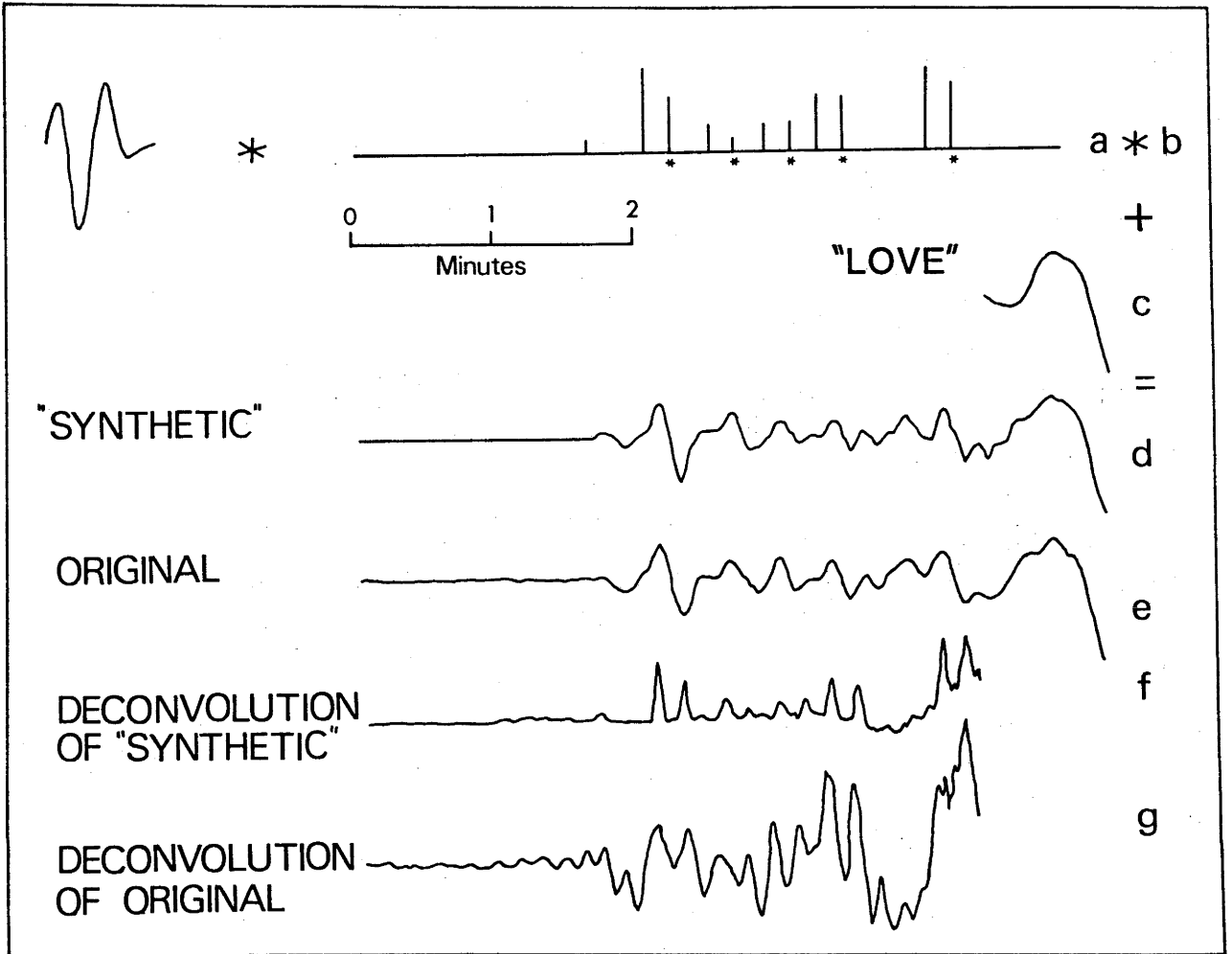


Figure 1.4: Convolution of the wavelet (a) with the spike sequence (b) of Figure 1.3, with the addition of an inferred Love wave arrival (c), results in a "synthetic" SH train (d) which is compared with the original record (e). When the synthetic (d) is automatically deconvolved using an inverse filter derived from wavelet (a), the resulting spike sequence (f) is similar to that of (b). If, however, the same technique is applied to the original record (e) using the same wavelet, the complex deconvolved record (g) results, illustrating the limitations inherent in deconvolving such trains by standard techniques. The asterisks at the bottom of the spike sequence indicate arrivals of probable "sS" type.

absence of polarity reversals between phase pairs indicates that the source mechanism was predominantly strike-slip (HelMBERGER, 1974), which is not unreasonable on tectonic grounds (McKENZIE, 1972), and is consistent with the configuration of the response wavelet. The only event other than the Crete event for which presumed "sS"-type reflections were found was the Greece event, with an apparent "sS-S" separation of 27 to 28 s, corresponding to a focal depth of 65 to 70 km compared with a calculation of 75 km by ISC. The other events were apparently shallow, with depths of 15, 11 and 24 km from NEIS, and 15, 11 and 16 km from ISC, for Albania, Greece-Albania and Turkey events respectively. It is therefore probable that the wavelets derived for these events were a combination of the direct wave and the surface reflection.

It is apparent from Figure 1.4 that the empirical procedure improves resolution dramatically, albeit subjectively, by seeking the least number of spikes that is consistent with the data. The automatic procedure, on the other hand, improves resolution less dramatically and at the expense of a signal-to-noise degradation. The quality of automatic deconvolution is limited, inter alia, by the fidelity of the wavelet used for filter synthesis. The method presented here is approximate in that it assumes the absence of phase distortion (although it allows for the possibility of phase inversion). The assumption of a stationary wavelet is, however, implicit in many seismic data analysis strategies (e.g., Clayton and Wiggins, 1976; Dey-Sarkar and Wiggins, 1976). The method should therefore be considered as providing a first approximation solution which can then be used as a starting model for the application of refinement techniques.

The following section interprets the complete sequence of body-wave arrivals found by the above method for the five Mediterranean events in terms of singly- and multiply-reflected/refracted SH phases in a layered upper mantle.

1.2.4 RESULTS AND INTERPRETATION

For each event, HT seismograms from the extreme sites of the NORSAR array were decomposed into their component wavelets according to the technique described earlier. Throughout this part of the study, the modelling strategy was to match wave shapes, times, and amplitudes, in

order to obtain the best possible approximations to the original records. Difficulties in modelling occurred in parts of the records where the Love waves began to arrive, and the spike sequences in these regions have no claim to high accuracy.

It is noteworthy that no arrival having a reversed phase was detected on any of the records. It can be shown from equation (12.25) of Pilant (1979) that the phase shift of an SH wave totally reflected at a plane interface between two elastic media varies from zero at the critical angle to π at grazing incidence. Under these conditions, the effect of geometrical spreading is such that the amplitude of the wave is large in the vicinity of the critical angle (zero phase shift) but decreases fairly rapidly as the angle of incidence increases - i.e., as the phase shift increases. On the other hand, when total reflection occurs within a second-order discontinuity (i.e., a transitional discontinuity), the wave energy tends to be distributed more evenly along the retrograde branch. The absence of detected phase reversals may indicate, therefore, that velocity changes in the upper mantle take place over depth intervals which are small compared with the wavelengths (~ 100 km) of the signals recorded by the NORSAR LP instruments, so that reflected phases with large phase shifts are sufficiently small to be masked by other arrivals. The apparent time shift (Ewing, et al., 1957, p. 90) and distortion (Choy and Richards, 1975, Figure 11) in the wave form is small for phase shifts up to at least 30° , so the presence of phase shifts of this order may not invalidate the technique.

The times of all the inferred arrivals have been summarized on a reduced time plot in Figure 1.5. Although this aggregation of the data - especially for the later-arriving phases - is somewhat bewildering at first, certain aspects of the figure give cause for encouragement. There is, for example, excellent agreement between the sequences A10 (Albania event, NORSAR site 10) and GA15 (Greece-Albania event, NORSAR site 15) for which the corrected distances were virtually identical. Corrected distance and travel-time calculations can be performed using, for example, the time-distance relation for a surface-focus source with a particular ray parameter p as given by Engdahl et al. (1968)

$$\Delta = 2 \int [\cos^{-1}(p/\eta_1) - \cos^{-1}(p/\eta_2)]$$

$$T_c = 2 \int [(\eta_1^2 - p^2)^{\frac{1}{2}} - (\eta_2^2 - p^2)^{\frac{1}{2}}]$$
1.1

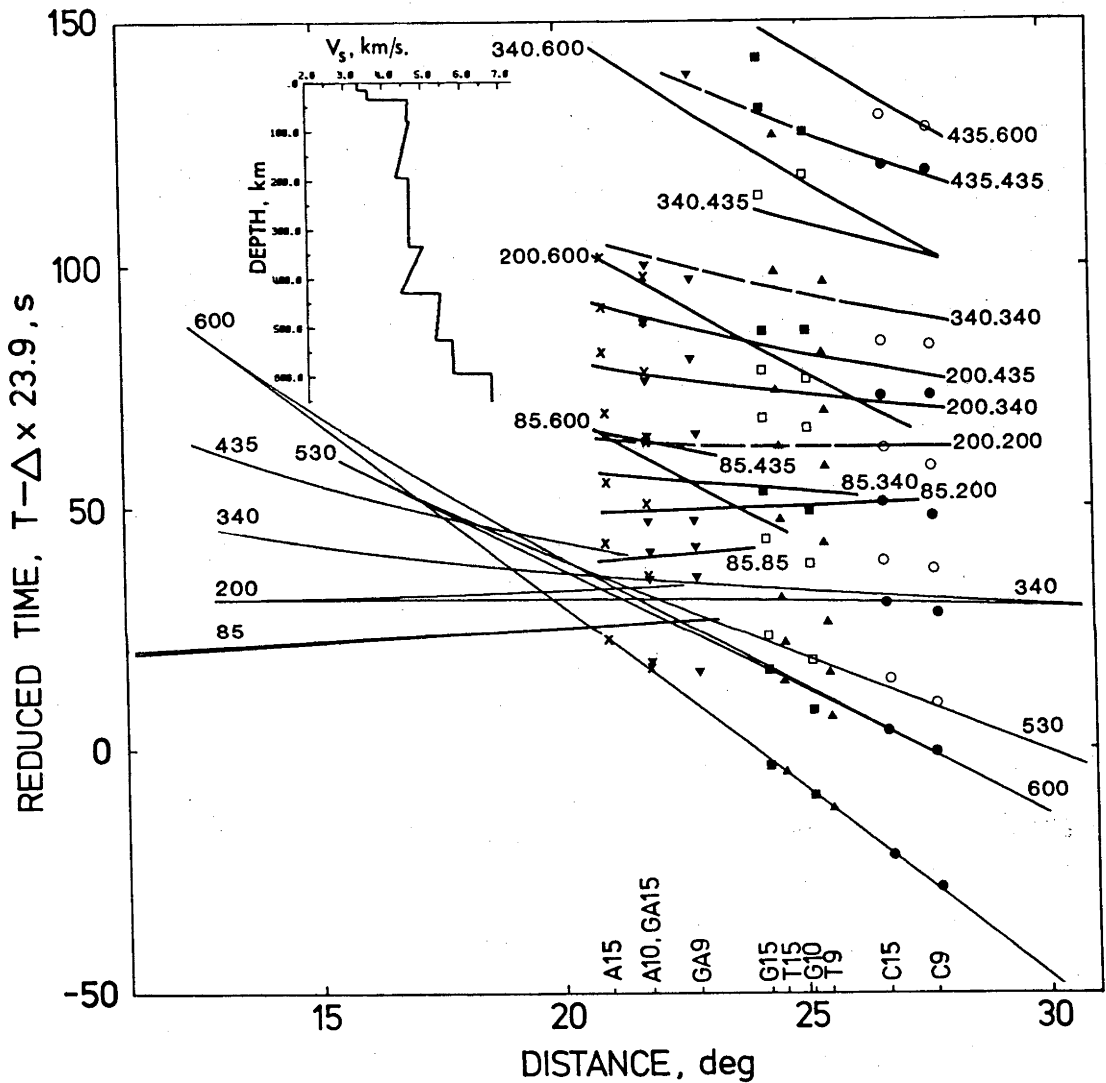


Figure 1.5: Reduced travel-time/distance plot for the spike sequences. The open symbols \circ , \square represent probable surface-reflected phases of "sS" type. Also shown are (i) a branched travel-time curve derived from the S-velocity distribution SHMEE (inset, and Table 3, Appendix 1), with cusps labelled according to the bottoming depths of the associated rays; and (ii) a series of multiple branches of " S_xS_y " type (where x, y are the bottoming depths of the two legs of the phase), labelled as x.y.

where the summation is taken over a series of thin homogeneous layers from the focal depth to the surface, and

$$T_c = \text{travel time at distance } \Delta(\text{radians})$$

$$\eta_i = r_i/v, \quad v = \text{velocity at radius } r_i$$

For the calculation of these corrections, the uppermost 75 km is assumed as given by the SCAN model of Der and Landisman (1972) with an appropriate conversion of P velocities to S velocities. A value of $v_s = v_p/1.735$ was taken from the study of Hales et al. (1980b). SCAN represents a synthesis of published seismic models of central Scandinavia; for simplicity, a single layer crust has been assumed. Choice of the velocity model is not important, as small departures in the model used will have only small effects on the corrected distance and travel times, which are less than the errors in estimating the arrival time.

Again, although the scatter of the data in Figure 1.5 undoubtedly inhibits the recognition of distance-related trends in the sequences of arrivals, some trends are visible on close inspection. In general, the scatter is worst towards the end of a sequence, where small arrivals have been disturbed by the presence of a Love wave. Scatter may also have been produced by factors such as phase distortion and structural variations along the path. Perhaps most importantly, phases arriving within about a quarter-wavelength of each other are very difficult to separate, and may be interpreted as a single phase.

Single ray paths in plausible upper mantle models can only account for the first few arrivals of the sequences in Figure 1.5. It was therefore necessary to consider multiples incorporating a free-surface reflection, both symmetric (of 2Sx type) and asymmetric (of Sx.Sy type; where x and y are the depths of reflecting/refracting horizons). It quickly became apparent that, in addition to the well-known discontinuities near 400 and 600 km (and possibly also near 500 km), additional discontinuities had to be postulated above these levels. From a model with discontinuities at 85, 200 and 340 km, reasonable approximations to the slowness vector estimates of the spike sequences were obtained with the multiples 2S85, S85.S200, S85.S340, 2S200, 2S340, S200.S435, S340.S435 and 2S435 as computed by geometrical ray theory. Asymmetric multiples involving more widely

separated combinations of these presumed discontinuities (e.g. S85.S435, S85.S600, S200.S600 and S340.S600) would also occur, and have been included in Figure 1.5. This indicates the potential complexity of the SH body-wave train, and the need to refine the model by comparison of observed with synthetic seismograms.

The presence of small discontinuities near 100 and 200 km has been inferred from P-wave data in various parts of the world (see Green and Hales, 1968; Mereu and Hunter, 1969; Hirn et al., 1973; Muirhead et al., 1977 for the former; and Lehmann, 1959, 1962; Hales et al., 1970; Steinmetz et al., 1974; Ram Datt and Muirhead, 1976; Muirhead et al., 1977; and Hales et al., 1980a for the latter). Indeed Anderson (1979a) has named the feature at 200 km the Lehmann discontinuity because of its global significance.

The 435 and 600 km discontinuities are well known in the literature; so, to a lesser extent, is the 530 km discontinuity (see for example, Jordan and Anderson, 1974; Helmberger and Engen, 1974). The presence of a discontinuity at 530 km has been inferred here from arrivals associated with only the Turkey event (T15 and T9 records), although similar phases could have been obscured in the Greece (G15, G10) and Crete (C15, C9) records by "sS"-type arrivals at about the same times (c.f. Figure 1.5). It may be remarked also that the separation between the direct and 600 km branches in Figure 1.5 is much greater in this distance range than that given by Helmberger and Engen's (1974) model. In fact, the Helmberger and Engen study included few observations in this range, and the position of the 600 km branch was inferred by them from other data rather than directly observed. The 600 km branch arrivals are the clearest and largest of all on the records. It is possible, however, that intermediate arrivals (corresponding, say, to a discontinuity at about 650 km) are also present, but because of low amplitudes were not separable. This could be the reason for the difficulty in matching the amplitudes of the first arrivals, and may also explain the late "first" arrival on GA9 (see Figure 1.5).

Although the model as a whole is more complicated than many published upper mantle S-wave velocity models (see Figure 1.1b), there are many indications that the upper mantle is more complex than previously supposed. Methods of data acquisition, processing and analysis are becoming more elaborate, thus enhancing resolution. This is reflected in the current trend to increasing complexity in the velocity models, yet each study, though using data with different limits of resolution from a variety of

regions, is driven by the principle of simplicity: that is, the resulting model is the simplest possible model consistent with the data.

1.3 SCOPE OF THIS THESIS

The further progress of observational seismology depends to a large extent on the utilisation of as much of the seismic record as possible, rather than just the more readily identifiable phases. In recent years, considerable advances have been made in this direction by the use of synthetic seismograms in modelling. Until now, however, attention has been largely restricted to the successful modelling of the first few cycles of the train (see for example, HelMBERGER and Engen, 1974). Never before has an attempt been made to model the entire SH body-wave train at periods of less than 20s. It has been shown in the previous sections that the entire SH train before the Love-wave onset can be modelled by a sequence of stationary phase wavelets and that this sequence can be interpreted in terms of refracted arrivals together with multiples incorporating free surface reflections for a somewhat complex upper mantle model. Although the approach has been an empirical one and neither the wavelet sequence nor the interpretation in terms of refractions and multiple reflections is likely to be unique, a model having a sufficiently close approximation to the real Earth to be capable of realistic refinement using synthetic seismogram techniques has been generated.

The ultimate success of the current project lies in the achievement of several objectives: implementation of an objective processing strategy; extension of the available data set; refinement modelling using synthetic seismograms. Therein lies the rationale for the principal aim of this project, viz., the development of an optimal strategy for the processing of long-period SH-wave data (recorded at large arrays) to enable isolation and identification of those features of the seismic record due to fine structure in the upper mantle shear wave velocity distribution. This development entails critical examination of various deconvolution methodologies: formal development and automation of the sequential decomposition process is an important part of this assessment. Before this study can proceed, an objective re-examination of the sequential decomposition procedure and the velocity-depth model SHMEE is in order.

Furthermore, it is important to ascertain the degree to which phase distortion and later arrivals of the type suggested in the previous section do contribute to the complexity of the seismic body-wave train.

CHAPTER 2

SEQUENTIAL DECOMPOSITION RE-EXAMINED

2.1 INTRODUCTION

The velocity-depth model obtained from the previous analysis is undoubtedly non-unique, not only on account of the well-known trade-off between the positions of the interfaces and the velocity gradients between them, but also because the aim of obtaining the simplest model consistent with the data has almost certainly resulted in an oversimplified series of spike sequences. Before refinement modelling of SHMEE can commence with the aid of complete synthetic seismograms, some points in the analysis of the previous chapter need to be checked. Geometrical ray theory was used to calculate the travel times of the multiply reflected rays predicted by the model SHMEE, but it remains to be seen if the multiples in Figure 1.5 are of significant amplitude relative to the amplitude of the first arrivals. This premise may best be tested by the use of the ray-synthetic seismograms.

2.2 RAY-SYNTHETIC SEISMOGRAMS OF SHMEE

The Generalized Ray method (Gilbert and Helmberger, 1972; Helmberger, 1973) is a wave-slowness technique. The frequency-time transform is evaluated first and the wave-slowness transformation is achieved by an integration along a path in the complex ray parameter plane. This method allows the operator to specify which rays are to be included in the "ray sum", and is thus well suited to calculating amplitudes on the branched travel-time curves in Figure 1.5.

Ray-synthetic seismograms for some of the important direct SH rays that have travelled once through the perfectly elastic spherically homogeneous SHMEE Earth are displayed as a record section in Figure 2.1. Geometrical

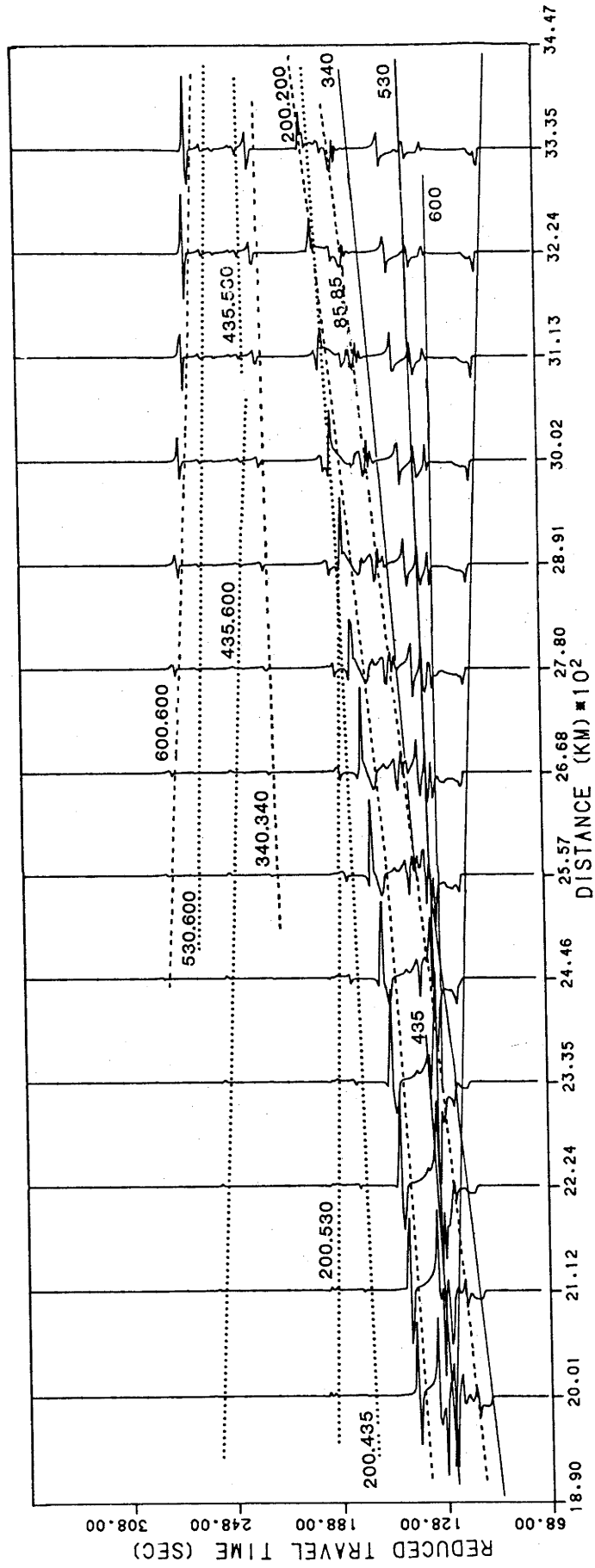


Figure 2.1: Generalized ray synthetic seismograms for the shear wave velocity model SHMEE in the distance range 20° to 30°. Only the direct rays and important multiples are calculated. As with Figure 1.5 the cusps of the corresponding branched travel-time curves are labelled according to the bottoming depths of the associated rays. Amplitudes are trace normalized.

ray theory travel times are superimposed on the synthetics, with branch notation similar to that used in Chapter 1. The synthetics are the far-field displacement response due to a step-function displacement-type source, and will be referred hereafter as the Earth's step response. For unilateral fault propagation in a homogeneous Earth, the far-field displacement is given by $dm_0(t)/dt$ where $m_0(t)$ is the moment-time function of the source (Harkrider, 1976). For a Heaviside-function source in the absence of attenuation, the ground displacement in the far field will be a delta function. Earthquake sources are perhaps better represented by ramp functions (Brune 1970). Brune's model for the scaling law of the seismic source spectra adequately describes the 'corner frequency' phenomenon and so, generally speaking, this model implies that the frequency content of the source-time function is invariably related to the fault dimension; the longer the fault (or lower the stress-drop) the longer is the duration of the source-time function (or lower the 'corner frequency'). On account of the low resolving power of LP waves, the source may be adequately represented by a step function rather than a ramp function. Figure 2.1 also shows important symmetric and asymmetric multiples. Ray-synthetic seismograms were computed for other types of multiples such as triple symmetric multiples (e.g. 3S200) but their contributions are negligible at the distances under consideration. It can also be seen that the relative amplitudes of the asymmetric multiples are not significant, because one leg of the reflection will have an angle of incidence which is considerably less than the critical, but their contribution has been included for completeness. Even though contributions from many multiples were carefully incorporated in the synthetics of Figure 2.1, the synthetics are not a true representation of the ideal Earth's step response: the Generalized Ray method cannot synthesize the complete response of an Earth model because of the need to truncate the ray sum.

Inspection of Figure 2.1 shows that amplitudes of some multiples are larger than the first arrivals. As will be shown later in this chapter, attenuation affects the amplitudes of the multiples to a greater extent than the direct branches, but not to the extent that their amplitudes no longer contribute significantly to the seismogram.

At distances between 2000 km (18°) and 3340 km (30°), the amplitudes of the multiples are small with the exception of the symmetric multiples 2S85, 2S200, 2S340 and 2S600. Their appearance adds to the extraordinary complexity to be found in this distance range. This behaviour is well

predicted by Cleary et al.; at these distances, the recovered spike sequences are little over one minute long, yet include up to eight arrivals.

The subjective formation of the basic wavelet by Cleary et al. may appear to be ad hoc, but its formulation is not dissimilar to construction of wavelets for deconvolution operators used by Clayton and Wiggins (1976) and Dey-Sarkar and Wiggins (1976). In their formulation, the basic wavelet was taken as the first arrival on records obtained between 30° to 40°. The basic wavelet of Chapter 1 was based on the anticipated arrival shape and calculated by

$$w(t) = m(t) * a(t) * q(t) * i(t)$$

where $m(t)$ = source function, say the medium stress-drop source of Langston and Helmberger (1975);

$a(t)$ = mantle operator = $\delta(t)$ for the refracted first arrival;

$q(t)$ = Futterman attenuation operator (Carpenter, 1966);

$i(t)$ = NORSAR-type LP instrument response.

The resulting wavelet was modified slightly as outlined in Chapter 1. The construction of the synthetic and modified wavelet is shown in Figure 2.2. The error formed by subtracting the modified wavelet from the synthetic is small (Figure 2.2).

A factor that may contribute to the variance of the components of the Earth's step response is Q and its attendant dispersion (velocity and amplitude as a function of frequency). For body waves, the effect of dispersion is small, so attention will be confined to Q . In this sense, the Q mechanism used throughout this study pertains to both the intrinsic attenuation, and the attenuation by other mechanisms such as scattering. The attenuation operators calculated in this chapter will use model SL1 (Anderson and Hart, 1978) with $t^* = 3.3$ ⁺. Burdick and Helmberger (1978) recognized that the Earth's step response is a sum over many rays, each with different ray paths, travel times and average Q along the paths. Burdick and Helmberger suggested combining the response for an ideal Earth and attenuation operator into a composite operator.

$$s(t) = \sum_{i=1}^n G_i * q_i \quad 2.1$$

⁺ (Where t^* is the ratio of a ray's travel time to the effective average Q for the path.)

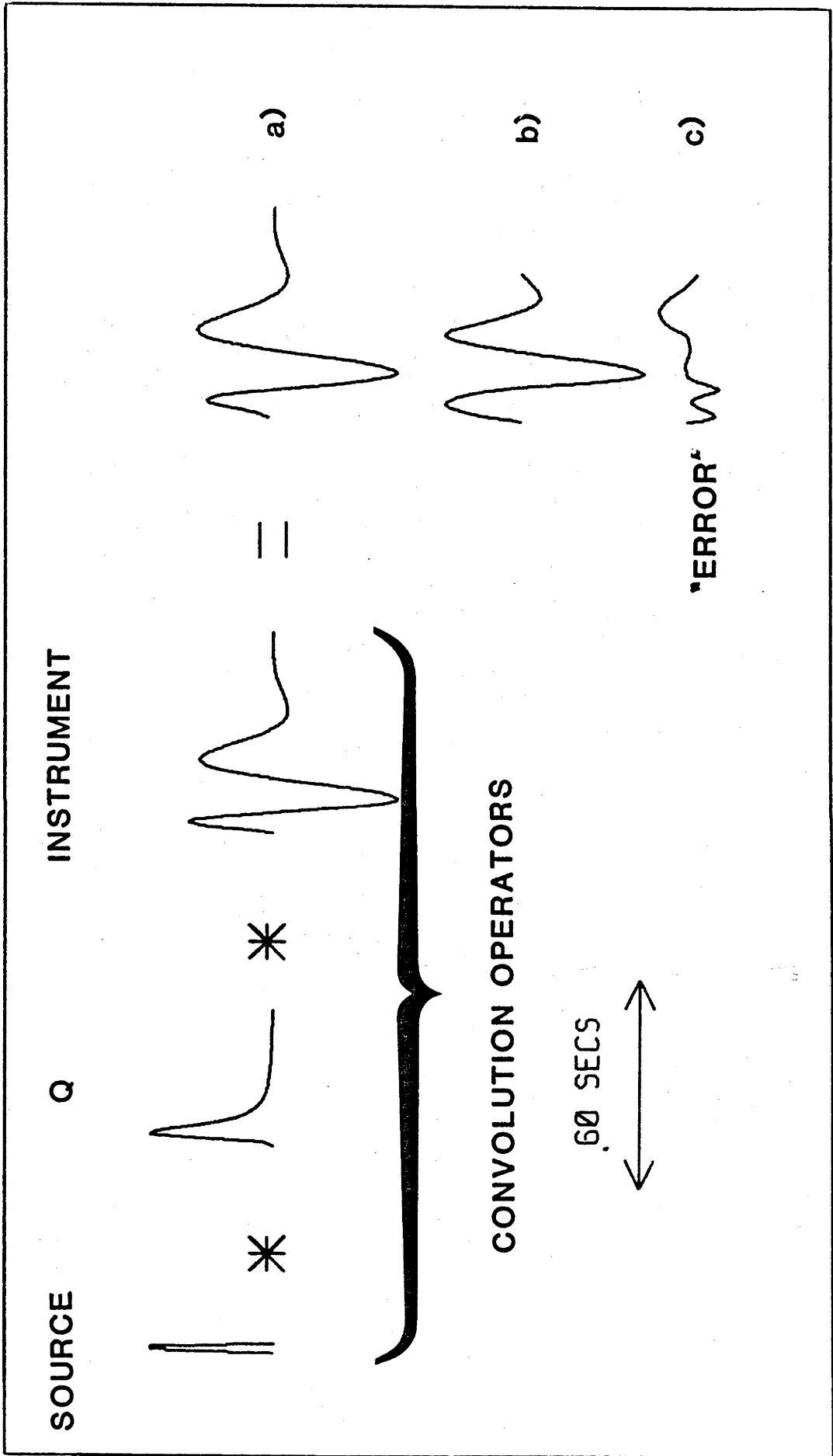


Figure 2.2: Evolution of the basic wavelet (a) used in Chapter 1. A triangular source-time function is convolved with a Q operator and NORSAR-type LP instrument response. The final wavelet as used by Cleary et al. (1982) is shown (c) along with the difference error (c) between the wavelets a) and b).

where G_i is the contribution from the i th ray, Q_i the attenuation operator evaluated at the appropriate t^* for the path, and the sum extends over all the rays. Burdick and HelMBERGER suggested that if the variation of q_i within the set of rays is small, then the composite operator could be approximated by

$$s(t) = q(t) * \sum_{i=1}^n G_i(t) = q(t) * a(t) \quad 2.2$$

where $a(t)$ is the step-function response of a perfectly elastic Earth. Burdick and HelMBERGER tested the approximation given in equation 2.2 for synthetics calculated at distances of 15° to 17° . Their results show that for the waveforms as calculated by equations 2.1 and 2.2 and for different Q models, the differences are very small and may be masked by scatter in the amplitude data. Kennett (1975a) calculated synthetic seismograms for perfectly-elastic and attenuative Earths, and showed that at shorter periods, the effects of attenuation could change peak amplitudes by up to 20%. However, for longer periods, the effects of differential attenuation are very small.

On the other hand, the approximation 2.2 may not be adequate when synthesizing complete seismograms. To determine whether this is the case, Burdick and HelMBERGER's experiment of producing synthetic seismograms for direct and multiply reflected rays has been repeated for the rays S600 and 2S600. The respective travel times of S600 and 2S600 at 27° for model SHMEE are 631s, and 774s. If the average Q for the ray path S600 ($t^*=3.3$) is assumed to be the same as that for 2S600, then t^* for 2S600 is 4.05s. To examine the appearance of the attenuation operators, a catalogue of operators for varying values of t^* from 0.5 to 6.0 is presented in Figure 2.3. Relative to S600, 2S600 will only be reduced in amplitude in the ratio 1/1.25. The distortion of the spectral content is even less obvious - although the operator representing lower Q has a slower rise time and exhibits broadening, the differences are not large and are unlikely to be picked by sequential decomposition. The differences could however create some problems for an automatic deconvolution method.

As stated by Cleary et al., the sequential decomposition technique and subsequent interpretation is highly non-unique. It has been shown that the body-wave train is composed of a sequence of refracted and reflected arrivals, and that multiple reflections from the deeper discontinuities have quite an appreciable amplitude. Yet there appear to be some

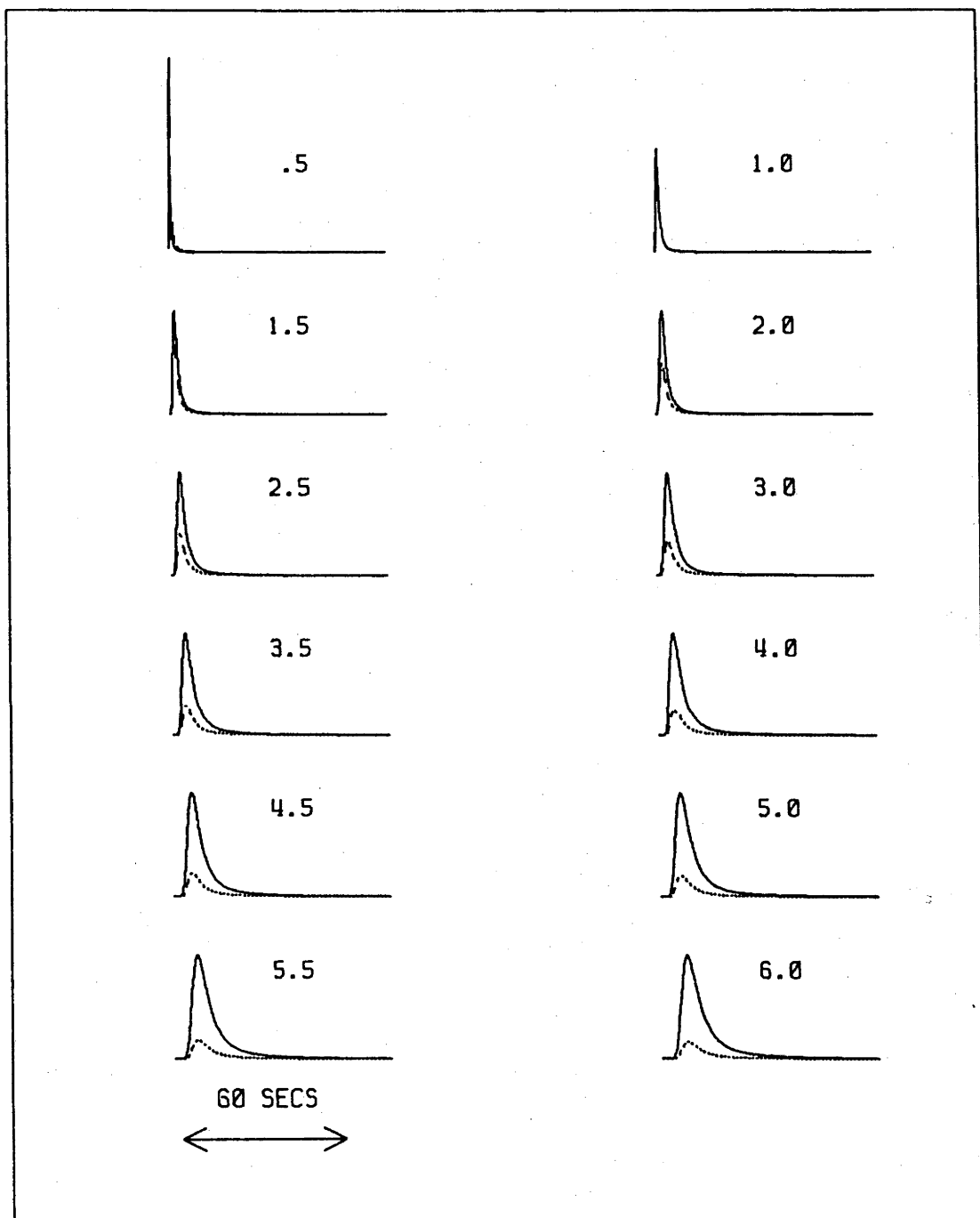


Figure 2.3: Catalog of Q operators for various values of t^* . Number at top right of each trace is the appropriate value of t^* . The dotted lines preserves peak amplitude, the solid line normalizes the trace to peak amplitude.

discrepancies between the ray-synthetics and the assumptions implicit or explicitly stated by Cleary et al.:

- (i). Cleary et al. assumed (correctly) that with increasing angles of incidence beyond the critical angle, the increasing phase shift is accompanied by decreasing amplitudes on the retrograde branches, and so phase shifting could be ignored. Phase distortion is apparent on the synthetics to a far greater extent than was anticipated by Cleary et al.
- (ii). The "530-km" branch arrivals as calculated by the Generalized Ray method, have a much larger amplitude than suggested by Cleary et al. The velocity contrast of 7% and negative velocity gradient immediately above this discontinuity ensures large amplitude reflected arrivals. This suggests that the "530-km" branch arrivals should be seen on all the sequentially decomposed records. Rather, Cleary et al. inferred the existence of this discontinuity from arrivals from one event. If the strategy by Cleary et al. is correct, then SHMEE should be remodelled with a small or non-existent discontinuity between 435 and 600 km.

It is required then to review these discrepancies (and others if they exist), and check the validity of the sequential decomposition procedure.

2.3 CRITICISMS OF SEQUENTIAL DECOMPOSITION

As a first step in examining the sequential decomposition method, it is necessary to examine, by example, the degree of non-uniqueness inherent in the method. Figure 2.4 reproduces the evolution of the synthetic for the Greece event, NORSAR site 15. The error sequence formed by subtracting the synthetic from the recorded seismogram is also shown. Using the same wavelet, an alternative and markedly different spike sequence was generated using as a starting model the automatically deconvolved trace. The corresponding synthetic and error series are given in Figure 2.4. The error series for both synthetics have similar amplitudes. One explanation for the negative polarity arrival is that a buried pure vertical dip-slip

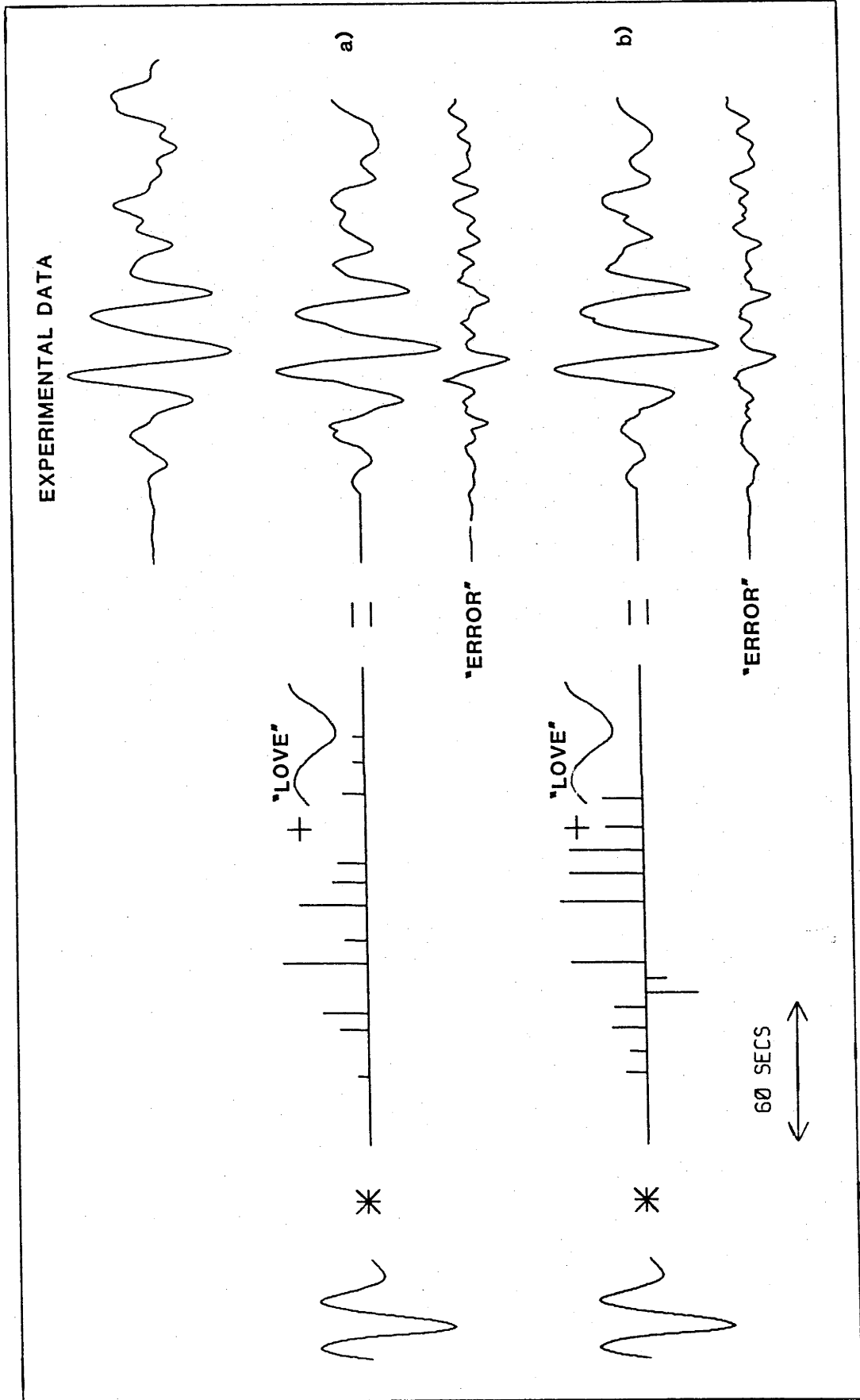


Figure 2.4: Comparison between alternative spike sequences generated by the sequential decomposition procedure of Cleary et al. (1982) for the Greece event, site 15. Both spike sequences are convolved with the same basic wavelet. A "cosmetic" Love wave has been added to each synthetic trace. The difference error formed by subtracting the synthetic a) and b) from the data are also given.

event will produce depth phases of opposite polarity from the first arrival (HelMBERGER, 1974). If the latter case were true, then the decomposed data would be expected to consist of a sequence of paired spikes, a member of the pair having different polarity to the other member. If the event under consideration were sufficiently deep, then the basic wavelet of Cleary et al. will not include the depth phase, and so should identify negative amplitude arrivals throughout the record. If, on the other hand the basic wavelet were based on the response of the instrument to a near-surface source, the contribution of the depth phase may be included in the basic wavelet and so the decomposed sequence will not include arrivals corresponding to the depth phases. Indeed, the former situation describes the decomposition of the Greece and Crete events, while the latter, Albania, Greece-Albania and Turkey events. Because paired arrivals could not be identified throughout the alternative spike sequence, the presence of a few negative arrivals indicate the presence of pre- and post-cursors of a phase shifted wavelet. A comparison of the synthetic seismogram at a distance of 2668 km (Figure 2.1) with the two spike sequences of Figure 2.4 show that the alternative spike sequence is a much better representation of the synthetics than the original spike sequence. Of course, both spike sequences fail to recognize the large negative "spike" of the 2S200 arrival.

On the question of phase shifting, there are several mechanisms for their origin. Besides distortion in reflected pulses at angles beyond the critical, the only other mechanism of interest here arises from waves propagating in a stratified medium that touch a caustic (focussing region) and undergo a constant phase shift. Such waves are characterized by a non-minimum travel time such as SS and SSS (i.e., mini-max phases).

It is clear from Figure 2.1 that the reflected wave energy continues further than anticipated along the geometrical ray theory travel-time curves. Even for large values of post-critical angles of reflection, the amplitudes of the reflected waves compared with the refracted energy will not be negligible. Thus the assumption of Cleary et al. that the amplitudes of post-critically reflected rays are small is incorrect. Consequently, phase shifting of arrivals is an important phenomenon on the seismogram, distorting each arrival from a "true" delta function and so invalidating the sequential decomposition procedure for this type of data.

2.4 CRITICISMS OF THE VELOCITY-DEPTH MODEL SHMEE

Upon examination of SHMEE and its associated travel-time curves (Figures 1.5, 2.1), the outstanding anomaly is that the predicted forward branch representing rays that have bottomed immediately below the "435-km" discontinuity never become a first arrival, due primarily to the large negative velocity gradient above this discontinuity. This behaviour is not predicted by any other current shear-wave-velocity models for the upper mantle (c.f. Chapter 6, Appendix 4). Most current models predict changes in the slope of the travel-time curve at distances of about 20° and 24° , corresponding to changes in the velocity gradient near 400 and 650 km. In the distance range 20° to 30° , the model SHMEE predicts a first arrival with an apparent velocity of 7 km/s. A re-examination of the NORSAR data for the two events between 20° and 24° using the Nth-root processing technique of Muirhead and Ram Datt (1976) indicate a mean apparent velocity of 5.5 km/s. The Albanian and Greece-Albanian records were the noisiest of those examined by Cleary et al. which may account for the erroneous readings.

The discontinuities in SHMEE consistently occur at depths that are significantly deeper than current shear-wave velocity models. The S600 branch is the clearest and largest of all on the decomposed records, implying a considerable velocity contrast. The magnitude of this structure is such that it can correspond only to the so-called "650-km" discontinuity so readily observed in other studies (c.f. Kovach and Robinson, 1969; Dziewonski et al., 1975; Hendrajaya, 1981). One notices that the sequential decomposition procedure consistently over-emphasizes the amplitude of the first arrival, particularly in the spike sequences for Albania, Greece-Albania, Greece and Turkey events. This could suggest the presence of another arrival between the direct arrival and the reflection from the "600-km" discontinuity, corresponding to another discontinuity at (say) 650 km. Alternatively, and as has been shown earlier, it could indicate that the decomposition procedure is having difficulty coping with a phase shifted spike immediately following the direct refracted arrival which suffers little or no distortion.

There is also the question of contamination by Love waves. Cleary et al. indicate the presence of surface waves by patching in a cosmetic long-period wave because of the difficulty of explaining several large arrivals at the end of the sequence. These large spikes may be an artifact. It is possible that at these periods higher mode Love waves will

arrive before the fundamental. For example, assuming Harkrider's (1976) continental model and a surface-wave period of 40s, the group velocities for the fundamental and third higher modes are 4.06 and 4.60 km/s respectively, with apparent travel times at 27° of 740 and 652s. However, Harkrider's calculations show that the relative excitation of the fundamental to higher modes for a continental model is greater than 20 db. Thus the fundamental will be the first surface wave of appreciable amplitude to arrive about 118s after the first S-wave arrival at 27°. For shorter periods, the differential arrival time is considerably longer, e.g. at periods of 30s (group velocity = 3.75 km/s), the differential time is 165s. Thus at this distance it may be difficult to separate the contributions from the long-period surface waves and the multiple reflections. The seemingly dispersive nature of the latter part of the wave train in Figure 1.3 indicates the presence of surface waves, but their existence is yet to be conclusively shown.

Overall, the nature of SHMEE is most unlike other models published for the Eurasian continent (e.g., Mayer-Rosa and Mueller, 1973; Massé and Alexander, 1974; King and Calcagnile, 1976; England et al., 1977, 1978; Nolet, 1977; Cara et al., 1980; Given and Helmberger, 1980; Burdick, 1981) which have a generally smooth appearance yet recognize sharp changes in the velocity-depth curve at depths of about 400 km and 650 km (Figure 2.5). Yet the profile of the model SHMEE is strikingly similar to those of recent complex P- and S-velocity models for the upper mantle beneath central Australia (Hales et al., 1980a; Hendrajaya, 1981; c.f. Figure 1.1).

2.5 CONCLUSIONS

In certain situations, the sequential decomposition technique is sound, particularly when the time series to be analysed is time invariant. Kanamori and Stewart (1978) have used a similar technique to decompose the February 4, 1976 Guatemala earthquake into a multishock sequence of ten subevents. It was assumed in their study that the source-time function and mechanism was similar for all subevents, thus satisfying the stationarity assumption. Under these conditions, sequential decomposition is likely to perform equally well.

The sequential decomposition technique may be less successful in

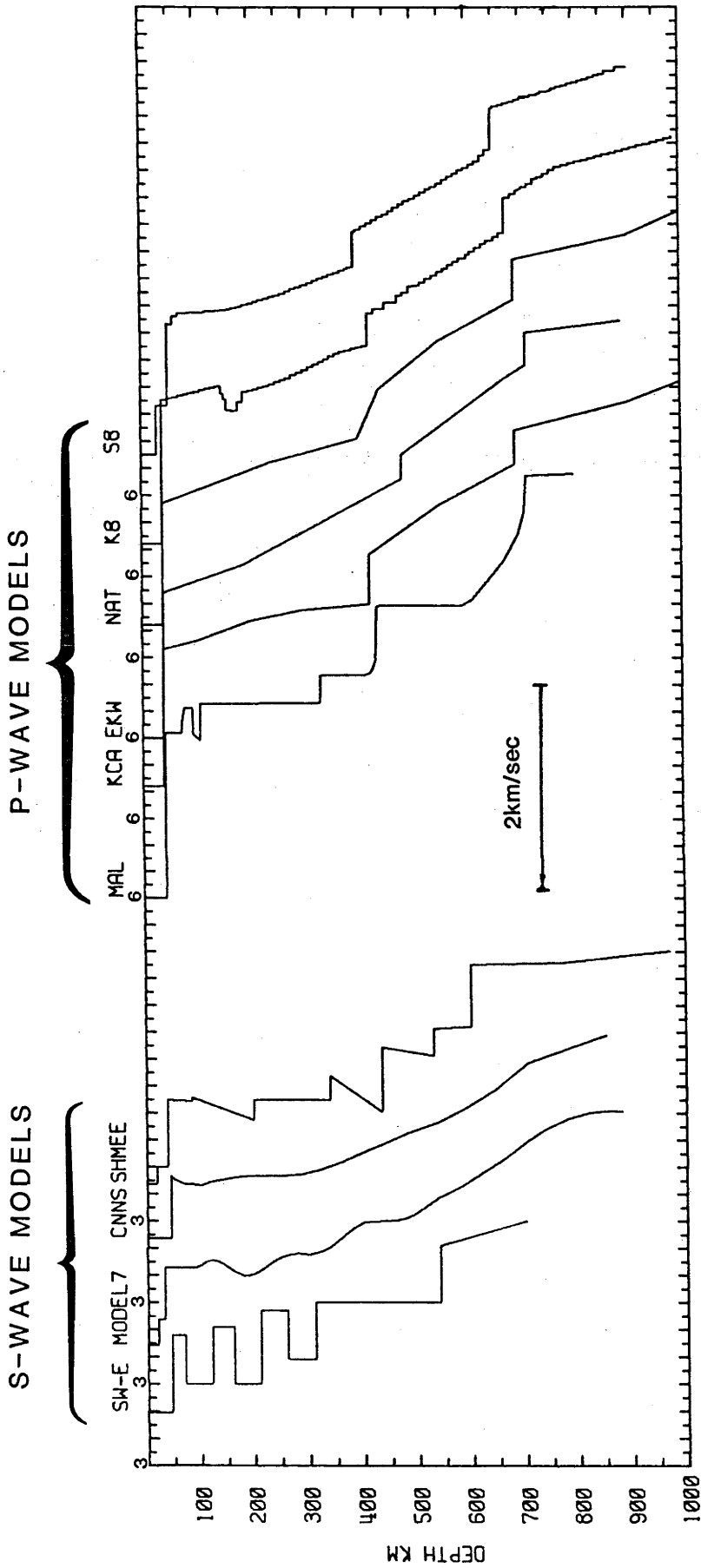


Figure 2.5: Suite of velocity models for the upper mantle beneath western Eurasia. S-wave models are SW-E (Mayer Rosa and Mueller, 1973), MODEL 7 (Nolet, 1977), CNNS (Cara et al., 1980), SHMEE (Cleary et al., 1982) and P-wave models include MA (Maße and Alexander, 1974), KCA (King and Calcagnile, 1976), EKW (England et al., 1977), NAT (England et al., 1978), K8 (Given and Helmberger, 1980) and S8 (Burdick, 1981). The curves are displaced for clarity.

examining long-period data in the distance range 20° to 30° because of the problems with non-stationarity of the component arrivals. Yet some of the tenets proposed by Cleary et al., for example multiple reflections from upper mantle structure, point to the possibility of using other than first arrivals to constrain the construction of a shear-wave velocity distribution. Despite the criticisms of SHMEE and the sequential decomposition method, it must be emphasized again that this study was the first to analyse the entire SH body-wave train at periods of less than 20s. It now remains to refine the strategy proposed in Chapter 1.

CHAPTER 3

THE DECONVOLUTION OF TELESEISMIC BODY WAVES

3.1 INTRODUCTION

From the standpoint of communications theory, the trace of a seismic event is the response of the system comprising of the Earth and recording apparatus to a finite source. In the final analysis, one is interested in the various components of the total response. As shown in the previous chapter, the response of an ideal (non-attenuating, non-dispersive and non-phase-shifting) Earth to an earthquake source, hereafter termed the Earth response, may be viewed in the far field as a sequence of "spikes".

As a first approximation, the seismic wavetrain may be modelled as the convolution of a seismic wavelet and the Earth response. The seismogram may be considered as being composed of a number of wavelets, some of which may be overlapping, all with the same shape but with differing amplitudes, viz.,

$$s_u = \sum_{t=0}^n a_t w_{u-t} \quad 3.1$$

where \underline{s} = seismogram = s_0, s_1, \dots, s_{n+m}

\underline{a} = Earth response = a_0, a_1, \dots, a_n

\underline{w} = seismic wavelet = w_0, w_1, \dots, w_m

where the seismic wavelet is the combined response of source, receiver instrument response, etc. The objective of deconvolution is to estimate one or both of the Earth response and the wavelet. The problem is essentially twofold: estimating the wavelet and designing inverse filters to reverse the convolution process. It is implicitly assumed in equation 3.1 that:

- (i). The source-time function is uniform and is independent of both azimuth and take-off angle. In general, the uniformity assumption

is not true, as the kinematic dislocation models of radiation indicate (Savage, 1966). Its validity can, however, be improved by restricting the azimuth angles, epicentral distances and time ranges of the suite of seismograms.

- (ii). Each "spike" in the Earth response represents disturbances which have travelled different paths through the Earth and that the effect of each path is the same for each "spike". This assumption is clearly the most restrictive - the path may include refraction, reflection, touching a caustic and attenuation. The overall effect will be different for different paths, but in each case, will significantly distort the "spikes".

Thus, even though seismograms recorded at teleseismic distances are not best represented by equation 3.1, available deconvolution schemes are explicitly formulated around equation 3.1. A seismogram is best represented by a linear sum of potentials, each depending upon azimuth, take-off angle from the source, source-time function and the particular ray path taken through the Earth. At present, there are no deconvolution strategies which address this problem adequately. To obtain the most from the data it is important that the seismograms are deconvolved in the best possible manner and hence the remainder of this chapter reviews the available deconvolution methodologies and their application to SH-seismic waves recorded at teleseismic distances.

3.2 SEISMIC WAVELET ESTIMATION

Before the majority of deconvolution methodologies can be used, an estimate of the wavelet must be made. It is apparent that with proper selection of $w(t)$, even without regard for its physical meaning, equation 3.1 may be solved for the unknown Earth response $a(t)$. O'Brien (1969) showed that physical measurements of the seismic pulse near the source can sometimes be used to provide wavelet estimates. This is practical in the case of source signatures of airguns which are used as an energy source for marine seismic data. Clearly it is not a realistic method of decomposing teleseismic events because of the spatially dependent nature of the

wavelet. Alternatively, statistical and deterministic techniques (which attempt to compress the recorded seismic energy into their original impulsive form) can be formulated in both time and frequency domains, and treated as problems in inverse theory. Several of these techniques are now reviewed.

3.2.1 DETERMINISTIC METHODS

For earthquakes recorded at distances beyond 30° , the first arrival may be well separated from later arrivals by a time which is greater than the dominant period of the seismic wavelet. The first arrival may then be used as an estimate of the seismic wavelet (Clayton and Wiggins, 1976; Dey-Sarkar and Wiggins, 1976). If the station coverage is sufficient and it is assumed that the source radiation pattern is uniform, the seismic wavelet may be estimated by averaging over several stations. Clearly, such an approach for estimating seismic wavelets from long-period seismograms recorded in the distance range 20° to 30° is not possible, for the first arrivals are never separated from secondary arrivals by more than 40 seconds.

3.2.2 WEINER-ROBINSON THEORY

Least-squares inverse, optimum zero-lag or simply Wiener filtering is a common method of performing deconvolution. The theory concerning digital Wiener filters and their design have been thoroughly described by Rice (1962) and Robinson and Treitel (1967). Wiener filters, by definition, give the best estimate of signal shape in the sense that the optimum filters are designed to minimize in a least-squares sense the mean-square-energy of the difference between the true signal (desired output) and the estimated signal (actual output). The resulting normal equations may be written in matrix notation as

$$\underline{Rf} = \underline{g}$$

where \underline{R} is an autocorrelation matrix of the autocorrelations of the input signal, \underline{g} is the cross-correlation of the desired output with the input and \underline{f} is the filter. Equation 3.2 may be solved by a computationally efficient recursive algorithm such as the one devised by Levinson (1947). If it is assumed that the Earth response is white, and that the wavelet is minimum-phase (so that its inverse is realizable), then, within a scale factor, the seismogram autocorrelation is equivalent to the wavelet autocorrelation and the Wiener filter may be designed without explicit knowledge of the seismic wavelet. Strictly speaking, the property of stationarity requires that all statistical moments of a time sequence be time invariant. Hence, the autocorrelation estimate is not only necessary in the design of a Wiener filter, but is also a means of monitoring the degree of non-stationarity. Since stationarity is assumed in the construction of a Wiener filter, such filters are designed on certain time gates of the data in order to accommodate this assumption. Although gate lengths are often chosen in a subjective fashion, sophisticated techniques (e.g. Wang, 1969), which utilize autocorrelation estimates may be used to determine a suitable length.

To obtain an estimate of the wavelet, another Wiener filter is applied to invert the original minimum-phase filter. Consequently, this wavelet estimation technique is termed the Wiener-Robinson double inverse method.

The minimum-phase wavelet assumption may be true for explosive sources, but it is generally not true for earthquake sources. Furthermore, Chapter 2 showed that although the Earth's response may consist of a large number of arrivals, source considerations and other factors will distort each arrival from a true delta function. Consequently, the seismogram and wavelet autocorrelations are not equivalent, and so the Wiener filter cannot be designed without explicit specification of the wavelet.

3.2.3 HOMOMORPHIC DECONVOLUTION SEISMIC WAVELET ESTIMATION

Oppenheim (1965) formulated the general theory of homomorphic filtering for the synthesis of non-linear filters which can be expressed as a convolution of components. This technique has the advantage that no assumptions about the whiteness of the Earth response and phase properties of the wavelet are required. The theory and principle of applying

homomorphic filtering have been thoroughly described by Oppenheim et al., (1968) and their use in seismology have been documented by Ulrych (1971), Ulrych et al. (1972), Lines and Ulrych (1977) and Tribolet (1979). Therefore, only a brief heuristic description of the technique will be presented.

A homomorphic filter represents a cascade of three systems; the characteristic system is a non-linear one which transforms the convolution operator of equation (3.1) to a space where the operator is additive. The complex cepstrum is the output of the characteristic system and is the input to a system where simple linear filtering or "liftering", using low, high, band-pass or comb filters are used. Finally, the inverse of the characteristic system transforms the liftered complex cepstrum from an additive space back to the original convolutional space.

A serious drawback to homomorphic deconvolution lies in the procedure of unwrapping (by adding multiples of 2π) the phase curve at each point of the estimate computed by the arctangent function. Phase unwrapping becomes more difficult if random noise is present in the time series being analysed, because the phase portion of the noise will also be random, and hence there is an uncertainty in the phase spectrum vector. To overcome this problem, Tribolet (1977) suggested that the most effective method for phase unwrapping is by adaptive integration of the phase derivative.

When using homomorphic deconvolution, it is implicitly assumed that the wavelet cepstrum has a lower quefreny (the independent variable of the cepstral domain and has the dimension time) content than the Earth response cepstrum. If this assumption is true, then the wavelet may be approximately recovered by liftering out the higher order quefreny terms. The inverse characteristic transform is then applied to the liftered cepstra. For complete separation of the wavelet cepstrum and Earth response, it is important to ensure a minimum-phase condition of the seismogram thereby removing singularities of the complex cepstrum off the unit circle. The minimum-phase condition can be imposed by exponential weighting of the seismograms.

Additive noise in the seismic model can cause major problems when using homomorphic deconvolution. Buttkus (1975) has shown that the quality of results obtained by homomorphic deconvolution is very sensitive to the signal-to-noise ratio because of the undesirable effects of noise on the phase spectrum. Clayton and Wiggins (1976) demonstrate that phase deviations due to noise become especially large when signal amplitudes are

low. Because there is no simple expression for the homomorphic transform of the additive operator, it is not obvious what happens to additive noise in the computation. Clayton and Wiggins suggest that data redundancy be used to suppress noise on the phase curves when using this method. The wavelet may be estimated by separately averaging the log-amplitude spectra and the phase spectra (equivalent to averaging the cepstra) of a suite of teleseismic recordings. However, smoothing of log spectra has the effect of decreasing the low amplitude spectral estimates relative to the dominant frequencies. In addition, error estimates of low amplitude components will be increased relative to errors in the estimation of dominant frequencies (Clements, pers.comm., 1980). The time domain representation of smoothed log spectra will thus be characterized by smooth dominant frequencies, attenuating quickly to noisy, low amplitude frequency components. These errors are cumulative during the deconvolution process.

3.2.4 WAVELET ESTIMATION BY MINIMUM ENTROPY DECONVOLUTION

Wiggins (1978) addressed the problem of determining a linear operator that maximises the "spikiness" of a representative set of traces, i.e., reducing them to the Earth response. His approach, termed minimum entropy deconvolution (MED) has been described by Ooe and Ulrych (1979) as "...representing a breakthrough in deconvolution" as it does not require any assumptions other than that the deconvolved output consists of a few large spikes of unknown and arbitrary amplitude and location separated by values close to zero. Rather than attempting to whiten data, MED seeks the smallest number of large spikes consistent with the data.

The success of MED lies in the definition of a norm that measures the simplicity of the deconvolved signal. Many of these norms have recently been applied in seismology: varimax (Wiggins, 1978), parsimonious (Claerbout, 1977) and kurtosis (Ooe and Ulrych, 1979). In their original context, these techniques were applied to multiple channel data, as the effective operators are seen to exploit differential moveout of phases across the array. Consider a multichannel input, x_{ij} , $i=1,2,\dots,N_s$, $j=1,2,\dots,N_t$, where N_s is the number of channels, and N_t the number of time samples per input trace. Application of the linear minimum entropy operator f_k , $k=1,2,\dots,N_t$, yields

$$y_{ij} = \sum_{k=1}^{N_t} f_k x_{i,j-k}$$

In terms of the simple multichannel output y_{ij} , the varimax norm is defined by

$$V = \sum_{i=1}^{N_s} V_i = \frac{\sum_{i=1}^{N_s} \sum_{j=1}^{N_t} y_{ij}^2}{\left(\sum_{j=1}^{N_t} y_{ij}^2 \right)^2}$$

The varimax norm is seen to be the sum of the normalized squares of the variances of the samples, and defines the sum of the simplicities of the filter outputs. Maximising the variance has the effect of simplifying the outputs. By comparison, maximising the kurtosis norm defines the simplicity of the set of all filter outputs. Clearly, the two are equivalent for a single input channel. In contrast, rather than emphasizing large amplitude spikes, the parsimonious norm emphasizes the small values in the data.

To solve for the filter operator (and in turn, the wavelet), the norm is differentiated with respect to the filter coefficients and equated to zero. The resulting normal equations may be written in matrix notation as

$$\underline{R}^* \underline{f} = \underline{g}^*$$

where \underline{R}^* is an autocorrelation matrix that is a weighted summation of the autocorrelations of the input signals. For the case where the varimax norm is to be maximised, \underline{g}^* is the cross-correlation column vector that is weighted summation of the cross-correlations of the cube of the outputs with the inputs. This equation is highly non-linear, but owing to the Toeplitz nature of \underline{R}^* , may be solved iteratively by assuming a value of \underline{f} , computing \underline{R}^* and \underline{g}^* , solving for \underline{f} , recomputing \underline{R}^* and \underline{g}^* , etc. This iterative sequence may not find a unique maximum value for V , as the function appears to have several maxima, but it may lead to a useful maximum.

The wavelet is estimated by taking the inverse (in either time or frequency domains) of the calculated MED filter. The performance of this filter will be evaluated later.

3.2.5 INSTRUMENT RESPONSE AS AN ESTIMATE OF THE SEISMIC WAVELET

Attenuation and dispersion preferentially modify the frequency components of the source function as it travels through the Earth. Thus, the components of the Earth response violate the stationarity assumption. Any estimation method which seeks to find an "average" seismic wavelet from one seismogram or a suite of seismograms will, of necessity, also include an "average" attenuation factor. If phase shifting were included in the basic Earth response model, then the principal effect of variations in the phase of various arrivals is that the estimated wavelet will have an "average" phase delay.

Intuitively, it seems that techniques which are not data adaptive and those that determine the operator directly from the data (such as homomorphic and MED) will "average" over the component wavelets, the deconvolved sequence neither producing spikes (in the case of a spiking filter), nor sufficient compression. Standard processing techniques will not be able to cope with a suite of wavelets all having travelled different paths through the Earth and consequently having different spectral information. Hence it is not possible to combine most of the effects such as source, attenuation and receiver-instrument functions into a "source function" in the manner attempted by Dey-Sarkar and Wiggins (1976). These problems may be circumvented by extracting only the known part of the seismogram, that is, the receiver-instrument response. Thus, unless stated otherwise, all future deconvolution in this study will use a long-period NORSAR-type instrument response as an estimate of the wavelet. The deconvolved output will then be an estimate of the ground motion.

3.3 DECONVOLUTION

In the following section, seven techniques for deconvolving seismograms will be compared. The success or failure of the methods depend on how well the input data satisfy the assumptions implicit in the various deconvolution approaches. The desirable properties of a deconvolution method are:

- (i). It should resolve arrival times and amplitudes with as little phase and amplitude distortion as possible.

- (ii). It should be stable with respect to small errors in the estimation of the components of the wavelet and non-stationarity of the Earth response. The latter point is not important if an estimate of the instrument response is used.
- (iii). It should be robust with respect to the rejection of random noise.

For the purpose of comparing the various methodologies, a synthetic Earth response as calculated in the previous chapter will be used. The synthetics calculated by the Generalized Ray method assumed infinite Q and a step-function source, so that $w(t)$ in equation 3.1 will be replaced by an estimate of the instrument response, i.e., the seismic wavelet is assumed not to include effects such as source, attenuation etc. The experiment has been designed in this manner so as to make easier visual comparison between the deconvolved sequence and the original "spike" sequence.

Figure 3.1 shows the evolution of the synthetics to be used in evaluating the various deconvolution methodologies. The wavelet (i.e., the instrument response) is convolved with the ideal Earth response at 3000 km (27°), from Figure 2.1, and the noisy synthetic is generated by adding 10% pseudo-white noise to the noise-free synthetic.

3.3.1 SPECTRAL DIVISION

The convolution model (equation 3.1) may be reformulated in the frequency domain as

$$S(i\omega) = A(i\omega) \cdot W(i\omega)$$

where the functionals are related to the time domain by Fourier transform. Deconvolution is achieved by division followed by inverse Fourier transform.

$$A(i\omega) = S(i\omega) / W(i\omega)$$

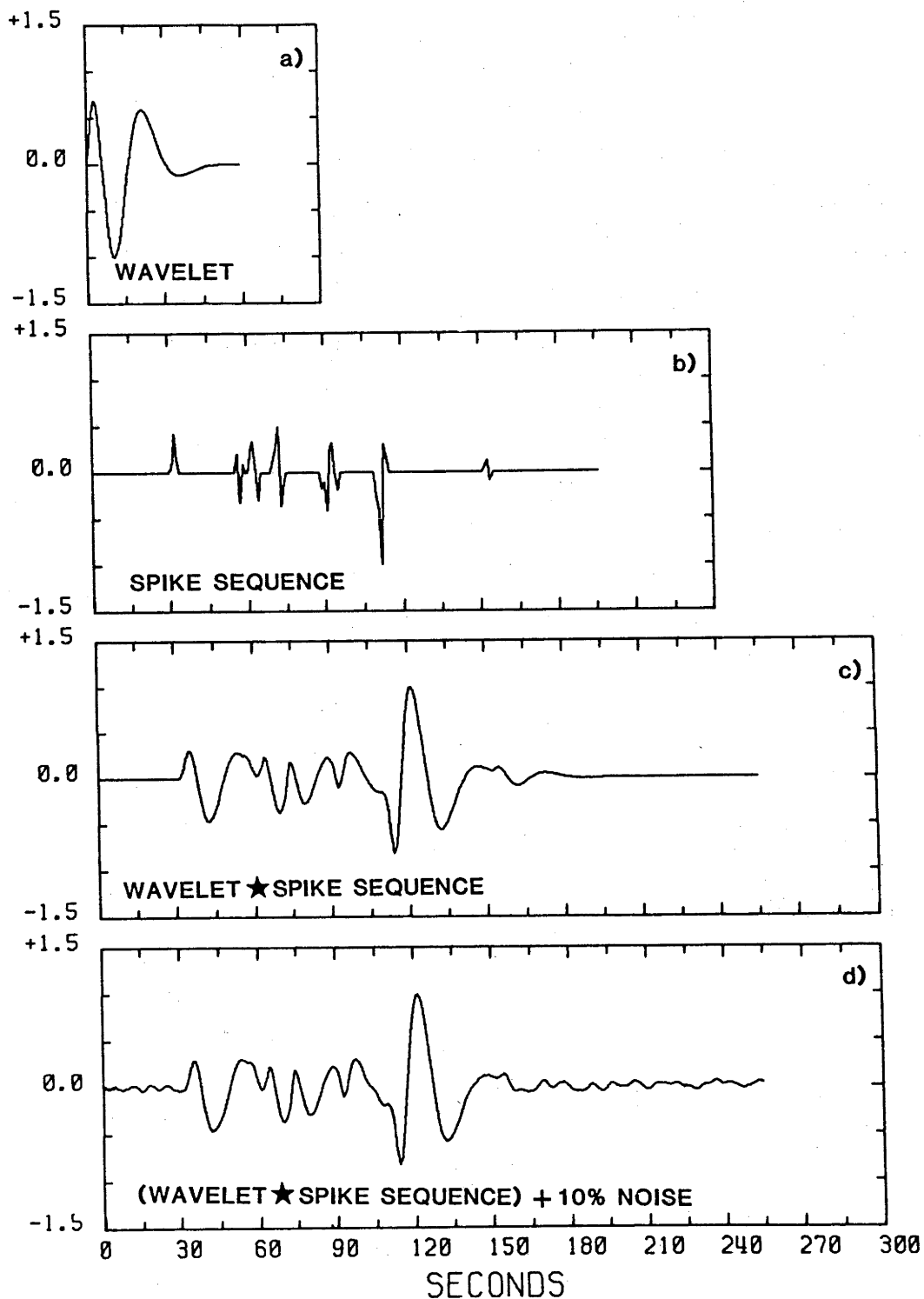


Figure 3.1: Evolution of the noise-free and noisy synthetics to be used in this chapter: a) the wavelet is the response of a NORSAR-type LP instrument; b) is the "spike" sequence (c.f. Figure 2.1, $\Delta=27^0$); c) the convolution of wavelet and spike sequence; d) synthetic with 10% additive band-passed noise. All traces in this chapter are shown trace normalized to peak amplitude.

This method has many advantages including simplicity of implementation, computational speed, and does not require assumptions about the phase properties of the wavelet $w(t)$. Problems may arise during division when spectral locations in the wavelet becoming vanishingly small. These may be overcome either by adding noise to the time series, or by constraining the minimum allowable source amplitude level, termed the waterlevel (Helmberger and Wiggins, 1971; Clayton and Wiggins, 1976; Dey-Sarkar and Wiggins, 1976). Thus, the deconvolution becomes

$$A(i\omega) = S(i\omega)W^+(i\omega)/Q_{SS}(i\omega) \quad 3.5$$

(Dey-Sarkar, 1974) where $+$ denotes conjugation, the numerator is the cross-spectrum of the desired output (in this case, the original seismogram) and input (the wavelet), and the denominator is given by

$$Q_{SS}(i\omega) = \max\{W(i\omega)W^+(i\omega), k_{\max, \omega}[W(i\omega)W^+(i\omega)]\}$$

where k is the waterlevel parameter ($0 \leq k \leq 1$). The division 3.5 prevents the denominator from being zero if at any frequency W goes to zero. The waterlevel parameter can be thought of as a limit on the gain of the filter $1/W$ in spectral regions where the seismogram has little or no information, and is conveniently expressed as a function of the maximum seismic wavelet amplitude. Note that if $k \rightarrow 0$, equation 3.5 becomes the unrestricted deconvolution 3.4, and for $k \rightarrow 1$, $Q_{SS}(i\omega) = \text{constant}$ and equation 3.5 becomes

$$A(i\omega) = S(i\omega)W^+(i\omega)/k$$

which is simply the scaled cross-spectrum of the original seismogram with the seismic wavelet. An optimum level of k is chosen by performing several runs for a range of k , $0 \leq k \leq 1$, and the stability of the deconvolution is checked by subjectively examining the recovered Earth response for the various waterlevels.

Figure 3.2 shows the example of deconvolution by spectral division of the synthetics in Figure 3.1. The top trace shows unrestricted deconvolution ($k=0$) of the noise-free synthetic, and appears exact. The second trace is

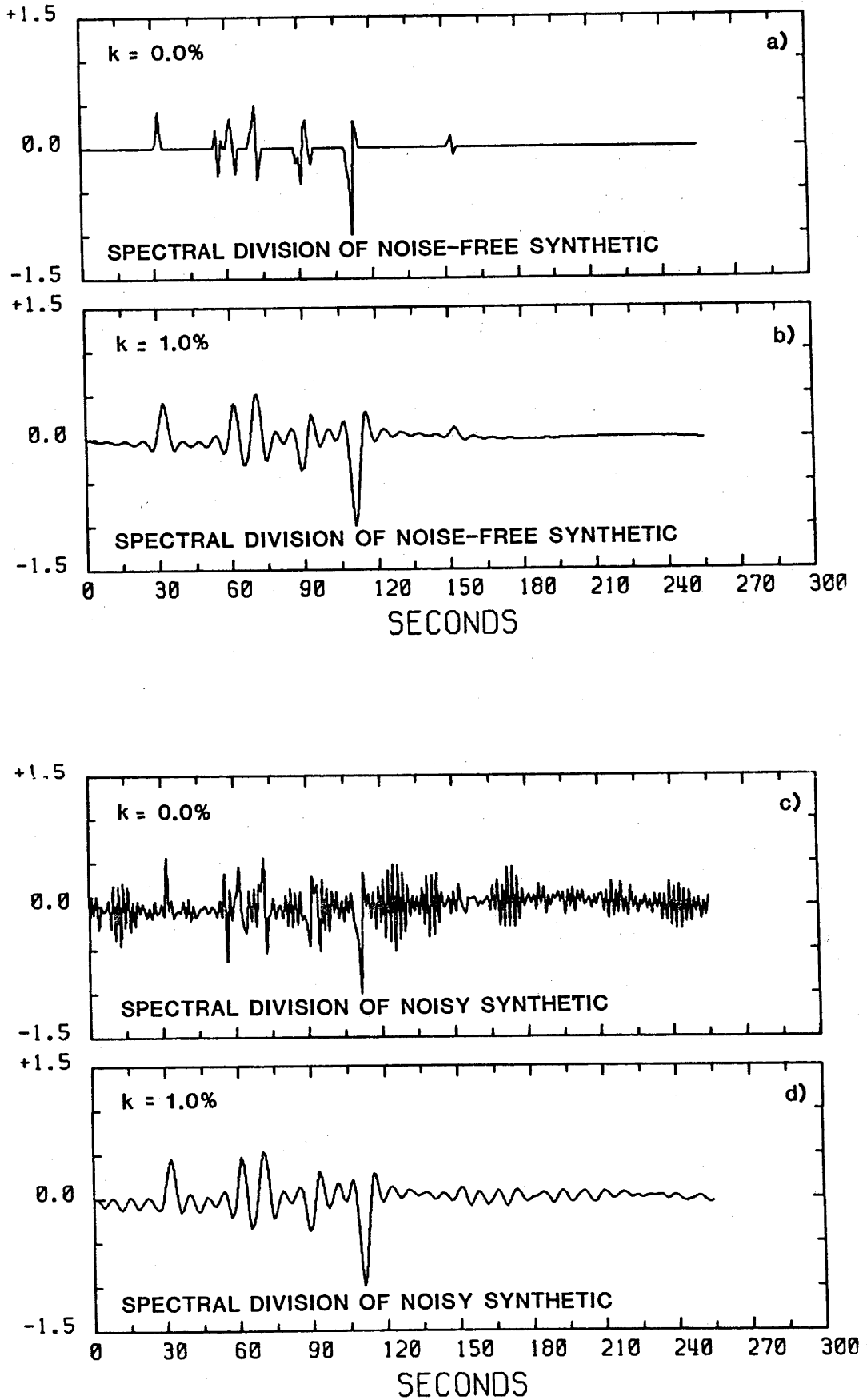


Figure 3.2: Deconvolution by spectral division: noise-free synthetic deconvolved with a) $k=0$; b) $k=1\%$; noisy synthetic deconvolved with c) $k=0$, d) $k=1\%$.

deconvolution with $k=0.01$. The result is a loss of precision in estimating the arrival times, and considerable smoothing of the higher frequencies. The third trace is an attempt at unrestrictive deconvolution of the noisy synthetic. Even though the seismic wavelet has a well-defined and smoothly varying spectra, the addition of noise has introduced regions of low gain in the seismograms spectra. Thus the spectra after division fluctuates rapidly which in the time domain appears as noise bursts. This is reduced by setting $k=0.01$ as shown in the lower trace. Again there has been a loss in precision of arrival times and wavelet shape, but the decision to compromise on arrival times and amplitudes is not hard to make. The effect of non-zero waterlevels is similar to prewhitening prior to deconvolution in the time domain, and will be discussed later.

3.3.2 HOMOMORPHIC DECONVOLUTION

As described elsewhere, sequences which are convolved in the time domain are additive in the cepstral domain. If the low quefreny assumption is true then the wavelet may be approximately recovered by "liftering" out the higher order quefreny terms. Using this estimate of the wavelet, an inverse filter may then be designed in either time or frequency domains. The inverse filter is then applied to the original seismogram, thus achieving deconvolution.

This process is examined in Figure 3.3. The top trace is the complex cepstrum of the noise-free synthetic. The wavelet cepstrum is estimated by setting the complex cepstrum to zero for values of $|t|$ (indicated by arrows) greater than some cut-off. If the width of the boxcar lifter is taken as the seismic wavelet length it now becomes clear why the low quefreny assumption is so important. For example, if the first and second arrivals in the Earth response are at $t=0$ and $t=t'$, respectively, the first spikes in the cepstrum of the Earth response are also at $t=0$ and $t=t'$. Thus ideal deconvolution or a complete separation of the wavelet cepstrum is localized within the cepstral window width $|t'|$. Now from Figure 3.1, this is clearly not the case: there are at least 4 arrivals within the wavelet length, about 60s long.

For the lifter points indicated in the cepstrum of Figure 3.3 the recovered wavelet (second trace) is seen not to be similar to the original

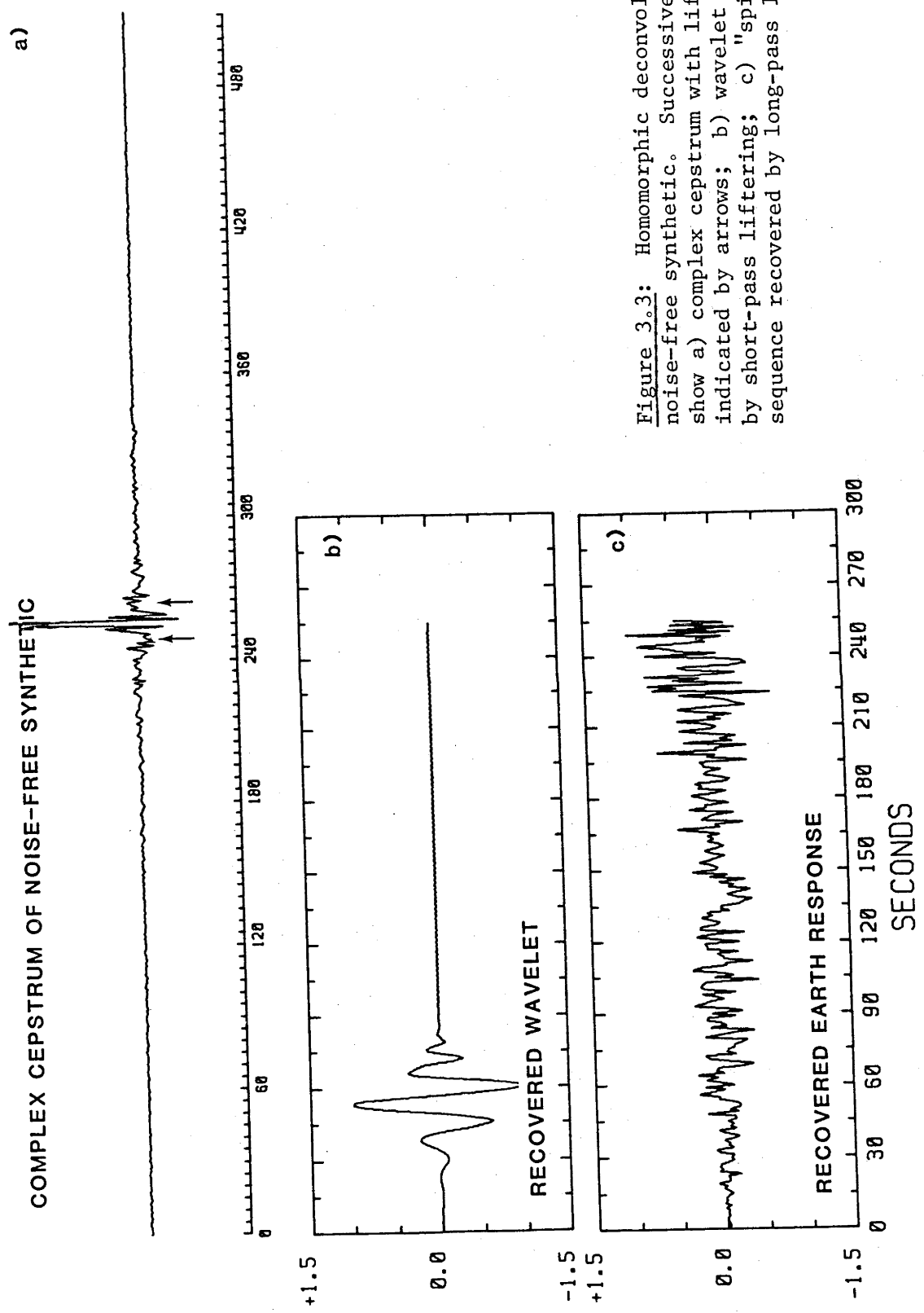


Figure 3.3: Homomorphic deconvolution of noise-free synthetic. Successive panels show a) complex cepstrum with lifter points indicated by arrows; b) wavelet recovered by short-pass liftering; c) "spike" sequence recovered by long-pass liftering.

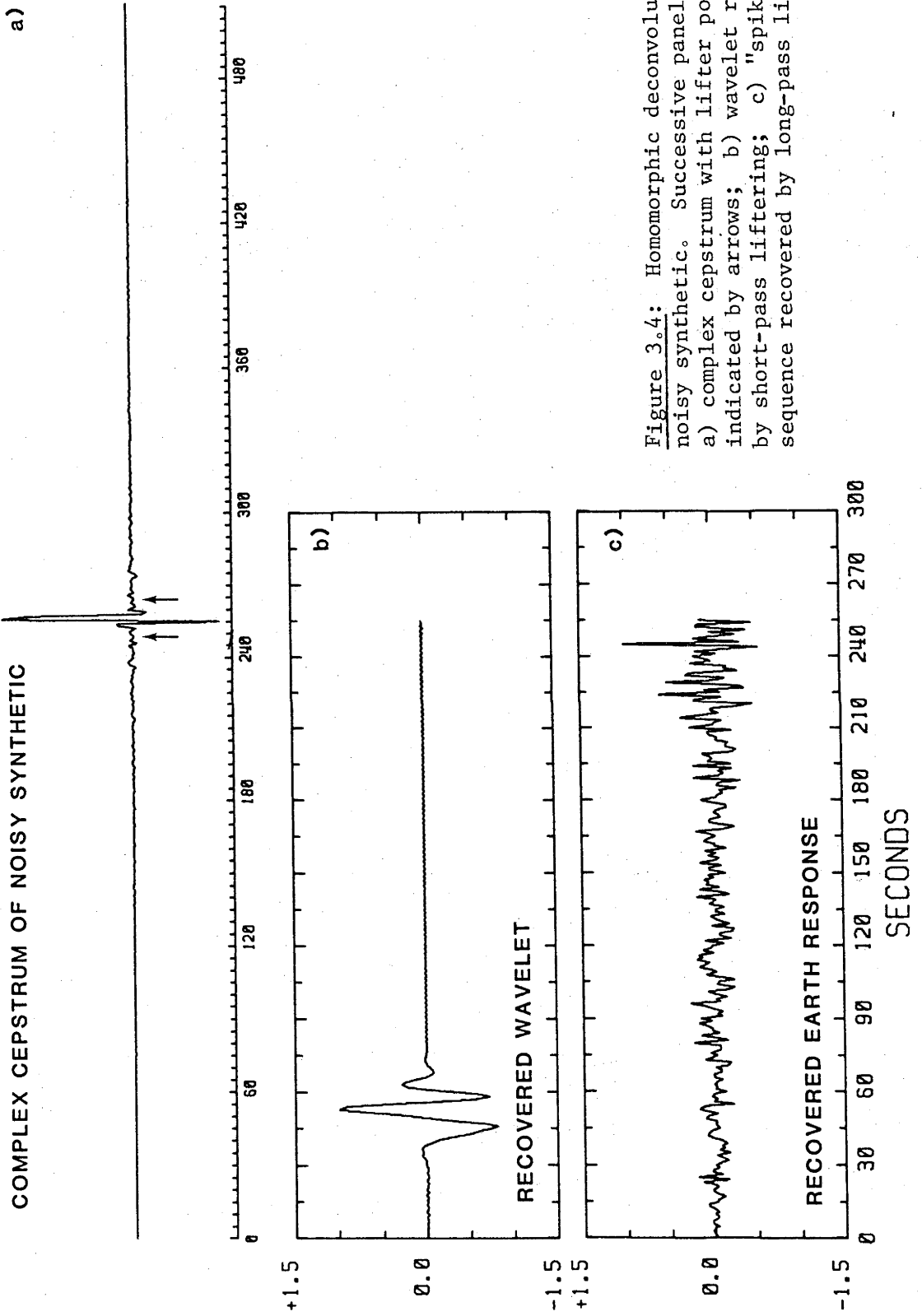


Figure 3.4: Homomorphic deconvolution of noisy synthetic. Successive panels show a) complex cepstrum with lifter points indicated by arrows; b) wavelet recovered by short-pass liftering; c) "spike" sequence recovered by long-pass liftering.

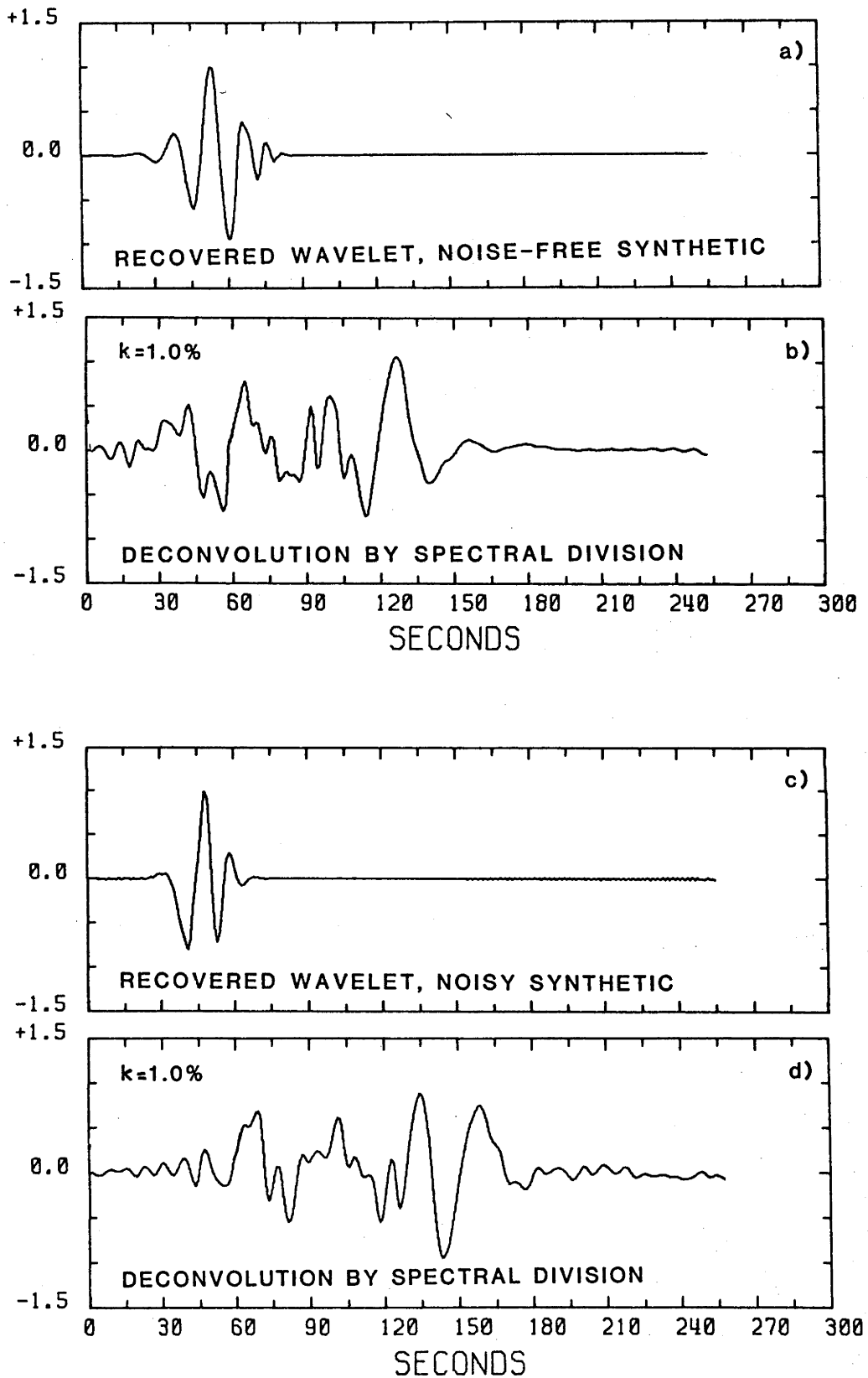


Figure 3.5: Deconvolution by spectral division ($k=1\%$) with homomorphic estimates of wavelet; a) wavelet recovered from noise-free synthetic (Figure 3.3b); b) deconvolved noise-free synthetic; c) wavelet recovered from noisy synthetic (Figure 3.4b); d) deconvolved noisy synthetic.

wavelet of Figure 3.1. The poor performance is due to the violation of the quefreny assumptions.

One may be tempted to recover the Earth response directly by setting to zero values of the complex cepstrum at times less than $|t|$. The estimated Earth response, i.e. the deconvolved synthetic, is the third trace of Figure 3.3.

Figure 3.4 examines the effect of additive noise in the deconvolution. The recovered wavelet and Earth response are not readily interpretable as representing a physical system. That the Earth response is poorly estimated is not unexpected: Lines and Ulrych (1977) warned against recovering the Earth response in this manner in the presence of noise.

Using the estimates of the seismic wavelet in Figures 3.3 and 3.4, the noise-free and noisy synthetics are deconvolved by spectral division with $k = 0.01$ and shown in Figure 3.5. A non-zero waterlevel was used because the character of the recovered wavelets indicated the possible presence of spurious spectral lines. Clearly, homomorphic deconvolution as applied to synthetic teleseismic data is not a workable method as it does not perform any of the fundamental tasks of a deconvolution method outlined above.

Clayton and Wiggins (1976) were able to use the technique of log-spectral averaging with short-period data. However, in view of the failure of long-period data to meet the low quefreny condition and the problems with additive noise and attenuation (which are not linear components in the cepstral domain), the homomorphic method will no longer be considered a viable technique in its application to the deconvolution of long-period, teleseismic data recorded in the distance range 20° to 30° .

3.3.3 TIME DOMAIN TECHNIQUES

Five methods of deconvolution in the time domain are now compared. In the design and operation of these methods, it is often necessary to apply prewhitening to prevent computational singularities. Prewhitening involves adding a constant to the spectrum of the seismic wavelet or equivalently, adding white noise to the wavelet, thus eliminating zeros in the wavelet spectrum. The concept of prewhitening is discussed by Treitel and Robinson (1966) as a means of satisfying two objectives in designing an inverse filter for a wavelet containing additive noise. These objectives are:

- (i). Shaping the wavelet to a spike, and
- (ii). Producing as little output power as possible when the input is stationary random noise.

When the additive noise is truly random, then the only contribution to the autocorrelation term $R(t)$ in the normal equations 3.2 is at zero lag, and so prewhitening replaces $R(0)$ by $\delta^2(R(0))$. An estimate of δ^2 , the prewhitening factor, determines which of these two filtering objectives is weighted most heavily. In this manner, the inverse filter can adapt to the noise in seismic recordings.

It will be noted that deconvolutions are considerably enhanced if the stability assumptions during recursion are relaxed. However, to diminish the risk of computational instability in solving the normal equations 3.2 for real data, prewhitening will be a matter of course.

Prewhitening may be seen as a means of preventing excessive roundoff errors which arise in the case of ill-conditioning. Because a well-conditioned system of normal equations is insensitive to moderate prewhitening, the application of 1% prewhitening to calculations prior to solution constitutes a reasonable compromise (Treitel and Wang, 1976). Indeed, ill-conditioning is the result of using a linear operator to deconvolve a non-linear system, and accounts for most of the problems encountered during deconvolution. This is yet another reason why it is important to remove only the effects of the instrument response.

When designing inverse filters for real data, rather than prewhitening, the desired output may be set equal to a triangular or trapezoidal function rather than a spike. The justification for this lies in the fact that the real Earth response is strictly band-limited, rather than the "spike" sequence used to generate the synthetics in Figure 3.1. Thus, in the band-limited case, the recursion algorithm would have difficulty designing an inverse filter with frequencies that do not exist.

WIENER-ROBINSON DECONVOLUTION

Using a wavelet estimate as input and choosing a spike as a desired output allows us to design an inverse filter. This inverse filter is then convolved with the original data to give the deconvolved output.

Other than level of prewhitening, two other factors must be decided upon before designing the spiking filter: filter length and position (lag) of the spike. The least-squares inverse filter will have zero error if it is of infinite length. However, the impracticality of infinitely-long filters and computational round-off errors are factors which restrict the filter length. An appropriate filter length often lies somewhere between one and two times the wavelet length (Lines and Ulrych, 1977). The optimum filter length may be achieved by performing trial runs, or using the objective final prediction error approach of Akaike (1969). This criterion chooses a filter length which minimizes the sum of the prediction error power and the error power associated with filter coefficient estimation.

The other factor is position of the spike in the desired output. The zero-delay position for the spike will only be optimal in cases where the wavelet is minimum-phase. Treitel and Robinson (1966) show that filter performance will improve if delays in the spike position of the desired output are allowed. For example, for a mixed-phase wavelet, the spike should be placed approximately in the middle of the desired output trace. However, to use a delay of n samples in the desired output requires a good estimate of the first n samples of the wavelet in order to determine $g(0), g(1), \dots, g(n), 0, \dots, 0$ in the normal equations 3.2.

Because this study will be using array data, it is necessary to examine the possibility of using multichannel Wiener-Robinson deconvolution (Wiggins and Robinson, 1965). Multichannel deconvolution involves estimating wavelets from the traces in a single-channel fashion and then designing a multichannel inverse filter which will convert these estimated wavelets to a single-channel spike sequence. The problems of estimating the seismic wavelet are the same as for the single-channel case. However, Davies and Mercado (1968) showed that the improvements of multichannel deconvolution over combinations of single-channel deconvolutions and stacking were insignificant. Thus, consideration will be given only to single-channel Wiener-Robinson filters.

In Figures 3.6 and 3.7 are shown the optimum finite length inverse filters of the instrument response for 0 and 1% prewhitening. The lowermost two traces in each of the figures represent the convolutions of the inverse filters with the noise-free and noisy synthetic data. The filters obtained using no prewhitening, give outputs that are more highly resolved than those with prewhitening, but contain considerable high frequency noise. In the case of the noise-free synthetic, the resolution

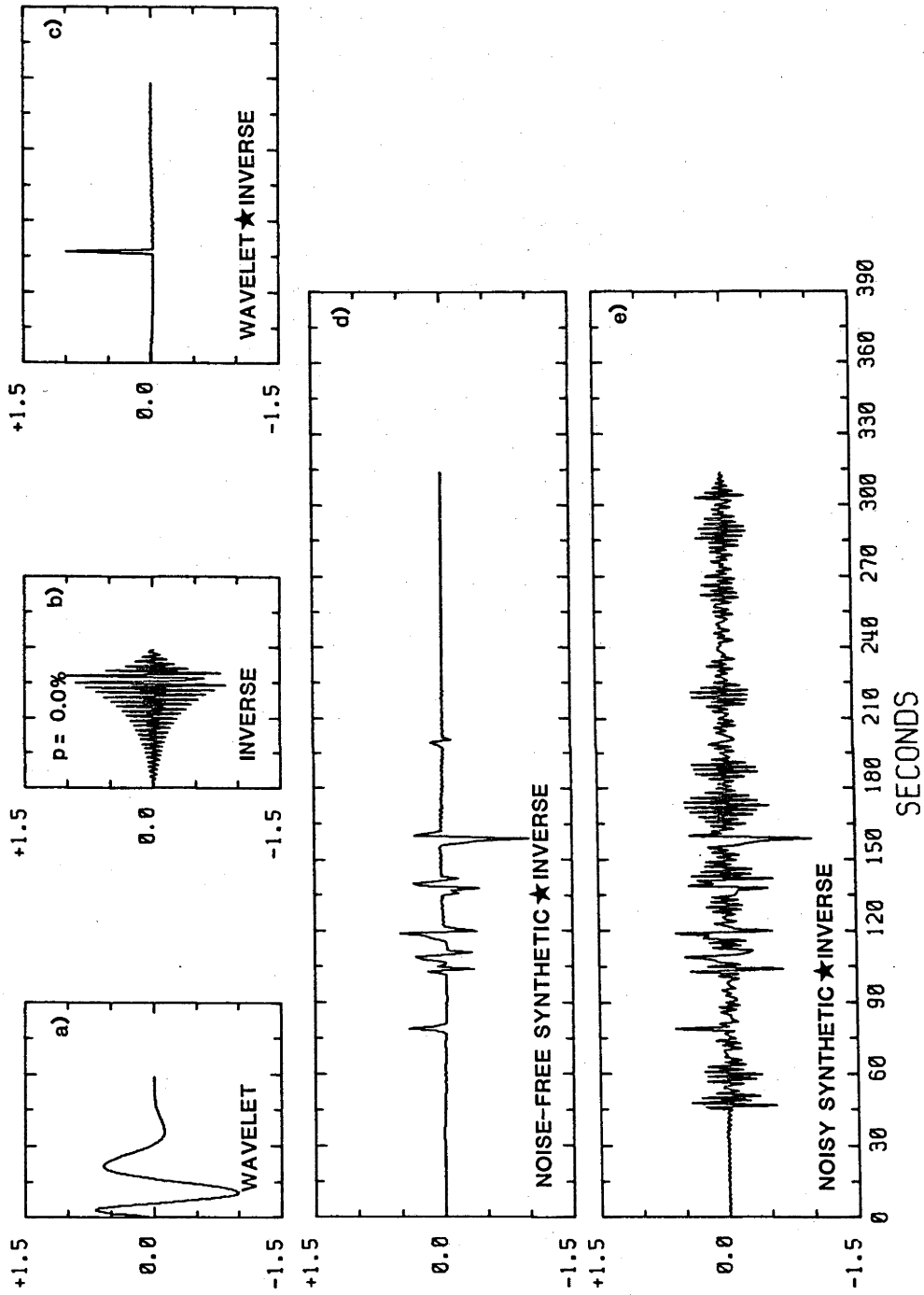


Figure 3.6: Wiener-Robinson filtering without prewhitening: a) wavelet; b) optimum least-squares inverse filter with $p=0\%$; c) convolution of wavelet with inverse; d) convolution of noise-free synthetic with inverse; e) convolution of noisy synthetic with inverse. The delay properties of the spike in c) are obvious.

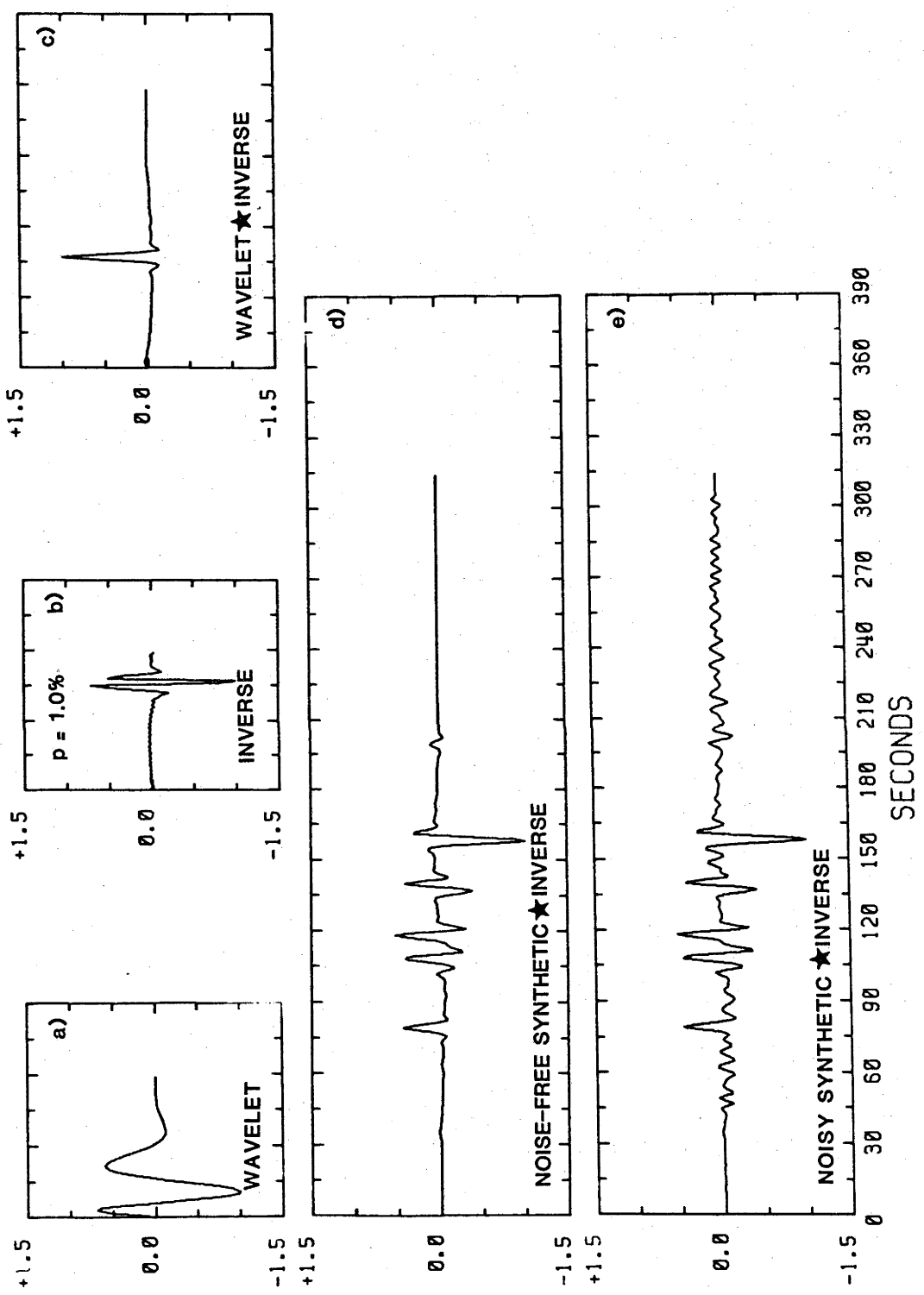


Figure 3.7: Wiener-Robinson filtering with prewhitening: a) wavelet; b) optimum least-squares inverse filter with $p=1\%$; c) convolution of wavelet with inverse; d) convolution of noise-free synthetic with inverse; e) convolution of noisy synthetic with inverse. The delay properties of the spike in c) are

is very good and the level of high frequency noise acceptable. Of course, this noise will be zero for infinitely-long filters. However, the level of high frequency noise in the deconvolved noisy synthetic is unacceptable. Thus, when choosing a level of prewhitening, a compromise between resolution and the amount of high frequency noise must be considered.

WAVELET EXTRACTION

Treitel and Robinson (1966), de Voogd (1974) and Mereu (1976) have demonstrated that filters which shape the seismic wavelet to some form other than a spike may also prove useful in deconvolution. For example, rather than a spike, a boxcar or semicircle may be specified. Such filters are called shaping filters.

Rather than designing a filter to shape the wavelet into some geometrically "pure" (or otherwise) function, it seems eminently reasonable to design a filter which shapes the wavelet to the seismogram. Thus, the designed inverse filter is directly found to be the Earth response.

Equation 3.1 can be directly solved for the unknown a_i using least-squares because with this model, the data time series is seen to be a superposition of overlapping identically shaped wavelets, each displaced in time and having amplitudes corresponding to the appropriate input value. Using conventional least-squares to minimize the total sum of the errors with respect to the unknown a_i leads to the matrix equation

$$\underline{R} \underline{a} = \underline{g}' \quad 3.6$$

where \underline{R} and \underline{a} have been defined earlier and \underline{g}' is identified as the cross-correlation vector of the wavelet with the seismogram. Equation 3.6 is the time domain equivalent of deconvolution by spectral division (equation 3.4).

If the wavelet $w(t)$, and thus the seismogram, is of a transient nature, the matrix \underline{R} is Toeplitz so that equation 3.6 may be solved by an efficient algorithm such as the Levinson recursion. Because no assumptions are made concerning the phase of either the wavelet or the seismogram, then in the absence of noise, the unknown a_i can be recovered with an accuracy which is

dependent only on the precision with which the wavelet is known and by computational round-off errors.

Inspection of equation 3.6 shows that this is precisely the same equation as is used in classical Wiener-Robinson filter theory. In fact, the convolution model is given in Robinson's (1957) treatise on predictive decomposition. Robinson's aim, however, was to design a filter rather than achieve deconvolution directly. Wiener-Robinson filtering requires two distinct steps:

- (i). Designing an inverse filter.
- (ii). Convoluting this inverse filter with the original data
(see Figure 3.8).

Generally, the desired output of a spiking filter will contain frequencies not found in either the wavelet or the data, and thus the filtering may be accompanied by considerable noise. On the other hand, the formulation leading to solving equation 3.6 seeks to shape the wavelet to the recorded data, i.e., the output of equation 3.6 is the deconvolved data and is achieved in a single operation (see Figure 3.8). Wavelet extraction utilizes the information inherent in the seismic wavelet and data only, and so in the noise-free case, no information is lost or added. Viewing the demarcation semantically, the Wiener-Robinson approach is a filtering operation rather than deconvolution, whereas the approach presented here is in fact de-convoluting the system, i.e., restoring the system to its pre-convolved state. The latter solution does not appear to have been exploited previously.

Implementation of equation 3.6 on a digital computer can be made via any standard least-squares shaping-filter algorithm. The input to such routines must, however, be redefined: the wavelet is the input, the desired output is the cross-correlation of the data with the wavelet, and the output of the algorithm (the "filter") is the deconvolved signal. At this point, the solution to equation 3.6 is seen to be minimum-phase by nature of the Levinson Recursion only if \underline{g}' is minimum-phase. This assumption does not invoke any difficulties as applied in seismology for the minimum-phase condition entails that the reflection and impedance coefficients constituting the time series \underline{a} are bounded by unity (Claerbout, 1976). It is important that both the wavelet and seismogram have zero DC component prior to wavelet extraction, otherwise the recovered

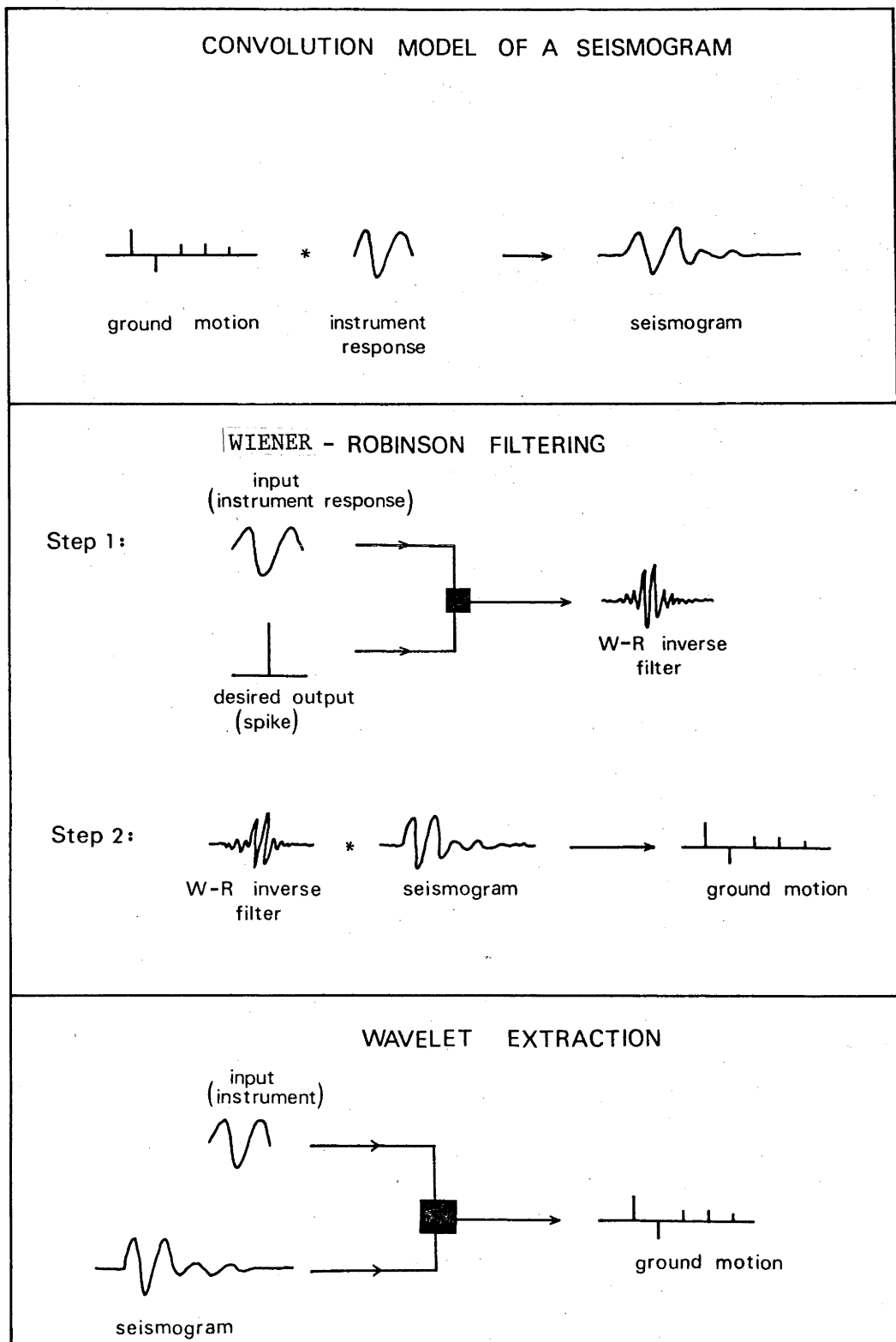


Figure 3.8: Cartoon comparing the Wiener-Robinson filtering system with the wavelet extraction system. The black box represents any algorithm solving the linear equations $\underline{R} \underline{a} = \underline{g}$.

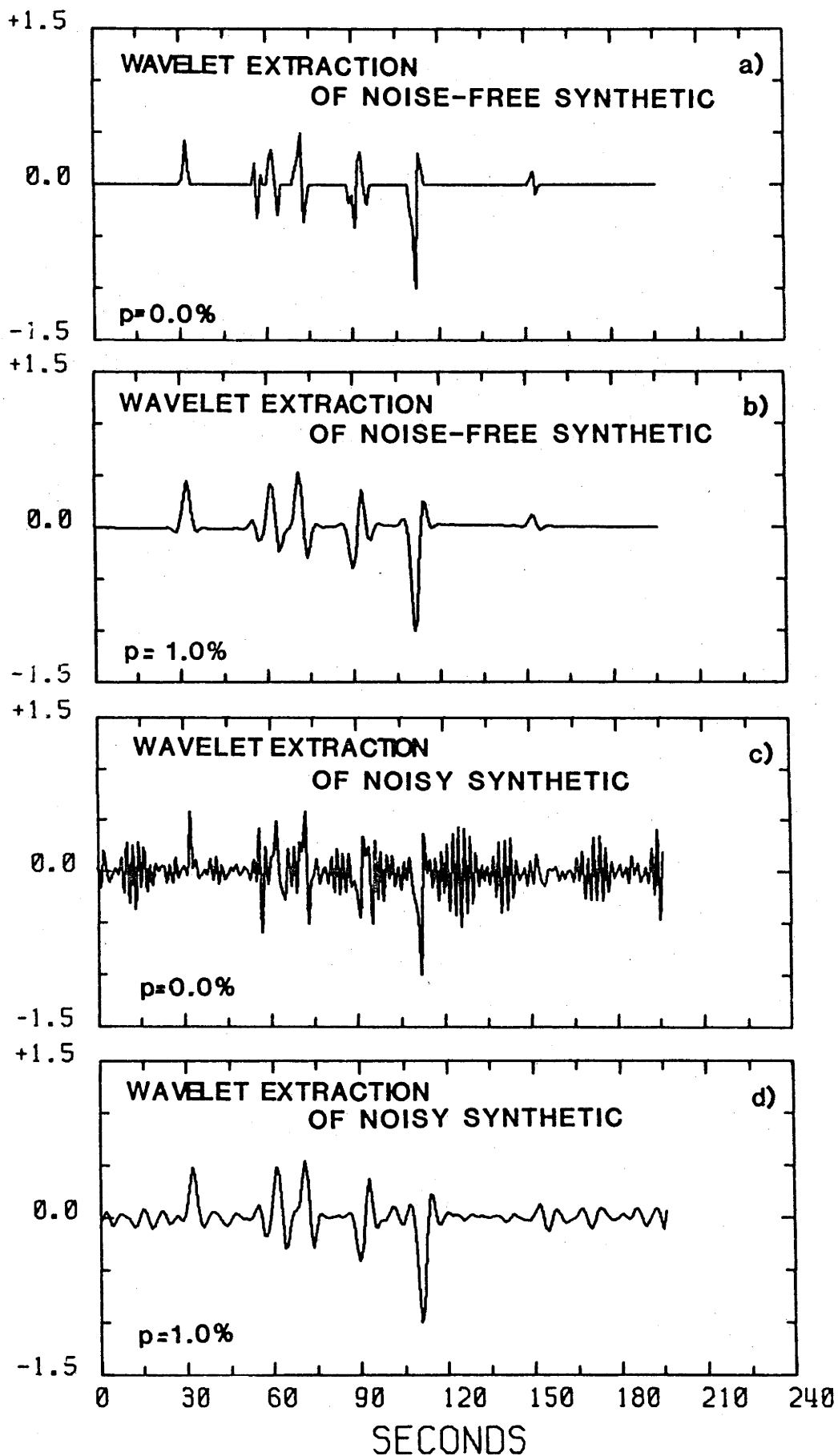


Figure 3.9: Performance of wavelet extraction: deconvolution of noise-free synthetics with a) 0% and b) 1% prewhitening; deconvolution of noisy synthetic with c) 0% and d) 1% prewhitening.

sequence may have an added ambient white spectra, resulting in considerable noise in the output. This behaviour indicates similarities with deconvolution by spectral division. However, division with a wavelet that has zeroed spectral lines is not possible (although $\lim_{x \rightarrow 0} x/x=1$) without establishing a minimum non-zero spectral amplitude, whereas wavelet extraction with a similar wavelet can be performed easily.

Even though wavelet extraction and deconvolution by spectral division are fundamentally equivalent, differences arise in the way the Fourier frequency components are estimated. This difference can be understood if the Fast Fourier Transform (FFT) is seen as a least-squares algorithm that fits an infinitely-long data vector with a sum of infinitely-long series of sine and cosine functions of differing frequencies, amplitudes and phases. The amplitudes of the different frequency components are thus averages over the entire window of the trace being fitted, rather than values appropriate to a single instant in time. Therefore, spectral deconvolution is a division of one "averaged" frequency by another, resulting in a poor estimate of the frequency of the deconvolved trace. The problem is compounded by the use of finite time series. On the other hand, equation 3.1 ensures that each point on the trace \underline{s} is uniquely composed of a linear combination of $2m + 1$ (which is much smaller than $n + m + 1$) points of \underline{w} . Thus solving equation 3.6 and fitting a transient function \underline{w} to the data may determine each point on the deconvolved trace more accurately than by spectral division.

The performance of wavelet extraction is examined in Figure 3.9. Deconvolution of the noise-free synthetic recovers the original "spike" sequence exactly. Where prewhitening of the autocorrelation matrix precedes inversion, equation 3.6 becomes the time domain analog of equation 3.5 which can be seen by comparing Figure 3.9 with Figure 3.2. Any differences between the two techniques are most likely due to the nature of the FFT as outlined above.

MINIMUM ENTROPY DECONVOLUTION

MED makes no assumption about the phase characteristics of the seismic wavelet or the whiteness of the putative spike sequence. Nevertheless, it is important to have:

- (i). For single-channel data, a trace length containing significant arrivals that is much longer than the filter. The filter length is dependent upon the length of the seismic wavelet, and spike position; too short a filter may not be able to resolve the "spike" sequence.
- (ii). For multichannel input, several traces for which arrivals exhibit moveout across the array. Constraints are considerably relaxed for multichannel input.

Figure 3.10 shows the application of MED to the noise-free single-channel case. The estimated filter operator and its least-squares inverse, i.e., the recovered wavelet, are shown at the top of the figure. In this example, no prewhitening was applied to equation 3.3. Even though the recovered wavelet is dissimilar to the original wavelet used to generate the synthetics (Figure 3.1), the MED operator has been successful in spiking the synthetic. Panels e) to h) of Figure 3.10 consider the case of 1% prewhitening applied to the autocorrelation in equation 3.3. Figure 3.11 is the same as Figure 3.10, except that the application of MED to the noisy single-channel synthetic is considered.

Because this study has access to array data, it seems reasonable to examine multichannel MED. Even though the data are long-period, the 110 km aperture of the NORSAR array should allow a certain amount of relative moveout of the different arrivals, thus allowing the operator to work more efficiently than in the single-channel case. The performance of multichannel MED on synthetic data have been thoroughly examined by Wiggins (1978), and Ooe and Ulrych (1979), where it can be seen to work very successfully, in nearly all cases contracting the seismic wavelet energy almost to a pure spike. To examine the shortcomings (if any) of MED, it is necessary to depart from the formulation followed in this chapter whilst examining other methods, and use observed data. If both the experiment and data are carefully chosen, then a greater understanding may be gained than if the same experiment were performed on synthetic multichannel data.

To this end, an event in the Hindu Kush has been chosen. The distance of 44° to NORSAR and ISC depth of 207 km ensures that the first S arrival is clearly separated from later arrivals. The long-period HT outputs are plotted as a function of distance in Figure 3.12, and the data window has been chosen to include S, sS and phases with different apparent velocities such as ScS, SS, SSS etc. The simple nature of the first two arrivals S

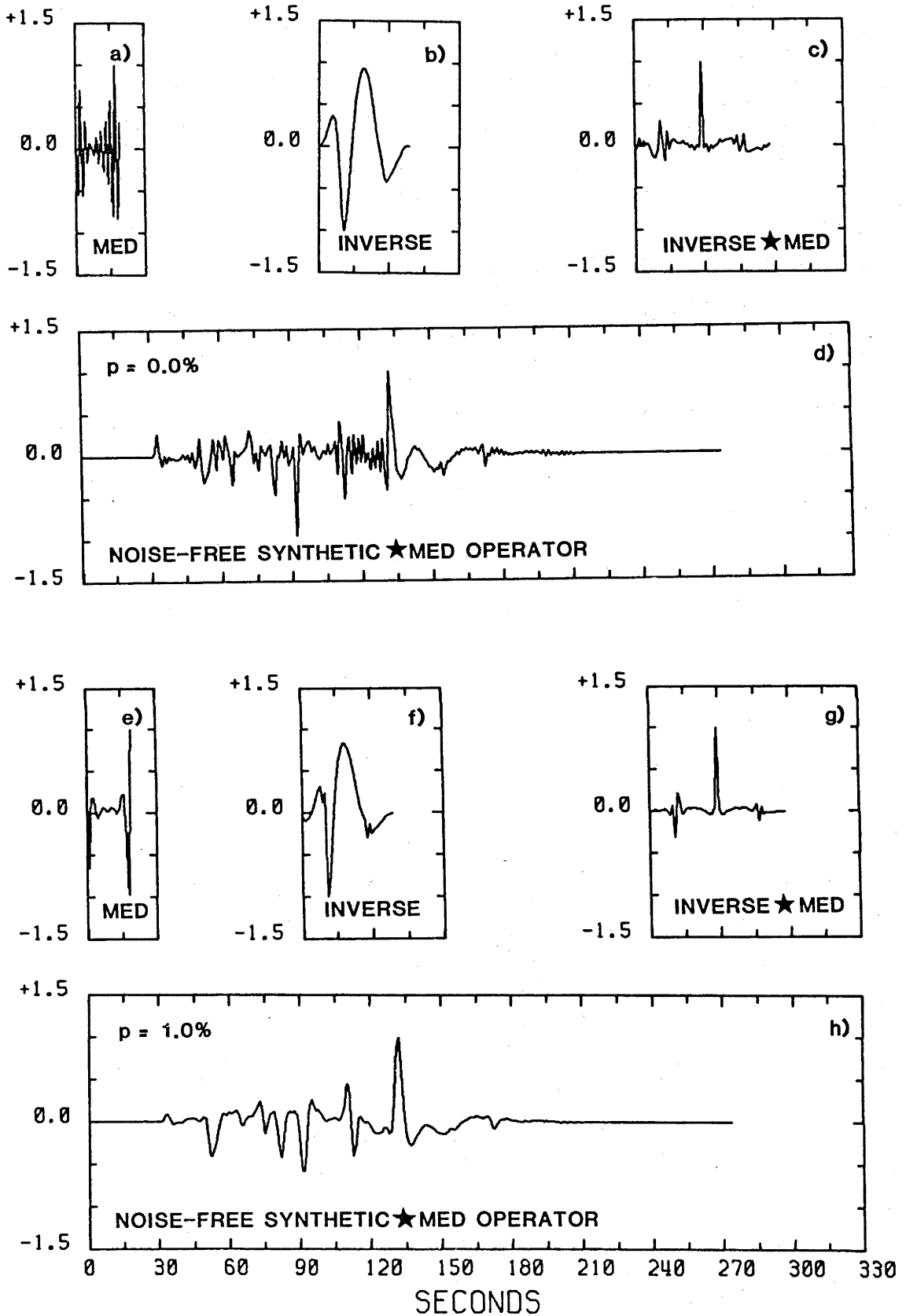


Figure 3.10: Performance of single-channel MED on noise-free synthetic: a) 15s MED operator determined with 10 iterations with no prewhitening; b) optimum least-squares inverse of operator; c) convolution of inverse with operator; d) convolution of synthetic with operator; panels e) - h) same as panels a) - d) but with 1% prewhitening.

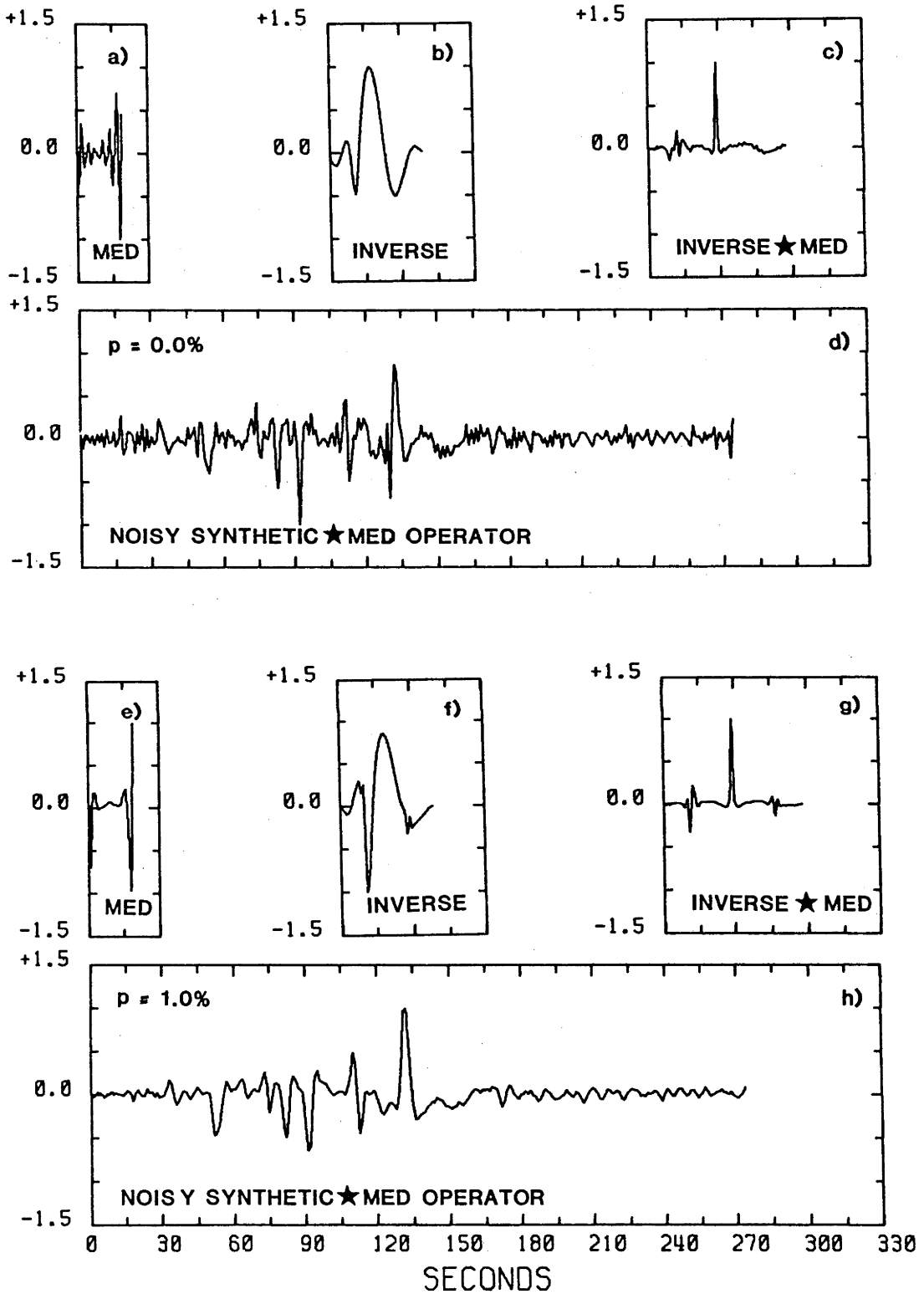


Figure 3.11: Performance of single-channel MED on noisy synthetic. Panel captions are the same as given in Figure 3.10.

and sS allow accurate measurements of arrival times and amplitudes. Incidentally, the sS-S separation of 75 seconds indicates a focal depth of about 195 km rather than ISC's estimate of 207 km. The sequence of arrivals after sS and S are obviously of a much more complex nature, consisting of a superposition of interfering ScS, SS, SSS and others. SS and SSS will be rotated in phase by $\pi/2$ and π radians from S respectively (Hill, 1974; Choy and Richards, 1975), rendering identification of phases in this part of the record even more difficult.

Figure 3.13 shows the application of MED to the multichannel data in Figure 3.12. Although only one output channel is shown, the entire array output has been utilized in designing the optimum filter operator, and was gated to use only S and sS phases. The optimum operator and its least-squares inverse are also shown in Figure 3.13. The full data window including ScS, SS and SSS phases was convolved with this operator. The deconvolution is most acceptable, the S and SS phases compressed into "spikes" and there has been significant signal compression in the later arrivals. Because the MED operator is designed on a criterion of simplicity, it has had no trouble in compressing the mirror-image S/sS pair into spikes. The rippling after the sS phase is due to crustal reverberation and has a period of 15 seconds. For the appropriate slowness of sS, this period equates to a crustal thickness of 64 km beneath the Hindu Kush, which is in accordance with the estimate of 65 km from deep seismic sounding (Kosminskaya et al., 1958) and 65 to 70 km from Rayleigh-wave dispersion analysis (Gupta and Narain, 1967). If, however, the later phases are included in the operator design, MED admits considerable phase distortion and is far from satisfactory (Figure 3.13k). In this instance, the MED operator has failed to achieve its most important design criterion. The phase uncertainty with the optimal MED operator with regard to shaping the S and sS arrivals indicates that there are arrivals with non-zero phase shifts in the latter part of the seismic wave train, emphasizing the fact that MED has had to "average" over the component wavelets.

For comparison, Figure 3.13m shows the data after the instrument response has been removed via equation 3.6 and thus represents the true ground motion. The deconvolved trace has been gated to exclude truncation effects near the edges of the data window. The S and sS phases are clearly shown as monopoles with a width of about 8 seconds. The monopoles are exactly the expected far-field ground motion for a ramp-function source.

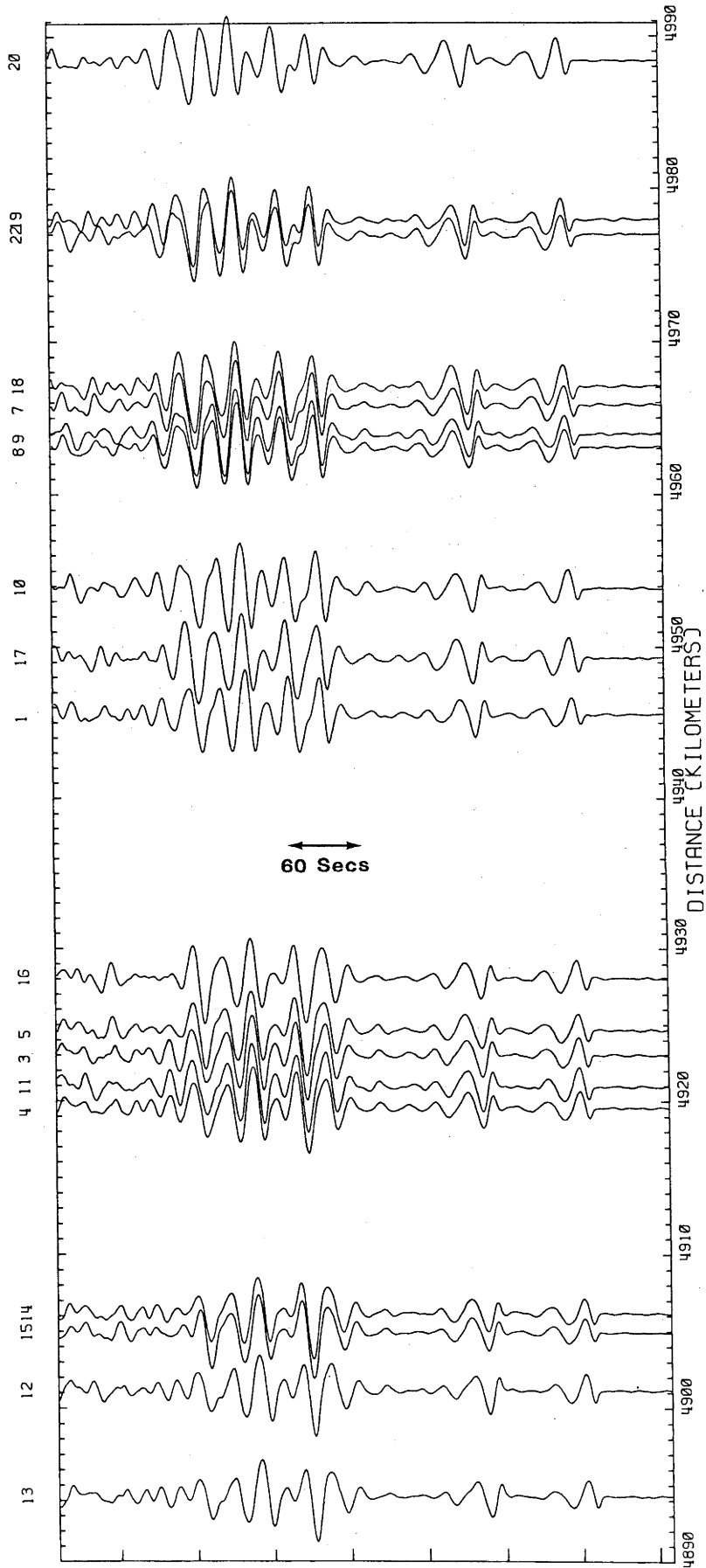
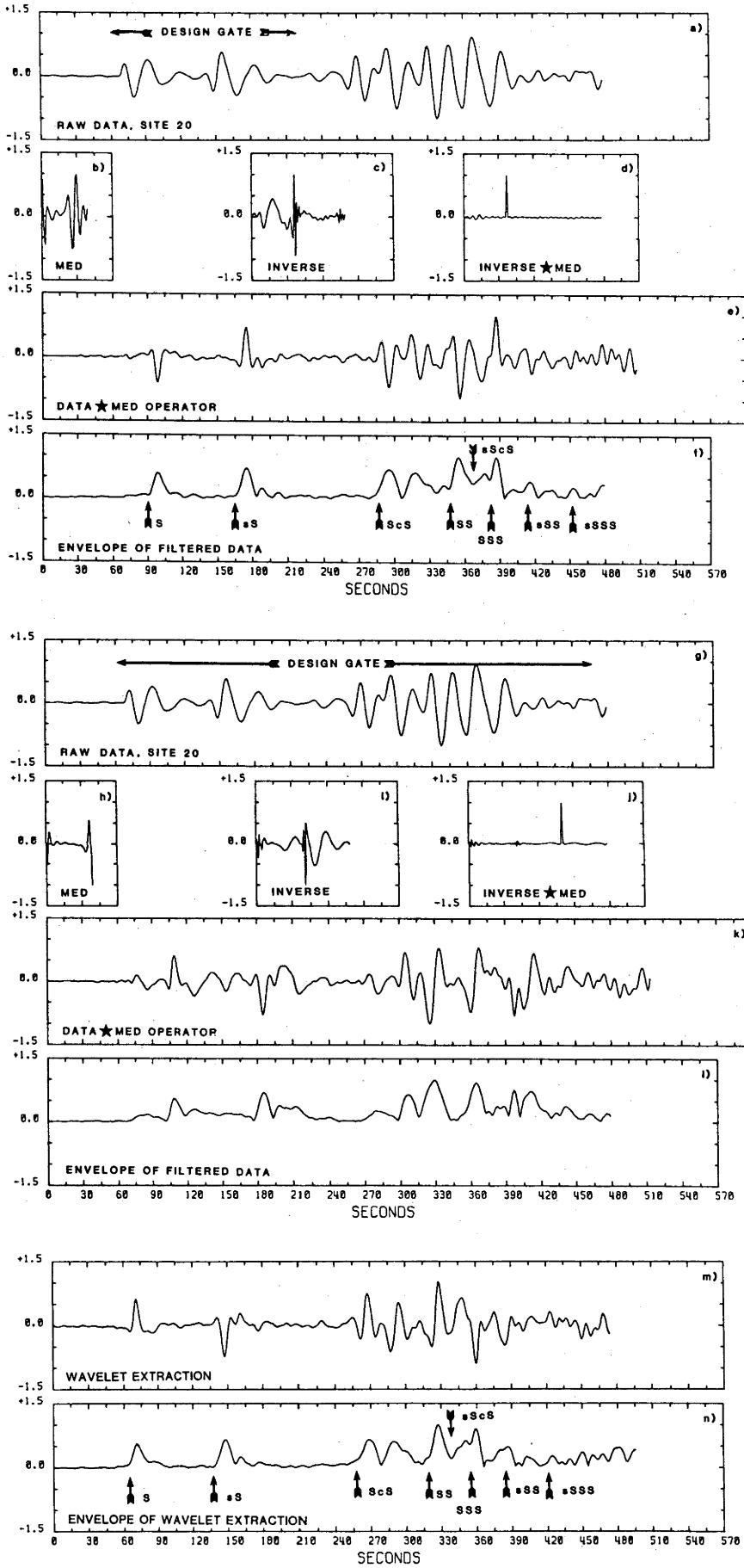


Figure 3.12: Record section of NORSAR LP sub-array outputs for a Hindu Kush earthquake. Lat.=36.42N, long.=70.73E, origin time=7ly 8m 4d 0h 37m 49s, depth=207 km, $m_b=5.6$. Data have been rotated to give only SH, and are trace normalized to peak amplitude.

Figure 3.13: Minimum entropy deconvolution of Hindu Kush event in Figure 3.12. Successive panels show: a) output of NORSAR site 20 showing MED operator design gate; b) 20s MED operator for 6 iterations and 1% pre-whitening designed from 19 channels of NORSAR data; c) optimum least-squares inverse of MED operator; convolution of inverse with MED operator; e) convolution of data with MED operator; f) envelope of filtered trace; g) output of NORSAR site 20 showing MED operator design gate; h) to l) same as captions b) to f); m) wavelet extraction of data in a); n) envelope of deconvolved data. The delay properties of the MED operator are obvious in panels e), f), k) and l). Panels f) and n) show important phases apparent in the complex envelopes.



To investigate the similarities (if any) between the MED processed and wavelet extracted data in terms of absolute spectral information content, the complex envelopes of the deconvolved data are given in Figure 3.13 (panels f, l and n). The similarities in envelopes indicate that the deconvolved data are much the same in terms of absolute spectral information, yet clearly the MED operator under conditions of wavelets with variable phase must "average" over the wavelets. Indeed, time-varying and data adaptive filters may circumvent this problem when dealing with wavelets well separated in time (e.g., S and sS in Figure 3.12), but will meet with the same problem when attempting to deconvolve, for example, the latter part of the wave train in Figure 3.12. Levy and Oldenburg (1982) appear to have overcome the problems of shifting phase with their analytical approach to MED, but it will still experience difficulties under conditions of varying spectral amplitude.

ITERATIVE LEAST-SQUARES DECOMPOSITION

An automatic approach to the sequential decomposition method of Cleary et al (1982) has been suggested by Kanamori and Stewart (1978) and Kikuchi and Kanamori (1982). Their approach is similar to the direct least-squares method described above, but rather than directly solve for the unknown $a(t)$ in equation 3.1, their method iteratively approximates the amplitudes and delays of the component wavelets. In the first iteration, a_0 and t_0 (the amplitude and timing of the component wavelet with the largest amplitude) are determined by minimizing the error defined by

$$\epsilon_0 = \int [s(t) - a_0'w(t-t_0)]^2 \quad 3.7$$

or in terms of correlation functions

$$\epsilon_0 = r_s(0) - 2r_{ws}(t_0) + r_w(0)(a_0')^2$$

where r_s and r_w are the zero-lag autocorrelation for the data and wavelet respectively, and r_{ws} the cross-correlation of the data and wavelet for lag

t_0 Taking the partial derivative with respect to a'_0 , the error in equation 3.7 is minimized if

$$a'_0 = r_{ws}(t_0)/r_w(0)$$

and for this value of a'_0

$$\epsilon_0 = r_s(0) - r_w(0)(a'_0)^2$$

which is minimized if the arrival onset time t_0 is chosen so that

$$[r_{ws}(t_0)]^2 = \text{maximum}$$

This procedure is then iteratively applied to the residual waveform

$$s'(t) = s(t) - a'_i w(t-t_i)$$

and thus, after N iterations, the amplitudes and arrival times of the N largest wavelets are obtained. The decomposed seismogram may then be conveniently represented by a sequence of delta functions, with timing t_i and amplitude a_i much like the sequential decomposition procedure.

At first, such a technique appears highly desirable. For example, a noise-free seismogram composed of a sequence of N identical wavelets will be decomposed after N iterations into N delta functions because the error term is zero. Indeed, for an n -length input, this method will after n iterations produce an output very similar to that of wavelet extraction. This method appears similar to the (subjective) sequential decomposition technique in that delta functions appear in the deconvolved output, and it allows for the possibility of phase inversion. An additional benefit of the objective approach of iterative least-squares decomposition is that the largest constituent wavelets are found first, then sequentially through to the smallest. The iteration may be terminated when there is no more significant decrease in the error ϵ .

The method has been used with success in the deconvolution of complex

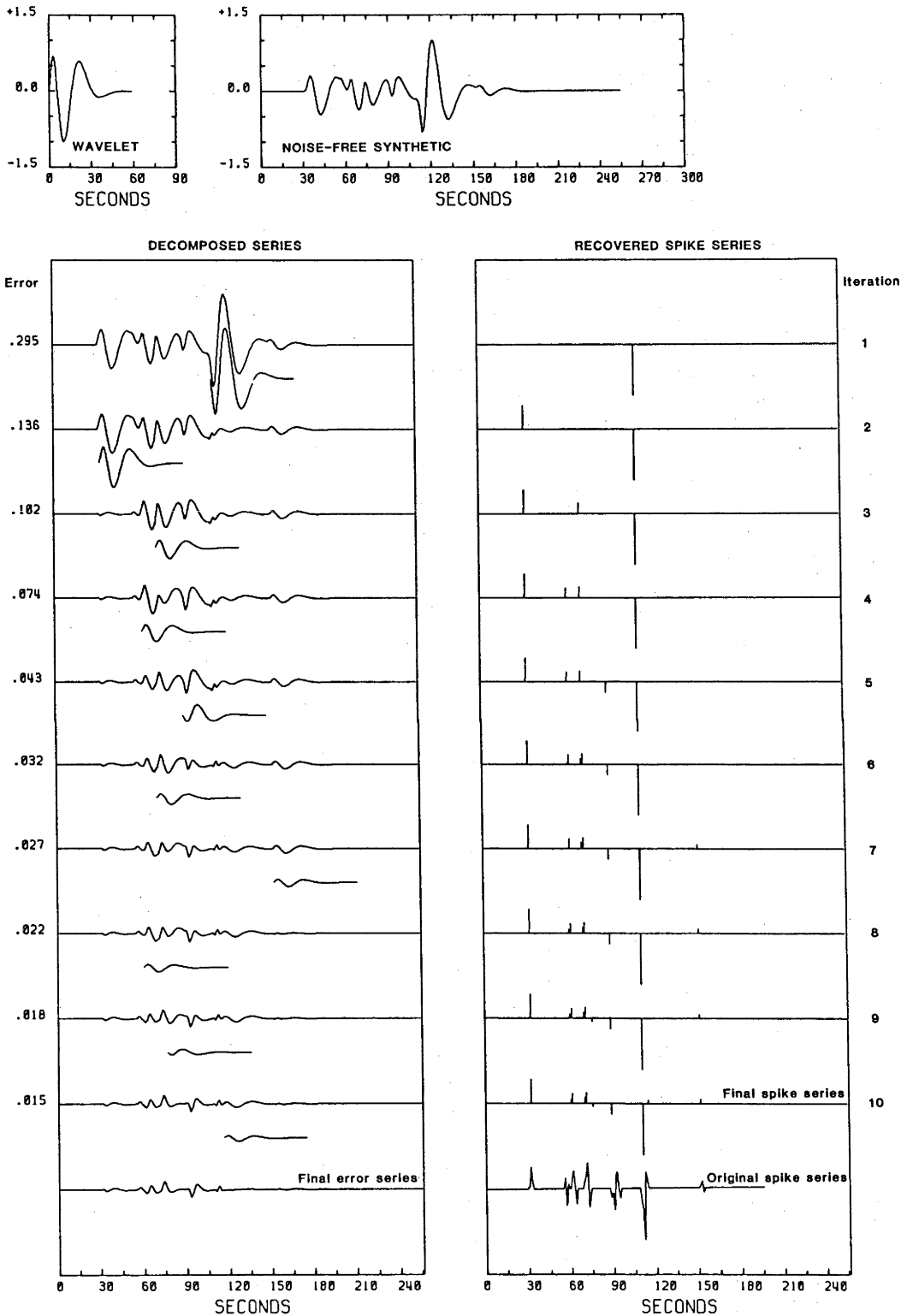


Figure 3.14: Iterative least-squares decomposition of the noise-free synthetic. The sequence on the left showing the wavelet to be subtracted and error sequence, the sequence on the right showing the equivalent spike sequence. The original "spike" sequence is shown at bottom right. No marked decrease in the error can be seen after the sixth iteration.

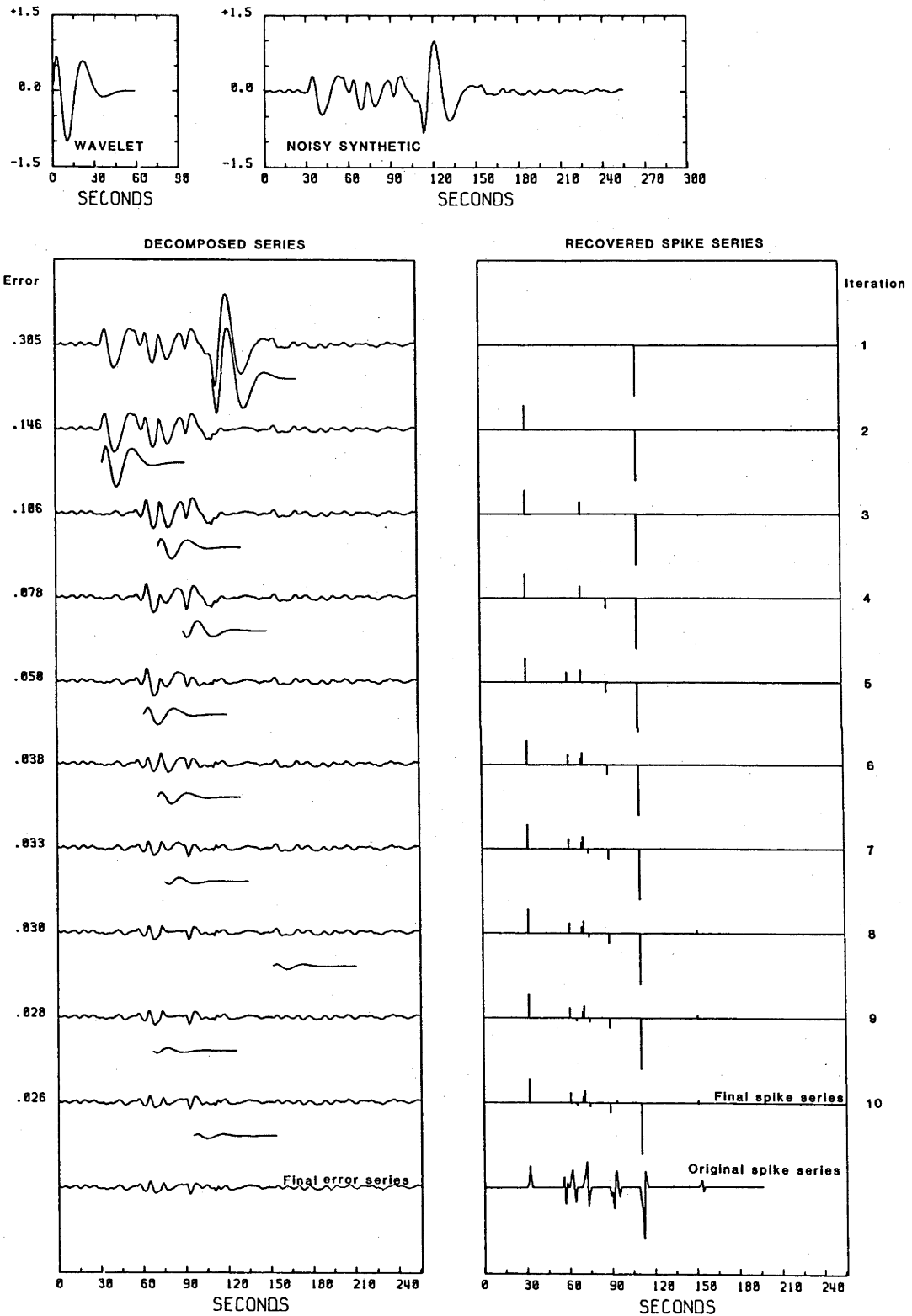


Figure 3.15: Iterative least-squares decomposition of the noisy synthetic. Figure caption is the same as Figure 3.14. No marked decrease in the error can be seen after the sixth iteration.

body waves into a multiple shock sequence. The success of the technique is dependent on the assumption that all the constituent events of the multiple shock have identical fault geometry and depth, i.e., components of the Earth response are stationary for the duration of the shock sequence. Indeed, under such conditions sequential decomposition may achieve similar results. However, the pertinent problem is that of non-stationary wavelets, and so the performance of iterative least-squares decomposition as applied to the synthetics of Figure 3.1 is examined in Figures 3.14 and 3.15.

Figure 3.14 shows the decomposition of the noise-free synthetic using the instrument response as the assumed seismic wavelet. The iterations were stopped after $N=10$, although there was no more significant decrease in the error for $N > 6$. It can be seen that in the first few iterations, delta functions are placed so as to approximately correspond to the timing of the largest arrivals. In the presence of noise (Figure 3.15), the method is slightly less effective than in the noise-free case. Again, only the largest arrivals are adequately found whereas in successive iterations the picked arrivals are of the same level as the noise. Later iterations must operate on an accumulating error, and so the accuracy in determining the timing of low amplitude wavelets, deteriorates quickly.

ADAPTIVE DECONVOLUTION

The original intention of this class of filter was to recognize predictable information in radar signals and to extract it from noise. It is included here in that a time-varying filter is designed so as to respond to any input waveform and give as output a whitened, preferably delta function, response. In this context, if the time-varying filter meets this specification, then it would be ideally suited to deconvolving the suite of data under consideration. The method to be evaluated here is the gradient descent approach of Griffiths et al. (1977) and Baker (1979). This approach to the solution of the normal equations for a deconvolution operator results in a new approximation to the Weiner-Robinson filter being calculated at each point of the input time series. A simple adaptive algorithm, based on the method of steepest descent, is used to update the filter coefficients as each data point is deconvolved.

The theory commences with solving the normal equations

$$\underline{R} \underline{f}_0 = \underline{g}(\gamma)$$

for an initial estimate of the filter, \underline{f}_0 and $\underline{g}(\gamma)$ the cross-correlation of the input and output with prediction distance γ (Peacock and Treitel, 1969). In this discussion, a prediction distance of one is used to whiten the spectrum, although reference to the prediction distance will be retained in the derivation for completeness. Rather than use the computationally more efficient Levinson recursion, the method of gradient descent is used so that starting with an initial guess, \underline{f}_0 , \underline{f} is then updated using

$$f(t+1) = f(t) + \mu [g(\gamma) - \underline{R}f(t)]$$

and μ is the adaption coefficient which determines the rate of convergence of $f(t)$ towards \underline{f}_0 , the ideal filter. In order to increase the efficiency of this algorithm, Widrow and Hoff (1960) replaced the smoothed correlations $\underline{g}(\gamma)$ and \underline{R} by their instantaneous values. Thus

$$f(t+1) = f(t) + \mu [s(t+\mu) - s'(t+\gamma)] s^T(t)$$

where $s'(t+\gamma) = s^T(t)f(t)$ is the predicted estimate of the seismogram $s(t+\gamma)$ and $s^T(t) = [s(t), s(t-1), \dots, s(t-n-m+1)]$. In the process of computing $f(t+1)$, a deconvolved time series,

$$a(t) \approx y(t) = s(t+\gamma) - s'(t+\gamma)$$

is formed, where $y(t)$ is the difference between the input (seismogram) and predicted traces.

As described by Griffiths et al. (1977), the best results may be obtained by (1) filtering in time-reverse, (2) filtering in time-forward and (3) stacking the two outputs. Filtering in time-reverse order is accomplished by computing the filter iteration starting at later times and proceeding

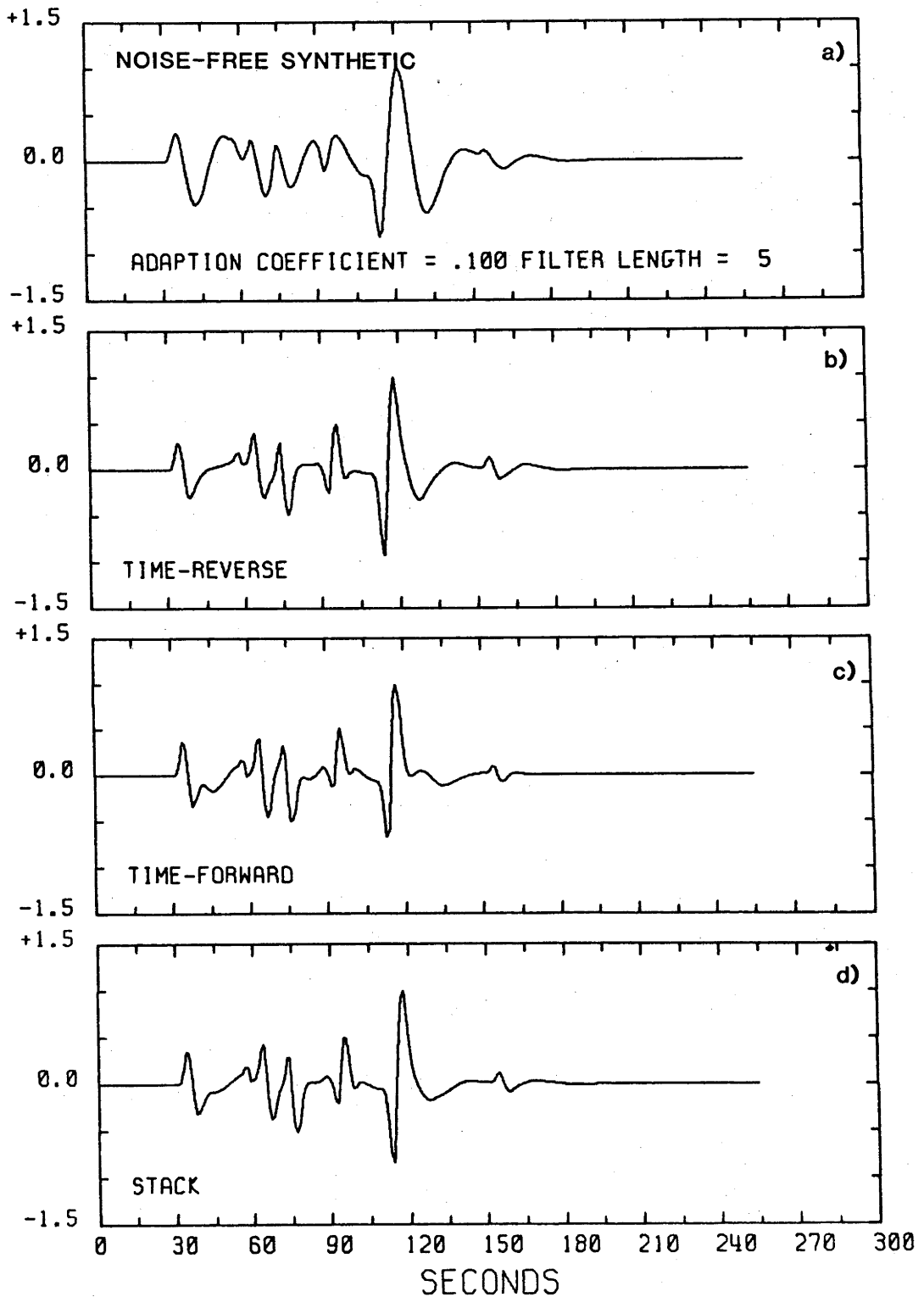


Figure 3.16: Adaptive deconvolution of the noise-free synthetic: a) noise-free synthetic; b) time-reverse deconvolution; c) time-forward deconvolution; d) stack of b) and c).

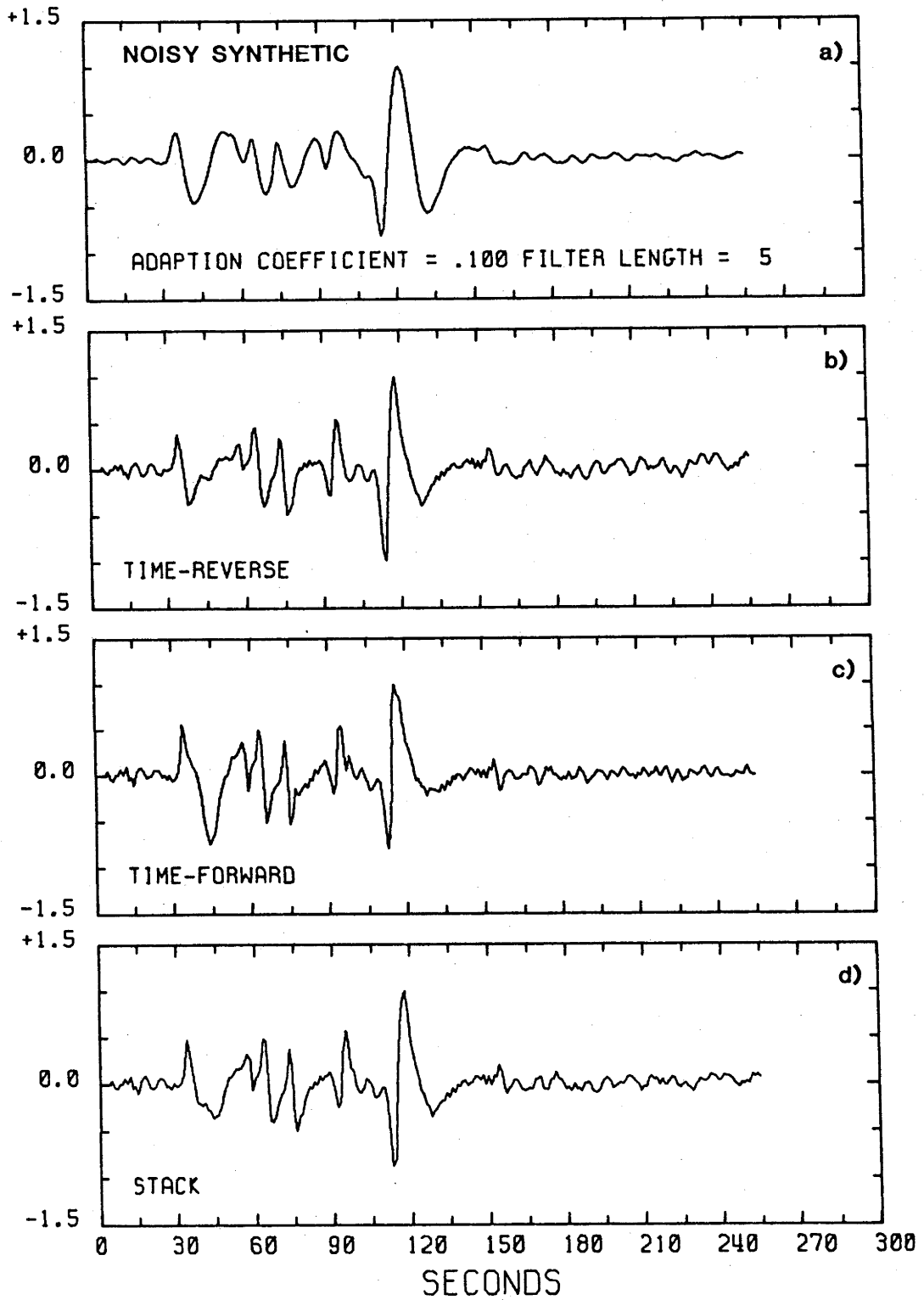


Figure 3.17: Adaptive deconvolution of the noisy synthetic: a) noisy synthetic; b) time-reverse deconvolution; c) time-forward deconvolution; d) stack of b) and c).

towards the earlier section of the seismogram, while time-forward proceeds from early to late times. The results of the algorithm operating on the noise-free synthetic and noisy synthetic are illustrated in Figures 3.16 and 3.17. Clearly, the adaptive filters are unable to adapt quickly enough to the closely spaced and widely varying wavelets, smearing the exact nature of the "spikes".

3.4 CONCLUSIONS

Of the various methodologies examined in their application to deconvolving long-period teleseismic data, none work sufficiently well to the point of producing a sequence of delta functions. The assumptions of stationarity of seismic waveforms is seldom justified in reflection data processing, which deals with the simple case of near-normally incident reflections, and is totally invalid for teleseismic signals which are composed of direct, pre- and post-critically reflected energy generated by a generally unknown finite source. The frequency-phase response of each arrival type may be distinctly different and due to the large and variable length of the different ray paths, phase shifting and attenuation may contribute to significantly alter the shape of the basic seismic wavelet implicit in the deconvolution process.

In view of the inherent non-stationarity of the individual components of the Earth response, methods such as homomorphic, minimum entropy deconvolution and Wiener-Robinson theory cannot be used to estimate a wavelet directly from the seismograms. In this regard the adaptive deconvolution procedures are seen unable to adapt quickly enough.

The best results that can be expected are by those methods that require an explicit estimate of the wavelet. In the convolution process, only the contribution made by the instrument-electronics package is known with any certainty. It is generally thought that the bandwidth of the instrument is the narrowest of any factors contributing to a seismogram. Due to uncertainties in estimating the source-time function and attenuation, it is not possible to recover the Earth response as a sequence of delta functions. Therefore the most satisfactory approach is to recover the ground motion by removing only the response of the instrument. This may be best achieved by spectral division, Wiener-Robinson inverse filtering or

wavelet extraction. Wiener-Robinson inverse filtering has been shown to be the least acceptable due to the minimum-phase assumption and its requirement of a finite-length filter. The equivalent methods of spectral division and wavelet extraction not only yield the best estimate of ground motion, but are the simplest techniques to implement on a digital computer, requiring, unlike other methods, optimization of a single parameter: the waterlevel for spectral division and prewhitening for wavelet extraction.

One aspect of deconvolution that has received little attention in the literature is that of errors introduced by the analog-to-digital-converter (ADC) as distinct from human operator digitization errors. Generally, the ADC will quantize the input to say, 1024 levels. The quantized noise-free synthetic will appear identical to the floating-point version in Figure 3.1. Deconvolution of the quantized signal by spectral division, Wiener-Robinson filtering and wavelet extraction admits some high-frequency noise, in contrast to the noise-free outputs of Figures 3.2a and 3.9a. This noise arises from loss of precision between the true seismogram and the desired seismogram, but is considerably less than the much higher levels of additive noise to be contended with.

For the remainder of this research, two reasonable processing strategies appear to be:

- (i). Recovering ground motion by wavelet extraction.
- (ii). Estimating relative arrival times and amplitudes of large arrivals by iterative least-squares decomposition. Although not a successful method of deconvolution, this technique may be particularly valuable for identifying overlapping large amplitude arrivals.

Wavelet extraction has been given preference over spectral division only because of the direct analogies that can be drawn between wavelet extraction, iterative least-squares decomposition and the sequential decomposition technique used to initiate this study. Indeed, wavelet extraction and iterative least-squares decomposition appear to be two independent approaches to automating the subjective sequential decomposition procedure.

CHAPTER 4

COMPLETE SYNTHETIC SH SEISMOGRAMS

4.1 INTRODUCTION

Most of the current models of Earth structure up to the present have been based on the study of the travel times of seismic waves and of their apparent slownesses. Extension of the analysis to take account of the observed amplitudes have provided, and will continue to provide, additional constraints on the model parameters. One convenient method of using the amplitude information is to compare the observed seismograms with synthetic seismograms and adjust the model parameters until there is a match albeit subjective between the observed and synthetic seismograms.

Several methods for calculating synthetic seismograms are currently available. Some of these methods are of the "ray sum" type, and consequently require some specification of the ray/wave path. For example, the Generalized Ray, WKBJ (Chapman, 1978) and Full Wave (e.g., Richards, 1976; Cormier and Richards, 1977) methods involve significant amounts of input and critical decisions to specify particular rays and setting up the necessary parameters for an execution. A degree of experience is necessary to correctly specify these parameters. On the other hand, the Reflectivity method (Fuchs, 1968), and in particular, the approach by Kind (1978), incorporates all possible ray paths, and is therefore capable of computing complete seismograms. In addition, the Reflectivity method is the easiest of the four methods to apply, as it requires few critical decisions for a successful execution of the programme, thus relieving the operator from the responsibility of ensuring the 'correctness' of the synthetic seismogram.

The Reflectivity method is based upon the matrix formulation developed by Haskell (1953) and independent analytical derivations of the displacement due to a source buried in a layered medium by Haskell (1960, 1963), Harkrider (1964) and Knopoff (1964). Systematic numerical procedures were developed by Fuchs (1968), Fuchs and Müller (1971), Kind (1978), Schott (1979) and Wang and Herrmann (1980). Kind's development of

synthetic P-SV seismograms for a buried shear dislocation source was based on the Harkrider (1964) paper. For the purpose at hand, the approach by Fuchs (1968) is inadequate because it generates synthetic seismograms for only explosive sources located at the surface. In addition, the lowest horizontal phase velocity admitted into the calculation must exceed the minimum shear velocity in the reflecting layers. The need to apply a taper over the velocity window will exclude some surface-wave energy from the synthetic seismograms. Kind (1976) suggested the possibility of using a P-SV synthetic seismogram programme to generate SH waves. This may be accomplished by assuming the equivalence of SH waves in a solid to P waves in a liquid (Satô, 1954) and making the appropriate transformations to v_p , v_s and ρ . This approach is not successful due to the long run times required by the P-SV programme as compared with a dedicated SH programme and the unsatisfactory seismograms generated, ascribed to the inability of the displacement-stress source vector to carry over in the transformation to a liquid medium. Furthermore, Satô's relation is really applicable only to surface waves and not body waves, because the impedance (the product of seismic velocity and density as a function of vertical travel time) $\rightarrow 0$ for grazing incidence of SH waves, and $\rightarrow \infty$ for grazing incidence of P waves in liquids (Aki and Richards, 1980). Similar comments apply to the application of the transform to Fuchs's (1968) P-SV programme. It is the purpose of this chapter to develop synthetic SH seismograms using Harkrider's analysis thus forming a natural adjunct to the papers of Kind (1978, 1979). The seismograms will be compared with complete synthetic SH seismograms calculated by Liao et al. (1978) who followed Knopoff's (1964) formulation, and also with the Haskell (1960, 1963) based seismograms of Wang and Herrmann (1980).

4.2 SH DUE TO A BURIED HORIZONTAL POINT FORCE IN A LAYERED MEDIUM

Following Harkrider (1964) an Earth model is assumed to consist of $n-1$ parallel, homogeneous, isotropic solid layers overlying a half-space. A cylindrical coordinate system (r, θ, z) is used with the origin at the surface and the z -direction downwards. The SH displacements at the surface as a result of a buried source in the layered medium can be derived from the matrix equation

$$\begin{bmatrix} \hat{\epsilon}'_n \\ \hat{\epsilon}'_n \end{bmatrix} = J \left[\begin{pmatrix} \frac{\dot{v}(0)}{c} \\ 0 \end{pmatrix} + A_S^{-1} \begin{pmatrix} \Delta_1 \\ \Delta_2 \end{pmatrix} \right] \quad 4.1$$

where $\hat{\epsilon}'_n$ is the potential of SH in the half-space, J is the Haskell matrix (Haskell, 1953) of the layered half-space for SH, and A_s is the product of the Haskell layer matrices above the source. The discontinuous displacement-stress vector at the source plane is given by (Δ_1, Δ_2) .

The matrix J can be written as the product of the layer matrices below and above the source depth:

$$J = B_s A_s \quad 4.2$$

where B_s is the layer matrix product of the layered medium below the source. With (4.2), equation (4.1) may be rewritten as

$$\begin{bmatrix} \hat{\epsilon}'_n \\ \hat{\epsilon}'_n \end{bmatrix} = B_s \left[A_s \begin{pmatrix} \frac{\dot{v}(0)}{c} \\ 0 \end{pmatrix} + \begin{pmatrix} \Delta_1 \\ \Delta_2 \end{pmatrix} \right] \quad 4.3$$

or

$$\begin{bmatrix} \hat{\epsilon}'_n \\ \hat{\epsilon}'_n \end{bmatrix} = B_s \begin{bmatrix} W \\ Y \end{bmatrix} \quad 4.4$$

Equation (4.4) is solved by subtracting line 2 from line 1. Using $B=F B_s$, where B and $F=(1,-1)$ are (1×2) matrices, it follows that

$$\left. \begin{aligned} 0 &= B \begin{pmatrix} W \\ Y \end{pmatrix} = B_{11}W + B_{12}Y \\ W &= C Y \end{aligned} \right\} \quad 4.5$$

with

$$C = -B_{12}/B_{11} \quad 4.6$$

From (4.3) and (4.4)

$$\begin{pmatrix} W \\ Y \end{pmatrix} = A_s \begin{pmatrix} \frac{\dot{v}(0)}{c} \\ 0 \end{pmatrix} + \begin{pmatrix} \Delta_1 \\ \Delta_2 \end{pmatrix} \quad 4.7$$

and eliminating W by inserting (4.6) into (4.7) leads to

$$A_{11} \frac{\dot{v}(0)}{c} - C Y = -\Delta_1$$

$$A_{21} \frac{\dot{v}(0)}{c} - Y = -\Delta_2$$

Solving the last two equations for $\dot{v}(0)/c$ yields

$$\frac{\dot{v}(0)}{c} = \frac{\Delta_1 - C\Delta_2}{-A_{11} + CA_{21}} \quad 4.8$$

To calculate $\dot{v}(0)/c$, one only needs a $(1 \times 2)(2 \times 2)$ layer matrix multiplication from the half-space to the source in order to obtain B_{11} and B_{12} , and a $(2 \times 1)(2 \times 2)$ layer matrix multiplication from the free surface to the source in order to obtain A_{11} and A_{12} . The (1×2) matrix B is obtained from the (2×2) matrix B_s by computing the difference between the first and second row of the inverse half-space matrix given by equation 27 of Harkrider (1964), and then multiplying this difference by the (2×2) layer matrix, equation (4.25) from Harkrider (1964).

Harkrider (1964) has given the displacement-stress vector for a horizontal point force at some depth directed in the $\theta = 0^\circ$ direction which is

$$(\Delta_1, \Delta_2) = (0, -kL(\omega)/2\pi) \quad 4.9$$

where L is the Fourier transformed force-time function and k the wavenumber. Finally, Harkrider arrives (his equation 129) at the following expressions for the Fourier transformed tangential and radial displacements at the free surface

$$v(r, \theta, 0) = \int_0^{\infty} \left[-\frac{1}{k} \frac{\dot{u}(0)}{c} \frac{J_1(kr)}{kr} + \frac{i}{k} \frac{\dot{v}(0)}{c} \frac{dJ_1(kr)}{dkr} \right] dk \sin\theta$$

4.10

$$q(r, \theta, 0) = \int_0^{\infty} \left[\frac{1}{k} \frac{\dot{u}(0)}{c} \frac{dJ_1(kr)}{dkr} - \frac{i}{k} \frac{\dot{v}(0)}{c} \frac{J_1(kr)}{kr} \right] dk \cos\theta$$

where the receiver is at an azimuth θ to the origin of the point source. In (4.10), $J_1(x)$ and $dJ_1(x)/dx$ are the Bessel function of order one and the first derivative of J_1 , respectively. The first terms in each expression of (4.10) describe the contributions of the P-SV wave field which will be neglected in the following, thereby decoupling SH from the P-SV wave propagation. The Fourier transformed tangential and radial SH displacements are given by

$$v_{SH}(r, \theta, 0) = \int_0^{\infty} \left\{ \frac{i}{k} \frac{\dot{v}(0)}{c} \frac{dJ_1(kr)}{dkr} \right\} dk \sin\theta$$

$$q_{SH}(r, \theta, 0) = -\int_0^{\infty} \left\{ \frac{i}{k} \frac{\dot{v}(0)}{c} \frac{J_1(kr)}{kr} \right\} dk \cos\theta$$

and the maximum SH displacement in the far field is obtained for $\theta = 90^\circ$

$$v_{SH}(r, 90, 0) = \int_0^{\infty} \left\{ \frac{i}{k} \frac{\dot{v}(0)}{c} \frac{dJ_1(kr)}{dkr} \right\} dk \quad 4.11$$

Using the approximation of Bessel functions for large arguments (see for example, Fuchs and Müller, 1971) and considering only wave propagation in the positive r-direction it follows from (4.11) that

$$v_{SH}(r, 90, 0) \approx \int_0^{\infty} \left\{ \frac{i}{k} \frac{\dot{v}(0)}{c} \frac{1}{\sqrt{2\pi kr}} \exp \left[-i \left(kr - \frac{\pi}{4} \right) \right] \right\} dk \quad 4.12$$

Equation (4.12) was used to test the computer programme. Numerical overflow problems may arise in the calculation of $\dot{v}(0)/c$ from (4.8) if the phase velocity c becomes smaller than the shear-wave velocity. This problem will be addressed in a later section.

4.3 SH DISPLACEMENTS AND STRESSES FOR A SHEAR DISLOCATION SOURCE IN A LAYERED MEDIUM.

The SH potential $\chi_\ell(r, \theta, z, k)$ is separated into radial, tangential and depth-dependent components. The index ℓ indicates summation over a number of terms. In the cylindrical coordinate system used

$$\chi_\ell(r, \theta, z, k) = \chi_\ell(z) J_\ell(kr) K_\ell(\theta) \quad 4.13$$

where $J_\ell(kr)$ is the Bessel function of order ℓ , $\chi_\ell(z)$ is depth dependent and $K_\ell(\theta)$ describes the dependence upon θ . The horizontal displacement component normal to the direction of propagation is the SH displacement and is given by

$$v_\ell(r, \theta, z, k) = - \frac{\partial \chi_\ell(r, \theta, z, k)}{\partial r} \quad 4.14$$

Inserting (4.13) into (4.14) yields

$$v_{\ell}(r, \theta, z, k) = \frac{i}{k} \frac{\dot{v}_{\ell}(z)}{c} \frac{dJ_{\ell}(kr)}{dkr} K_{\ell}(\theta) \quad 4.15$$

with

$$\frac{\dot{v}_{\ell}(z)}{c} = ik^2 \chi_{\ell}(z)$$

Because the source is described by a discontinuity of the displacement-stress vector, we also need expressions for the circumferential stress $P_{\ell\theta z}$ which is given by

$$P_{\ell\theta z}(r, \theta, z, k) = \mu \frac{\partial v_{\ell}(z)}{\partial z} = -\mu \frac{\partial^2 \chi_{\ell}(r, \theta, z, k)}{\partial r \partial z} \quad 4.16$$

where μ is Lamé's constant. In equations (4.12) and (4.14) only the far-field terms have been considered. Using equations (4.13) and (4.15), it follows that

$$P_{\ell\theta z}(r, \theta, z, k) = -\tau_{\ell}(z) \frac{dJ_{\ell}(kr)}{dkr} K_{\ell}(\theta)$$

with

$$\tau_{\ell}(z) = k\mu \frac{d\chi_{\ell}(z)}{dz}$$

Following Harkrider (1976, equation A5), the integral solution for the SH potential for a shear dislocation source of arbitrary orientation at depth s is given by

$$\chi = \frac{M(\omega)}{4\pi\rho\omega^2} \sum_{\ell=0}^2 \frac{\partial \Lambda_{\ell}(\theta)}{\partial \theta} C_{\ell} F_{\beta} J_{\ell}(kr) \quad 4.17$$

with the spectral moment $M(\omega)$, density ρ , circular frequency ω and the geometry of the dislocation source as given in Figure 4.1. The terms Λ_{ℓ} which describe the radiation pattern for SH are given by

$$\Lambda_0 = \frac{1}{2} \sin\lambda \sin 2\delta$$

$$\Lambda_1 = \cos\lambda \cos\delta \cos\theta - \sin\lambda \cos 2\delta \sin\theta$$

$$\Lambda_2 = \frac{1}{2} \sin\lambda \sin 2\delta \cos 2\theta + \cos\lambda \sin\delta \sin 2\theta$$

so that

$$\frac{\partial \Lambda_0}{\partial \theta} = 0$$

$$\frac{\partial \Lambda_1}{\partial \theta} = -\cos\lambda \cos\delta \sin\theta - \sin\lambda \cos 2\delta \cos\theta$$

$$\frac{\partial \Lambda_2}{\partial \theta} = -\sin\lambda \sin 2\delta \sin 2\theta + 2\cos\lambda \sin\delta \cos 2\theta$$

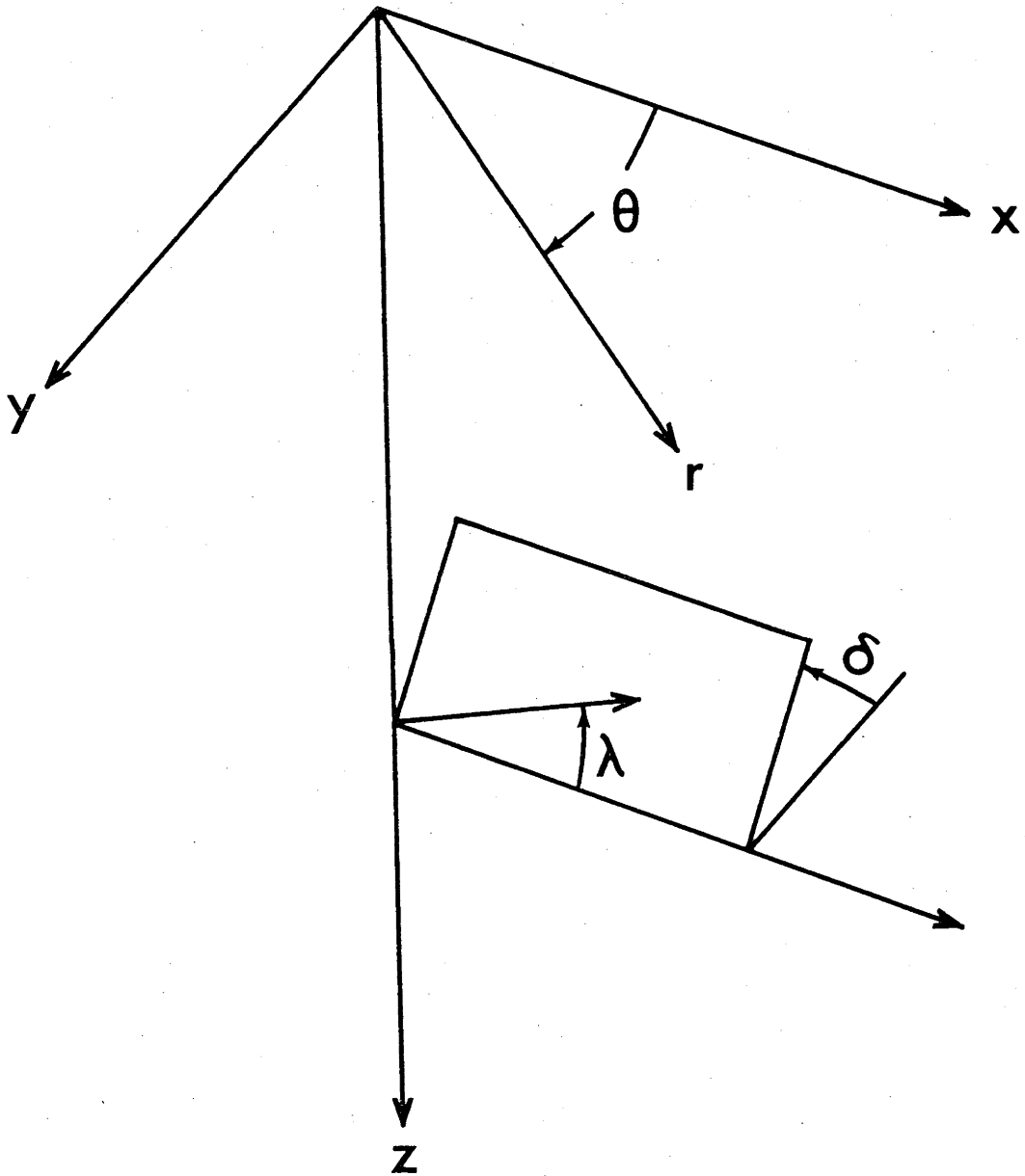


Figure 4.1: Geometry of a dislocation source. θ : angle between strike of the fault and observer; δ : dip angle of fault; λ : slip direction.

and so the summation over ℓ need only be taken from 1 to 2. The other terms in equation (4.17) are given by

$$C_1 = \epsilon k_\beta^2 v_\beta \quad C_2 = -\frac{k_\beta^2}{2}$$

with

$$\epsilon = \text{sign}(z-s), \quad k_\beta = \frac{\omega}{\beta}, \quad v_\beta = k^2 - k_\beta^2,$$

$$F_\beta = k \exp\left(\frac{-v_\beta}{z-s}\right) / v_\beta$$

where β is the shear-wave velocity. By comparing (4.13) with (4.17) it follows that

$$X_\ell(z) = C_\ell R F_\beta$$

$$K_\ell(\theta) = \frac{\partial \Lambda_\ell(\theta)}{\partial \theta}$$

with

$$R = \frac{M(\omega)}{4\pi\rho\omega^2}$$

Harkrider (1964) describes the source by the displacement-stress vector Δ_1 and Δ_2 , which are continuous except at $z = s$, the source depth. The

components of this vector are

$$\frac{\dot{v}_\ell(z)}{c} = i k^2 R C_\ell / v_\beta$$

$$\tau(z)^\pm = \mp k^2 \mu R C_\ell$$
4.18

$\ell = 1, 2$, and the exponential term has been omitted. The plus sign is for layer depths greater than the source depth, and the negative sign for layers above the source. The difference of these expressions for $z > s$ and $z < s$ yields

$$\begin{bmatrix} \Delta_{\ell 1} \\ \Delta_{\ell 2} \end{bmatrix} = \begin{bmatrix} \frac{\dot{v}_\ell(z)^+}{c} \\ \tau_\ell(z)^+ \end{bmatrix} - \begin{bmatrix} \frac{\dot{v}_\ell(z)^-}{c} \\ \tau_\ell(z)^- \end{bmatrix}$$
4.19

and it follows for $\ell = 1, 2$

$$(\Delta_{11}, \Delta_{12}) = (2i k^2 k_\beta^2 R, 0)$$

$$(\Delta_{21}, \Delta_{22}) = (0, k^2 k_\beta^2 \mu R)$$
4.20

This describes the discontinuity of the displacement-stress source vector at $z = s$.

The relations presented so far in this section are for a homogeneous medium. In the following the relations for the SH displacements at the surface of a layered medium are given with the shear dislocation source buried in the layered medium. They can be derived from equations (4.1) and (4.8) given in the previous section. The transformation from plane waves to spherical waves is achieved by integration over the wavenumber k . Summing over the two source terms (4.20) which describe the shear dislocation we obtain the Fourier transformed SH displacement at the surface of the layered half-space

$$v(r, \theta, 0) = \int_0^{\infty} \frac{i}{k} \sum_{\ell=1}^2 \frac{v_{\ell}(0)}{c} \frac{dJ_{\ell}(kr)}{dkr} \frac{\partial \Lambda_{\ell}}{\partial \theta} dk \quad 4.21$$

Rather than integrate over wavenumber, Fuchs (1968) suggested a change in variable and sum over slowness, thus preventing spatial aliasing. Using again the approximation of Bessel functions for large arguments and considering propagation in positive r -direction only leads to

$$v_{SH}(r, \theta, t) \approx \int_{-\infty}^{\infty} \int_0^{\infty} \frac{i}{k} \frac{1}{\sqrt{2\pi kr}} \exp \left[-i(kr - \frac{\pi}{4}) \right] \cdot \left[\frac{\dot{v}_1(0)}{c} \frac{\partial \Lambda_1}{\partial \theta} + i \frac{v_2(0)}{c} \frac{\partial \Lambda_2}{\partial \theta} \right] dk d\omega \quad 4.22$$

which is finally the equation for SH displacements at the free surface for

a shear dislocation source buried in a layered medium. The calculation of $\dot{v}_\ell(0)/c$ is given in Appendix 2 (equation A2.4).

Equations (4.11) and (4.22) are the basic relations to calculate synthetic SH seismograms. The effect of attenuation is easily included by considering the complex velocity

$$\beta^c = \beta + i\beta/2Q \quad 4.23$$

(Schwab and Knopoff, 1973). It is well known that the elements of the Haskell layer matrix become very large if the phase velocity is smaller than the shear wave velocity. This can lead to overflow problems in the numerical calculations. This will be discussed in more detail in the following section.

4.4 NUMERICAL CONSIDERATIONS

In all seismograms presented in this chapter, the exact Earth-flattening transform for SH of Andrianova et al. (1967) is used, thus preserving exactly the kinematic and dynamic properties of the wavefield in the plane-layered medium (cf. Müller, 1977). This is particularly convenient as it eliminates the problems inherent in the approximate Earth-flattening transform for P-SV wave propagation studies.

Implicit thus far are the numerical 'tricks' in the evaluation of the integrals (4.11) and (4.22) such as the far-field approximation for Bessel functions and integration by the trapezoidal or Simpson's rule. Considerable work has been devoted to overcoming precision problems at high frequencies by Dunkin (1965), Schwab and Knopoff (1973), Abo-Zena (1979) for the case of Rayleigh-wave dispersion problems, and Schwab and Knopoff (1973) for Love waves. Overflow problems arise in the calculation of the product of the layer matrices: the magnitude of the term Q_m (Appendix, equation A2.2) must be monitored so that layer thickness (d_m) is sufficiently thin to prevent overflow in the computer. Also, the elements of the B matrix can be normalized to the largest element of the matrix. Such scaling factors will drop out in the calculation of B_{12}/B_{11} . However, layer matrix normalization cannot be applied to A_s , the product of layer

matrices above the source. Layer reduction as discussed by Schwab and Knopoff (1973) offers a possible way to overcome this problem. In the examples presented in the next section this was not necessary because there were only a few layers above a shallow source. Normalization may or may not be done routinely, depending upon the model. Trial runs with normalization should first be performed.

The integrations (4.11) and (4.22) are necessarily finite, and care should be taken in assigning upper and lower limits. Integration over frequency is achieved by Fast Fourier Transform, and problems pertaining to ringing in the time domain due to truncation of the frequency domain window are well documented; thus some sort of taper should be applied. The slowness limits must be chosen with care since their values correspond to limits of a pie-slice filter, with all concomitant effects of having sharp boundaries in ω - k space. Again some sort of taper should be applied over the wavenumber window, otherwise spurious signals arise, travelling with the cut-off phase velocities with amplitudes proportional to the amplitudes of the reflected wavefield starting at those points of the travel-time curve where these cut-off phase velocities are encountered (Fuchs, 1980). Alternatively, at the expense of increased computational effort, the velocity window may be arbitrarily enlarged so as to shift these spurious signals out of the seismic wave-train window under consideration. To prevent aliasing in the time domain, complex frequencies may be used in the manner suggested by Kind and Seidl (1982). Though relatively easy to implement into the basic algorithm, complex frequencies are not considered here as there is no real need when calculating complete synthetic seismograms.

4.5 EXAMPLES

One of the most perplexing questions facing seismologists concerns the 'correctness' of a synthetic seismogram. It is difficult to ascertain if synthetics obtained by one technique are truly representative of the real world if another method yields different results. In the past some attempts have been made to compare the Reflectivity method with Generalized Ray theory (Burdick and Orcutt, 1979), Full Wave theory (Choy et al., 1980), Asymptotic Ray theory and the Ray-reflectivity method (Daley and

Hron, 1982). The task was to generate identical seismograms when applied to the same body-wave problem; the same Earth model, source parameters, distance ranges and body waves are used. In these studies, the synthetics were found to be reasonably similar, any differences between the seismograms being due to assumptions and approximations inherent in each method.

Burdick and Orcutt (1979) compared body-wave forms generated by the Generalized Ray and Reflectivity methods. Both techniques share similar assumptions, but the ray method is most seriously effected by the necessity to arbitrarily truncate the partial ray sum. Burdick and Orcutt were able to overcome this by considering only the first few arrivals, and achieved a good match between the synthetics. However, such a study today is rather simplistic, as current research requires the use of secondary and later arrivals. Choy et al. (1980) computed core phases with Full Wave theory and the Reflectivity method, and found that the two techniques yield only reasonably similar results if the stack of homogeneous layers in the Reflectivity method was sufficiently thin to avoid contamination by reverberations. Furthermore, the inexact Earth-flattening transform for P-SV wave synthesis by the Reflectivity method introduces phase and amplitude distortion at depths appropriate to the core-mantle boundary. Full Wave theory is ideally suited to analysis of wave interaction at an isolated interface such as the CMB, but is less well suited to examining later arrivals. The following section generates complete SH seismograms similar to those presented by Wang and Herrmann (1980) who used complex contour integration techniques in the Reflectivity method, and Liao et al. (1978) who summed up to 100 radial modes using Normal Mode theory. Kennett (1980) has computed complete three-component synthetic seismograms. Kennett's seismograms are in error because of coding problems (Kennett, pers.comm., 1982) and so no comparison can be made.

In the first example, synthetic tangential time histories due to a vertical dip-slip fault at a depth of 10 km for the simple crustal model of Wang and Herrmann (1980) are compared with their synthetics in Figure 4.2a. The seismograms are almost identical but differences do arise, implicit in the different approaches to integration and application of frequency/wavenumber tapers. Wang and Herrmann chose to use complex contour integration to evaluate the complex wavenumber integrals. This was done because of the possibility of the Love-wave poles lying on the real k -axis. Complex contour integration is able to deform the path of

integration sufficiently so as to exclude this discontinuity and others (such as branch-line cuts) from the integration. The approach chosen here was first suggested by Kind (1978) who incorporated absorption in the model by making the wave velocities complex (see equation 4.23). This has the effect of shifting the surface-wave poles away from the real k -axis, allowing the implementation of simple numerical techniques (such as the trapezoidal rule) to evaluate the wavenumber integral. The differences between the two seismograms therefore reflect the differences between perfectly elastic and inelastic models. The introduction of absorption has the expected effect of smoothing the higher frequencies, and reducing the amplitudes of those arrivals that have long travel paths.

Figure 4.2b shows a further comparison of SH synthetics for the five-layer central United States model given by Wang and Herrmann, with a 45° dip-slip source at a depth of 1 km. The Q model assumed in the generation of the synthetics again leads to differences in the time histories, particularly in the body wave part of the trace where different sets of multiples have interfered with each other. The surface-wave train has a shorter duration because a Q value of 450 has been allocated in the topmost wave guide. It is possible to demand a very high Q factor, but the complex velocity in a layer (equation 4.23) will have a very small imaginary component. This has led to precision problems during the complex arithmetic operations, but for realistic values of Q, ill-conditioning should not be encountered. The effect of very high Q is to introduce a high-frequency noise superimposed on the time series, while low Q values have, as expected, a considerable smoothing effect.

The final comparison (Figure 4.3) is with synthetics generated for the oceanic model of Liao et al. (1978), who used a model derived from CIT11 of Anderson and Toksöz (1963) to synthesize S_a . To generate their complete torsional seismograms, Liao et al. (1978) summed between 90 and 100 modes using the Normal Mode programme of Kausel and Schwab (1973). Unfortunately, details of the model Liao et al. (1978) used are not given explicitly, so it would seem that the task of generating synthetics for comparison is impossible. However, the seismograms have a minimum period of 10 seconds entailing wavelengths of at least 80 km, and so minor departures in the model should not have a significant effect on the time histories. A model was derived from Figure 8 of Kausel et al. (1977), though not ultimately the same as that used by Liao et al. (1978). Nevertheless it appears to generate comparable seismograms.

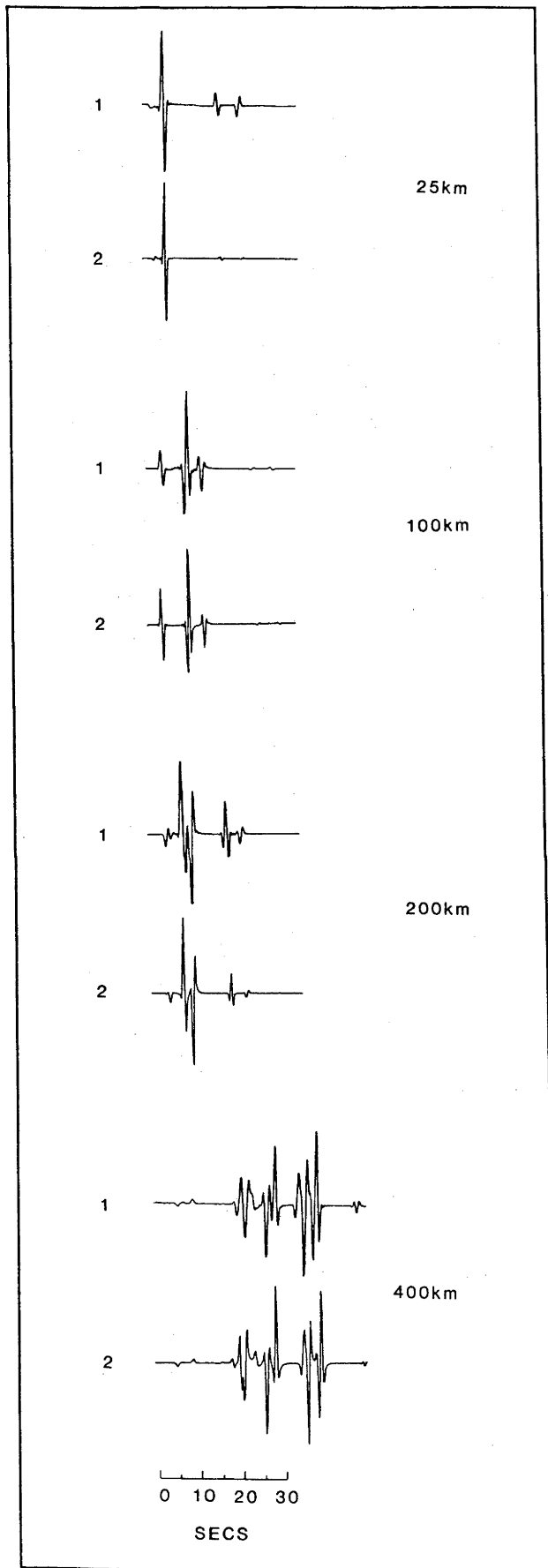


Figure 4.2(a): Comparison of the SH synthetics for a simple crustal model (upper seismogram) of Wang and Herrman (1980, Table 1) with the SH synthetics (lower seismogram) of this work due to a vertical dip-slip source at a depth of 10 km. Amplitudes are trace normalized.

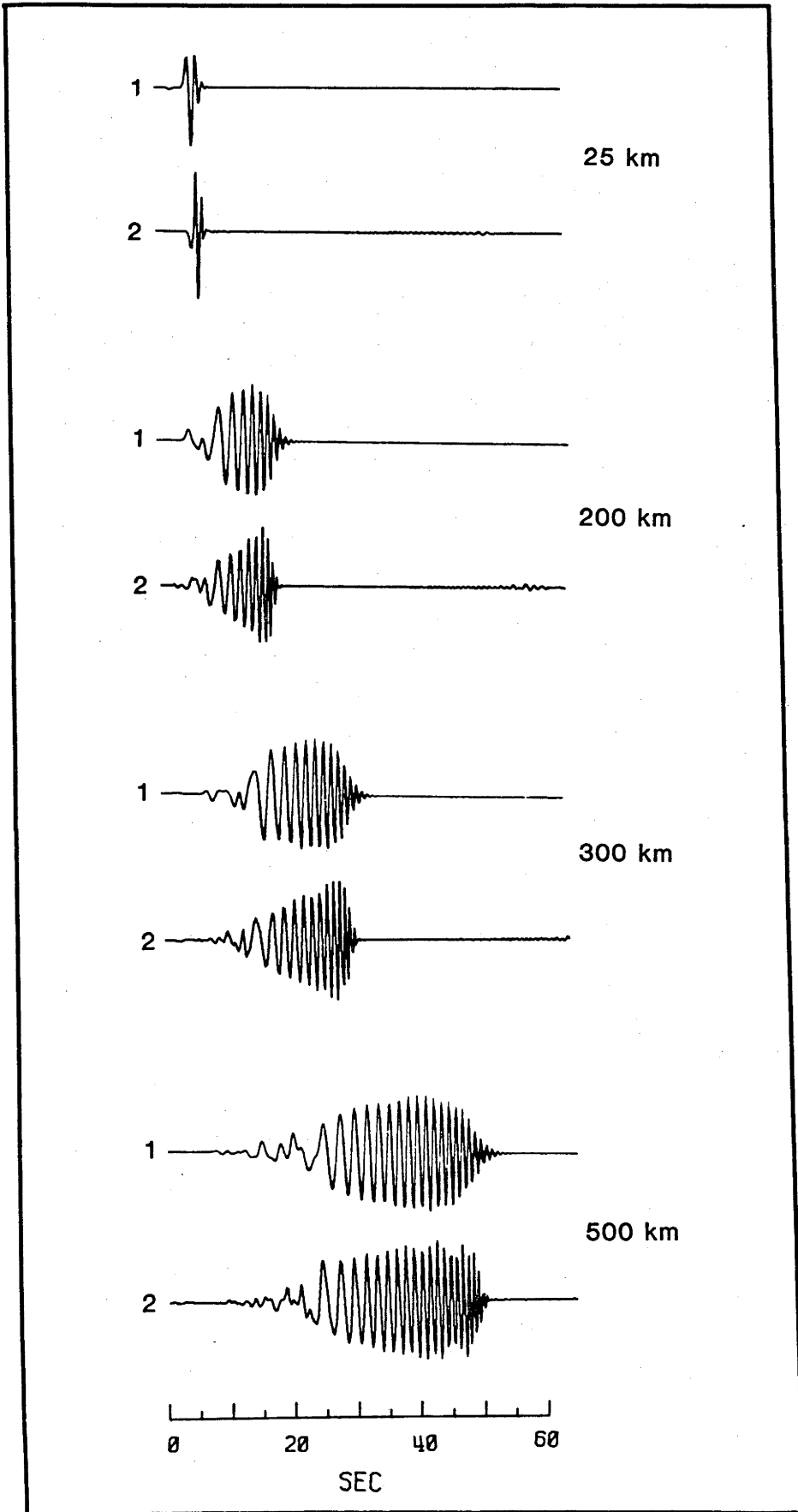


Figure 4.2(b): Comparison of the SH synthetics for the central United States model (upper seismogram) of Wang and Herrman (1980, Table 1) with the SH synthetics (lower seismogram) of this work due to a 45° dip-slip source at a depth of 1 km. Amplitudes are trace normalized.

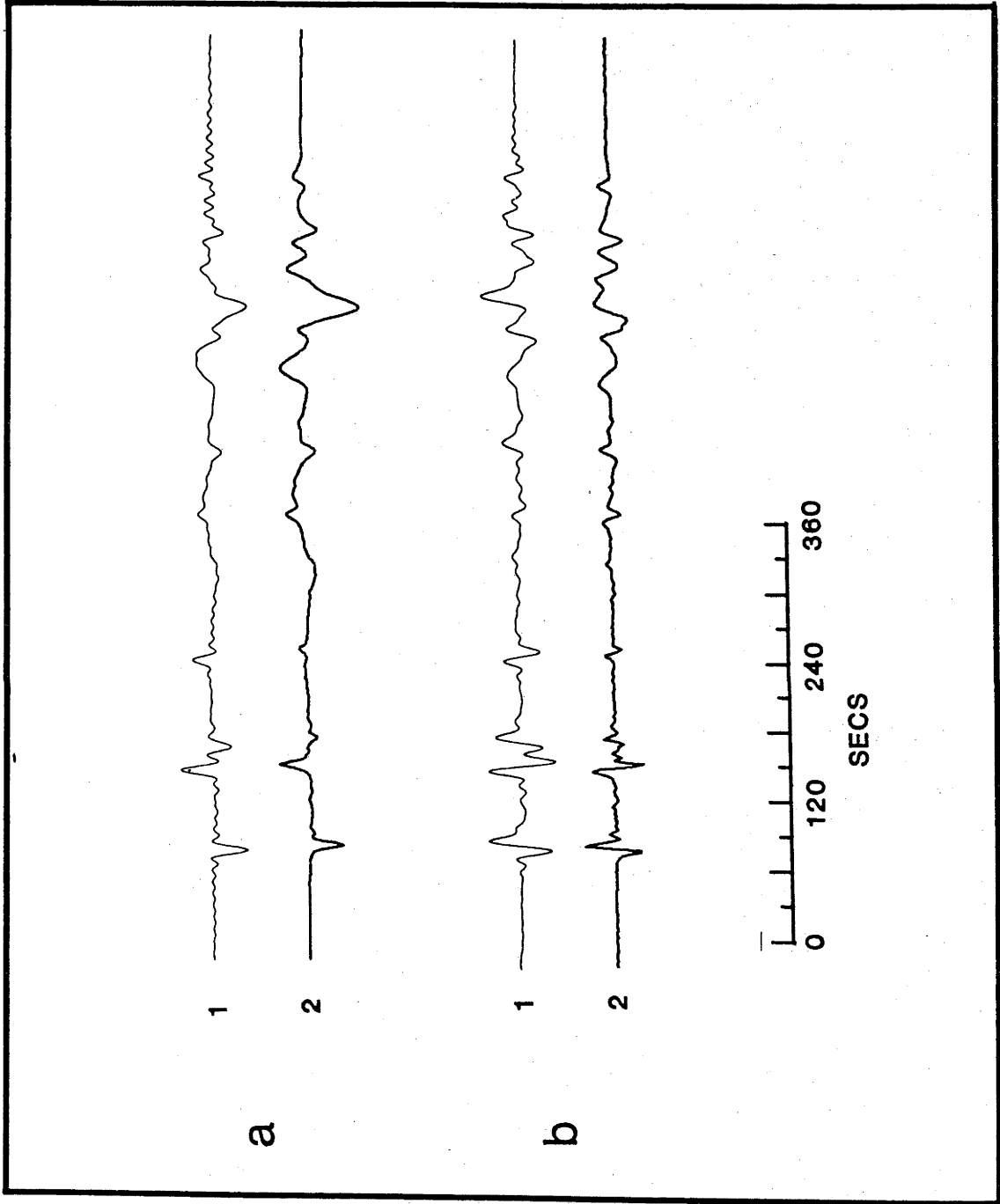


Figure 4.3: Comparison of the SH synthetics for CIT-11 at $\Delta=67^\circ$ (upper seismogram, 1) of Liao et al. (1978) with the SH synthetics (lower seismogram, 2) of this work. (a) Ground motion due to a step-function displacement dislocation. (b) Includes 30-100 WSSN instrumental response.

It is obvious thus far that comparisons have only been made between Reflectivity and conceptually similar programmes. Indeed it is not possible to generate complete seismograms with any other method, therefore any further comparisons are irrelevant to this study. Rather than try to match first arrivals only from competing synthetic seismogram methods, the importance and need to carefully examine the latter parts of a seismic wave train has been emphasized. Herein lies more information about the internal structure of the Earth.

4.6 CONCLUSIONS

The Reflectivity method of Kind (1978, 1979) has now been extended to generate complete SH-wave trains from buried horizontal and dislocation point sources of arbitrary orientation. A simple formulation which is easily implemented on a digital computer is presented. The technique is demonstrably simple. The 'correctness' of the programme is ascertained by its ability to reproduce complete synthetic SH seismograms from other programmes. Contour-Reflectivity of Wang and Herrmann (1980) is perhaps the most numerically stable (if care is taken not to exclude any phases during the definition of the contour) programme available, but at the expense of computer time. The Normal Mode programme of Kausel and Schwab (1973) is by far the fastest for generating seismograms with minimum periods greater than 10 secs. At shorter periods though, an increasing number of torsional modes must be summed, thus making untenable demands on computer time. Thus the formulation presented in this chapter would appear to be better suited to generating realistic SH seismograms for a variety of Earth models.

CHAPTER 5

UPPER MANTLE SHEAR-WAVE VELOCITY MODELS - PAST AND PRESENT

1 DATA AND PRELIMINARY ANALYSIS

5.1 INTRODUCTION

In past studies of the shear-wave velocity distribution of the mantle, the most often utilized suites of S-wave data have been travel times (e.g. Ibrahim and Nuttli, 1967), slowness values from seismic arrays (e.g., Kovach and Robinson, 1969; Hendrajaya, 1981) and waveform studies of first arrivals (e.g. HelMBERGER and Engen, 1974). Surface-wave dispersion and eigenperiods of free-oscillation data constitute another subset of S-wave data for analysis (e.g. Jordan and Anderson, 1974; Cara et al., 1980). It is not surprising then, that the range of shear-wave velocity models from these studies encompass considerable variations in style and distribution of internal velocity contrasts and gradients.

The aim of this study is to examine closely the verity of currently available S-wave velocity models against data from a specific region, in particular the Mediterranean and North Atlantic source regions. In recent years comparing synthetic with recorded LP first arrivals has been a generally accepted strategy (e.g. HelMBERGER and Engen, 1974; Burdick, 1981) but with poor resolution, imposed mainly by the spectral content of the observed data. It was shown in Chapter 1 (c.f., Appendix 1) that inclusion of later LP arrivals, particularly arrivals that have been multiply reflected from deep seated discontinuities may be used to constrain models for fine velocity structure. Conversely, the later arrivals may be used to discriminate between competing models.

5.2 THE MEDITERRANEAN DATA

Central Europe, and in particular the Mediterranean, is a complex tectonic area which exhibits evidence of several past orogenies. Present day activity is dominated by the relative motion of the Eurasian, African and Arabian plates and the Aegean and Turkish microplates (see Figure 5.1). The Adriatic Sea is sometimes denoted the Apulian microplate, or alternatively is regarded as a finger of the African Plate into Eurasia. The latter suggestion is, however, based on few reliable fault-plane solutions (Cagnetti, et al., 1978) and may be modified by later work. There has been some success in interpreting the tectonics of Italy, Greece and Turkey in terms of plate tectonics, but as a whole the region is complex and many questions remain unanswered. The zones of seismicity are diffuse and do not delineate clear plate boundaries as they do in oceanic regions. The absence of magnetic anomalies make it difficult to calculate the relative motions of smaller plates (McKenzie, 1972; Dewey et al., 1973). Indeed, McKenzie (1972) suggested a continuum theory that treats the northern Aegean as a mobile belt without strain rate discontinuities, and in some ways resembles the earlier concepts of orogenic belts proposed by Carey (1955).

Applying the simple concept of plate tectonics to the Mediterranean region, the motion of Africa with respect to Eurasia may be obtained from the spreading rates and strikes of fracture zones in the Atlantic to the north and south of the Azores triple junction at 34° N, together with the slip vectors from shocks on the Azores-Gibraltar ridge. The Azores-Gibraltar ridge complex shows a progressive change from strike-slip faulting near the Azores, with some components of extension to thrust faulting near Gibraltar (see Figure 5.1). This is due to the proximity of the Africa/Eurasia pole which is situated south of the Azores. The pole and rate so obtained are shown in Figure 5.1 and show that Africa is moving northward towards Eurasia (McKenzie, 1972).

Although the present relative motion of Africa with respect to Europe is northward compression, the relative motion that is occurring at the southern border of Europe is not simply compressional but varies due to the interaction of the intervening microplates. In general, the Mediterranean exhibits almost the complete sequence of events in the collision of continents: in the west the African Plate has not yet collided with the Eurasian Plate (except at Gibraltar). In the eastern Mediterranean, the Aegean Plate is consuming the oceanic part of the African Plate, and no sea floor remains between Arabia and Iran. No single fault forms the boundary,

but the motions on all faults are approximately in the same direction as that between Arabia and Eurasia. The result of this geometry is to thicken the continent throughout the active region, and hence to continue to elevate the Caucasus. This behaviour, like that of western Turkey, is not similar to that on oceanic plate boundaries. The inset of Figure 5.1 shows a more realistic framework based on the integration of geology, geometry of plate motion and seismicity studies (after Dewey et al., 1973). The real situation is probably more complex.

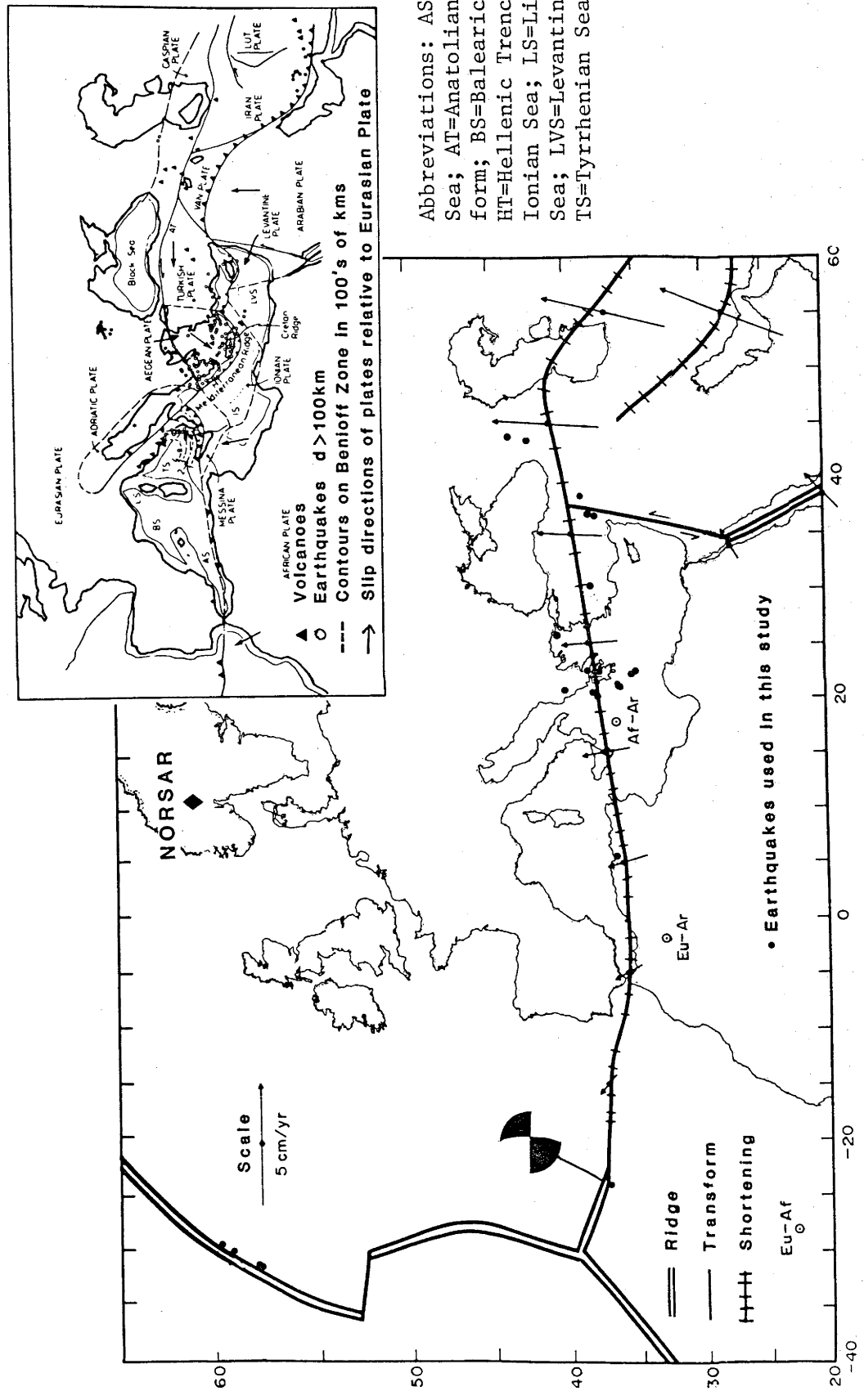
All Mediterranean events for the period 1971 to 1976 with magnitude greater than 4.8 are available in the NORSAR data archive. However, only fourteen events were finally chosen on the basis of having large SNR's (Table 5.1). Their geographical distribution is given in Figure 5.1. For each event studied, an estimated mechanism is presented (Table 5.1) on the basis of solutions published by McKenzie (1972), Cagnetti et al. (1978), North (1977) and Rotstein and Kafka (1982). For each event, an attempt was made to determine the focal mechanism from first-motion data given by ISC, but because of the poor seismic network distribution and inaccuracy of observatory reporting, clear mechanisms for all of the events could not be determined. Because of the complex nature of Mediterranean tectonics, it is difficult to generalize a style of faulting. Many focal-plane solutions of events on major tectonic structures in the Mediterranean have been published and it seems reasonable that if two epicentres map onto the same tectonic feature (such as a well-defined fault plane) then the two events will have similar mechanisms. As anticipated, the focal mechanisms differ greatly in type, especially when two events are proximally situated near a junction of two tectonic features. An attempt was made to employ the techniques of Langston (1982) and Ingate (1983, Appendix 3) for determining focal-plane mechanisms from single-station data. However, this form of analysis requires that the direct arrival be well separated from secondary arrivals such as seen on LP records in the distance range 35° to 80° . At distances less than 35° , the first arrival is contaminated with secondary arrivals and so to continue this analysis, a model for the upper mantle must be assumed known. Correct knowledge of timing and amplitudes of the second arrivals are critical for such techniques to work successfully, and as will be shown in the second part of this study (Chapter 6), this knowledge is not yet known with any certainty. This fact, and poor control on focal depth (c.f. Section 5.4), precludes this form of analysis to determine focal-plane solutions.

Table 5.1 List of events used in this study (after ISC)

No.	Date	Origin Time		Location		Depth km	Epicentral ⁺ Distance km	M _b	Region	Presumed Source [#]	
		HH	MM	SS	Deg. N						Deg. E
4	05 04 72	21	39	57.0	35.15	23.56	14	2998	5.9	Crete	DS
6	09 13 72	04	13	19.7	37.96	22.38	75	2670	5.8	S. Greece	SS
10	11 04 73	15	52	12.6	38.87	20.54	13	2535	5.6	Greece	DS
11	11 29 73	10	57	44.3	35.18	23.81	37	3001	5.6	Crete	DS
13	05 26 75	20	19	33.2	36.04	-17.56	17	3411	5.5	N. Atlantic	SS
16	06 12 76	00	59	18.1	37.52	20.58	17	2683	5.4	Ionian Sea	SS
19	04 03 72	18	52	59.8	54.28	-35.14	32	2788	5.3	N. Atlantic	DS
20	04 03 72	20	36	20.0	54.33	-35.20	13	2788	5.1	N. Atlantic	DS
23	02 26 75	04	48	53.2	84.98	98.50	23	3283	5.3	Severnaya Zemlya	DS
24	12 08 75	22	53	2.1	79.14	2.06	38	2069	5.2	Greenland	SS
32	03 17 75	05	35	17.6	40.48	26.08	18	2494	5.0	Turkey	SS
33	09 30 76	00	32	58.0	37.42	20.34	10	2690	5.1	Ionian Sea	SS
34	03 31 76	00	01	2.1	58.38	-31.85	19	2386	5.0	N. Atlantic	DS
35	09 05 76	22	07	34.4	38.51	40.94	17	3245	5.0	Turkey	SS
36	05 12 71	06	25	15.4	37.64	29.72	30	2900	5.5	Turkey	DS
43	07 28 76	20	17	44.1	43.18	45.57	18	3031	5.3	E. Caucasus	SS
46	01 05 73	05	49	17.6	35.80	21.91	34	2894	5.3	Mediterranean	DS
48	06 29 71	09	08	12.0	37.11	36.85	35	3210	5.0	Turkey	DS
49	07 11 71	20	12	56.2	37.16	36.85	19	3206	5.0	Turkey	DS
50	06 10 71	21	32	41.0	59.37	-30.38	51	2264	5.0	N. Atlantic	DS
53	04 29 76	22	18	7.7	40.96	42.87	30	3101	5.0	Turkey	SS
54	07 01 76	11	19	4.1	82.23	-7.10	19	2448	5.0	N. Svalbard	SS
55	06 28 74	11	9	38.5	36.57	5.26	20	2727	5.0	Algeria	DS
56	01 08 75	19	32	34.1	38.24	22.65	26	2646	5.4	Greece	SS

+ to centre of NORSAR array

see text SS=strike-slip, DS=dip-slip on an inclined plane.



Abbreviations: AS=Alboran Sea; AT=Anatolian Transform; BS=Balearic Sea; HT=Hellenic Trench; IS=Ionian Sea; LS=Ligurian Sea; LVS=Levantine Sea; TS=Tyrrhenian Sea.

Figure 5.1: Neotectonics of the Alpine system. The plate boundaries are simplified to a single line in order to show the direction and magnitude of the relative motions of the larger plates. The vector in the north-east Atlantic shows the scale of all other vectors in the figure, and does not represent motion between America and Eurasia. Locations of most earthquakes used in this study (Table 5.1) are given by •. A focal mechanism solution from ISC first-motion data is given for event #13. Inset shows details of major tectonic entities (after McKenzie, 1972; Dewey et al., 1973).

The data have been plotted in the form of a record section in Figure 5.2. Note that the data in Figure 5.2 are trace normalized and aligned in time such that the first arrival corresponds to the JB travel time for a surface focus. In the interests of conformity, the polarity of some events was changed so that first motion is always to the left. This was necessary because some events had first excursions that went to the right. This is explained easily in terms of orientations of the focal plane. For example, events occurring on either side of the North Atlantic ridge axis will have opposite polarity first motions. Events presumed "deep" are arranged such that the depth-phase with its apparently larger amplitude than the first arrival (particularly on events #6, #48 and #49) is aligned with the JB curve. The near surface and deep events are combined to extend the limited data set, and from the preceding example, if the depth phase has a larger amplitude than the direct arrival, then the character of the seismogram will be largely dictated by the depth phase, and not the relatively smaller direct arrival.

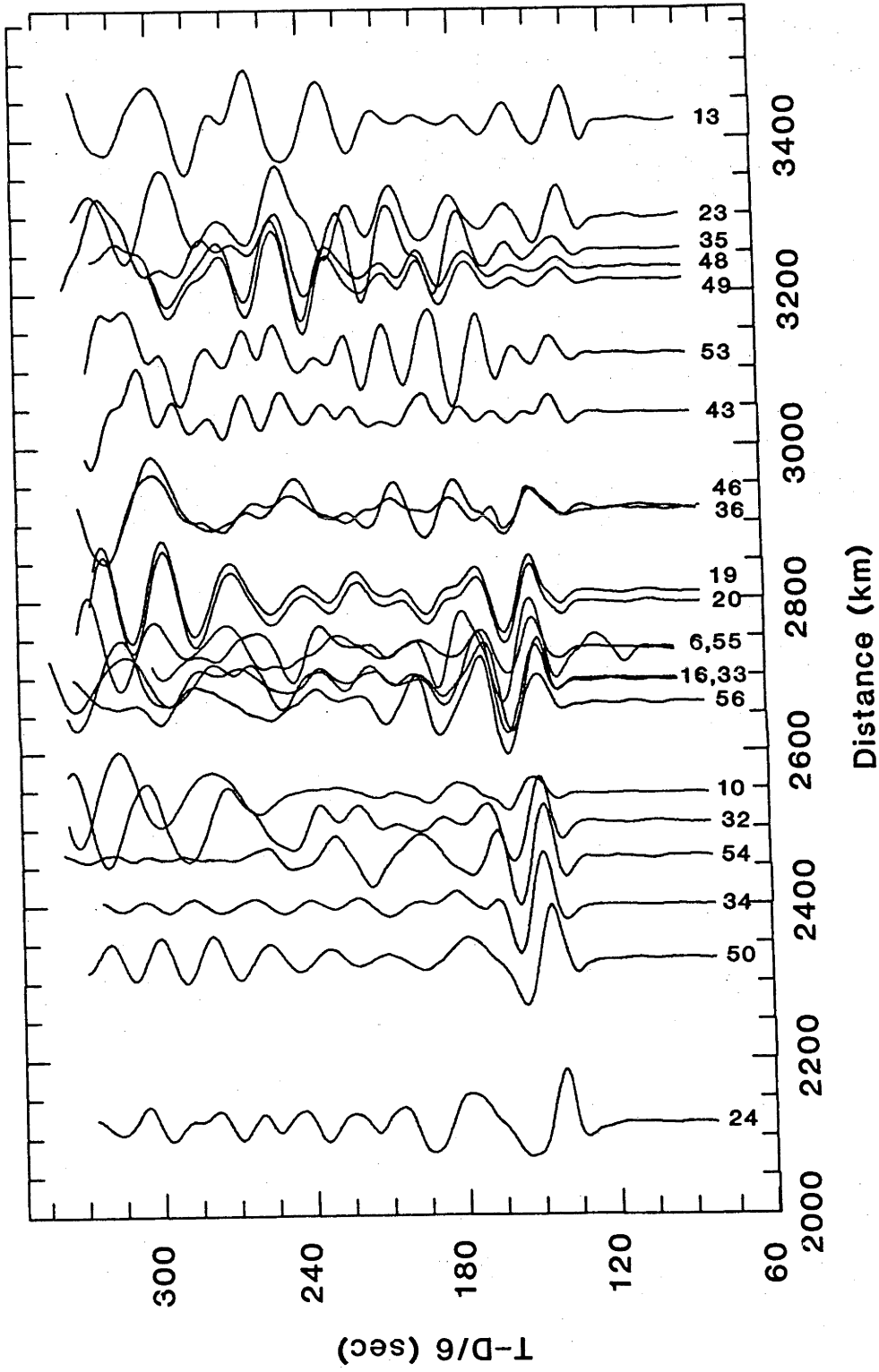


Figure 5.2: Composite seismic section of LP recordings of events in Table 5.1. Output of NORSAR array have been stacked to produce one trace per event. Arrival times are corrected (except event #6) to lie on the surface-focus Jeffreys-Bullen travel-time curve. Traces are normalized to peak amplitude.

5.3 THE NORTH ATLANTIC DATA

The mid-Atlantic accreting ridge and the mid-Arctic ridge to the north of it separate the American Plate from both the African and Eurasian Plates. The poles of motion show that the spreading rates are fastest in the south (2 to 2.3 cm/yr) where the African and South American plates diverge, with the slowest rates in the north (1.5 cm/yr) where the Eurasian and North American plates join (le Pichon, 1968; Pitman and Talwani, 1972).

Seismograms for eight events sited in the North Atlantic and Arctic Oceans were obtained from the NORSAR data archive satisfying the requisite parameters of distance and SNR (Table 5.1). That three Arctic Ocean events have been included with the north Atlantic data can be justified on the similarity of waveforms from the two regions. Furthermore, England et al. (1978) found that travel times were consistent for events of widely differing azimuths in the North Atlantic and Arctic Oceans. As with the Mediterranean data, ISC first-motion data was used to determine fault-plane solutions. Only one solution could be unambiguously defined: event #13 lies on the Azores-Gibraltar ridge complex, and the strike-slip fault-plane solution is in accordance with studies of other events on this complex (e.g. Hirn et al., 1980). The oceanic data have the fortuitous property of having very simple focal mechanisms. Ocean floor earthquakes generally occur as a result of tension normal to the mid-ocean ridge axes, and may be mapped onto features of considerable topographic detail as dip-slip faulting on an inclined plane, similar to a graben-type structure (Sykes, 1967; Weidner and Aki, 1973). Transform faults owe their existence to the mechanics of slab motion on a sphere and preserve continuity of the lithosphere. Transform faults are found to be between displaced ridge crests and may be generalized to have a simple strike-slip mechanism (Sykes, 1967). Given that the oceanic events lie on either ridge axes or transform faults, Table 5.1 suggests possible mechanisms for each event, and the geographical distribution of the North Atlantic events are given in Figure 5.1.

5.4 A PRIORI ASSUMPTIONS

For this study the data from both the Mediterranean and North Atlantic have been combined to form a composite data set. This action was necessary

because the two sets of data do not adequately cover the distance range separately. Combining the two sets fills the gaps in the record section. The move to combine two data sets may be partly justified by accepting the fact that previous studies have determined that at distances beyond 20° , the data representing travel paths through oceanic and continental material are at least similar for LP waves. This suggests that the mantle is laterally homogeneous below about 250 km. Sipkin and Jordan (1975) questioned this and used vertical travel times of ScS from deep-focus events to find that the average one-way travel times for oceanic islands averaged about 8s greater than the times for continental stations. Their interpretation invoked significant heterogeneity between different regions below 400 km. Jordan (1975) suggests that the tectosphere (the region which translates coherently in the course of horizontal plate motions) may occupy the upper 700 km of the mantle beneath mountain belts such as the Alps. Contrary to this, Okal and Anderson (1975) point out that ScS paths "average" velocity throughout the mantle, and cannot resolve where the differences lie. Hales (1976) contends that regional differences in ScS and multiple ScS residuals can be accommodated in the upper 250 km. Cara et al. (1980), in a detailed study of regional differences using higher mode surface waves, required strong regional variations between the Pacific Ocean, western U.S. and eastern U.S. above 250 km, with no significant differences below this depth. Dziewonski (1971) demonstrated that the phase velocity differences for oceanic and continental surface waves may be explained by models with the significant velocity contrasts confined above 200 km. He concludes that surface-wave data alone do not require continent-ocean heterogeneity at greater depths.

The situation for Europe, however, is less clear. There are strong indications for marked lateral heterogeneity, but the distribution and refinement of anomalous velocities are particularly in need of refinement. Lateral heterogeneity was reported by Cleary and Hales (1966) after an extensive study of deviations from the Jeffreys-Bullen travel-time curve. Their findings included positive residuals for the Carpathians, and generally early arrivals in Scandinavia. Mayer-Rosa and Mueller (1973) in a unified inversion of P, S and surface waves concluded that regional differences occur between southeast and southwest Europe down to a depth of 200 km and that there are pronounced low-velocity zones (LVZ's) in the depth ranges 70 to 120 km, 160 to 210 km and 260 to 310 km. Caputo et al. (1976) (and also Panza, 1979; Panza and Mueller, 1979) determined from

Rayleigh-wave dispersion that very low S-wave velocities exist beneath the Alps to depths of 300 km. King and Calcagnile's (1976) reappraisal of the model of Massé and Alexander (1974) derived a very simple model for western Russia which did not include the LVZ of Massé and Alexander. Using polarization anomalies of higher mode surface waves, Crampin and King (1977) suggested 7% velocity anisotropy for P waves in central Europe. Crampin and King were unable to place an upper limit on the depth to which the anisotropy exists, but suggest that as little as 10 km of material possessing 7% velocity anisotropy is probably sufficient to produce the observed surface-wave polarizations. Thus it is likely that the LP data set of this study may be adequately modelled by a homogeneous Earth. England et al. (1977, 1978) used travel times to find no appreciable variation between the oceanic and Russian platform velocity structure below 300 km, but the velocity distribution for western Eurasia was anomalous in the depth range 300 km to 500 km. Nolet (1977) inferred a model similar to that of Mayer-Rosa and Mueller (1973), except that he could find no justification for the third LVZ between 260 and 310 km nor the large size of the velocity discontinuities. Using higher mode surface waves, Cara et al. (1980) could find no LVZ in northern Eurasia, although a LVZ could explain the apparent birefringence of S-wave velocities in western Europe. Given and HelMBERGER (1980) derived their model K8 from waveform modelling of SP and LP waves, and found evidence for a LVZ in the depth range 150 to 200 km for northwest Eurasia. Romanowicz (1980) and Hovland et al. (1981) inverted high quality ISC travel times for a three dimensional model that invoked lateral heterogeneity to depths of at least 600 km. Both studies determined that lateral heterogeneity was marked in the depth range 0 to 100 km, with very little lateral heterogeneity in the range 100 to 400 km, and anomalous velocities in the range 400 to 600 km which may have been produced by topography on the "650-km" discontinuity. Romanowicz suggested that a LVZ existed beneath the Alps but on the other hand, Hovland et al. found evidence for a high-velocity zone in the same region and suggested that it was due to a relic subduction zone. Burdick (1981) in another study of LP waveforms failed to substantiate the findings of England et al. (1977, 1978) for lateral heterogeneity in Europe. His model has no LVZ but it is probable that the lateral heterogeneity indicated in the above studies would go unresolved in LP data.

Such contention with regard the existence of LVZ's, etc. beneath Europe may go unresolved in this study, and so it must be stressed that because

the data sample both the Mediterranean and North Atlantic it is only possible to look at "average" velocity structure. This restriction is implicit when combining the data sets, but the above studies show that any anomalous behaviour in the velocity distributions between the two regions at depths greater than 250 km would probably go unnoticed in a study of LP data.

Other than factors such as epicentral distance and SNR, the other important criterion for selecting events is that of focal depth. For the purpose of this study, it is important to select a suite of events with near-constant focal depth, otherwise to compare the data with synthetic seismograms would necessitate the time consuming task of individually synthesizing seismograms for each event taking into account the focal depth. For the events listed in Table 5.1, ISC give focal depths ranging from near surface to 75 km (event #6). Mislocation errors can produce errors of several seconds in calculating the travel times. In order to compare the absolute travel times of each event, the event timing should be corrected for focal depth using equation 1.1.

Figure 5.3a shows the observed travel times corrected for focal depth against the JB (Jeffreys-Bullen) travel-time curve for a surface focus. There is considerable scatter in the data, the observed times being later than the JB times by an average of 3s. Examination of the array outputs for events #6, #11, #48 and #49 show a secondary arrival with the same apparent velocity as the first arrival; this is presumably a depth phase. The absence of a depth phase on the other events suggest that they are near surface. Here, near surface is taken to mean less than 6 km for pure strike-slip events and less than 15 km for pure dip-slip faults. Langston and Helmberger (1975) showed that for pure strike-slip sources of less than 6 km, the depth phase contributes little to the overall appearance of the seismogram. The same is true for pure dip-slip faults at depths less than 15 km. To elucidate further the probability of ISC mislocation, comparisons will now be made between events presumed to lie on the same fault surface because they have similar locations but given by ISC to have different depths. Figure 5.4 compares SH seismograms for events #4 and #11 presumably located within 25 km of each other. The deconvolved outputs of the 22 channels of NORSAR have been stacked (delayed and summed) using the appropriate slowness values. Although the benefits of stacking are not immediately as obvious on LP data as on SP data due to the small array aperture to wavelength ratio, incoherent noise is suppressed by $1/\sqrt{N}$ ($N =$

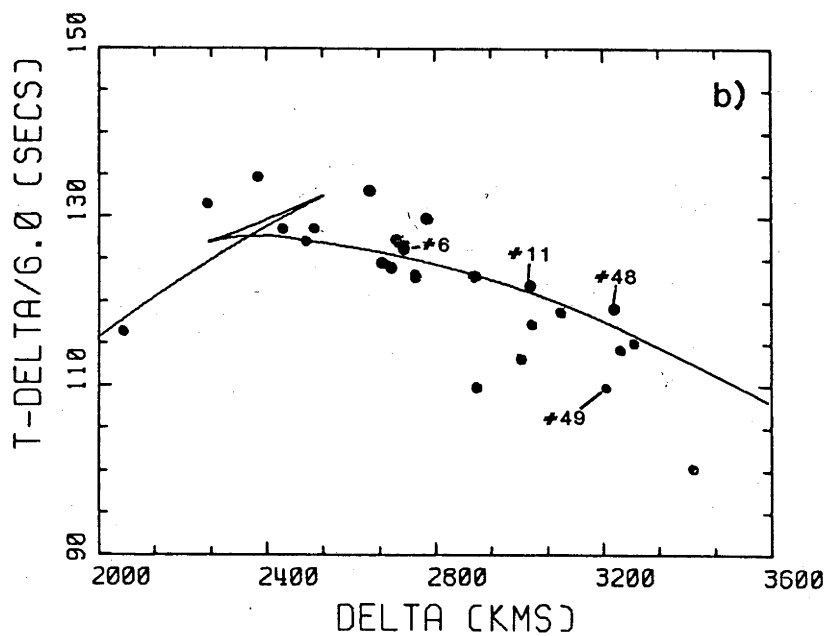
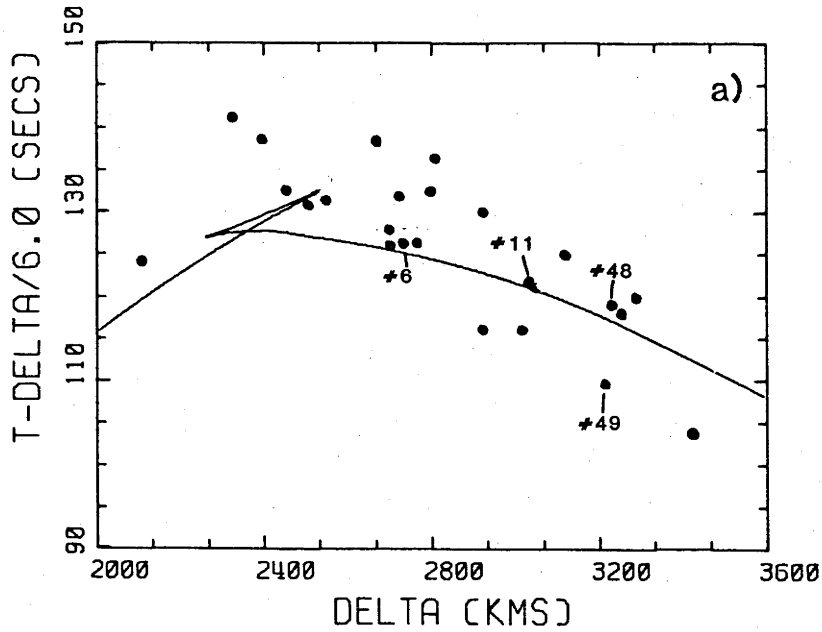


Figure 5.3: (a) Event travel times corrected for focal depth plotted against surface focus JB travel-time curve. Events #6, #11, #48 and #49 are positively identified as having epicentral depths >10 km. (b) Event travel times not corrected for focal depth (except events #6, #11, #48 and #49).

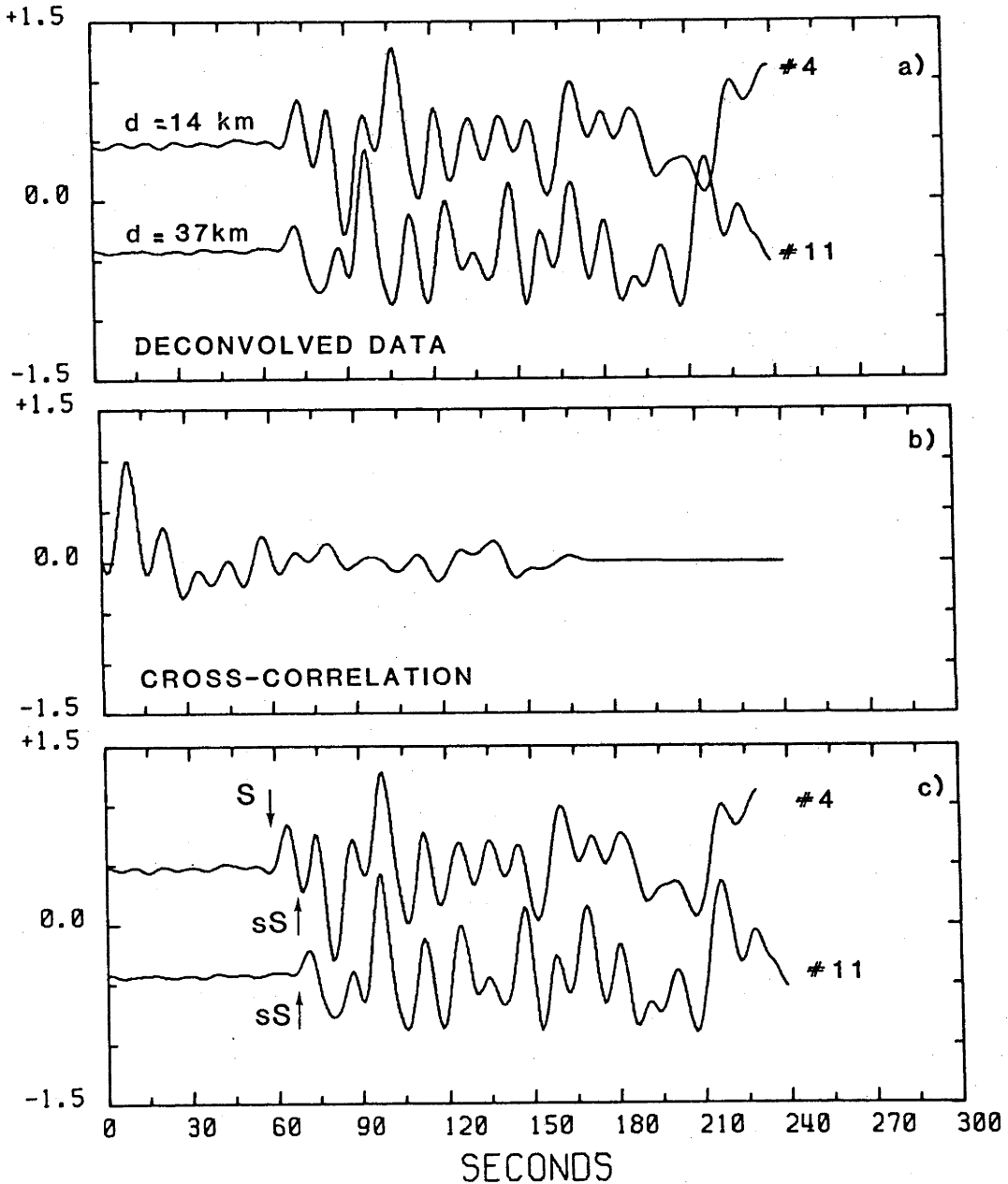
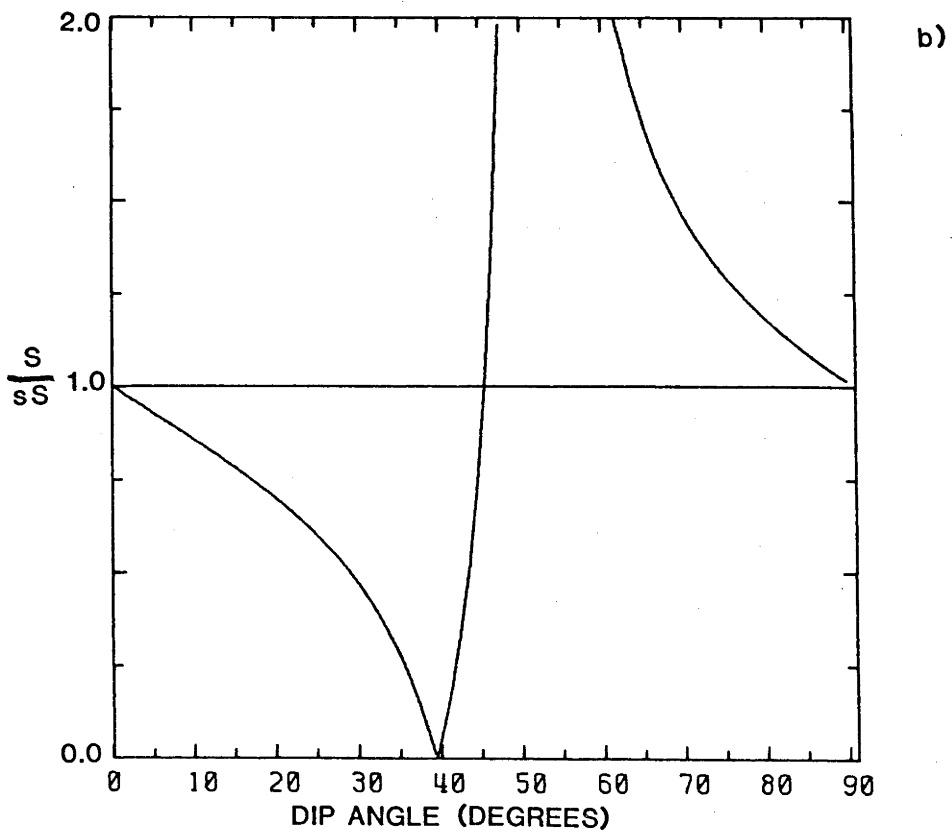
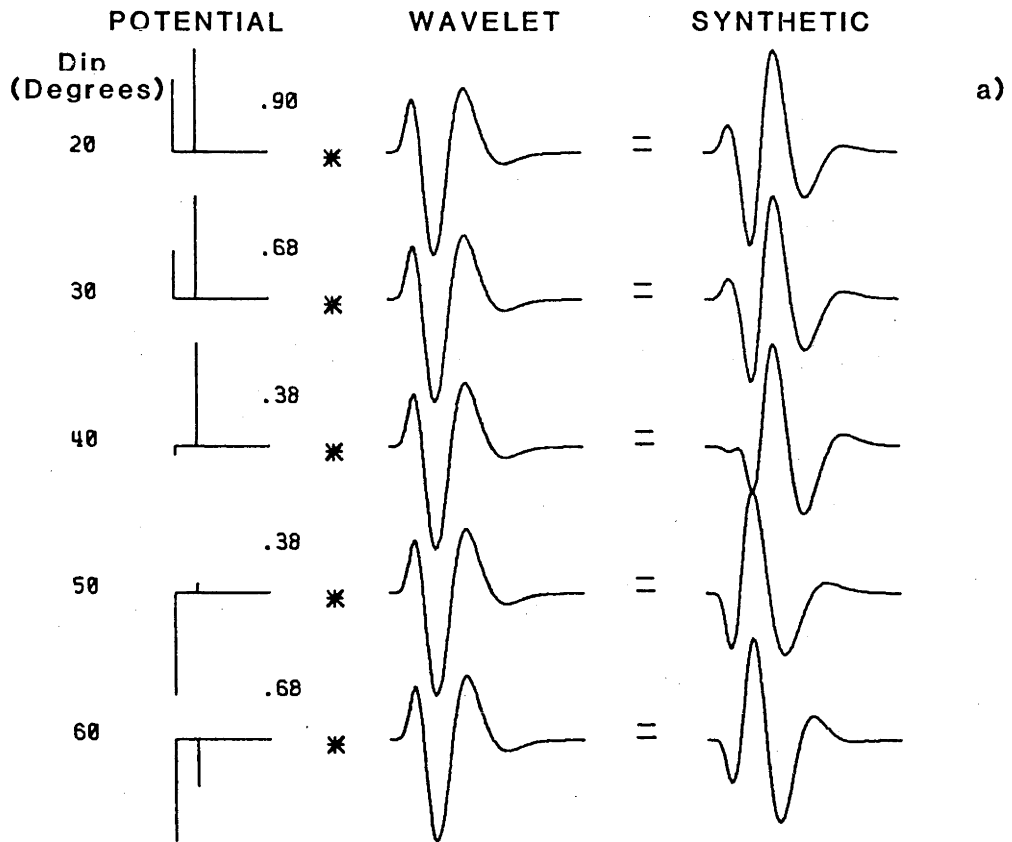


Figure 5.4: Comparison of events #4 and #11. (a) Stacked deconvolved data with ISC estimates of focal depth. (b) Cross-correlation of #4 and #11. (c) #4 shifted in time relative to #11 by an amount indicated by timing of peak in cross-correlation. Interpreted phase arrivals are indicated. The absence of S on #11 may indicate S radiation was along a node.

the number of instruments) and the stacked channels represent the best average response of the earthquakes under study (Mack, 1969). The seismograms for events #4 and #11 are clearly different, presumably on account of differences in focal depth (ISC give 14 and 37 km respectively). The cross-correlation of #4 with #11 yields a large peak at a delay of 9s. If #4 is displaced to earlier time relative to #11, there appears a good match in waveforms between #4 and #11. This may indicate one of two things: either that #4 was near surface or that #4 was buried, but some mechanism decreased the amplitudes of the direct phase at the expense of the depth phase. The latter interpretation arises by considering that #11 exhibits a direct and depth phase, with an sS-S separation of 9s corresponding to a focal depth of 14 km. Small differences between the aligned wave trains probably arise from interference between the direct phase and depth phase in event #11. The apparently large amplitude of the depth phase relative to the direct phase on #11 and presumably #4 may be explained in terms of energy radiation patterns from a shear-dislocation source. Although the SH reflection coefficient at the free surface is always real and unity, orientation of the focal plane may produce a node for the direct phase but not the depth phase. The expected style of faulting for #4 and #11 are dip-slip on an inclined plane, as anticipated for events mapping onto a Benioff zone (Gregersen, 1977). For this fault orientation, the dip angles required to produce a node are critical as shown in Figure 5.5, but on either side of the node are dip angles where the amplitude of the direct phase is smaller than the depth phase. Of course, for other orientations, nodes can be produced for the depth phase and not the main phase. From Figure 5.5, an estimate of the dip of the Benioff zone is seen to lie between 30° and 40° . Although this is a very crude method, this estimate is in accordance with a dip of about 35° obtained by Gregersen for the upper boundary of the subducting Aegean Plate. Unfortunately, this study was unable to acquire data for this event from stations at other epicentral distances, and so it was not possible to positively answer this speculation.

Figure 5.6 examines other pairs of events given by ISC to have different depths and similar geographic coordinates. For these events the deconvolved and stacked records are almost identical, so it appears reasonable to assume the ISC depth for most events is incorrect. The zero-focal-depth assumption is quite sound on tectonic principles for, at least, the North Atlantic data. Even at large distances from the ridge

Figure 5.5: Apparent amplitudes of S and sS recorded at a distance of 30° for changing dip of a dip-slip fault. Dislocation source is buried in a "normal" crust at a depth of 10 km. The potentials (a) are calculated using equations of Langston and HelMBERGER (1975) for different angles of dip and convolved with a basic wavelet consisting of a Q operator and instrument response. The resulting synthetics straddle a node of the direct S phase. The graph (b) gives a continuous description of the ratio S to sS against dip angle. Note that the sS phase has a node near 50° .



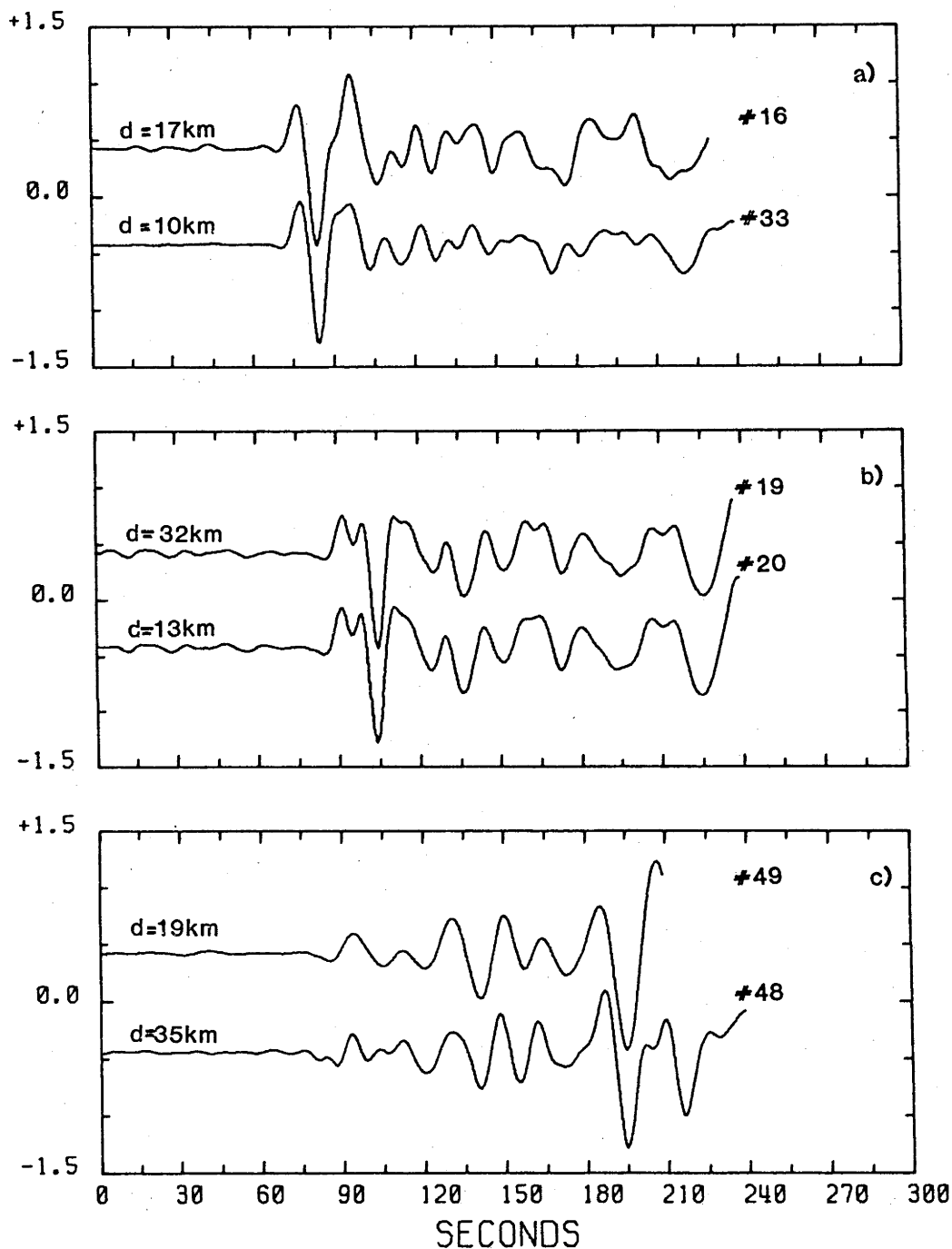


Figure 5.6: Comparison of pairs of events presumably located on the same tectonic feature for which ISC has given different focal depths. Data have been deconvolved and stacked. (a) Events #16 and #33. (b) Events #19 and #20. (c) Events #49 and #48.

axis, the crustal thickness is quite thin, between 8 to 10 km. Below the crust, the geothermal contours are quite high (Solomon, 1973) and a state of partial melting may exist. Thus, if significant stresses cannot be accommodated below the crust then the source must be located within the crust. This is in accordance with work by Weidner and Aki (1973) who used Rayleigh-wave spectra to determine the focal depth of some mid-Atlantic ridge events to be no more than 5 km.

Based on the near-surface assumption, the travel times of Figure 5.3a have been recalculated assuming that the events have zero focal depth, and are plotted against the JB curve in Figure 5.3b. Even though the scatter is still large, the events not marked as being deep (i.e. those events not having noticeable depth phases) now lie much closer to the predicted travel times of the JB model with an average residual of $-0.7s$. This assumption will make the forthcoming analysis easier, because individual events need not be modelled. Radiation patterns aside, the synthetics will be independent of the orientation of the fault, and so the synthetics now need to be calculated only once without a priori knowledge of focal depths and mechanisms.

5.5 DATA PROCESSING

The data are deconvolved according to the wavelet extraction method with 1% prewhitening outlined in Chapter 3, the array outputs stacked and the events plotted in the form of a record section (Figure 5.7). The wavelet used in the deconvolution was the integral of the NORSAR instrument response. The reason for using the integral of the instrument response rather than the instrument response will be explained in the following discussion. The source function for the synthetics is assumed given by

$$M(\omega) = \frac{1}{2}(1 + \cos(\pi\omega/\omega_0)) \quad 5.1$$

The derivative of this moment function, $m'_0(t)$ will be proportional to the ground motion in the far field and is approximately one sine period with period $T \approx 15/\omega_0$, where ω_0 is the cut-off frequency (usually the Nyquist). Earthquake sources however, are better represented by ramp or step functions and will be spike-like in the far field. Thus, the true ground motion and the synthetic ground motion are approximately related by the Fourier derivative theorem. In order to compare the two ground motions, either take the derivative of the deconvolved output or equivalently, deconvolve the recorded data with the integral of the instrument response. An alternative procedure would be to integrate the synthetics. Unfortunately, numerical integration was seen to act as a low-pass filter and so to recover the high frequencies requires increased computing requirements (computing requirements for the Reflectivity method are squared if the bandwidth is doubled).

Inspection of Figure 5.7 shows that the coherence between the later, large arrivals is only fair, particularly in the latter parts of the wave train. This may be due in part to the failure of the near-surface assumption, but the most likely reason may be scattering and reverberation in the structurally complex Mediterranean source crust. To avoid such scatter in the data, one could use only deep events, but their paucity and apparently poor SNR have excluded their use in this study.

Definite correlations between seemingly different wave trains can be made on Figure 5.7. For example, there appears to be a break in the travel times at about 2690 km (24.2°). At distances beyond 24.2°, the second arrival carries with it energy till 3340 km (30°). The first arrival at distances greater than the cross-over has a large amplitude relative to the rest of the wave train which decreases until 3000 km (27°), then increases

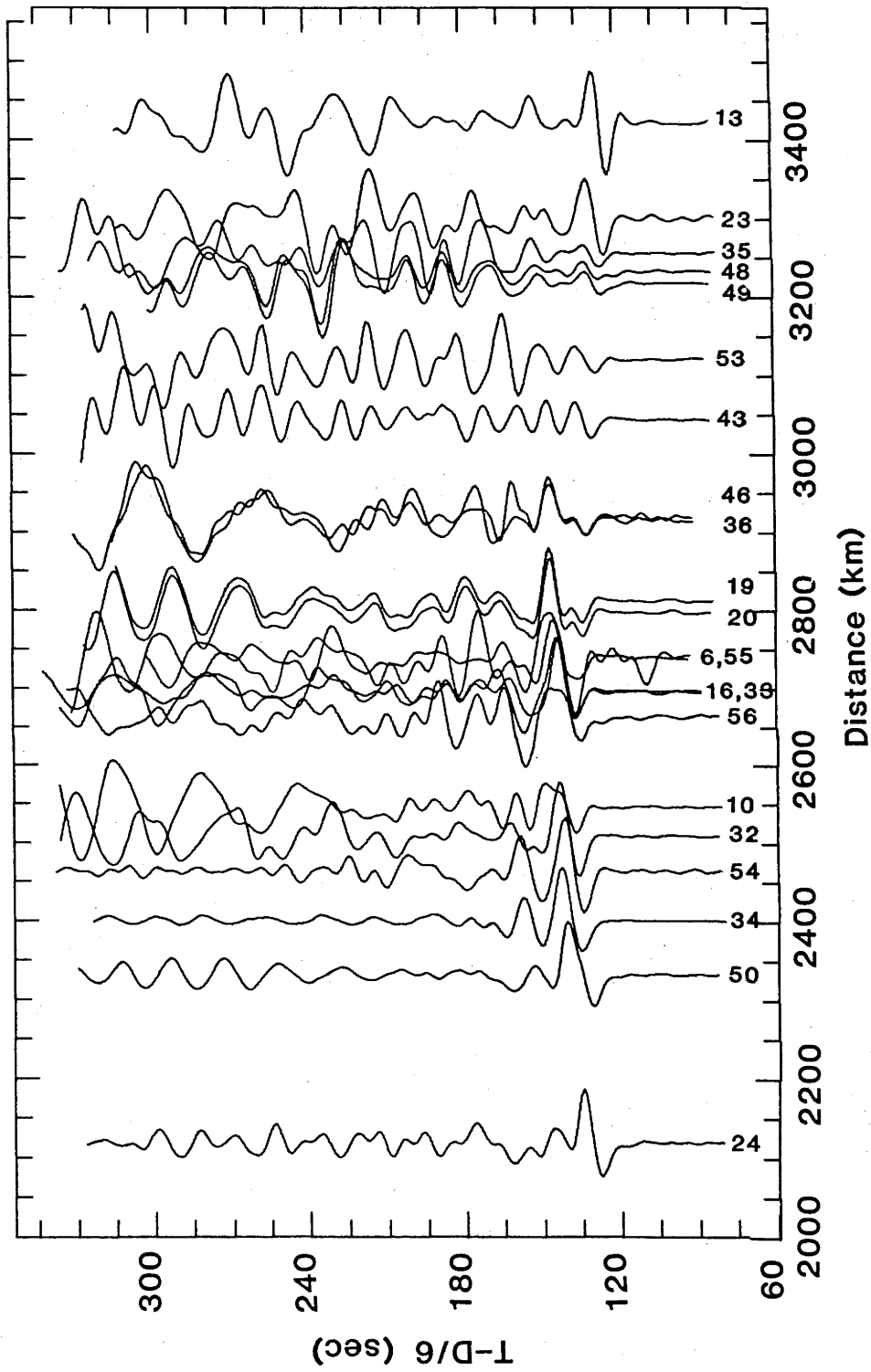


Figure 5.7: Wavelet extracted data of Table 5.1. The NORSAR-type instrument response was used as an estimate of the wavelet. The deconvolved array outputs have been stacked to produce one trace for each event. Arrival times have been corrected to lie on the surface-focus Jeffreys-Bullen travel-time curve. Traces are normalized to peak amplitude.

in relative amplitude until the end of the data set at 30° . Other large arrivals can be seen which may be followed for several degrees. Love waves can be seen near the end of the wave train in some cases, but appear to be completely absent in others. This question will be discussed later. It is clear that with this data suite it will not be possible to exactly match observed and synthetic seismograms. Liao et al. (1978) and Dziewonski et al. (1981) were able to match synthetics with seismograms but their studies used intermediate to deep events recorded at distances greater than 4500 km (40.5°). In addition, they matched longer periods than the periods of the data in this study. It does appear possible and reasonable to isolate those features that are most obvious on the data, since such features may be multiple reflections from regions of very rapid velocity increases as shown in Chapter 2.

The deconvolved data of Figure 5.7 appear too complex upon which to perform a preliminary analysis. The data analysis strategy proposed in Chapter 3 included the iterative least-squares method of Kanamori and Stewart (1978) which enhances travel times of the largest arrivals at the expense of the smaller, and possibly anomalous, arrivals. That the component arrivals of the Earth response are non-stationary precludes this technique from decomposing the entire wave train into its component arrivals. Nevertheless, it has been shown that timing information of the largest arrivals can be determined, even in the presence of noise. This processing was carried out on the composited data of Figure 5.2 and shown in Figure 5.8. Note that although noise exists in the "spikograms" (a seismogram composed of delta functions) in the form of incoherent arrivals, some events may be coherent from channel to channel, but not event to event. Some correlations are quite outstanding, extending over several degrees and it is probable that such arrivals are important to this study. On the whole, Figure 5.8 is quite remarkable, revealing trends unseen in the deconvolved seismograms of Figure 5.7, although the spikograms do not reveal all the information on important arrivals. For example, the second arrival from 2670 km (24°) to 3340 km (30°) is quite apparent on the deconvolved seismograms, even where it has small amplitude on event #13 at a distance of 3400 km (30.7°). The spikograms fail to reliably identify this arrival beyond 2890 km (26°) where the relative amplitude decreases noticeably. It is necessary then, to include both data presentations in the analysis.

Superimposed on Figure 5.8 are tentative travel-time branches

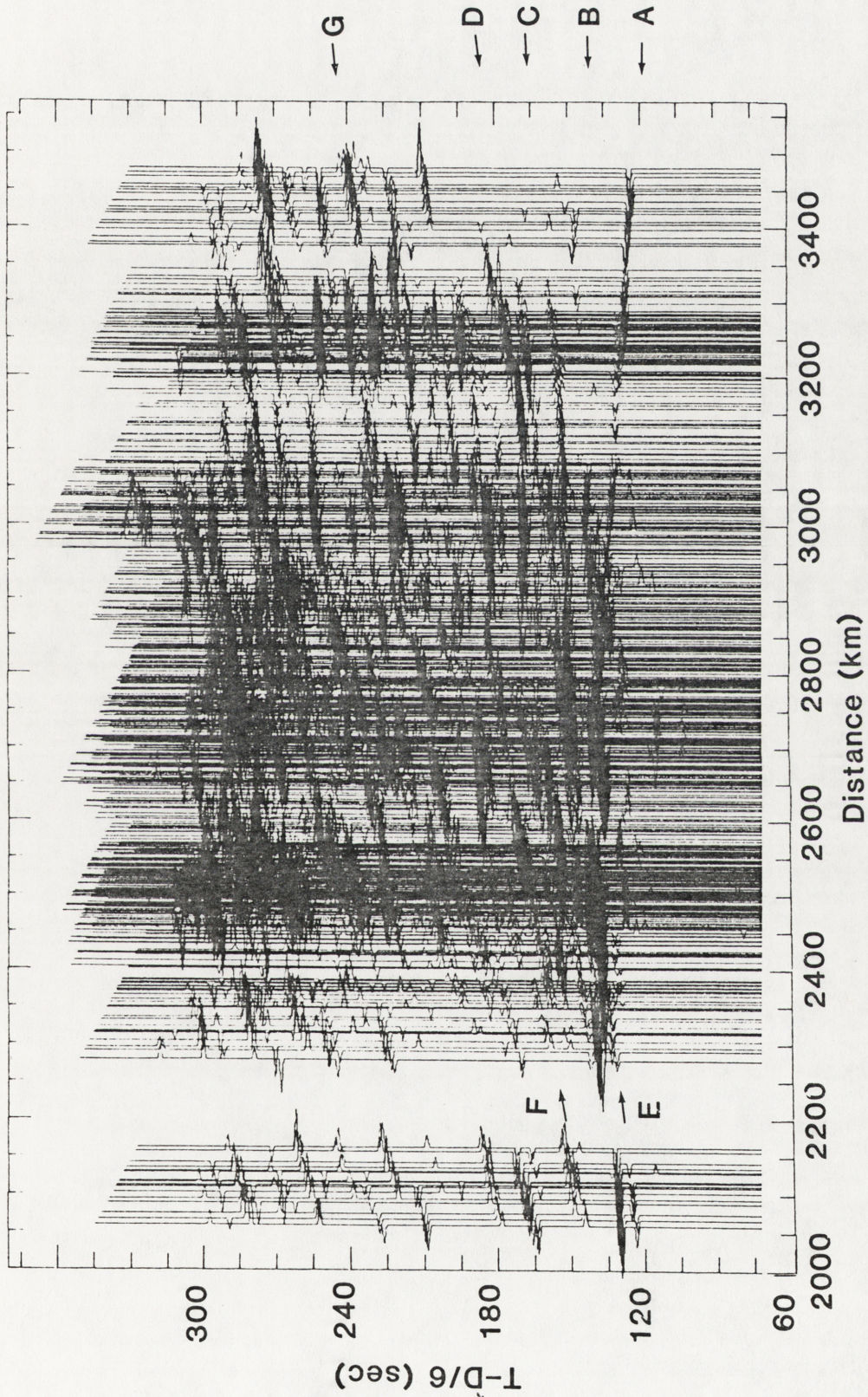


Figure 5.8: Iteratively decomposed traces of the data in Table 5.1. Nine iterations were used in the decomposition. Arrival times have been corrected to lie on the surface-focus Jeffreys-Bullen travel-time curve. Traces are normalized to peak amplitude. Interpreted travel-time branches are indicated. A transparency of this figure is provided in a pocket at the rear of this thesis.

representing correlations of arrival travel times and amplitudes. The branches have been labelled A, B, C, D, E, F and G. The branches A through E are probably direct arrivals, and branches F and G may correspond to mini-max arrivals. The branches are not based on any current S-wave velocity model. There will be no attempt to analyse in detail the nature of these branches or the structure necessary to simulate them - the purpose of the travel-time branches is to aid in the comparison of the synthetics with the observed data. Figure 5.9 is a repeat of Figure 5.7, but with tentative travel-time and waveform correlations. The following section will present an intuitive preliminary analysis of the data in Figures 5.8 and 5.9. A detailed study will be given in Chapter 7.

5.6 PRELIMINARY ANALYSIS

Figures 5.8 and 5.9 do show that at distances beyond 2900 km (26.1°), the latter parts of the wave train are dominated by large amplitude arrivals, which are presumably multiple reflections from deep seated velocity discontinuities. This verifies in part the analysis of Chapter 1.

In addition to the cross-over near 2690 km (24.2°), there are signs of a break in the spikogram travel-time curve for event #50 near 2360 km (21.2°). The size of the discontinuities cannot be determined from the data with any certainty, and must await quantification by synthetic seismogram modelling. However, the relative positions and estimated slownesses of the presumed branches B, C and D may indicate prominent velocity discontinuities at depths near 650, 500 and 400. As stated earlier, the coherence of waveforms between events is only fair, and so exact matching of synthetics and data is untenable. The consistency of amplitudes along the travel-time curves is an important feature in the inversion. The amplitude relations on the A branch have already been discussed. Amplitudes on the B branch are quite large in the vicinity of the 24.2° cross-over, but decrease quite rapidly with increasing distance. At greater distances, there are no indications of arrivals corresponding to the B branch on the waveform data, yet the spikograms do show that this branch extends to the edge of the data set. The C branch arrivals contribute to the large amplitudes encountered near 24° and decrease in amplitude near the edge of the data set at 3560 km (32°). The D branch has some of the largest amplitudes on the data that decrease in relative

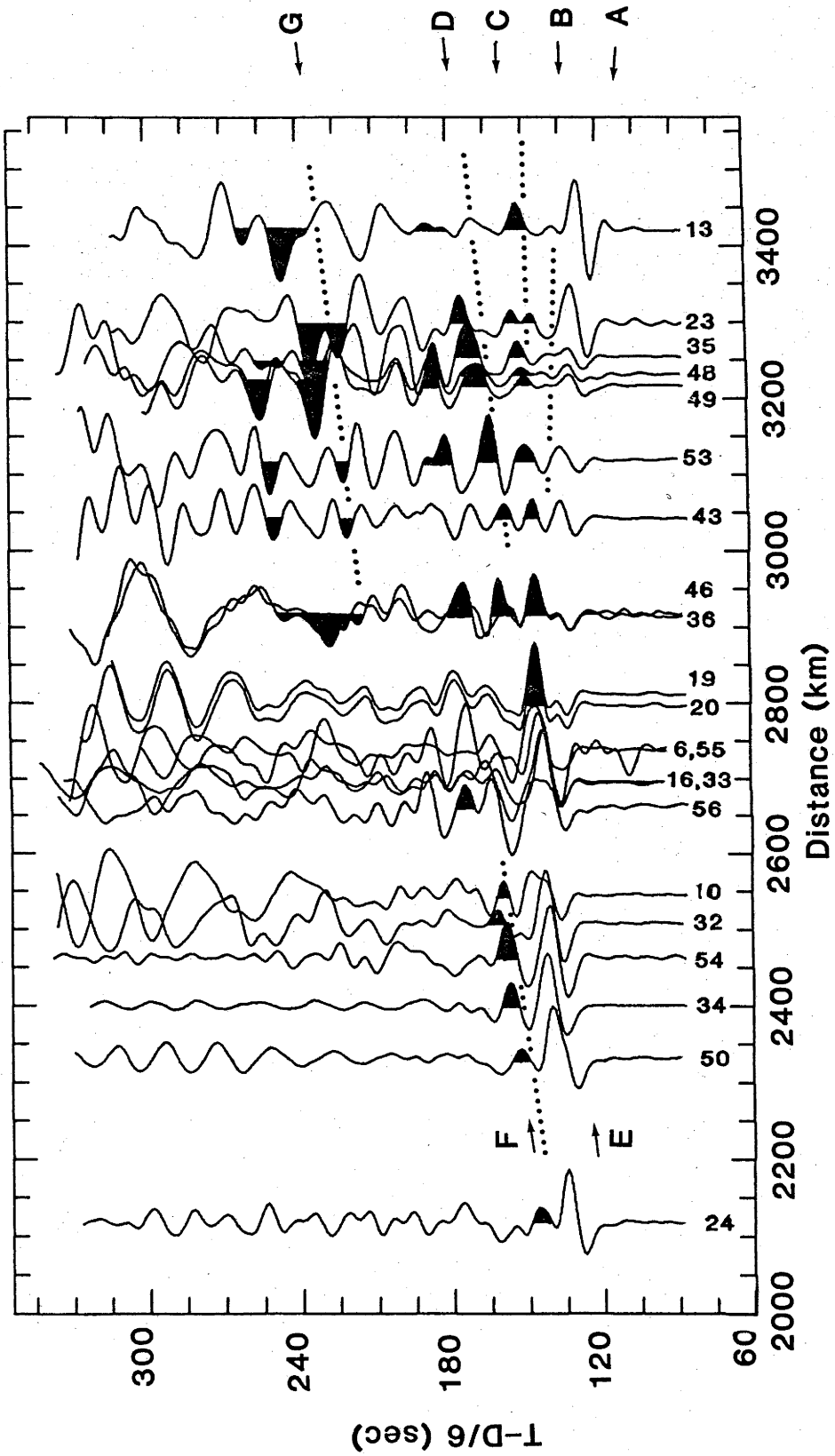


Figure 5.9: Repeat of Figure 5.7 with interpreted travel-time branches indicating identified arrivals in the data. Dotted lines indicate correlations of waveform peaks. A transparency of this figure is provided in a pocket at the rear of this thesis.

amplitude quite rapidly near the edge of the data set and can only correspond to the "400-km" discontinuity. At small distances, the E branch appears characterized by small amplitudes and high slowness relative to the much larger arrival that is formed by the constructive interference of the C and D branches. The apparently high slowness indicates the manifestation of a relatively shallow structure. The F branch appears as well-defined large amplitude arrivals that can be easily traced over the range 2000 km (18°) to near 2700 km (24.3°). It too has a relatively high slowness, and is probably the result of multiple reflections from relatively shallow structure. Although the G branch indicates one set of large amplitude arrivals at distances greater than 3100 km (28°), the spikograms and waveform data clearly indicate the presence of other arrivals. The exact nature of the later large amplitude arrivals must await analysis with synthetic seismograms.

Examination of the spikograms of Figure 5.8 shows that although there are good correlations in timing and amplitude of the large spikes, the branches appear to be characterized by either positive only or negative only amplitude spikes. For example, the direct branch A consists of positive amplitude (positive to the left) spikes, whereas the C branch is of predominantly negative amplitude spikes. This behaviour is due to the limitations of the iterative least-squares decomposition technique in an environment where phase of the constituent arrivals varies with epicentral distance. It was shown in Chapter 3 that under such conditions, errors increase and propagate rapidly in the iterations, and so credence should be given only to the larger spikes in the spikograms. It will be noted too that there will be errors in the timing of the spikes. However, this technique is being used only to indicate the presence of large amplitude arrivals, and not to accurately delineate travel times, phase or relative amplitudes. Thus, the travel-time branches in Figures 5.8 and 5.9 are not accurate representations of the actual travel times.

To investigate further this behaviour of iterative least-squares decomposition, recourse will be made to applying the technique to a suite of synthetic seismograms displaying a well-defined triplication. The velocity-depth model chosen corresponds to a classical first-order discontinuous increase in velocity. The synthetic SH body-wave seismograms (Figure 5.10a) for the layer over a half-space model are calculated by the Reflectivity method. The Nyquist frequency has been set such that the individual branches appear well-separated. The prograde (or diving) branch

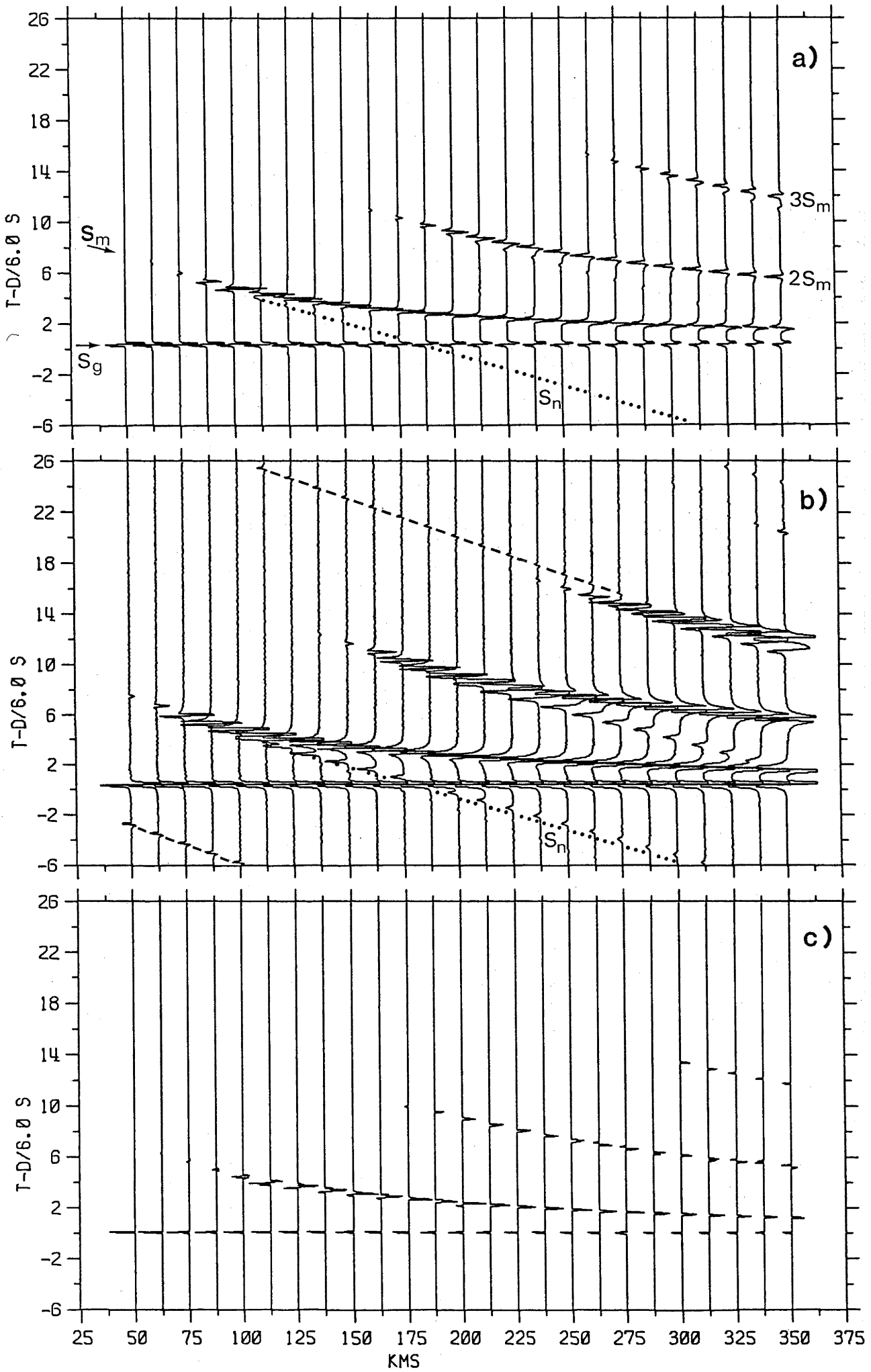
has relatively weak arrivals compared with the dominant arrivals on the retrograde branch. The Reflectivity method implicitly incorporates multiples in the calculation, and so SS and SSS are quite obvious.

The head wave separating from the group near 125 km has a relatively small amplitude that decreases rapidly with increasing epicentral distance. Figure 5.10b is the same as Figure 5.10a, but with a tenfold increase in amplitude scale. In the SV analog of this numerical study, Kind and Müller (1975) noted that the short-period onset of the head wave was followed by a signal with much longer period. There is no evidence of a long-period wave in the SH synthetics. One suggestion for the long-period signal was that it was due to dispersion of SV_n , but is unlikely due to the absence of dispersion in the SH synthetics. Another suggestion is that of a pseudo-Rayleigh wave which radiates S body waves to the free surface. It is interesting that there appears to be no Love wave equivalent. It follows then that both suggestions may be incorrect, and that the long-period signal observed by Kind and Müller may be a Stoneley wave. Stoneley waves will not be observed in the synthetics of Figure 5.10 because no SH-type of wave can propagate along the interface of two isotropic media.

The phase relationships with distance of arrivals on the reflected retrograde branch are covered in Appendix 1: with increasing angles of incidence beyond the critical angle, the reflected wavelets undergo increasing phase shift. The refracted branches are characterized by a constant-phase wave form. These amplitude/phase relationships for the reflected and refracted rays are given in Figure 5.11. The curves have been calculated with equations given by Pilant (1979).

The application of iterative least-squares decomposition for four iterations is given in Figure 5.10c. The spikograms clearly show the refracted energy on the forward branch as positive amplitude spikes. Near the critical distance, the reflected waves do not suffer any phase shift, and are seen as positive amplitude spikes. With increasing epicentral distance and rapidly increasing phase shift, the equivalent spike changes polarity. At greater distances, the higher iterations try to match in a least-squares sense, arrivals having suffered large phase shift with a small positive spike followed immediately by a large negative amplitude spike. This behaviour is consistent with an intuitive experiment that "decomposes" into discrete spikes, a time series consisting of a delta function and a delta function that has been shifted in phase by $\pi/2$.

Figure 5.10: Synthetic SH seismograms for a 30km thick homogeneous layer with shear-wave velocity of 3.8 km/s overlying a 4.7 km/s half-space. A strike-slip surface-focus source has been assumed. Amplitudes have been corrected for geometrical spreading. (a) Notation used is S_g = direct wave, S_m = reflected wave, $2S_m$ = twice reflected wave, etc., S_n = head wave. (b) Same as (a), but with tenfold increase in amplitude scale. The amplitude of the direct and reflected waves are clipped. The arrival marked by the dashed lines is a purely numerical effect and travels with the highest velocity that is used in the integration. Some time-domain aliasing occurs. (c) Seismograms after the application of least-squares decomposition for four iterations. A facsimile of the direct wave was used as the wavelet. The direct wave is seen as a spike, while the phase shifted reflected arrivals are seen as a combination of opposing polarity spikes.



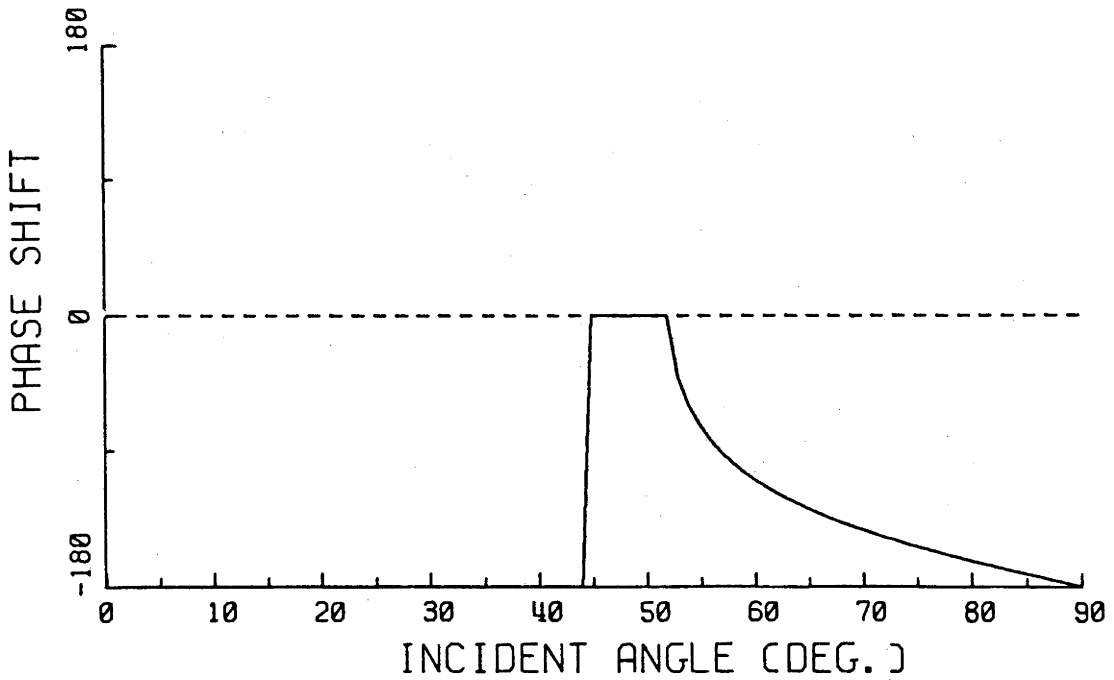
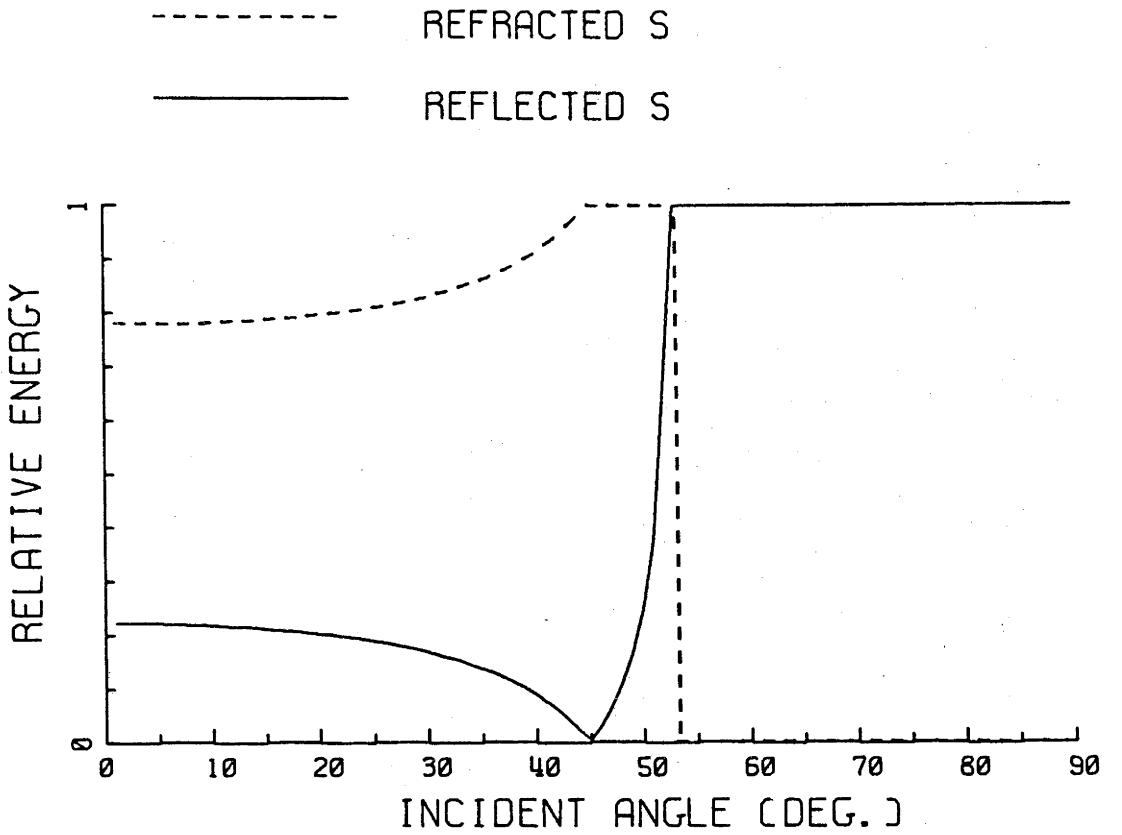


Figure 5.11: Amplitude and phase relations for reflected and refracted SH incident on a boundary involving a 24% velocity increase.

radians.

Thus, in general, refracted energy may appear on the spikograms as spikes of positive amplitude, while relatively large reflected energy may be characterized by predominantly negative amplitude spikes. This rather crude analysis may indicate that the A and E branches are dominated by refracted energy, whilst the remaining branches contain significant amounts of reflected energy.

The absence of surface waves on some events is quite startling. The propagation of surface waves, and in particular the higher modes, requires comparatively uniform crustal and upper mantle structure. The higher modes in particular have a large proportion of their energy travelling in the uppermost lithosphere and are consequently very sensitive to variations in the structure near the Moho. Higher modes are rapidly attenuated in regions of structural change, such as mountain roots and continental margins (Crampin and King, 1977). The Mediterranean events to be considered in this study have propagation paths that include a traverse of the Alpine and Caucasus mountain belts where crustal thicknesses of 50 km to 60 km may be expected, whereas the average crustal thickness for central Europe is about 30 km (Hovland et al., 1981), and the Tyrrhenian and Ionian Seas exhibit an oceanic type of crustal structure (Calcagnile et al., 1979; Panza, 1979). Gregersen (1977) used anomalous residuals from events in the Ionian Plate to delineate a dipping zone of high velocity, interpreted as a dipping lithospheric plate with P-wave velocity 6-7% higher than its surroundings. The 90 km thick plate extends northwards from the Cretan Ridge to a depth of 250 km beneath the Aegean Plate. Hovland et al. (1981) have suggested the existence of a fossil subduction zone trending with depth from east to west beneath the Alps. Similar indications of fossil subduction exist for the Adriatic microplate. This seems to suggest that lateral heterogeneity in the uppermost 250 km is a possible mechanism for scattering the higher modes. The presence of Love-wave energy on some of the North Atlantic and Mediterranean data indicate that the event was of suitable depth and focal mechanism to excite a single mode, probably the fundamental, along a suitable path. The occasional absence of surface waves from the North Atlantic records certainly indicate scattering due to thickening of the oceanic crust with age (i.e. distance from the ridge axis), and also at the continental margin. The problems of treating wave propagation across a vertical interface are considerable (c.f. Lysmer and Drake, 1972; Kennett, 1975b) and will not be given further consideration.

It may be suggested that the zone of extensive partial melting below the ridge axis (Solomon, 1973) may be another mechanism for surface-wave attenuation, but the limited spatial extent of such a zone is unlikely to significantly attenuate the surface waves.

The second part of this study calculates synthetic seismograms for a suite of S-wave velocity models and compares them with the observed data.

CHAPTER 6

UPPER MANTLE SHEAR-WAVE VELOCITY MODELS - PAST AND PRESENT

II SYNTHETIC SEISMOGRAMS

6.1 INTRODUCTION

Now that the data set of Chapter 1 has been extended to include data from two seismically active regions, the Mediterranean and the North Atlantic, complete LP synthetic seismograms will be calculated for a suite of S-wave models derived from free-oscillation, surface-wave dispersion and body-wave studies, and the synthetics will be directly compared with the observed data. It will be shown that different models generate very different synthetics and that many models are clearly unacceptable as a shear-wave model for western Europe on the basis of misfit between synthetics and observed data. It will be shown that on the basis of relative travel times and amplitudes of component arrivals, some synthetics fit the data sufficiently well that the corresponding models may be used as a starting point for further refinement. Such an exercise will also act as a tutorial as to what features of velocity-depth models contribute significantly to a seismogram, and show that there are useful rules and procedures that can be adopted by future researchers in attempts to refine velocity-depth models. This study is fundamentally an exploratory exercise to determine the level of maximum simplicity required of a model to explain the available data, and so model refinement will not be immediately considered.

Reflectivity based synthetic seismograms are clearly advantageous for discriminating between competing velocity models. This arises from their ability to synthesize completely the interaction between wavefield and Earth model. A ray sum method was used in Chapter 2 but it is not adequate for current purposes because the total ray sum must be completely specified in order to generate seismograms in their entirety and requires careful preparation by the user. Even with the disadvantageously long run times of

the Reflectivity method, the ease of implementation and reliability with which it includes all possible contributions make it an ideal tool for this study.

It should be remarked that unlike inversion of travel times and slownesses, the forward or inverse problem applied to synthetics can recover only impedance and not the seismic velocity as a function of depth. Although this is a fundamental problem of great concern in the exploration industry, many recent papers in seismology appear unaware of this subtle fact. Of course, for a given density-depth model, the velocity structure may be found. The density model used here is Birch's (1961) empirical relation

$$\rho \approx 0.252 + 0.379v_p$$

derived from laboratory experiments with peridotites. However, choice of density model is not important because waveforms are more dependent upon velocity: the layer matrix equations A2.2 are dependent upon density and the square of the velocity.

6.2 IMPLEMENTATION OF THE REFLECTIVITY METHOD

The formulation presented in Chapter 4 (Ingate, et al. 1983) will be used. This algorithm has the advantage of simplicity and shorter computation time when compared with the approach of Wang and Herrmann (1980). The Normal Mode programme of Liao et al. (1978) is faster when generating synthetics with minimum periods of 10s. Examination of the deconvolved NORSAR seismograms (Figure 5.7) show that the seismograms have a dominant period less than 15s, and so for shorter periods, an increasingly greater number of torsional modes must be admitted into the mode sum, significantly extending the computational requirements. Low-pass filtering to give the deconvolved and synthetic data a common bandwidth would not use all of the available information. As it stands, LP data lacks the fidelity of SP data for investigations of fine-scale structure, so it is important that this resolving power should not be further degraded.

The phase velocity window should be sufficiently wide to include all anticipated arrivals. In this chapter, surface waves have been excluded by setting the velocity integration limits between 4.3 km/s and 22 km/s with a 20% split-cosine-bell taper applied at each end of the window to avoid truncation effects. Of course, this window excludes contributions from phases with a relatively shallower bottoming depth, but such phases cannot be seen in the data. Appendix 4 recomputes synthetics for each model with the lower phase velocity limit set to 3.0 km/s. The effect of the synthetic surface waves is to partially obscure the lower amplitude later arrivals.

The sampling rate is set such that the data and synthetics in Appendix 4 have a common dominant period. The synthetics in this chapter have been calculated with a much higher Nyquist frequency to enable the easier identification of the different arrivals. At this point it should be remarked that the far-field pulse given by the derivative of the moment function $m_o(t)$ (equation 5.1), and therefore also the direct wave from the double-couple, are acausal. This acausality has been partially removed from the synthetics by a shift to greater times by $T/2$, but there will be some uncertainty with the onset times, particularly at the periods under consideration. It must be reiterated that the observed data were aligned with travel times that were consistent with the JB model. It will not be possible to compare absolute travel times between data and synthetics.

Perhaps one of the major shortcomings of the Reflectivity method is the approximation of velocity gradients by thin layers of constant velocity. Experiments show that for the given dominant frequency in the synthetics, layer reverberation was not present for layer thickness less than $1/6 \lambda$ (λ = wavelength). This is in accordance with the seismic wavelet resolution limits of $1/4 \lambda$ to $1/8 \lambda$ suggested by Sheriff (1977). For all models, the half-space was placed at or near a depth of 870 km because experiments showed that at the distances under consideration, the direct ray never bottomed below this depth.

The synthetics are calculated using the long-period Q-model MM8 (Anderson et al. 1965). Where necessary, the Q model was altered slightly so that discontinuities in velocity and Q coincided. Choice of Q model for the analysis of LP body waves is not important, as shown in Chapter 2. When synthetics were first generated, it was noticed that a surface wave completely dominated the synthetic. For example, the synthetics for the JB model with MM8 attenuation are given in Figure 6.1a. At first, the very

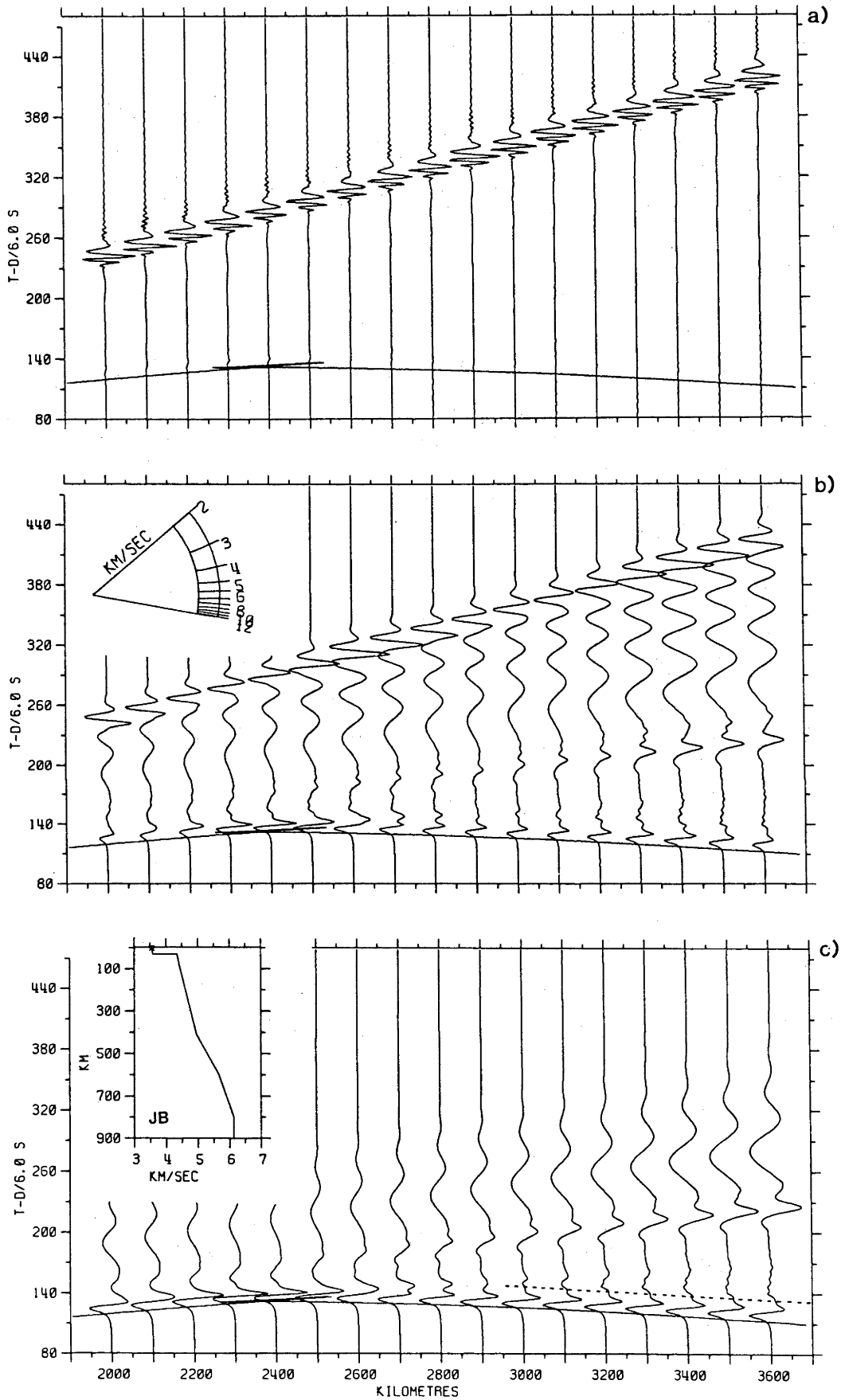


Figure 6.1: Synthetic SH seismograms for the JB model with MMS-Q model. Branched travel-time curves have been superimposed on the synthetics. (a) Crustal $Q=450$. (b) Crustal $Q=50$. (c) Crustal $Q=10$. Dashed line shows crustal reverberation. Traces are normalized to peak amplitude.

large phase was thought to be an Airy phase but the apparent horizontal phase velocity suggested a channelled wave in the crust. Such a phase is absent in the data, with scattering proposed as a possible mechanism (c.f. Section 5.6). In order to generate synthetics with reasonable amplitude surface waves for Appendix 4, the computation was repeated with decreasing values of Q . A value of 10 in the upper half of the crust was required to attenuate this phase to an acceptable level (Figure 6.1c). Of course the body waves sample the crust only twice, and have sufficiently long wavelengths to be unperturbed by this very low- Q zone. Similar comments apply to the fundamental surface wave which travels at depths significantly deeper than the Moho. The rippling in the coda of the first arriving body waves in Figure 6.1c are crustal reverberations in the source and receiver crusts. This will be seen on all the synthetic seismogram sections. This phase is most obvious at a distance of 3600 km at 15 and 30s after the first arrival. This rippling could be decreased by introducing structure into the crust or making the whole crust a very low- Q zone.

Figure 6.1b shows an intermediate result where Q of the upper crust has been set to 50. The channelled wave now has an amplitude of the same order of magnitude as the body waves. Of interest is the phasing in and out of three of these arrivals, each corresponding to different orders of multiples. This is clear evidence that this phase is in fact a multiple within the crust.

6.3 THE MODELS

Synthetic seismograms have been calculated for a suite of shear-wave velocity models for the distance range 2000 km (18°) to 3600 km (32.4°) (Figures 6.2, 6.4 to 6.24). Superimposed on the synthetics in Appendix 4 are the theoretical travel times, with cusps labelled according to the bottoming depths of the associated rays. For clarity, only the direct branches are included. The models are JB (Bullen, 1963), IN (Ibrahim and Nuttli, 1967) US26 (Anderson and Julian, 1969), IN2 (Nuttli, 1969), STAN 3 (Kovach and Robinson, 1969), REDDOG-C (Robinson and Kovach, 1972), SW-E (Mayer-Rosa and Mueller, 1973), SHR14 (Helmberger and Engen, 1974), B1 (Jordan and Anderson, 1974), B1066 (Gilbert and Dziewonski, 1975), PEM-C (Dziewonski et al., 1975), MODEL 7 (Nolet, 1977), CNNS (Cara et al., 1980),

PREM (Dziewonski and Anderson, 1981), S-2 (Hendrajaya, 1981) and SHMEE (Cleary, et al., 1982). This rather extensive list is representative of models derived from a variety of data in different regions. For completeness, shear-wave velocity models have been derived from the P-wave velocity models for Europe shown in Figure 2.5 using $v_S = v_P/1.735$. The additional models include MA (Massé and Alexander, 1974), KCA (King and Calcagnile, 1976), EKW (England et al., 1977), NAT (England et al., 1978), K8 (Given and HelMBERger, 1980) and S8 (Burdick, 1981). Parallel inversion of P- and S-wave data often indicate quite different velocity profiles for P and S (e.g. Jordan and Anderson, 1974) especially for southwestern Europe (Mayer-Rosa and Mueller, 1973; Cara et al., 1980), so it is not strictly possible to relate the S-wave to the P-wave velocity distribution by way of a constant Poisson's ratio. Nevertheless, the P-wave models have been included because they are supposedly representative of the mantle beneath Europe.

Each model will now be discussed in detail, particularly with regard to how well the synthetic wave trains fit the observed data. To facilitate this comparison, the processed data given in Figures 5.8 and 5.9 have been reproduced on transparent overlays and provided in the pocket at the end of this thesis.

6.3.1 JB - BULLEN (1963), FIGURES 6.2, A4.1a.

Derived from travel-time studies in Japan and Europe, the velocity in the JB model is continuous throughout the mantle except for a change in dv/dz (the slope of the velocity gradient) near 413 km which causes the break in the travel-time curve near 2380 km (21.4°). The distance to where the break occurs was found to be in error at small epicentral distances, and was due to using data from different regions. Even though there was no support for the change in dv/dz , it has remained in the literature (Lehmann, 1967). The corresponding synthetic seismograms are relatively straight forward, exhibiting on the whole a very simple appearance. The body-wave portion of the seismogram is dominated by the first arrival, and by 2S413 at distances beyond 3200 km (28.8°). The effect of the triplication near 21.4° becomes quite clear on the synthetics as the forward branch can be seen extending to 2900 km (26.1°), at least 400 km

beyond which geometrical ray theory predicts. LP waves will "feel" out structure over a large depth range, and so the cusps will be seen to extend over a greater distance range than for a corresponding short-period wave study. This manifestation of the simple change in dv/dz at a depth of 413 km is much more obvious in the synthetic seismograms than the change of slope in the travel-time curve.

Uncertainty with focal plane orientation has made it necessary to normalize the data traces to maximum peak amplitude. In order to appreciate this practice, Figure 6.3 examines different amplitude presentation schemes. The seismic section spans the distance range 1000 to 5000 km, and the velocity integration limits have been chosen to exclude mostly surface-wave energy. Panel (a) examines the scheme of trace normalizing to peak amplitude. With increasing distance, the SS phase increases in amplitude relative to direct S, but relative amplitudes of S413 and 2S413 cannot be compared. Panel (b) synthetics have been corrected for geometrical spreading. With increasing distance, the SS and direct S amplitudes decrease. The largest amplitudes on the section are seen to occur near the break in the travel-time curve near 2400 km (21.6°). The largest SS amplitudes will occur at twice this distance.

Comparing the deconvolved data^(Figure 5.9) with the synthetics^(Figure 6.2) reveals that the JB seismograms are unable to explain the complex nature of the data. The synthetics predict only one clear second arrival: 2S413. According to the JB model, 3S413 should arrive approximately 21s after 2S413 at 3300 km (29.7°) but the ray parameter of 3S413 is such that little energy is returned to the surface at this distance. Of course, at greater distances, 3S413 will become more prominent on the synthetics as shown in Figure 6.3. While S has a "dipolar" wavelet arising from the definition of the moment function, the 2S413 phase appears as a monopole. Choy and Richards (1975) showed that phases travelling a mini-max path will be shifted in phase from the direct ray. This shift amounts to $\pi/2$ radians which is approximately the relationship between the S and 2S413 shapes on the synthetics. There is no structure in the JB model for generating arrivals labelled B and C on the data record section, nor can it describe the cross-over at 2690 km (24.2°) in the data. JB is not a good approximation to the upper mantle beneath Europe.

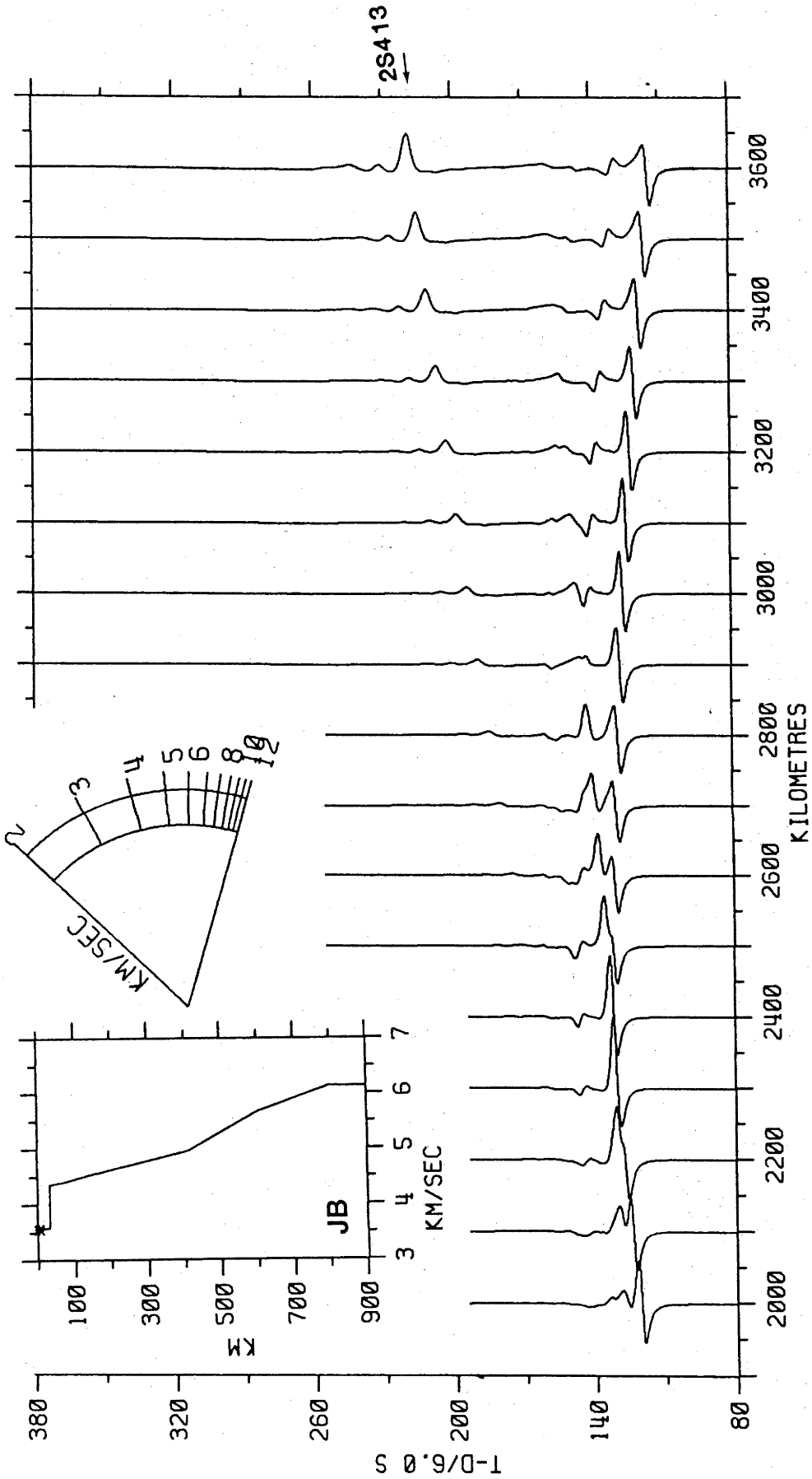


Figure 6.2: Synthetic SH seismograms for the JB model (Bullen, 1963). Important multiples are indicated. Traces are normalized to peak amplitude. Strike-slip surface source is assumed. Velocity integration limits are 4.3 to 22 km/s, thus excluding surface waves.

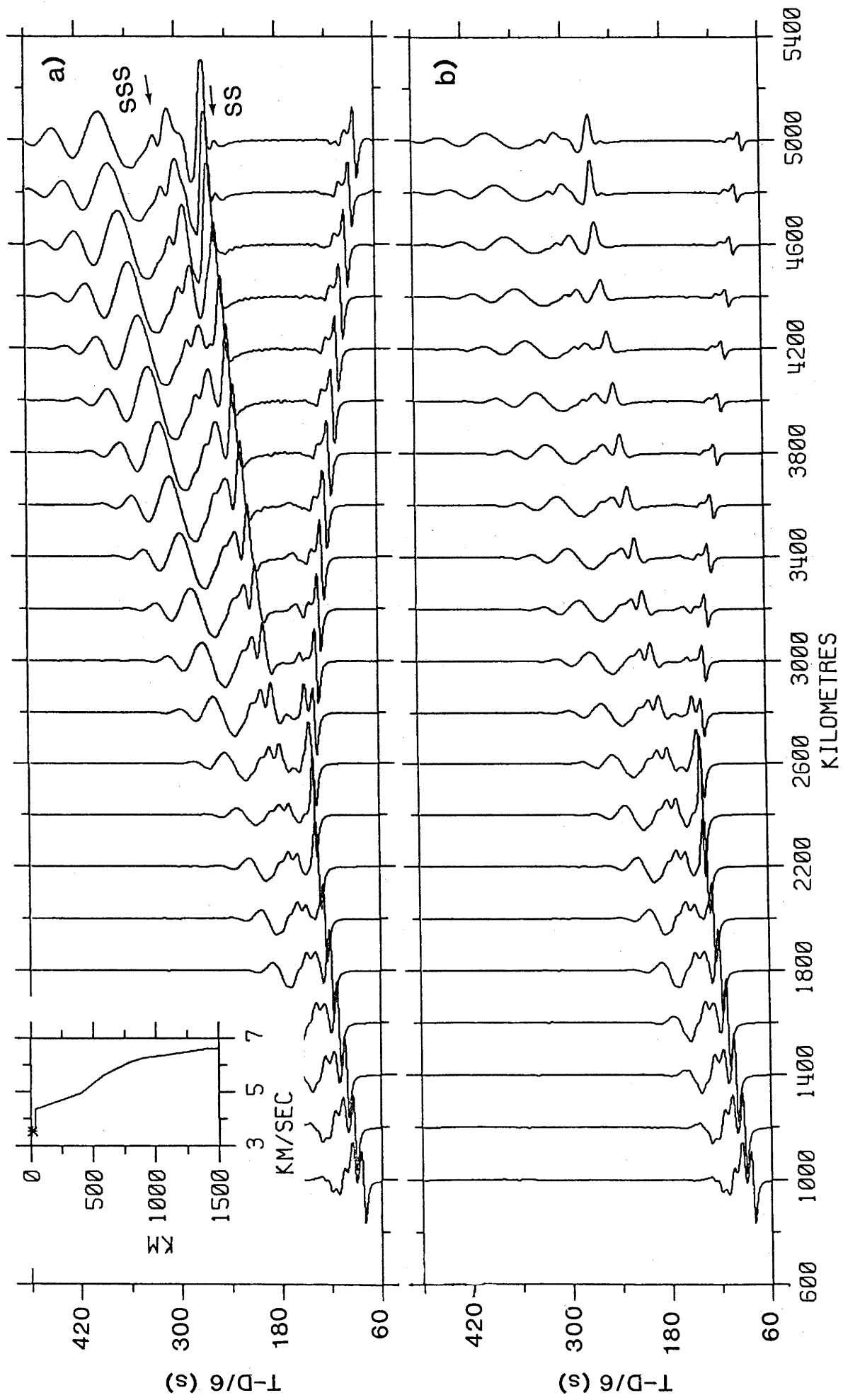


Figure 6.3: Synthetic SH seismograms for the JB model. Velocity integration limits are 3.9 to 22km/s. (a) Traces are normalized to peak amplitude. (b) Trace amplitudes are corrected only for the geometrical spreading factor, $1/r$ (r = epicentral distance).

6.3.2 IN - IBRAHIM AND NUTTLI (1967), FIGURES 6.4, A4.1b.

IN was based on travel times and particle motion diagrams of long-period S waves from earthquakes with focal depths 37 to 120 km recorded on the Long Range Seismic Measurement (LRSM) network to obtain empirical travel times of S for an "average" United States model. IN contains pronounced low-velocity zones at depths between 150 to 200 km, 340 to 370 km and 670 to 710 km and regions of rapidly increasing velocity beginning at depths near 400 km and 750 km. It must be remarked that their limited secondary arrival information, particularly near putative branch turning points, is unable to reliably constrain the velocity depth structure. The associated ray travel times and synthetics are expectedly much more complex than for the simple JB model. The ray travel times are characterized by breaks in the curve near 2320 km (20.9°) and 3000 km (27°). At small distances, S181 fits the G branch, and S371 predicts quite well the E branch. At distances greater than 27° , the amplitude of the first arrival decreases relative to the larger amplitude S371 and S721 reflected arrivals and 2S371. Amplitudes on the S371 branch could be decreased by eliminating the negative velocity gradient above the "721-km" discontinuity, and also by reducing the velocity contrast. The large amplitude of 2S371 arises from constructive interference from the reflected and refracted rays that bottom at or immediately below the "371-km" discontinuity. The other large multiple is labelled 2S181, and has a relatively high slowness. IN is a much better approximation of the S-wave velocity structure in Europe than JB because the complexity of the IN synthetics approaches that of the data which indicates the degree of structure required to approximate the data.

6.3.3 US26 - ANDERSON AND JULIAN (1969) FIGURES 6.5, A4.1c.

US26 was a reinterpretation of Ibrahim and Nuttli's (1967) data, and is an excellent opportunity to qualitatively examine the effect of observer bias. US26 replaces the constant velocity gradients of IN in the depth range 220 to 350 km and 400 to 670 km with negative gradients.

As one would expect, the ray travel times and synthetics are noticeably different to those of IN. Considering only the ray travel times, the US26 arrivals are generally later than IN, up to 15s for distances less than 2000 km (18°). This observation is verified by the synthetics though less

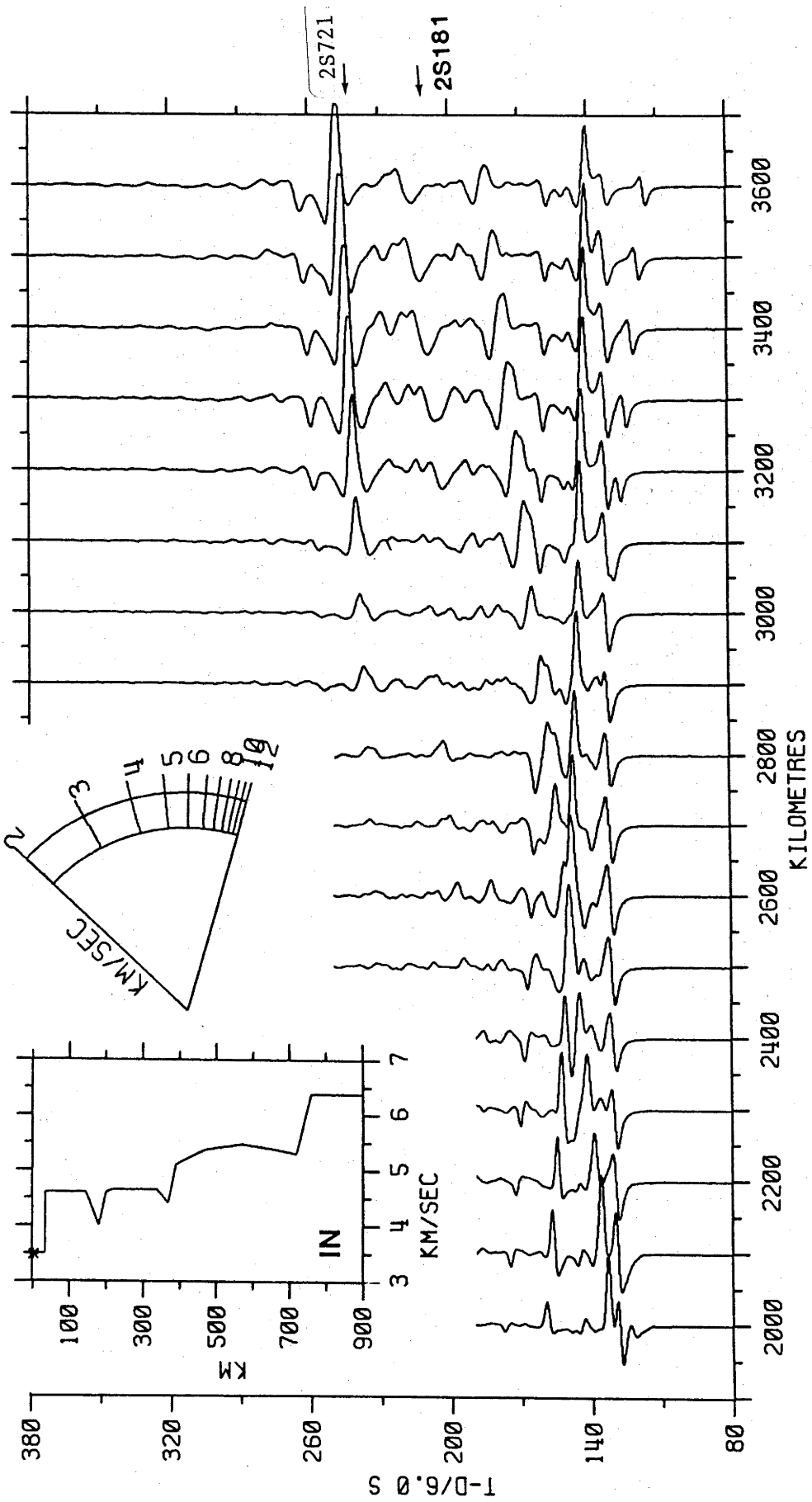


Figure 6.4: Synthetic SH seismograms for the IN model (Ibrahim and Nuttli, 1967). Caption as given by Figure 6.2.

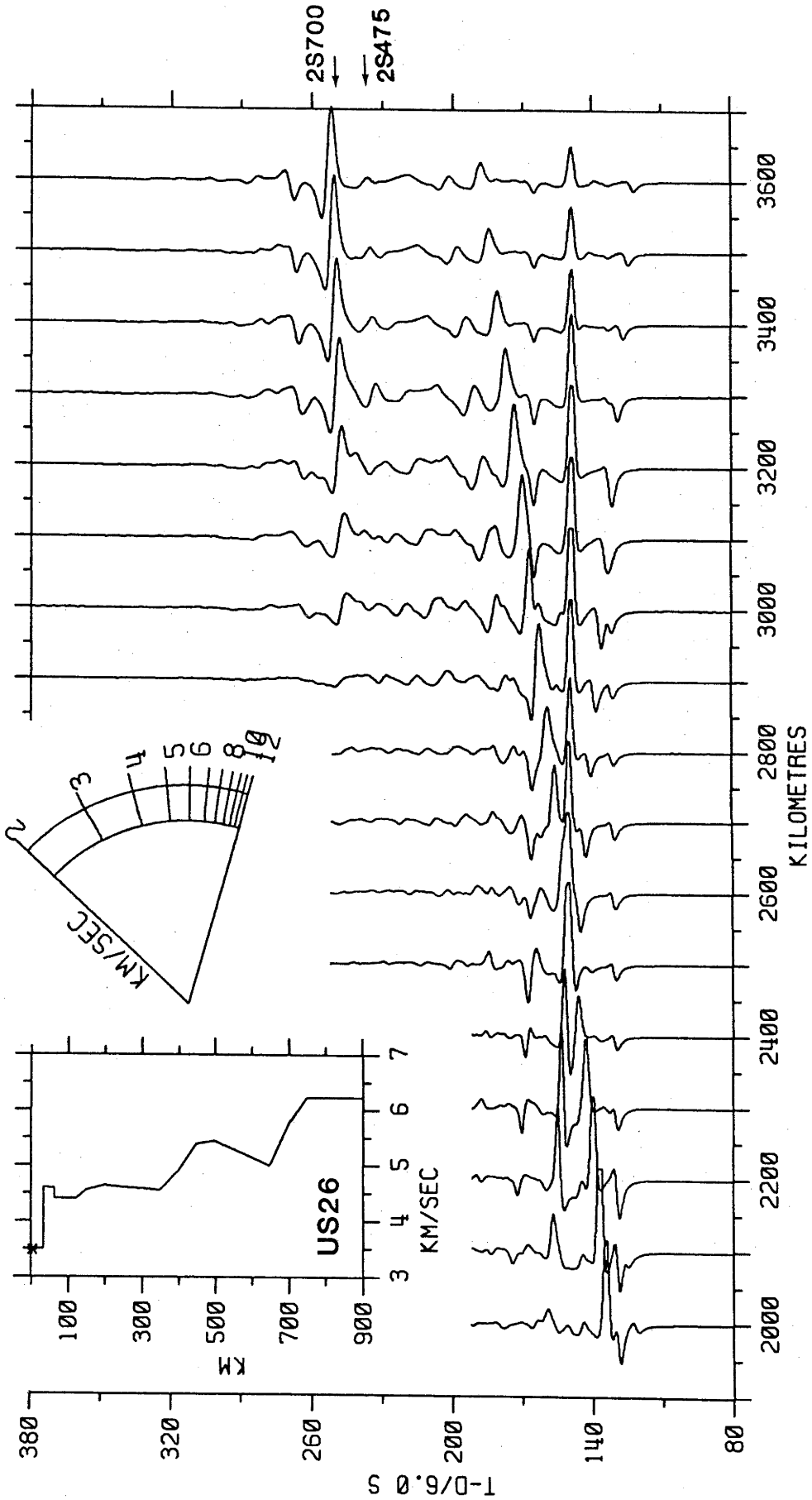


Figure 6.5: Synthetic SH seismograms for the US26 model (Anderson and Julian, 1967). Caption as given by Figure 6.2.

so because of the difficulty of estimating their onset times.

One of the prominent features on the synthetics are the decreasing relative amplitudes of the direct ray at distances less than and greater than the cross-over near 2900 km (26.1°) due to the negative velocity gradient near the bottoming depth of the direct wave. To decrease amplitudes on the S700 branch, the velocity contrast at this discontinuity should be decreased. This branch may correspond to the B branch. The S375 branch may be the D branch. At distances less than 26.1° , the ray refracted below the "475-km" discontinuity is a first arrival, and is characterized by very low amplitudes. 2S475 in US26 arises from the very steep velocity gradient between 350 and 450 km. 2S475 appears as a simple, large amplitude wavelet, similar to 2S371 in IN, but with different slownesses. It is easy to see that waveform studies based on first arrival data alone are not sufficient to discriminate between IN and US26. In this case, observer bias alone has introduced substantial differences in the synthetics. Nevertheless, US26, like IN, displays complexities in the synthetics comparable with the data.

6.3.4 IN2 - NUTTLI (1969), FIGURES 6.6, A4.1d.

Nuttli used travel times and amplitudes of long-period P, SV and SH waves generated (presumably by some mechanism of tectonic stress release) by the explosion of nuclear devices at the Nevada Test Site (NTS) to construct a model very similar to IN. IN2 was one of the models considered by Ibrahim and Nuttli (1967). Nuttli found, however, that the NTS data could be equally well satisfied by a model without the LVZ in IN between 350 and 380 km. The negative velocity of IN between 600 and 710 km was replaced with a zone of constant velocity. The travel times have cross-overs at 2240 km (20.2°) and 3000 km (27°). On the whole the synthetics have a character similar to that of IN and US26 with major demarcations only in timing of the first arrivals. By comparison with the B branch, IN2 has over-emphasized the amplitudes and apparent velocity on the S740 branch. The S391 branch is too fast for the D branch. The large 2S391 phase is due to the "knee" in velocity between depths of 391 and 471 km. Without considering any data recorded at distances less than 20° , it is unlikely that such interpretational subtlety is within the resolution of

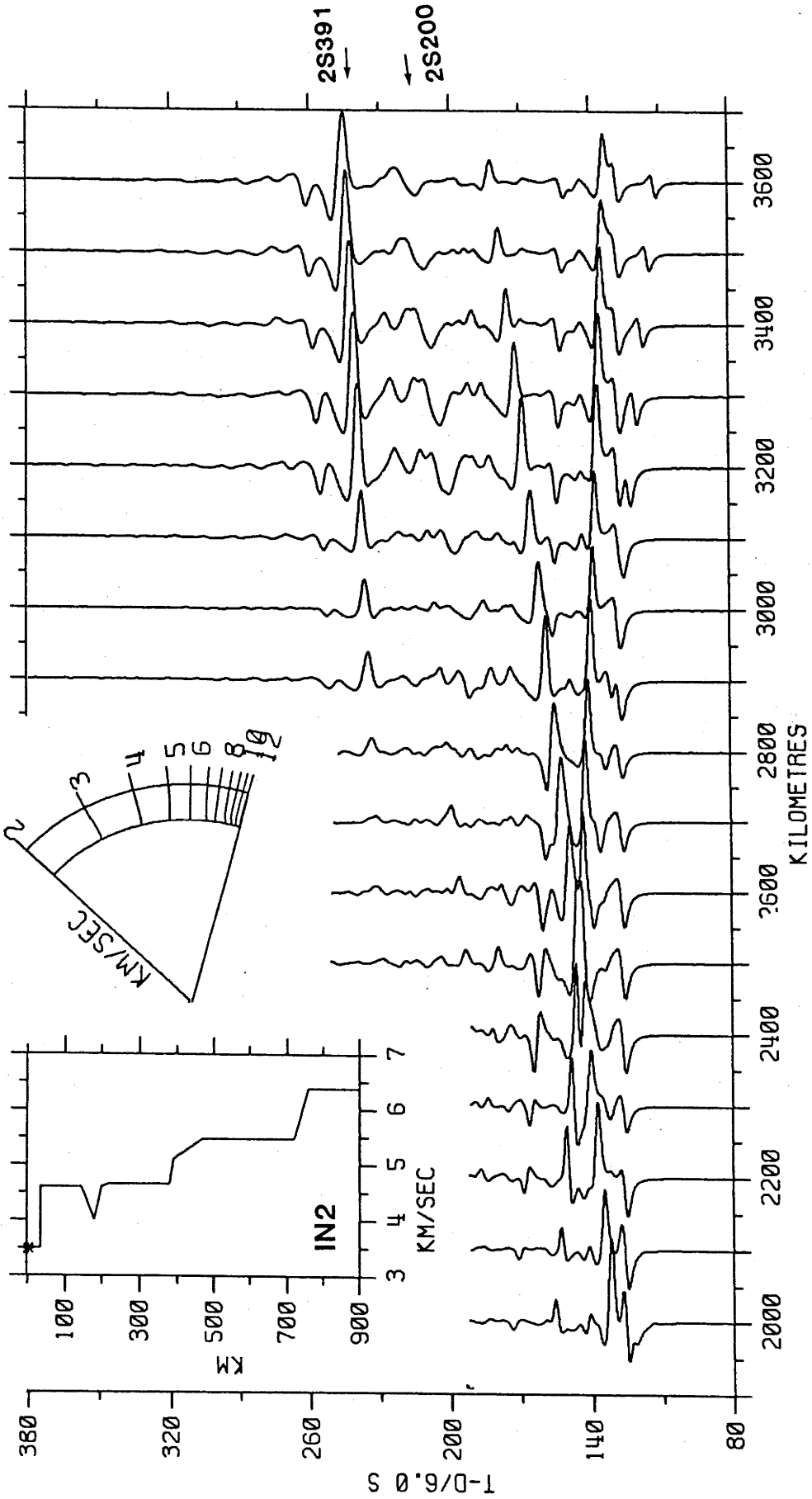


Figure 6.6: Synthetic SH seismograms for the IN2 model (Nuttli, 1969). Caption as given by Figure 6.2.

the first arrival LP data sets used to construct IN, US26 and IN2. Overall, the velocities of IN2 appear too fast, and IN2 should not be considered as an adequate starting point for model refinement.

6.3.5 STAN 3 - KOVACH AND ROBINSON (1969), FIGURES 6.7, A4.1e.

Robinson and Kovach used particle motion analysis techniques to measure the slowness of first arrivals across the linear LRSM array centred on the Tonto Forest Seismological Observatory. The interpreted model is compatible with P-wave models of the same region, and is characterized by a thin (9 km), high-velocity (4.5 km/s) lid overlying a low-shear-velocity zone. With increasing depth, there is a change in the velocity gradient at about 160 km and discontinuities begin at depths of 310 km and 620 km.

On the whole, the predicted ray travel times and synthetics are quite simple, but show that geometrical ray theory fails to predict the extension of the S675 branch to at least 3560 km (32°). STAN 3 has failed to predict the large amplitude D branch. As with previous models, SS (2S400) has very large amplitudes beyond about 3000 km (27°) but slow horizontal phase velocity when compared with the experimental data. This arrival is the constructive interference of multiply reflected and refracted rays that bottom above and below the very steep velocity gradient near 400 km. A pattern is now emerging that, depending on the model, the synthetic SS phase at distances of about 30° has an amplitude generally larger than the synthetic direct phases. This behaviour is not exhibited by the data where the mini-max multiples have amplitudes apparently equal to the first arrivals. This may indicate that the critical distance for SS is displaced to greater distances than given by the synthetics. An alternative explanation is that the MM8 Q model may have values too high near the bottoming depth for the multiples. A physical mechanism which predicts low-Q zones associated with velocity discontinuities (in particular, solid/solid phase transitions) is the phase relaxation process (Vaisnys, 1967). A low-Q zone would attenuate SS relative to the direct waves that pass through it at low angles of incidence. However, it was shown in Chapter 2 that Q is not a critical factor in determining the amplitudes of the long-period multiples.

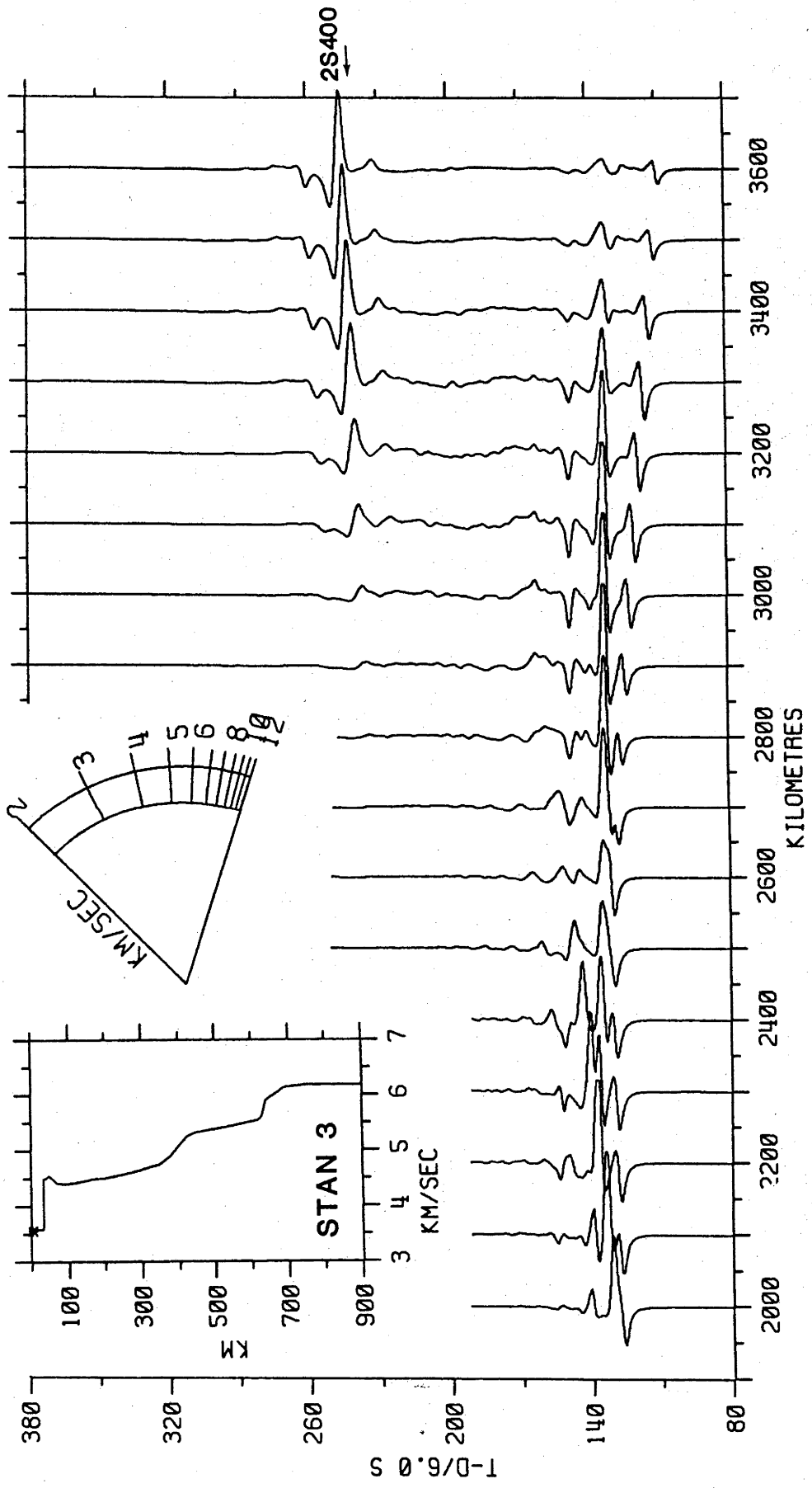


Figure 6.7: Synthetic SH seismograms for the STAN 3 model (Kovach and Robinson, 1969). Caption as given by Figure 6.2.

6.3.6 REDDOG-C - ROBINSON AND KOVACH (1982), FIGURES 6.8, A4.1f.

Robinson and Kovach proposed three shear-wave velocity distributions for western North America and areas of the Pacific Ocean which are collectively known as REDDOG-2. From polarization studies of travel times and slowness, the continental model REDDOG-C was derived with a low-velocity zone centred at 100 km, and zones (30 to 40 km thick) of high-velocity gradients at 400 km, 650 km and 900 km and a moderate-velocity gradient between 150 and 400 km. Using an averaged model and the shear-velocity density relations of Wang (1970), they constructed a density model with a density reversal between 200 km and 400 km, which was interpreted as the compositional change of an eclogite mantle to a pyrolite composition where a high thermal gradient was involved. The travel-time curve shows three triplications, two at a distance of about 2100 km (18.9° - high velocity gradients at 300 km and 400 km) and at 2660 km (23.9° - high velocity gradients at 700 km). The synthetics are remarkably similar to those of STAN 3. One difference between the models is the separation times of the direct and S680 branch at distances greater than 3330 km (30°) and another difference lies in the position of the third cross-over, 23° for STAN 3 and 24° for REDDOG-C. Other than these details, it would be very difficult to discriminate between the two models. Even the multiples have near identical waveform and travel times. That such similarities occur is not unexpected for these simple models are nearly identical to a depth of about 650 km.

6.3.7 SW-E - MAYER-ROSA AND MUELLER (1973), FIGURES 6.9, A4.1g.

Mayer-Rosa and Mueller used apparently well-constrained P-, S- and surface-wave data from European earthquakes in the distance range 5° to 25° to infer a complex step-like model. Their model for southwest Europe, SW-E, has pronounced low-shear-velocity layers between 70 and 120 km, 160 and 210 km and between 260 and 310 km, delineated by large, first-order discontinuities. SW-E also shows rapid increases in velocity at 310 km and 540 km. The travel-time curves for SW-E are apparently simple with a cross-over near 2400 km (21.6°), but one would expect the synthetics to be very complex because of the many first-order discontinuities and the anticipated efficient wave-guide properties of the LVZ's. Indeed, the resulting synthetics exhibit structure of the same complexity as the data

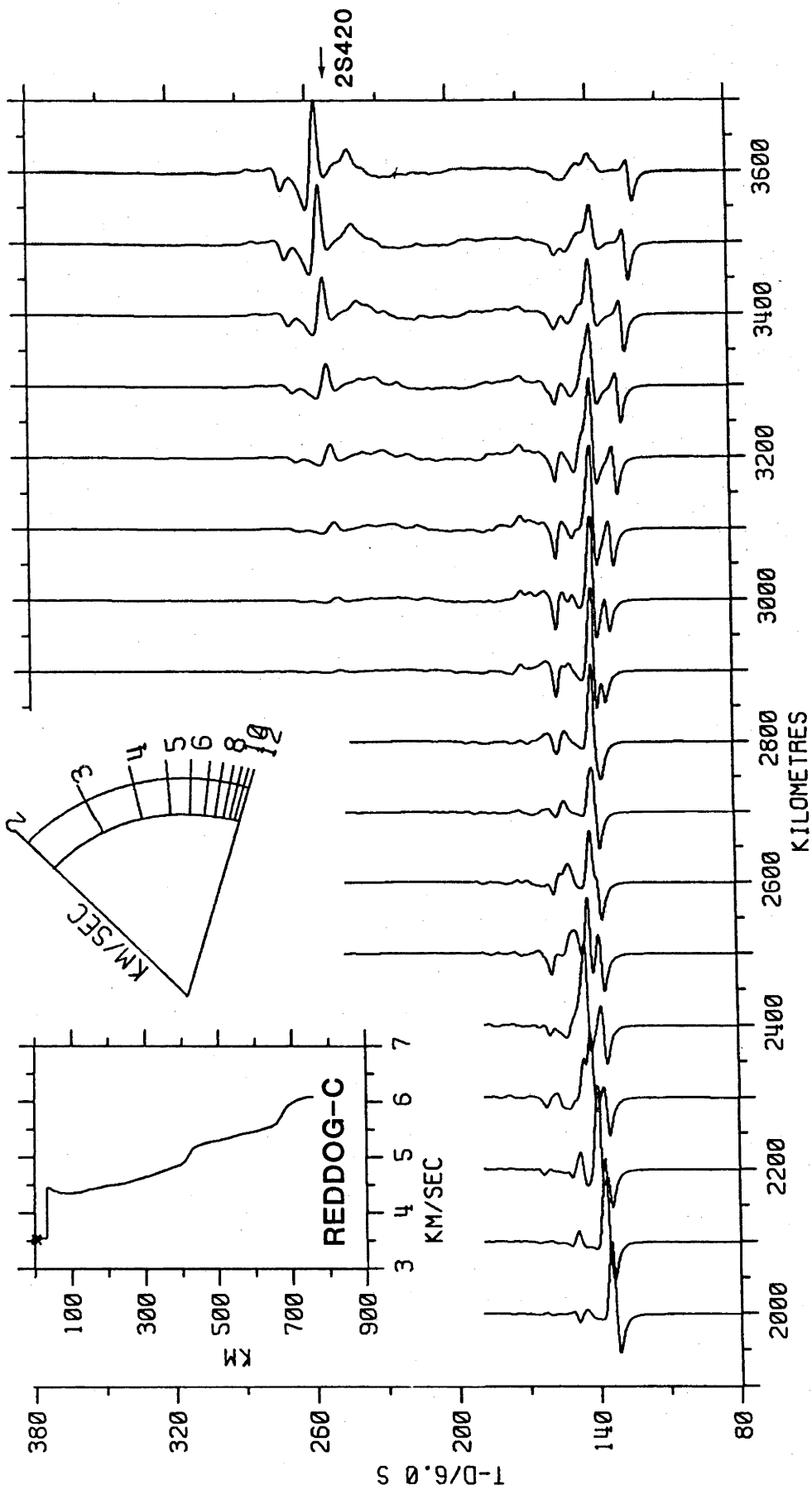


Figure 6.8: Synthetic SH seismograms for the REDDOG-C model (Robinson and Kovach, 1972). Caption as given by Figure 6.2.

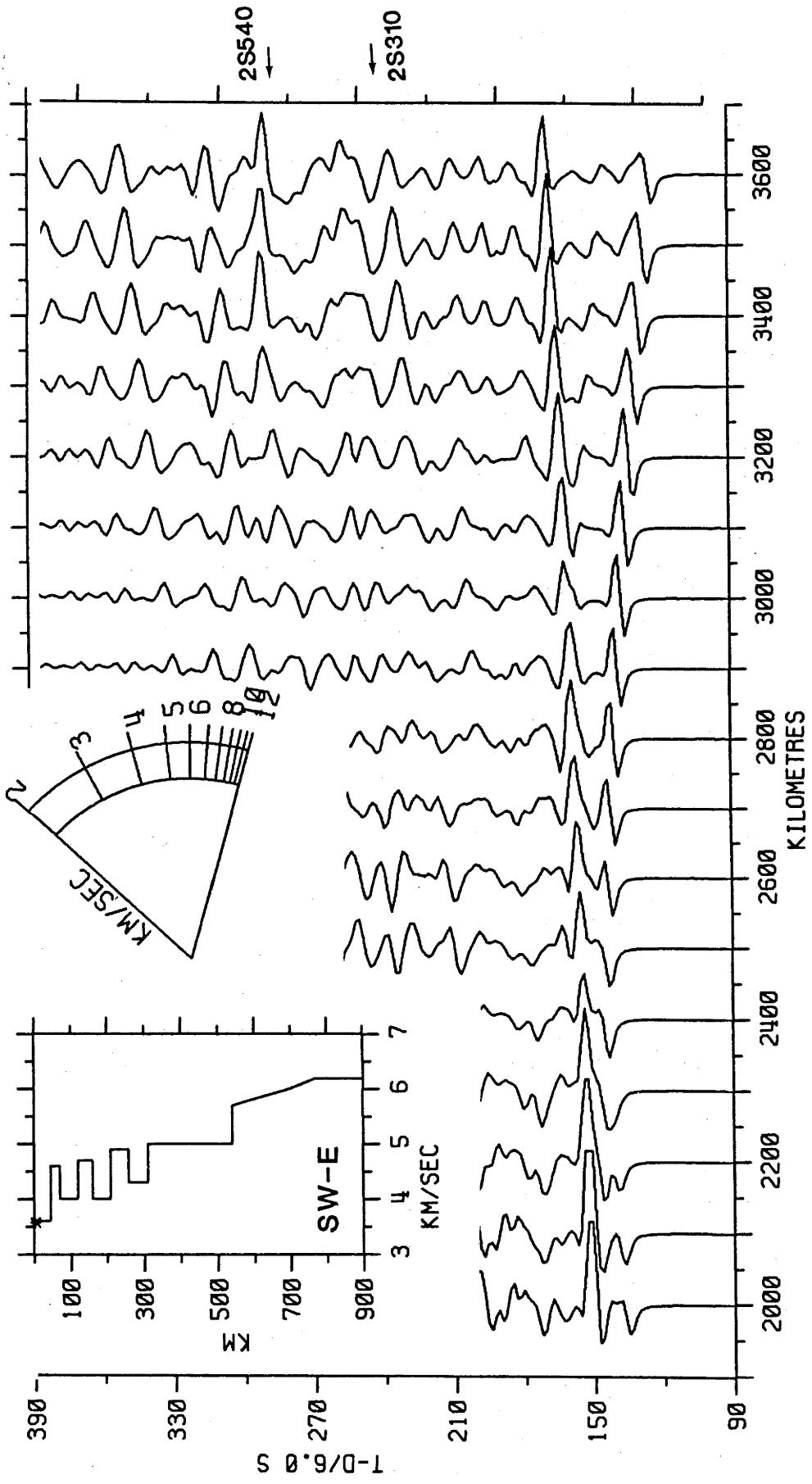


Figure 6.9: Synthetic SH seismograms for the SW-E model (Mayer-Rosa and Mueller, 1973). Some aliasing in the time domain is present. Caption as given by Figure 6.2.

although at larger distances, the first arrivals are too simple, with the S540 branch having no obvious equivalent in the recorded data. The phase labelled 2S540 has very large amplitudes. The channelled waves are quite obvious in the synthetics as a series of strong reflections that are remarkably coherent over large distances. These high-order multiples extend throughout the entire distance range under consideration. The absence of such waves in the data may indicate that such complex shallow structures do not exist below Europe.

Preliminary analysis of the data in section 5.6 indicated the possibility of a discontinuity near 500 km. The large phases labelled S540 and SS do not have equivalently large amplitudes on the observed data. This suggests that when it is time to model, a discontinuity near 500 km is required, but not with such a large velocity contrast. It is apparent though that SW-E is less appropriate as a velocity model for Europe at shallower depths. Nevertheless SW-E has merit because of the complexity of the wave train after the first arrivals.

6.3.8 SHR14 - HELMBERGER AND ENGEN (11074), FIGURE 6.10, A4.1h.

SHR14 is an apparently well-constrained continental model which satisfies both travel times and waveforms of long-period SH first arrivals recorded by the WWSSN and LRSM stations in North America. SHR14 is a very smooth model, having a LVZ between 50 and 100 km with sharp velocity transitions near 400 km and 670 km, but no negative velocity gradient between 446 km and 671 km as suggested by Jordan and Anderson (1974). SHR14 is further characterized by a broad discontinuity at about 500 km. The existence of the discontinuity near 500 km was previously suggested by Whitcomb and Anderson (1970), from their interpretation of precursors to P'P' as underside reflections from upper mantle discontinuities under oceanic areas.

The travel times and synthetics for SHR14 are quite simple, predicting well the cross-over in the data near 2700 km (24.3°). The S420 branch can be followed out to 3600 km (32.4°) which is not predicted by geometrical ray theory. The B, C and D branches may correspond to the S671, S500 and S420 arrivals. Reducing the depth to the "671-km" discontinuity would probably satisfy waveform considerations of the first arrivals. The lack

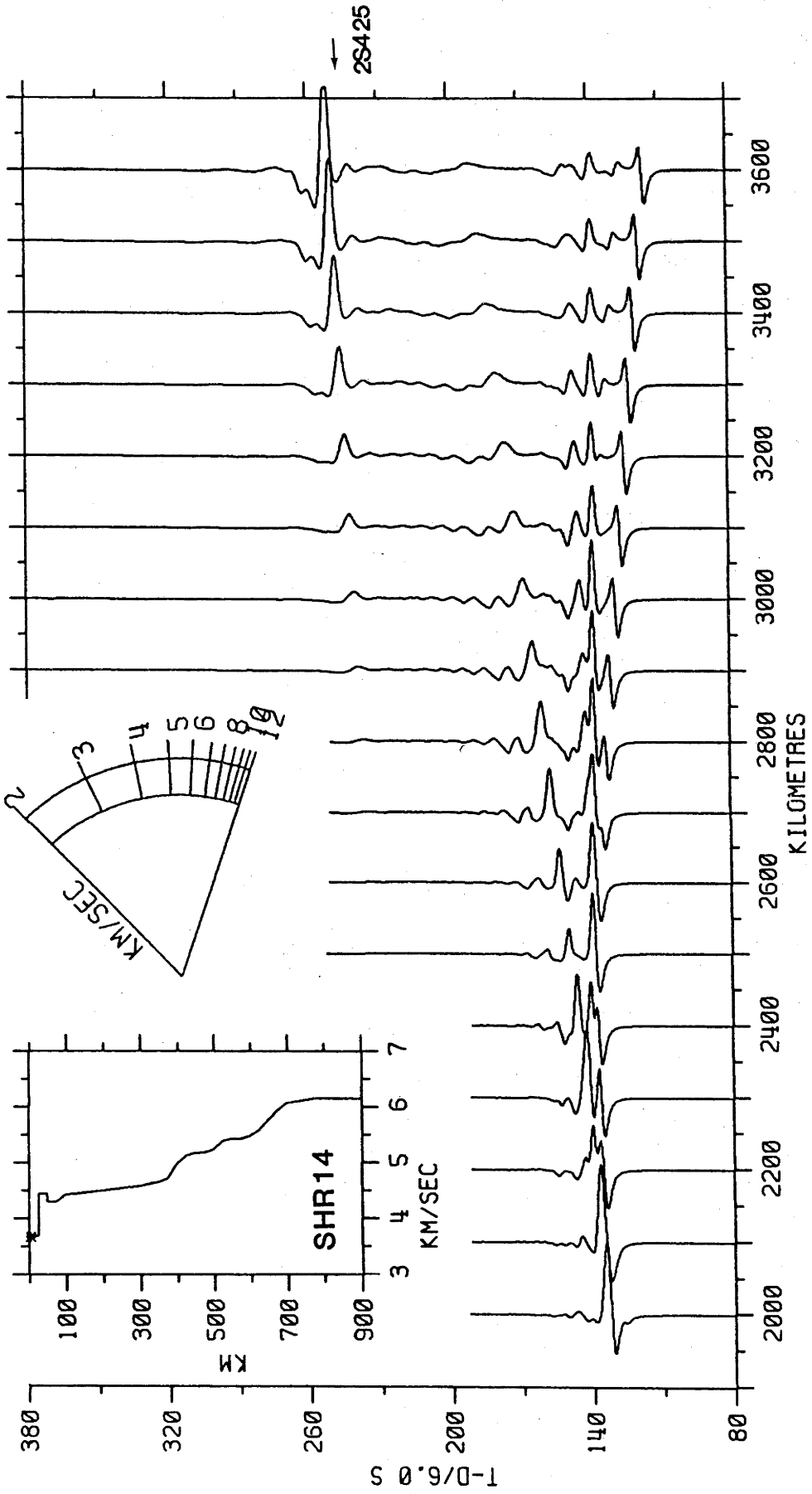


Figure 6.10.: Synthetic SH seismograms for the SHR14 model (HelMBERger and Engen, 1974). Caption as given by Figure 6.2.

of other arrivals in the latter part of the seismogram clearly show that SHR14 inadequately describes the shear-wave velocity structure in Europe, yet the seemingly correct travel time and amplitude relations of the first arrivals warrant SHR14 further consideration for model refinement.

6.3.9 B1 - JORDAN AND ANDERSON (1974), FIGURES 6.11, A4.1i

Gross Earth model B1 was computed using Backus-Gilbert (1967, 1968, 1970) theory to invert a basic data set of the Earth's mass and moment of inertia, average periods of free oscillations, PcP-P and ScS-S differential travel times. A low-shear-velocity zone is admitted into B1 but a possible low-compressional-velocity zone could not be resolved by their data. The upper mantle transition zone contains two discontinuities near 420 km and 671 km with a negative velocity gradient between them. The synthetic seismograms are dominated by the very large reflection from the "420-km" discontinuity. Geometrical ray theory has not predicted the lateral extent of the S420 branch beyond 3300 km (26.7°) because of the large LVZ immediately above the "420-km" discontinuity. The synthetics predict unexpectedly large arrivals on the S671 branch and so ray theory has anticipated poorly the position of the cusp. The synthetics are very simple, with the direct arrival at distances greater than 3000 km (27°) having a relatively small amplitude, neither feature being characteristic of the data. Amplitudes on the S420 branch seem to predict well the nature of the D branch, but there is nothing in the synthetics to explain the C branch arrivals. Destructive interference between 2S321 and 2S420 results in small but reasonably simple arrivals later in the wave train. Interestingly, the surface waves are not well developed, possibly due to the LVZ.

6.3.10 B1066 - GILBERT AND DZIEWONSKI (1975), FIGURES 6.12, A4.1j.

With the addition of 1066 distinct, observed eigenfrequencies, B1 was used as a starting model in the inversion that produced B1066. It is not surprising then that not a great difference exists between the models

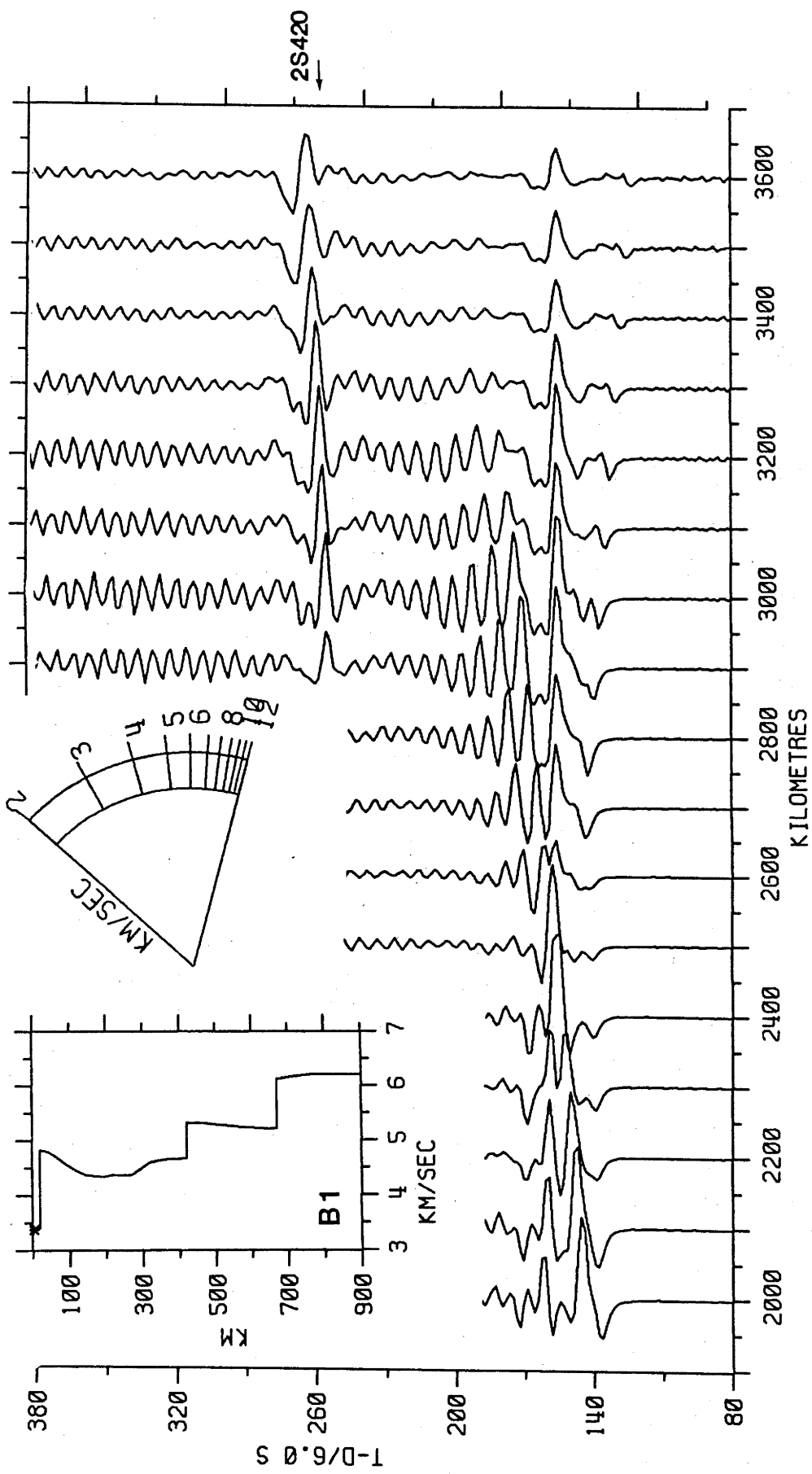


Figure 6.11: Synthetic SH seismograms for the B1 model (Jordan and Anderson, 1974). The ringing is due to too great a layer thickness. Caption as given by Figure 6.2.

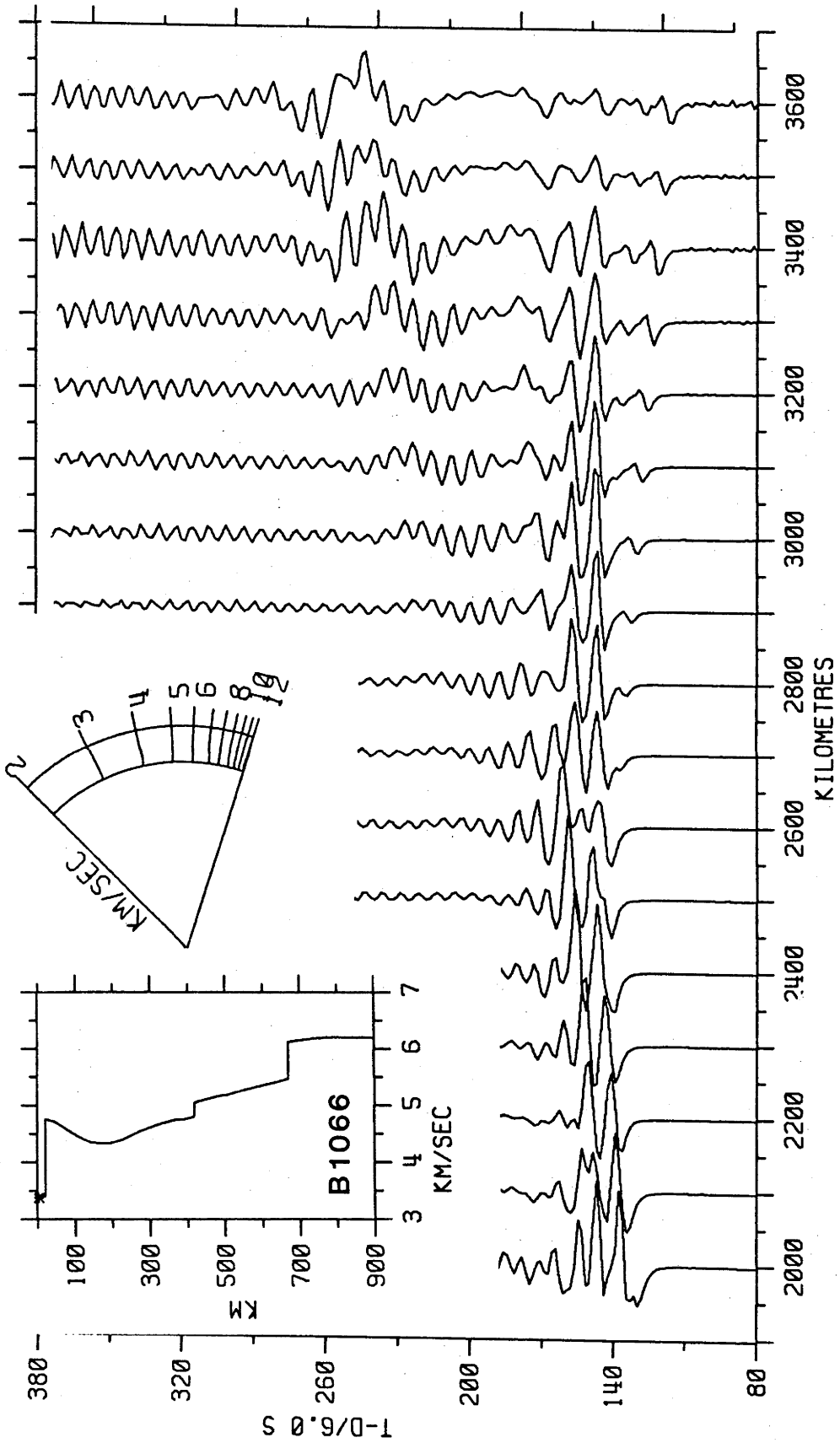


Figure 6.12: Synthetic SH seismograms for the B1066 model (Dziewonski and Gilbert, 1975). The ringing is due to too great a layer thickness. Caption as given by Figure 6.2.

except that the negative velocity gradient between 420 and 671 km in B1 is replaced with a positive gradient in B1066. The synthetics for both gross Earth models are very similar except for the secondary arrivals in the distance range 2500 to 3000 km, where the differences are likely to be lost in scatter in the real data. B1066 has modelled well the complex interaction of several branches near 2500 km (22.5°), but at larger distances, the S671 has over-emphasized contributions for the B branch, and S420 has small amplitudes although the correct velocity when compared with the D branch. SS is all but absent in the B1066 synthetics except for a very small amplitude arrival near 3400 km (30.6°). Relative to S, SS has a larger amplitude on the B1 synthetics than on the B1066 synthetics which relates to the steeper velocity gradient immediately below the LVZ in B1. The direct arrival is quite small relative to later arrivals near 3400 km (30.6°). This feature is not seen on the observed data, and so the gross Earth models B1 and B1066 are unable to explain the complexity in the observed data.

6.3.11 PEM-C - DZIEWONSKI et al. (1975), FIGURES 6.13, A4.1k.

PEM-C was designed as a continental model as one of a set of parametric Earth models in which radial variations in velocity are represented by piecewise continuous analytical functions of radius. The data used in the inversion consisted of eigenperiod observations, body-wave travel times and regional surface-wave dispersion data. The average Earth model, PEM-A will not be used as only the free-oscillation period data of Gilbert and Dziewonski (1975) were used in its construction. PEM-C fit the observed data about as well as does the other gross Earth models of the time, B1 and B1066. This is not unreasonable as all models obtained by generalized inversion procedures are dependent on the characteristics of the starting model upon which the inversion is based, ultimately B1. PEM-C is characterized by a sharply defined LVZ between 120 and 220 km, with large first-order discontinuities at 420 and 670 km, although differing from B1 and B1066 by having a "200-km" discontinuity. At large distances, the S420 branch has small amplitudes and a high apparent velocity compared with the D branch. 2S420 has a very small amplitude because its ray parameter is such that large amplitudes will not develop within this distance window.

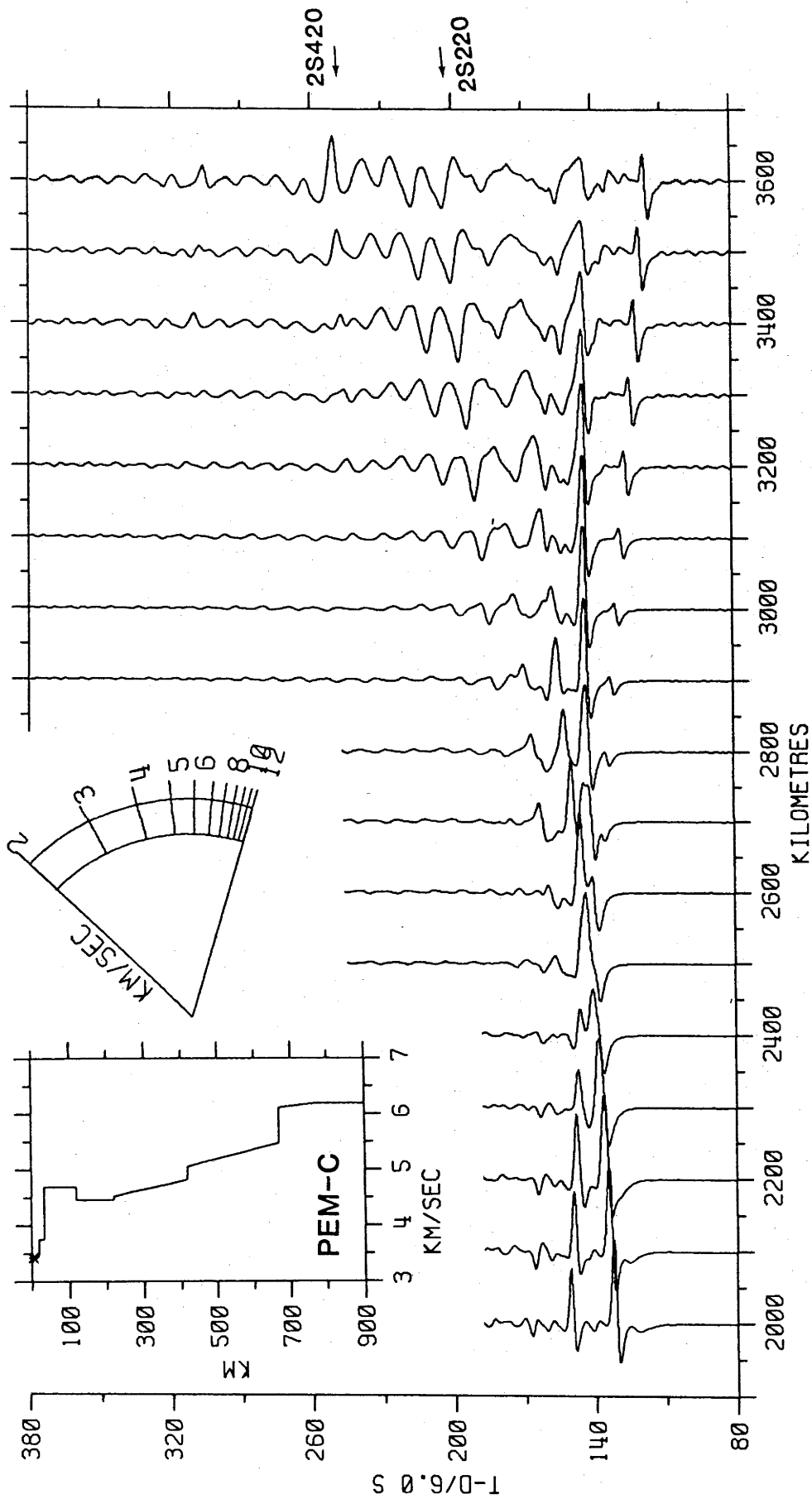


Figure 6.13: Synthetic SH seismograms for the PEM-C model (Dziewonski et al., 1975). Caption as given by Figure 6.2.

The same is true of the other multiples, but this situation may be easily remedied by increasing the velocity contrasts at the discontinuities and increasing the slope of the velocity gradients between the discontinuities. The synthetics for PEM-C are apparently more complex than those for B1 and B1066. Nevertheless, neither model in this group of gross Earth models do not adequately explain the data.

6.3.12 MODEL 7 - NOLET (1977), FIGURE 6.14, A4.11.

Nolet used a stacking technique to measure phase velocities of the fundamental and several higher mode Rayleigh waves over an array of LP stations located in western Europe. The source region was the west Pacific, so the ray paths traversed only relatively stable shield regions. The inferred model is quite similar to a highly smoothed SW-E of Mayer-Rosa and Mueller (1973). The velocity increase in MODEL 7 between 100 km and 150 km coincides with a zone of high velocity between 120 km and 160 km in SW-E. The third LVZ in SW-E coincides with a zone of stationary velocity at 300 km in MODEL 7. The higher-mode data was consistent with the placement of a large velocity gradient at a depth near 520 km which is less pronounced but coincides with a discontinuity at 540 km in SW-E. That sharp discontinuities of SW-E have been smoothed out in the inversion of the dispersion data, may indicate that a series of LVZ's exist beneath Europe although not to the degree exhibited by SW-E.

The ray-theoretical times and synthetics are quite simple, with a triplication at 2450 km (22°) and at greater distances are characterized by three arrivals after direct S. The S460 branch has the correct amplitudes and wrong velocity for the B branch. Alternatively, it matches the apparent velocity of the C branch but with wrong amplitudes. The later arrivals are due to the steep gradients near 500 km, 350 km and just below the LVZ near 200 km. The small amplitude arrival prior to the large SS (bottoming depths between 275 and 420 km) arrivals is the multiple reflection from the steep velocity gradient between 200 and 280 km. The large amplitude of this multiple is not unexpected as the LP waves will "see" this gradient as a first-order discontinuity. As stated earlier, studies of LP data do not have the resolution to define the distribution and magnitude of very steep velocity gradients: transitional zones are

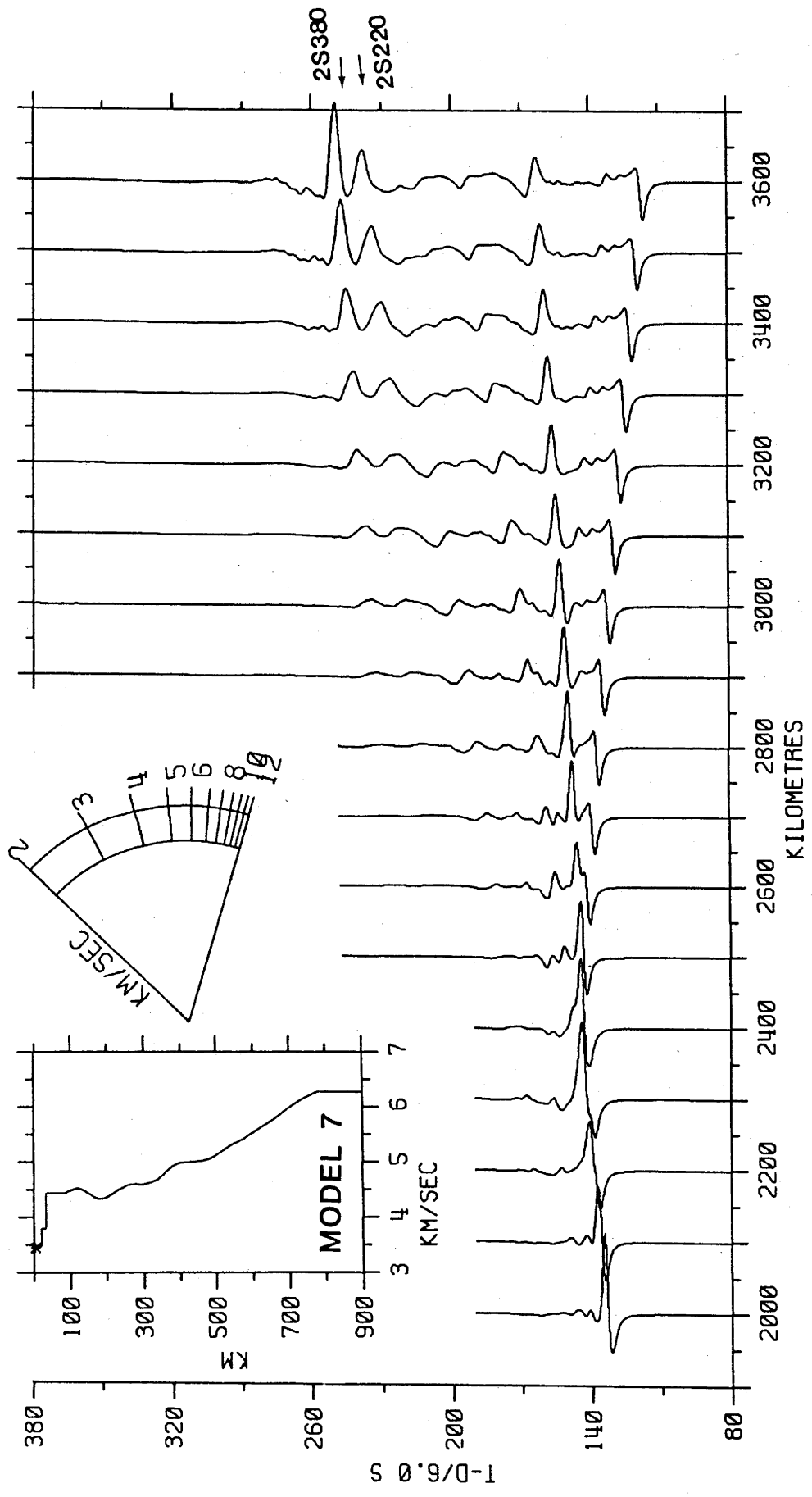


Figure 6.14: Synthetic SH seismograms for the MODEL 7 model (Nolet, 1977). Caption as given by Figure 6.2.

therefore better represented by first-order discontinuities. This point will be made clearer in Section 6.4.

6.3.13 CNNS - CARA ET AL (1980), FIGURE 6.15, A4.1m.

The stacking methods of Nolet (1977) were applied to higher mode Love- and Rayleigh-wave data in western Europe and northern Eurasia to yield S-wave models that exhibit birefringence. The model is essentially a smoothed MODEL 7.

Although the character of CNNS and MODEL 7 are one of smooth but differing velocity gradients, the travel times and synthetics are surprisingly similar. The travel-time branches for CNNS predict two cross-overs within 1° of each other, and only two major direct arrivals, the direct and S705 branches. Examination of the synthetics show that the retrograde branch of the second triplication at 2500 km (22.5°), the S705 branch, extends to at least 3220 km (29°) and represents the most obvious difference between MODEL 7 and CNNS. The relatively modest amplitudes of SS indicates the true nature of mini-max phases in an environment of almost constant velocity gradients: an increase in the period of SS brought about by constructive interference. In previous synthetics SS had a period of about 12 to 15 s, but here, the period is 30 to 40 s.

In the models examined thus far, an interesting effect has come to light: small decreases in the slope of a velocity gradient can produce rather significant branch phenomena. The effect may not manifest itself as an obvious break in the travel-time curve, but may extend the retrograde branch to large distances.

6.3.14 PREM - DZIEWONSKI AND ANDERSON (1981), FIGURES 6.16, A4.1n.

Inversion of a very large data set consisting of about 1000 normal-mode periods, astronomic-geodetic data and nearly 2×10^6 body-wave travel times of P and S waves produced PREM. Transverse anisotropy was introduced into the outer 220 km of the model to satisfy shorter-period mode observations and to obviate the need for a LVZ. The model presented here is the

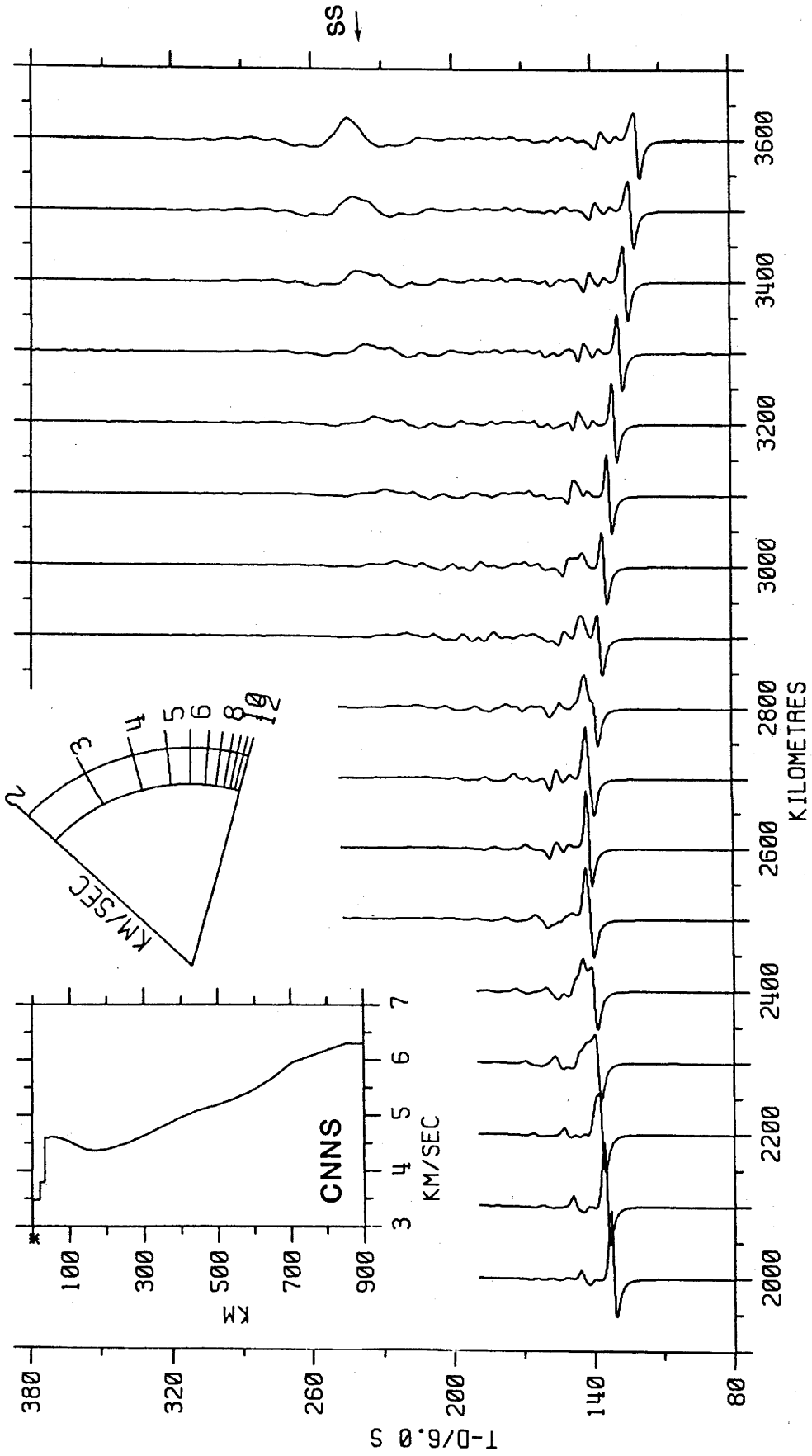


Figure 6.15: Synthetic SH seismograms for the CNNS model (Cara et al., 1980). Caption as given by Figure 6.2.

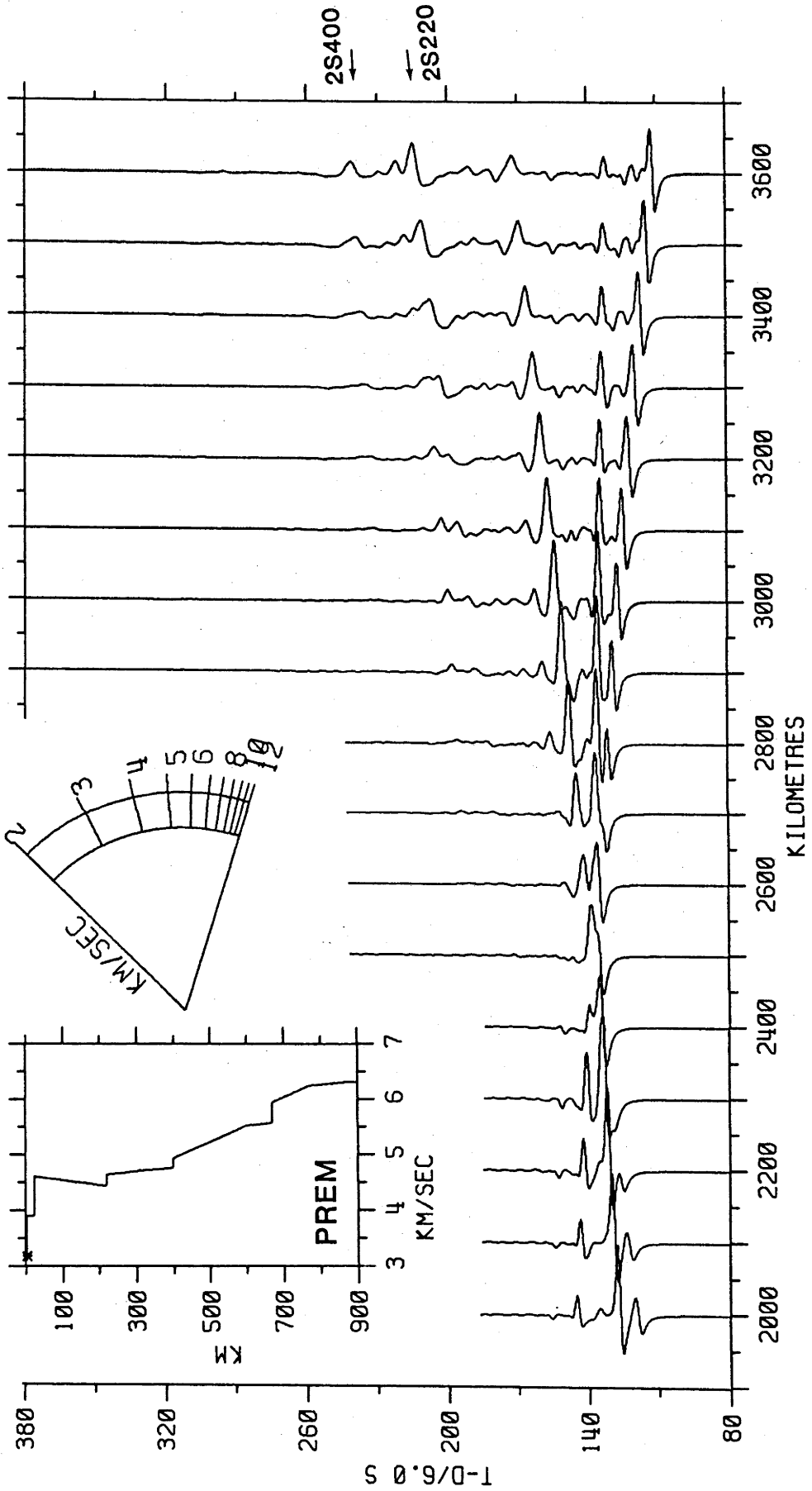


Figure 6.16: Synthetic SH seismicograms for the PREM model (Dziewonski and Anderson, 1981). Caption as given by Figure 6.2.

horizontal velocity distribution and predicts shorter travel times than for SV. PREM has no LVZ but has a negative velocity gradient immediately beneath the crust to about 220 km where there is an abrupt increase in velocity, and other first-order discontinuities at 400 and 670 km. The travel times and synthetics are comparatively simple. It is interesting to note that the first arrival at distances beyond 3000 km (27°) carries with it more energy relative to the S400 and S670 branches than the other gross Earth models. The S220 arrival matches well the F branch. Amplitudes on the S400 and S670 branches correspond quite well to the D and B branches, although the synthetics have a higher apparent phase velocity. If the average velocity in the zone immediately above the "670-km" was lowered, S670 may become more like the B branch and may model well the complex interaction of waveforms beyond 24° . The phase 2S400 is of very low amplitudes, the cusp having been shifted to greater distances because of the low gradients above 400 km. The crustal multiples are quite obvious. The small phase preceding 2S400 at 3100 km (27.9°) is 2S220. The amplitudes on the S670 branch are smaller than on the S400 branch even though the "670-km" discontinuity involves a larger velocity contrast. This apparent anomaly occurs because of the large positive velocity gradient immediately above the "670-km" discontinuity, thus defocusing refracted energy at larger distances. In turn, this feature alone may be used as a discriminant between PREM and the other gross Earth models. Although the synthetics have no arrivals corresponding to the C branch, PREM is a promising candidate for further model refinement.

6.3.15 S2 - HENDRAJAYA (1981), FIGURE 6.17, A4.10.

S2 is based on slowness measurements of first and later arrivals recorded in the distance range 13° to 46° from the Warramunga SP Array. The model is characterized by large first-order discontinuities at 200, 300, 415, 520, 650 and 775 km. The structure above 300 km was inferred from the P-wave model CAP8 (Hales et al., 1980a). The many predicted breaks in the travel-time curve are characterized by small increments in slowness, and so an LP study is likely to smooth out the curve to be Herrin-like. Nevertheless, from previous experience, models with such complex structure are expected to give correspondingly complex synthetics.

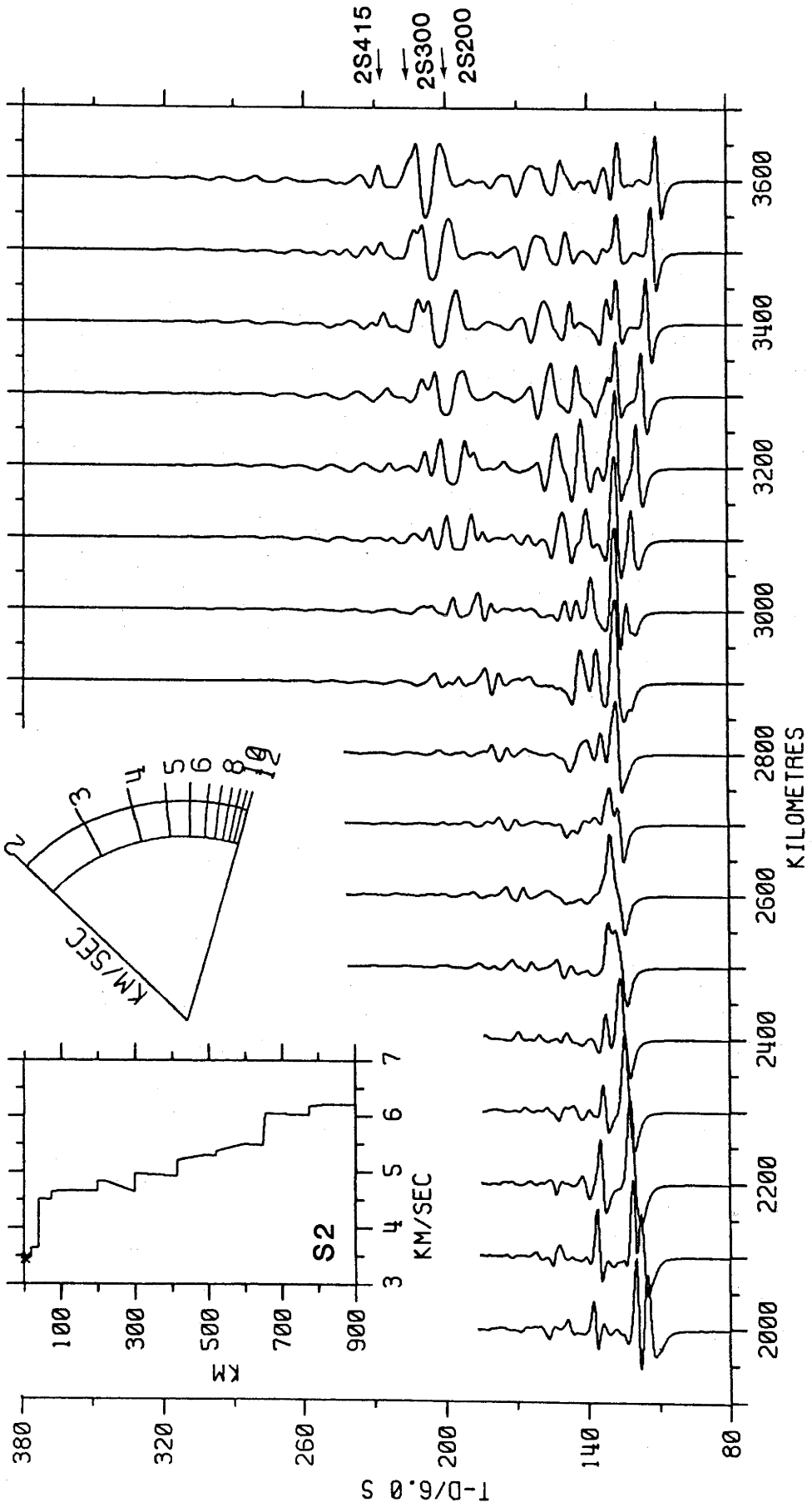


Figure 6.17: Synthetic SH seismograms for the S2 model (Hendrajaya, 1981). Caption as given by Figure 6.2.

Like SW-E, the synthetics show considerable energy between the first arrival and the mini-max arrivals.

The most obvious phases on the very complex synthetics are the direct S520, S415 and multiply reflected arrivals. The S520 branch may be an interference of the S650 and S520 branch arrivals because the small velocity contrast at 520 km is unable to explain such a large arrival. The arrivals near the expected time of SS are a complex sequence of arrivals, 2S200, 2S300 and 2S415, each exhibiting different moveouts, rendering positive identification of the multiples difficult without knowledge of the theoretical travel times. The multiples appear, however, to be confined to a window of about 50s, whereas on the data they extend into the surface waves, a window of at least 100s. Of course, if one accepts the intuitive explanation for Love-wave propagation as an interference condition of internally reflected SH body waves, then the distinction between multiply reflected body waves and surface waves on a seismogram is very fine. Although the synthetics are of a complex nature, the overly complex nature of the first arrivals preclude S2 as a starting point for further refinement.

6.3.16 SHMEE - CLEARY ET AL. (1982), FIGURE 6.18, A4.1p.

Synthetics for the model SHMEE calculated by the Generalized Ray method have been covered in Chapter 2 (Figure 2.1). The Reflectivity method synthetics are comparatively more complex than the Generalized Ray method synthetics, but have now been filtered by several mechanisms and include many other multiply reflected arrivals (including Love waves in Figure A4.1p). A comparison of the Generalized Ray method and Reflectivity method synthetics show some considerable differences in the relative positioning of the larger amplitude multiples. For example, the Generalized Ray method synthetics has large 2S600 arrivals 168s after direct S at 3224 km (29°), but the Reflectivity method synthetics have comparatively smaller amplitudes for 2S600. This may be attributed to the effects of the Earth-flattening transformation which introduces an artificial velocity gradient, and therefore necessitates partitioning into fictitious homogeneous layers which are artifacts of the transformation. The Reflectivity method uses the same transformation, but the incorporation of

all possible direct and multiple rays by the Reflectivity method as opposed to the calculation of only the primary rays (a subjective decision) in the case of the Generalized Ray method, will produce refracted energy amplitudes similar to that produced by the spherical Earth analytic synthetic seismogram techniques such as Full Wave theory (Leven, 1980). The effect will be more pronounced for the multiply reflected arrivals, and shows that considerable care should be taken when interpreting synthetic seismograms calculated by the Generalized Ray method.

The Reflectivity method synthetics are very complex, particularly in the latter parts of the wave trains. It is interesting to note the almost complete absence of the S600 branch and the large amplitudes on the S530 branch. Intuitively, one would expect that a 14% velocity contrast on the "600-km" discontinuity to return more energy to the surface than the 7% velocity contrast of the "530-km" discontinuity. The reason why the S530 branch contains so much energy is due to the negative velocity gradient immediately above it - no energy is refracted upwards in this layer. If the depth of the "600-km" discontinuity were increased to say, 670 km, the amplitudes on this branch would increase, and so correspond to the B branch. Furthermore, a major criticism of SHMEE would be remedied: the cross-over near 2250 km (20.2°) would be moved to a greater distance. The S530 branch has timing and apparent velocity similar to that of the C branch. In order to decrease the amplitudes on this branch the velocity contrast should be decreased across the "530-km" discontinuity. The largest multiples seen on the synthetics are 2S435 and 2S600. The large amplitudes on S340 are the result of constructive interference of S340 and S435, and model well the D branch. Ray theory has predicted the extension of the S435 branch to distances of only 2400 km (21.5°) because of the very low velocities above this discontinuity. Yet the large velocity contrast (18%) ensures that large amplitude reflections propagate to large distances. In order to decrease the amplitudes on this branch beyond 3200 km (28.8°), the "435-km" discontinuity should be raised to about 400 km. Unlike the other favourable models SHR14 and PREM, SHMEE is able to generate synthetic seismograms with the complexity of the recorded data. With the suggestions given above, SHMEE constitutes an excellent starting point for further modelling.

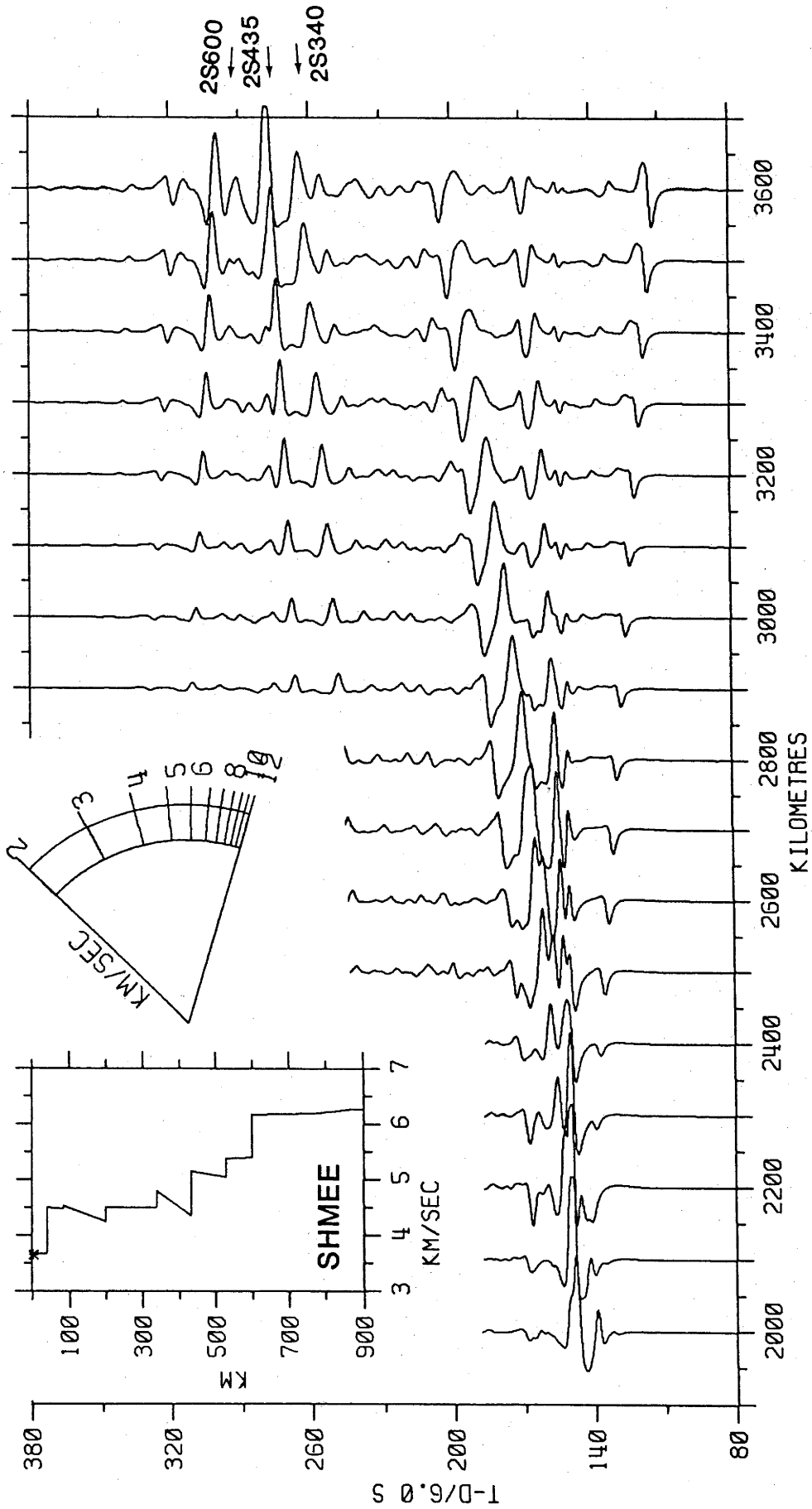


Figure 6.18: Synthetic SH seismograms for the SHMEE model (Cleary et al., 1982). Caption as given by Figure 6.2.

6.3.17 MA - MASSÉ AND ALEXANDER (1974), FIGURES 6.19, A4.1q.

An upper mantle seismic profile for Fennoscandia was constructed from Russian explosion recordings made at NORSAR. The upper mantle P-wave velocity distribution beneath Scandinavia and western Russia was determined from this profile to be the same as that beneath the Canadian Shield (Massé, 1973), with discontinuities at depths of approximately 74, 107, 328, 430 and 710 km, and a gradual increase in velocity in the depth range 590 to 710 km. Although including a rather complex structure between 90 and 110 km, MA is a step-like model consisting largely of zones of constant velocity and first-order discontinuities. This simple structure entails simple travel times and synthetics with cross-overs near 2250 km (20.2°) and 2700 km (24.3°). At distances beyond the second cross-over, the direct, S710, S430 and S328 branches become well separated. The S710 branch has very large amplitudes (clipped on the plot) due to the strong positive velocity gradient immediately above the "710-km" discontinuity. Furthermore, the slowness of the S710 branch is too small for the B branch. The S320 branch matches the velocity of the D branch, but differs in amplitudes. This could be remedied by placing a more positive velocity gradient above the "320-km" discontinuity. The amplitudes and velocity on the S420 branch would fit the C branch, but the timing relative to the first arrival would need attention. MA generates a complex succession of multiples (2S107, 2S328, 2S430, 2S710) which appear to match quite well the style of the multiples of the observed data but the cusps of the presumed branches should be moved to smaller distances. Unfortunately, the poor misfit of the waveform data with the synthetic first arrivals exclude MA as a possibility for future refinement modelling.

6.3.18 KCA - KING AND CALCAGNILE (1976), FIGURES 6.20, A4.1r.

Using a data set similar to that of Massé and Alexander (1974), i.e., presumed explosions in western Russia recorded by NORSAR, KCA was generated to show that a model simpler than MA could adequately explain the observed data. KCA has first-order discontinuities at depths of 420 km and 690 km, and fairly uniform velocity gradients elsewhere. The S690 branch becomes a second arrival at distances beyond 2700 km (24.3°), but lacks sufficient move-out to become completely separated from the direct phase within this

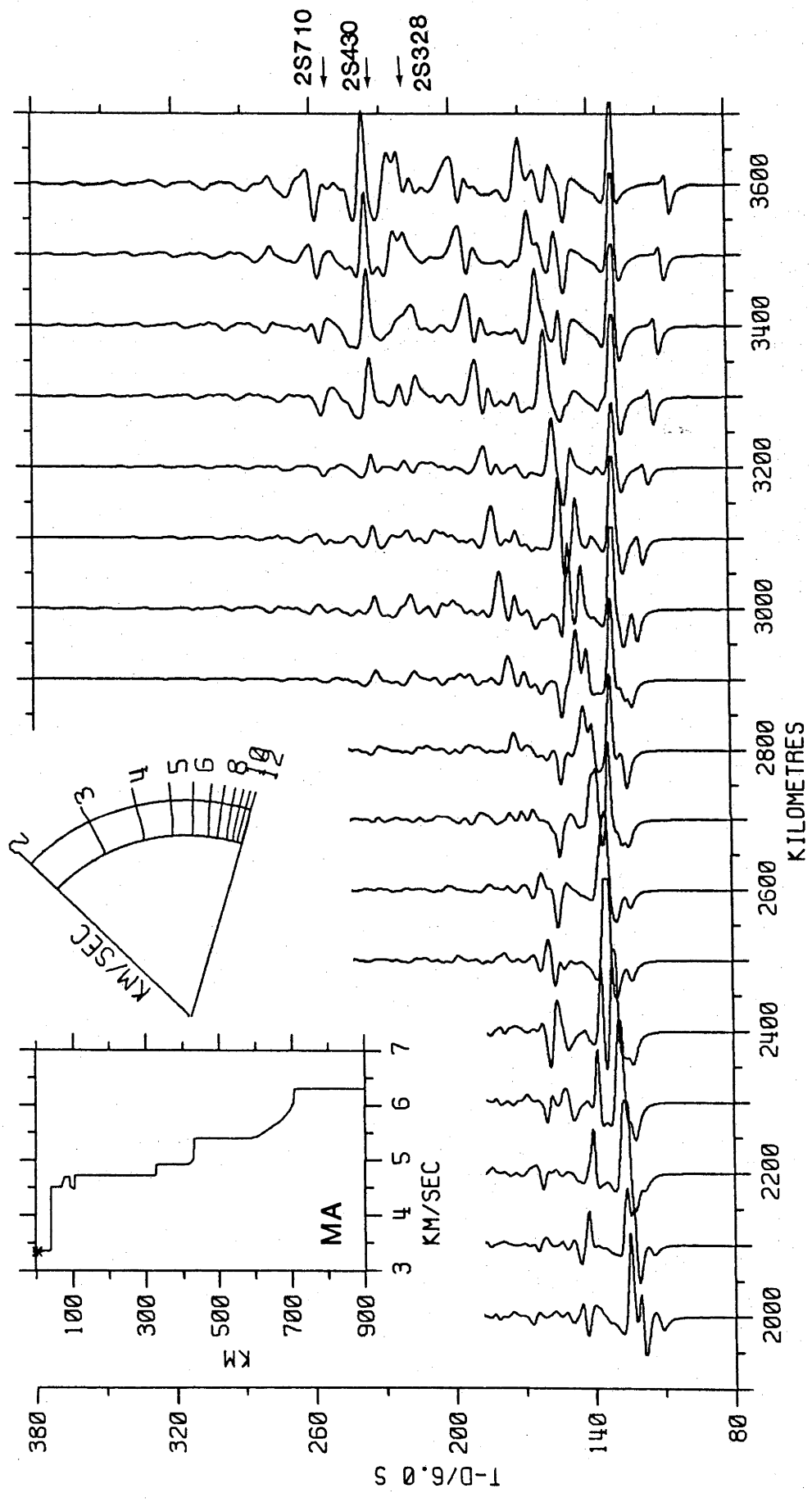


Figure 6.19: Synthetic SH seismograms for the MA model (Massé and Alexander, 1974). Caption as given by Figure 6.2.

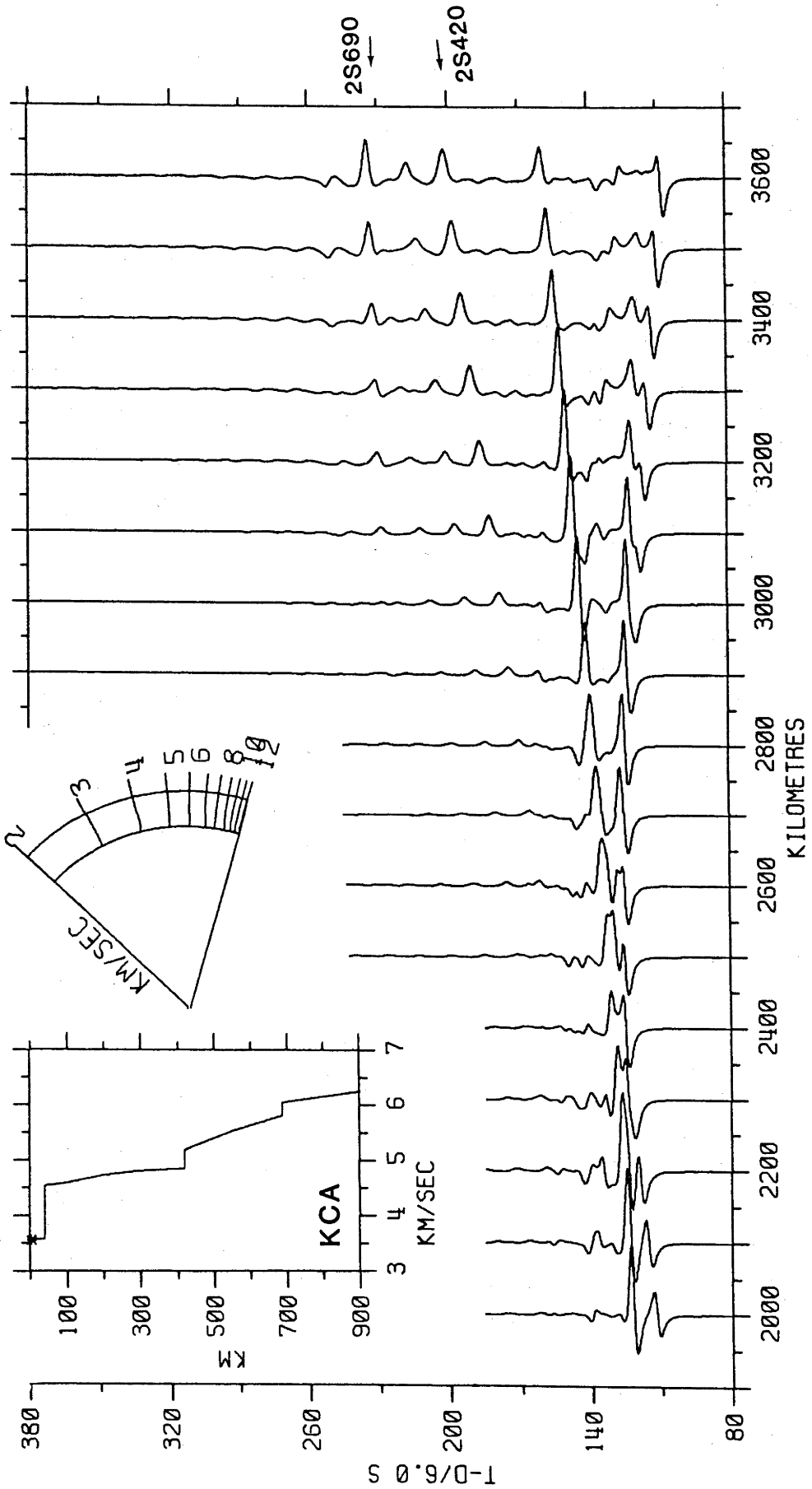


Figure 6.20: Synthetic SH seismograms for the KCA model (King and Calcagnile, 1976). Caption as given by Figure 6.2.

distance window, and thus does not match the B branch. The S690 arrival can be seen at 3300 km (29.7°) where an inflection in the direct phase indicates the presence of a second arrival, but the amplitude quickly attenuates with distance. Ray theory predicts that this branch extends to only 3100 km (27.9°). S420 may correspond to the D branch, but the amplitudes at large distances would need attenuating by decreasing the size of the velocity contrast of the "420-km" discontinuity. The multiply reflected arrivals are 2S420 and 2S690. Although the character of the first arrivals is quite simple, the ability of KCA to account for large amplitude arrivals later in the wave train give the seismograms a complex appearance much like the data. KCA cannot account for the C or F branches on the data.

6.3.19 EKW - ENGLAND ET AL. (1977), FIGURES 6.21, A4.1s.

The data and method of inversion for the P-wave velocity model have been covered in Chapter 5. EKW is very similar to KCA except that the depths to the first-order discontinuities are slightly deeper at 480 km and 710 km. There is also a reduction in the size of the velocity contrasts, 3% and 3.5% for the upper and lower discontinuities in EKW, and 7% and 4% in KCA. These differences, though very slight, become very obvious on the synthetics. The branch representing rays that bottom immediately above the "710-km" discontinuity are difficult to find for either model, but whereas the S420 branch in KCA contained significant energy, the S480 branch in EKW is large only at distances near where it becomes a second arrival, i.e., near the cross-over at 2650 km (23.8°). However, the timing and apparent phase velocity of the S480 branch do not adequately describe the D branch. At larger distances, there is nothing in the synthetics corresponding to the B, C or D branches. The almost complete absence of multiples is anticipated because of the small velocity contrasts at the discontinuities. SS (bottoming above the "480-km" discontinuity) is very large (clipped at 3600 km) because the uniform gradient from 40 km to 480 km is ideal for its efficient propagation. The low amplitude arrival 27 s after 2S480 at 3600 km (32.4°) is the ray that has twice bottomed in the depth range 480 to 710 km (2S710). The model EKW is too simple to adequately account for the data.

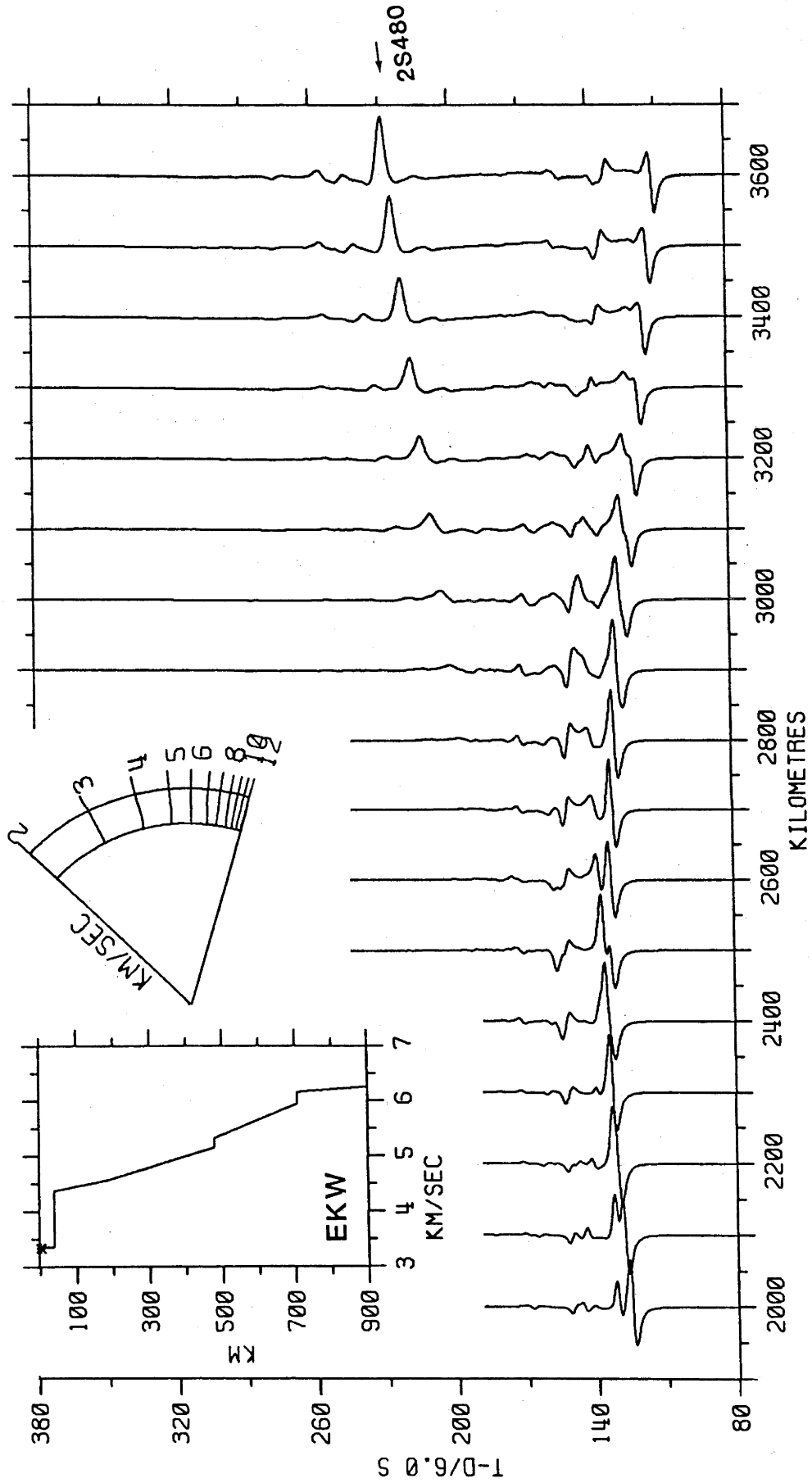


Figure 6.21: Synthetic SH seismograms for the EKW model (England et al., 1977). Caption as given by Figure 6.2.

6.3.20 NAT - ENGLAND ET AL (1978), FIGURES 6.22, A4.1t.

From travel-time curves for P waves recorded at NORSAR from earthquakes in the North Atlantic and Arctic Oceans, NAT invokes lateral heterogeneity to depths of at least 300 km between western Russia (KCA) and central Europe (EKW), but for depths greater than 300 km, models NAT and KCA approximately fit the same observed travel-time curves. NAT is very similar to the simple EKW model, except that the upper discontinuity is replaced by a transition zone between 400 km and 440 km, and the lower discontinuity is raised to 690 km. Using long-period data alone in the distance range 20° to 30° , it is unlikely that travel times could discriminate between NAT and EKW. This is certainly the case for NAT and KCA. Without considering multiple arrivals, the synthetics for the shear-wave velocity model NAT show that the arrival representing rays that bottom immediately above the discontinuity near 420 km is sufficient to discriminate between the three models. The S420 branch extends with large amplitudes to at least 3600 km (32.4°) for model KCA, but only to 3600 km for model NAT and has a much higher apparent phase velocity than the D branch. The S420 branch can be traced to only 3100 km (27.9°) and with significantly higher velocity for model EKW. At distances less than 2900 km (26.1°) the synthetics for NAT and EKW are most similar. There are no large amplitude multiples in the synthetics for NAT and EKW, in contrast to KCA. However, the timing of 2S420 is 25s earlier at 3600 km on NAT than on EKW and must constitute additional weights to demarcate between the two. Models NAT and EKW must be considered too simple to be considered for further refinement.

6.3.21 K8 - GIVEN AND HELMBERGER (1980), FIGURES 6.23, A4.1u.

Long- and short-period WWSSN seismograms from nuclear explosions in Russia were incorporated with apparent velocity observations to derive an upper mantle model for northwest Eurasia. K8 is characterized by a LVZ between 150 and 200 km, and is relatively smooth from a depth of 200 km down to 420 km where a 5% increase in velocity produces a cross-over near 2280 km (20.5°). Another first-order discontinuity is placed at 675 km with a 4% change in velocity producing another cross-over near 2700 km (24.3°). K8 was modelled on the assumption that the S420 branch extended

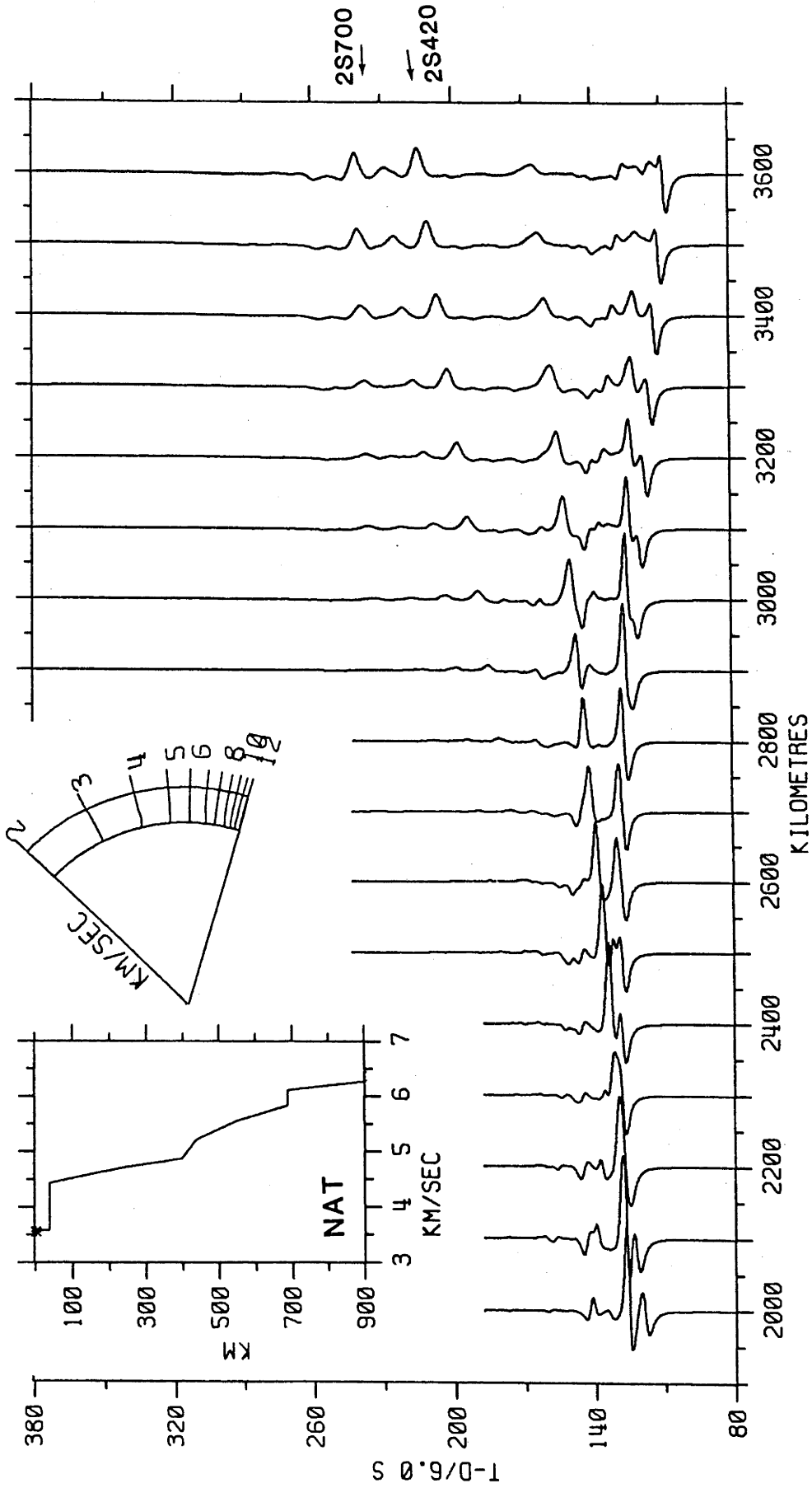


Figure 6.22: Synthetic SH seismograms for the NAT model (England et al., 1978). Caption as given by Figure 6.2.

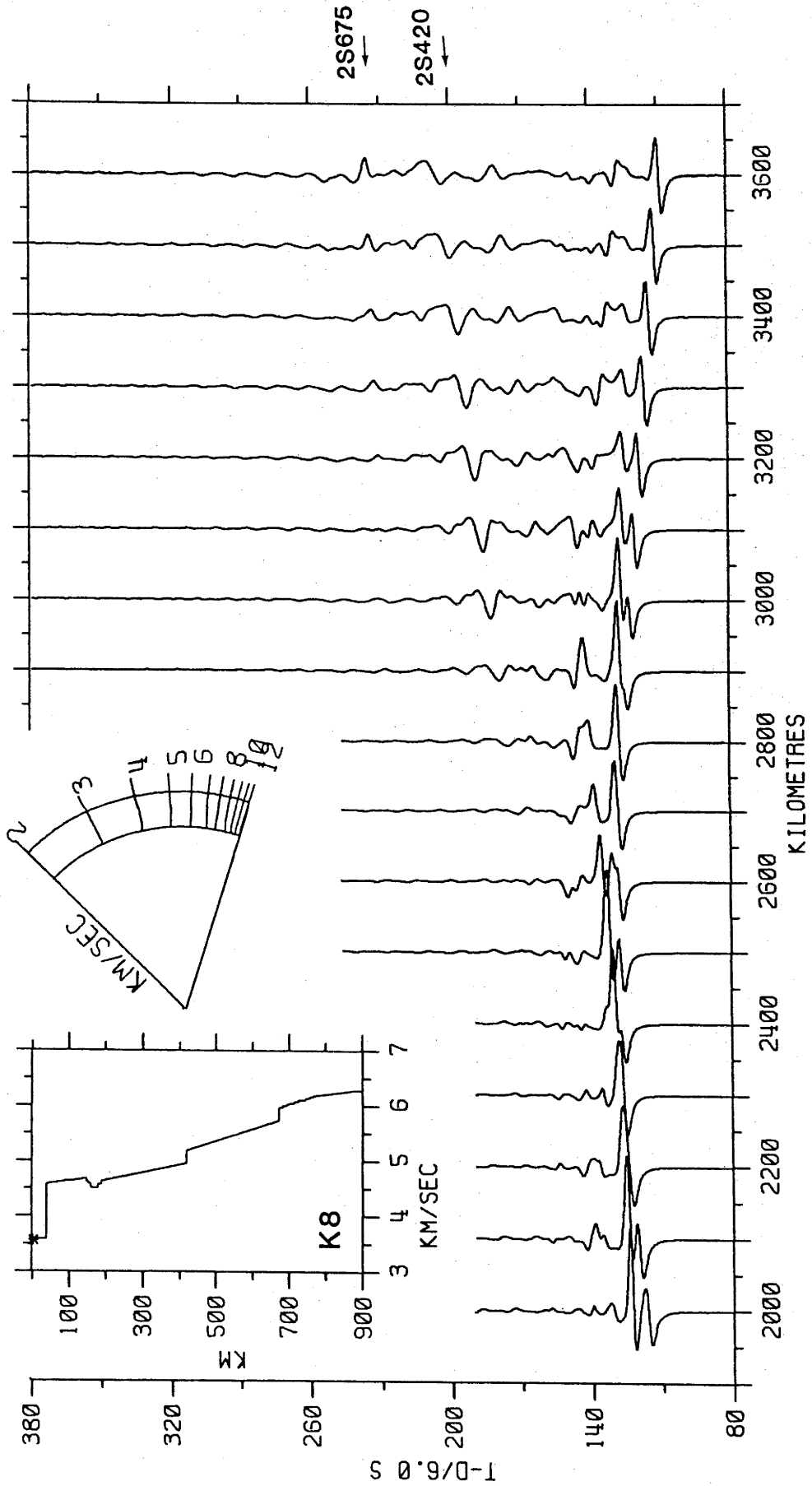


Figure 6.23: Synthetic SH seismograms for the K8 model (Given and HelMBERGER, 1980). Caption as given by Figure 6.2.

to 2560 km (23°), but the synthetics show that the cusp extends to near 2900 km (26.1°). Similarly, the S675 branch was presumed to extend to 3000 km (27°), but can be clearly seen on the synthetics to at least 3600 km (32.4°). The reflection from the lower boundary of the LVZ near 200 km is apparently lost in the crustal reverberation noise. The multiples, composed of 2S155 and the cusp associated with 2S420 are of relatively low amplitude. Given and HelMBERGER successfully used the S675 branch to discriminate against KCA, but examination of the complete synthetics reveal other features that could have been used: the S420 cusp extends to near 26° for K8, but to at least 3600 km for KCA; the multiples arrive relatively earlier in K8 than KCA. K8 is a simple model that generates relatively simple seismograms of the same style as EKW and NAT.

6.3.22 S8 - BURDICK (1981), FIGURES 6.24, A4.1v.

Using long-period waveforms of Mediterranean earthquakes recorded by European WWSSN stations, Burdick claimed that the data could not substantiate major lateral variations in structure to depths of at least 500 km as suggested by the models KCA, EKW and NAT. Burdick's model S8 is most similar to the Eurasian model K8 and T9 for North America. Burdick admits that differences in the velocity structures do exist to depths of 250 km, and that this is the most likely cause of relative shifts to the depths of the deeper discontinuities of all the P-wave models examined thus far. This result is hardly surprising: the data of Given and HelMBERGER (1980) and Burdick include the degrading effect of the instrument response. The twenty two models examined in this section appear to yield reasonably similar first arrivals even without the smoothing effects of the long-period instrument response. Using first-arrival waveforms alone, it is unlikely that such interpretational subtlety is available to delineate with such finality the nature of lower discontinuities.

The travel times for S8 are almost identical to those of K8 once a timing error in the data of Given and HelMBERGER has been removed, even though S8 does not include the LVZ of K8. To compensate for the lack of a LVZ, the deeper discontinuities are placed approximately 20 km higher than in K8. A comparison of the synthetics for K8 and S8 reveals more differences than the travel times would indicate. At distances less than

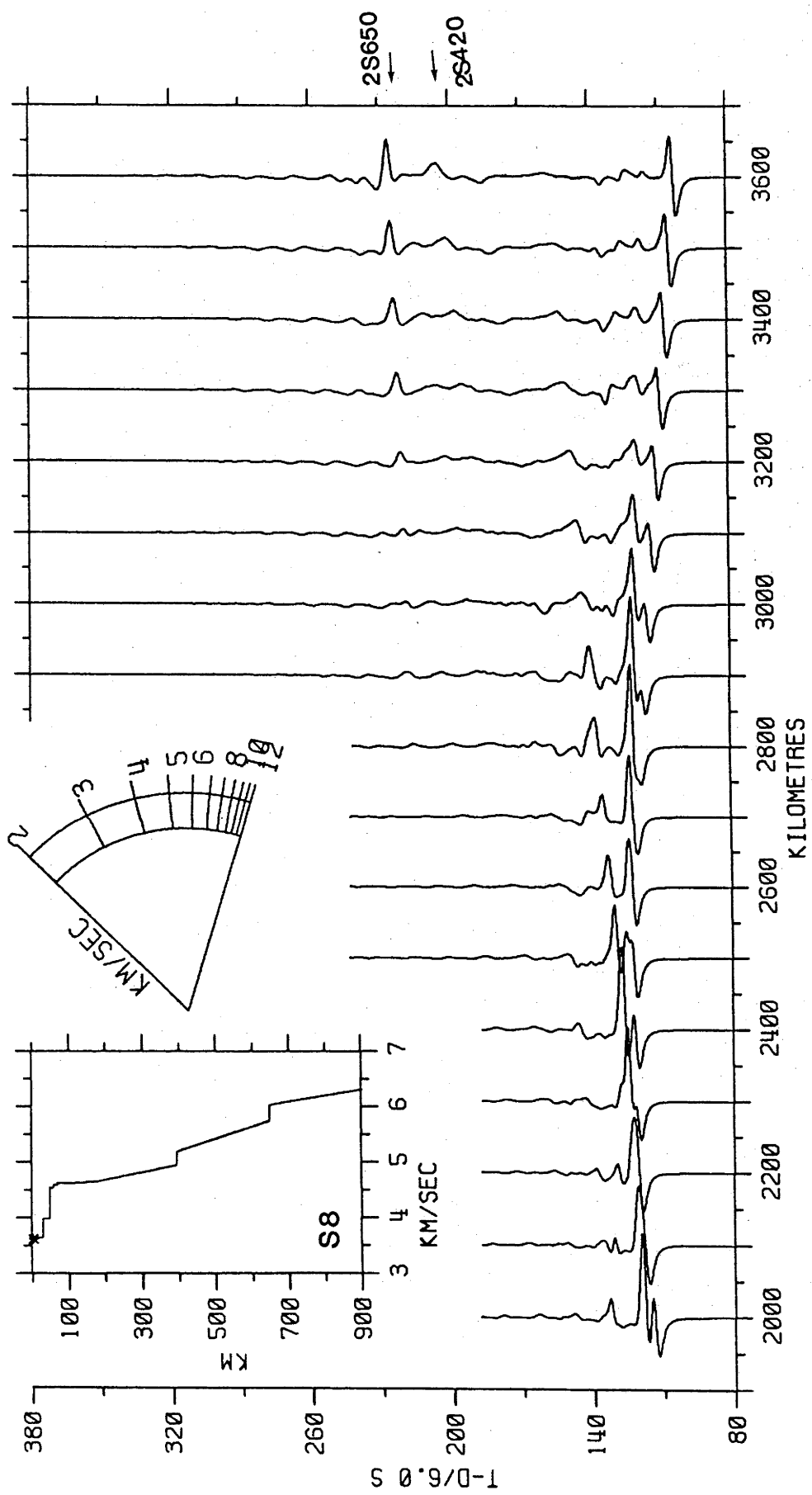


Figure 6.24: Synthetic SH seismograms for the S8 model (Burdick, 1981). Captions as given by Figure 6.2.

2000 km (18°), the interaction between the first arriving S and the backward branches of S180 and S420 is considerably more complex than the simple S395 arrival of S8. At this distance, there appears to be little contribution from the backward part of the retrograde S675 (K8) and S650 (S8) branches. In addition, the effect of the S420/S395 branch can be seen in the very narrow distance interval 2500 to 2600 km (22.5° to 23.4°) although S8 and K8 are unconstrained in this distance range. At distances beyond 23.4° , the differences between the first arrivals of K8 and S8 are masked by crustal reverberation noise, although large differences do exist between the timing and amplitudes of the multiples. Like EKW, NAT and K8, S8 at larger distances has none or little energy between the first arrival and SS to account for the B, C and D branches. The applicability of the models K8 and S8 are challenged by the data on account of the simplicity of the computed synthetics.

6.4 WAVEFORM MODELLING CONSIDERATIONS

Before applying synthetic seismograms to the analysis of upper mantle seismic phases, it is desirable to investigate the behaviour and resolution attainable with LP waves. This will give some insight into the modelling procedure, and dictate certain characteristics that will feature in the final model.

6.4.1 THE MODELLING OF TRANSITIONAL AND FIRST-ORDER DISCONTINUITIES

The nature of prominent velocity increases near depths of 200, 400 and 650 km differ greatly in style between models; either smooth transitions in velocity or a discontinuous velocity increase, defined here as a first-order discontinuity. Surface-wave dispersion studies and nearly all studies that employ formal inversion techniques are almost invariably characterized by velocity models with transitional zones. On the other hand, velocity models derived from the analysis of body waves are most often characterized by first-order discontinuities. This is particularly true of more recent studies where the discontinuities are separated by

regions of near constant velocity. Further to this, an occasional feature of the body-wave models are small changes in the velocity gradients between the discontinuities. This feature is generally invoked to satisfy amplitudes on the forward branch near presumed cusps of the travel-time curve (e.g., IN, STAN3, US26, REDDOG-C, S2). Kennett (1975a) used synthetic seismograms to model an attenuative Earth, and indicated that interpretation of observations for an attenuative Earth in terms of perfectly elastic models may give rise to apparently fine detail which would be smoothed out in an interpretation which allows for attenuation. The corollary of this is that major transitions may be sharper than has previously been suggested from amplitude studies. It is proposed here that unless there is evidence to the contrary, a first-order discontinuity should be assumed wherever a sharp increase in velocity is suspected. Transitional discontinuities are more difficult to model with the Reflectivity method and maintain without clear evidence to verify the upper and lower limits of the zone and the internal velocity gradient. It will now be shown that LP data cannot discriminate between transitional discontinuities and first-order discontinuities.

A numerical study has been undertaken to investigate the differential effects on synthetic seismograms of transitional and first-order discontinuities. SHR14 (HelMBERger and Engen, 1974) is characterized by transitional discontinuities at depths near 425, 500 and 675 km. Although SHR14 was generated by a careful trial-and-error search of amplitudes and travel times of LP SH first arrivals, the data do not apparently suggest the existence of the transitional discontinuities. The use of STAN3 (Kovach and Robinson, 1969) as a starting model may have influenced the evolution of SHR14 because STAN3 is characterized by broad transition zones near 400 and 675 km.

The SH synthetics of HelMBERger and Engen as calculated by the method of Generalized Rays are reproduced in Figure 6.25. For comparison, synthetics as computed by the Reflectivity method are given alongside the ray-sum synthetics. The synthetics differ somewhat in detail due to differences in the methods used (c.f., Choy et al., 1980; Burdick and Orcutt, 1979) and assumed source-time histories; for the purpose of this study however, the relative amplitudes and waveforms are sufficiently similar. Because of the Reflectivity method's inherent ability to completely specify the Earth response, the similarity of the seismograms vindicates the Generalized Ray method for this sort of analysis. As implemented here, however, the

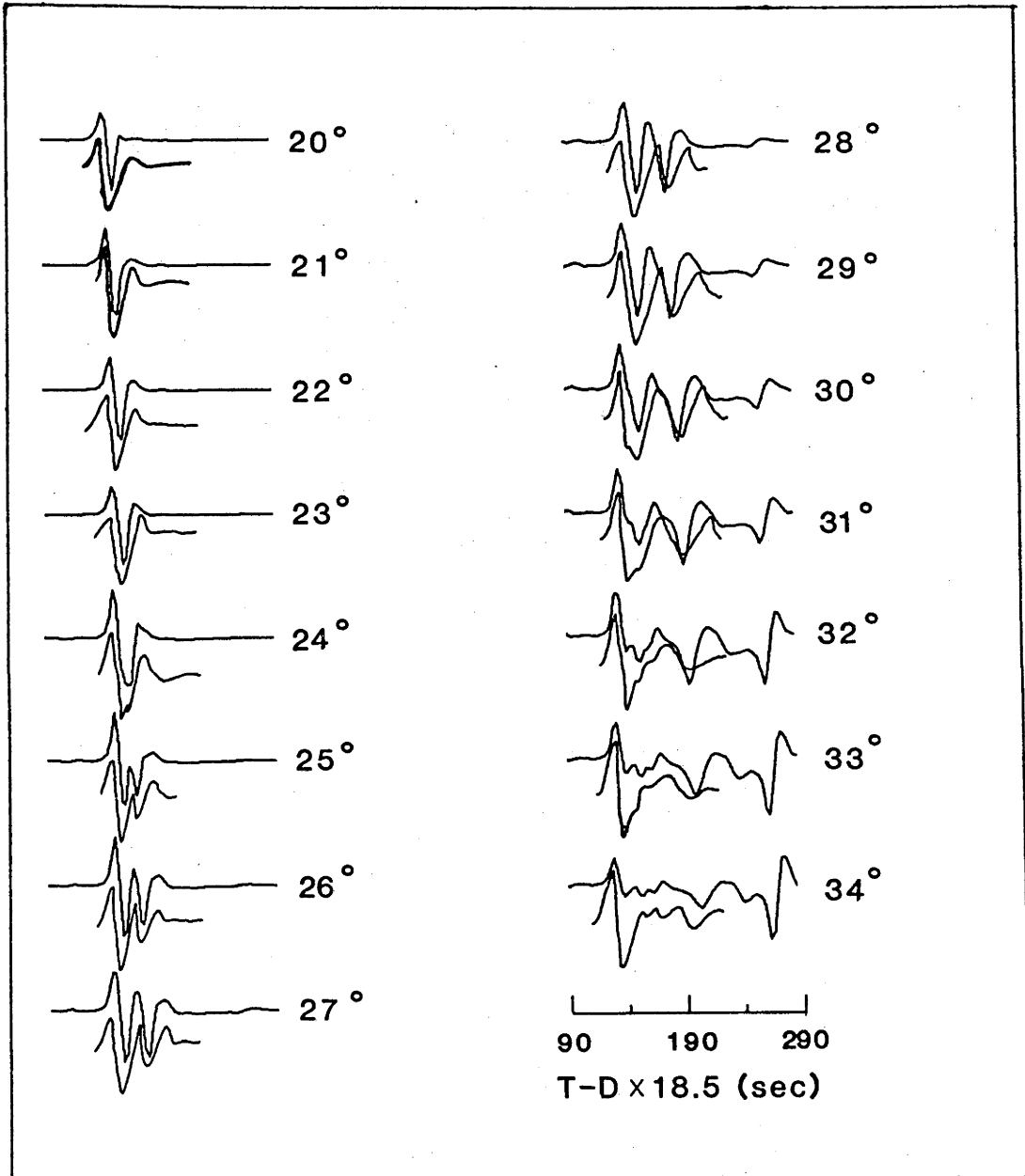


Figure 6.25: Comparison of synthetic SH seismograms as calculated by the Reflectivity method (upper trace) and Generalized Ray method (lower trace) for a strike-slip source of a depth of 6 km in a SHR14 Earth model. Distances are given in degrees and traces are normalized to peak amplitude.

computer requirements for both methods are similar and so the Reflectivity method may be preferred for computing synthetic seismograms.

Model A (Figure 6.26) is derived from SHR14 but replaces the transitional discontinuity near 425 km in SHR14 with a first-order discontinuity, preserving the overall velocity contrast and velocity gradients above and below the "425-km" discontinuity. The ground-motion synthetics for both SHR14 and model A due to a surface source show negligible differences in waveform. Helmberger and Engen included amplitudes in their analysis, and so in order to directly examine changes in amplitudes and waveforms between models, an error time series is formed by taking the difference of the synthetics for SHR14 and model A. The error time series have amplitudes proportional to the absolute peak amplitudes of the SHR14 synthetics, and are given in Figure 6.26c. In this case, the largest errors arise from the timing of SS (2S425), and are not due to differences in amplitudes or waveform. Slight differences in waveform can be seen in the region of interaction of the prograde S425 and S500 branches, and which show in the error time series as small rippling.

Model B is derived from model A, but with a first-order discontinuity at 500 km. The synthetics for SHR14, model B and the error train are given in Figure 6.27. As with the previous example, no significant differences are immediately obvious and indeed, the error time series given in Figures 6.26c and 6.27c are almost identical, implying that the overall nature of the "500-km" discontinuity may go unresolved in an amplitude/waveform study.

Finally, synthetics for model C which has first-order velocity discontinuities at 425, 500 and 675 km are given in Figure 6.28. The "675-km" discontinuity is the largest discontinuity in this set of models and is expected to be a major influence in the formation of the seismograms in the distance range under consideration. Although differences in waveforms for models SHR14 and model C appear small, the error amplitudes are up to 25% of that of the seismograms. Some of this error arises from timing differences of wavelet onsets. The conclusions of this example are clear: unless conclusive evidence exists in the highest quality data available, models composed of first-order discontinuities rather than transitional zones will be consistent with the LP waveform data.

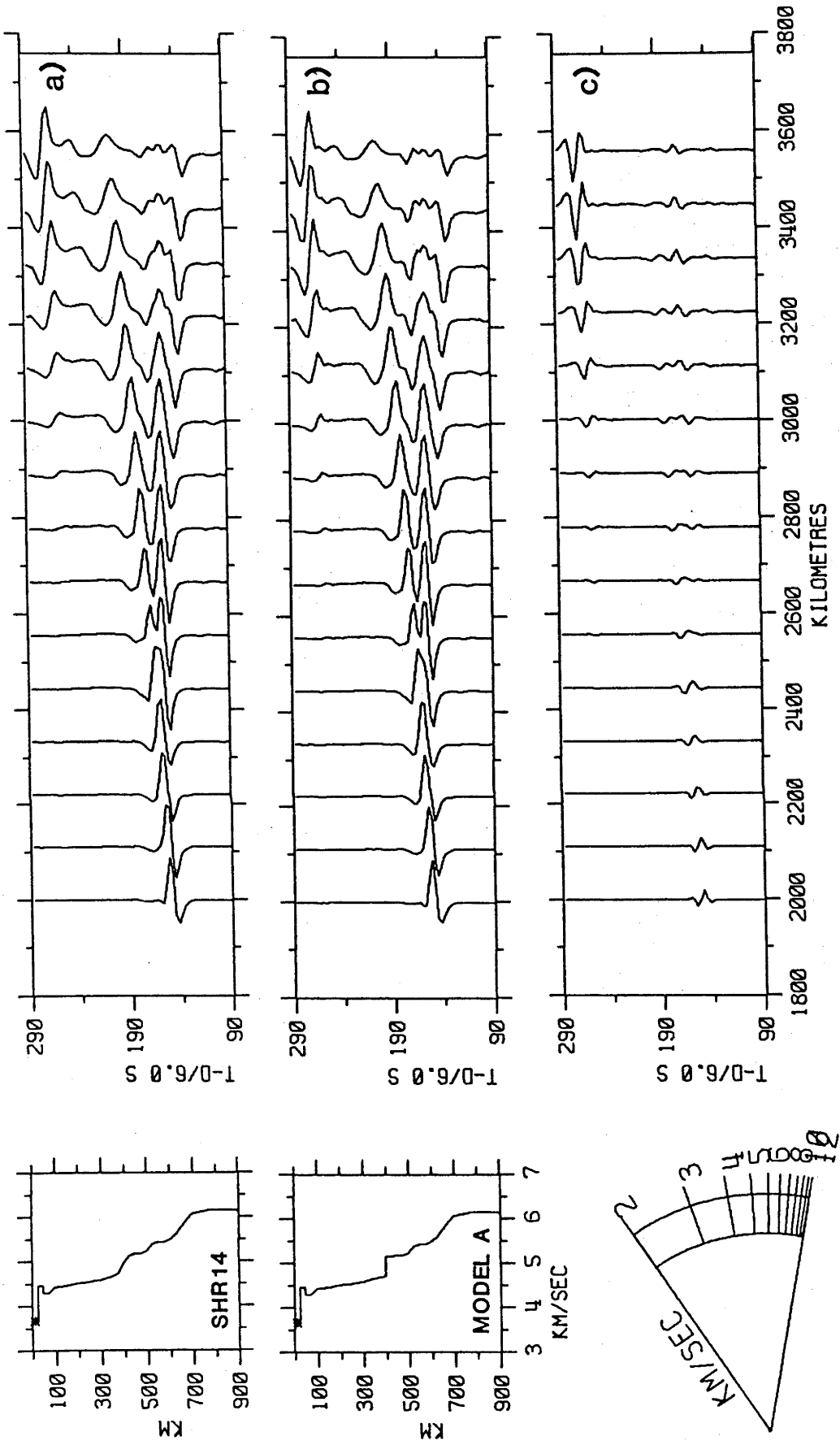


Figure 6.26: Synthetic SH seismograms for a) SHR14 and b) MODEL A. MODEL A has a first-order discontinuity at a depth of 400 km. Panel c) represents the differences of the traces in a) and b), with amplitudes plotted relative to the trace amplitudes in a).

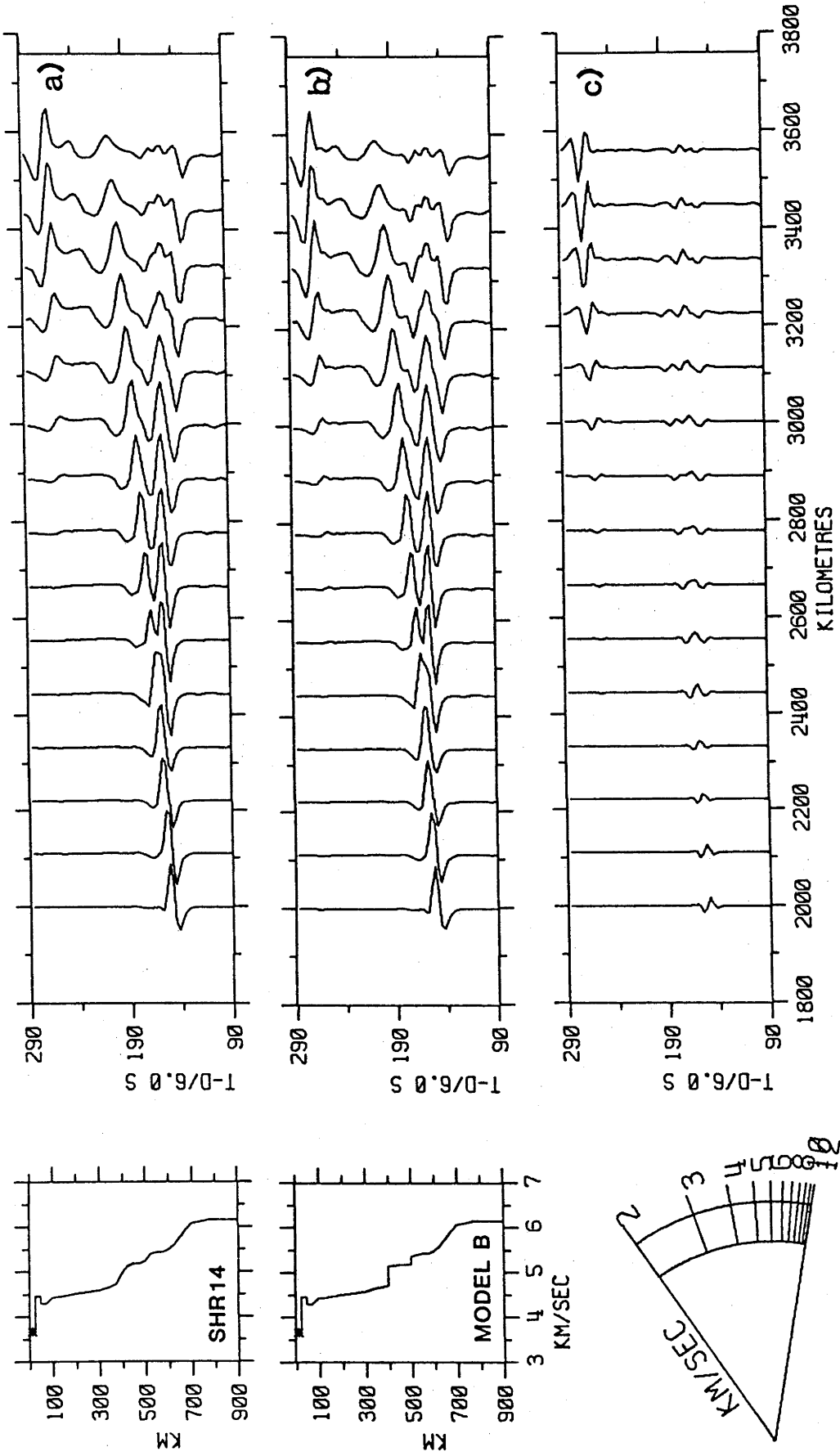


Figure 6.27: Synthetic SH seismograms for a) SHR14 and b) MODEL B. MODEL B has first-order discontinuities at depths of 400 and 530 km. Panel c) represents the differences of the traces in a) and b), with amplitudes plotted relative to the trace amplitudes in a).

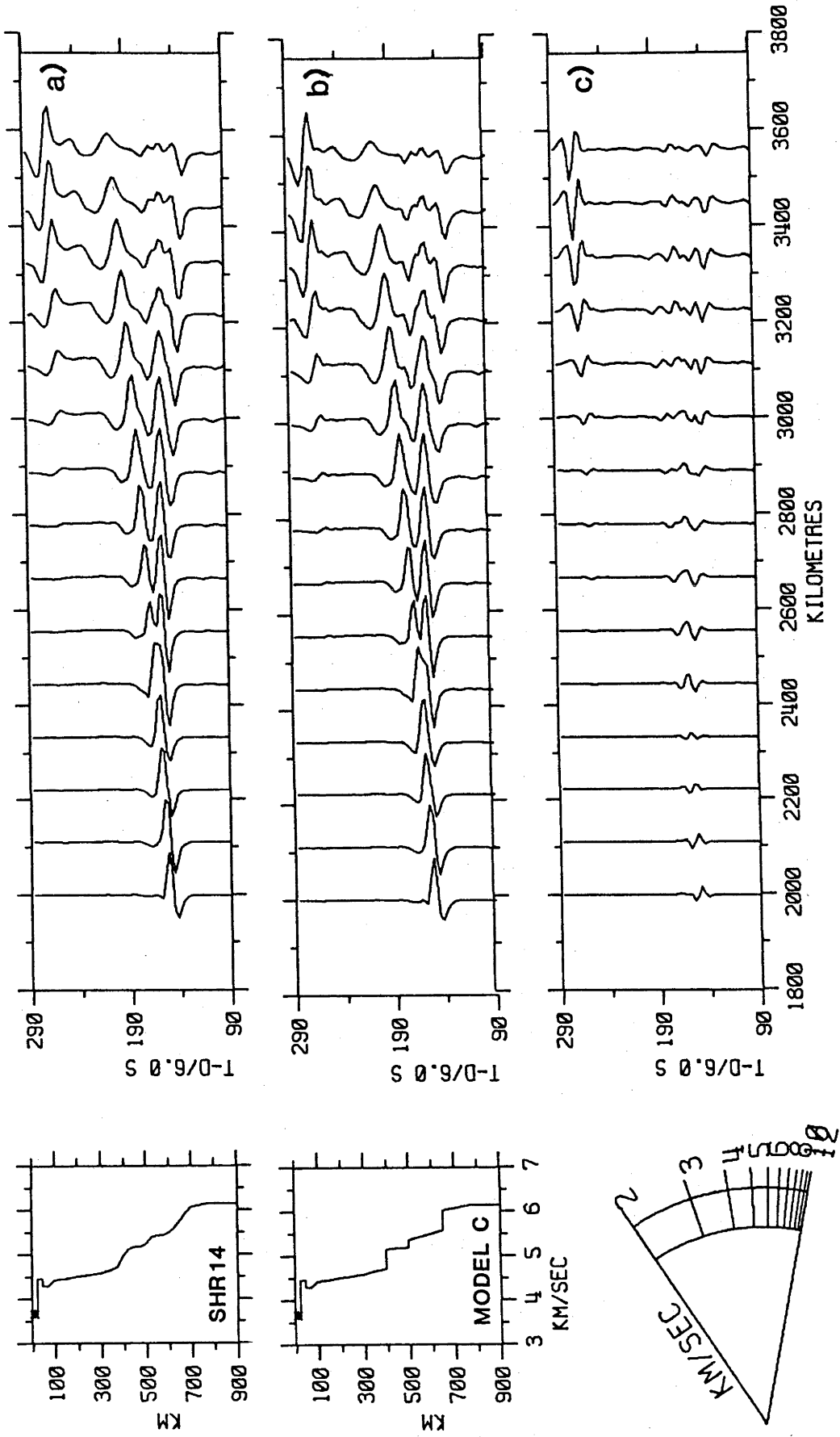


Figure 6.28: Synthetic SH seismograms for a) SHR14 and b) MODEL C. MODEL C has first-order discontinuities at depths of 400, 530 and 650 km. Panel c) represents the differences of the traces in a) and b), with amplitudes plotted relative to the trace amplitudes in a).

6.4.2 MODELLING SMALL DISCONTINUITIES

Recent studies of LP P waves have not been able to find conclusive evidence for the existence of small discontinuities such as the "500-km" discontinuity. For example, Burdick and HelMBERGER (1978) used a starting model which included a small discontinuity at 550 km. By waveform modelling of the first 25s of LP P-wave data, Burdick and HelMBERGER eliminated this discontinuity from their final model on account of the lack of evidence supporting its existence. Yet the "500-km" discontinuity has been reported in several studies (Wiggins and HelMBERGER, 1973; HelMBERGER and Engen, 1974; Jordan and Anderson, 1974; Ram Datt, 1977; Hales et al., 1980a; Hendrajaya, 1981) with an average velocity contrast of about 2%. A numerical study by Ha and Muirhead (pers.comm., 1982) show that on waveform considerations alone, LP data lack the resolving power to discriminate between models with and without small discontinuities such as the "500-km" discontinuity. As an additional exercise, their experiment will be repeated here for S waves but with the emphasis on amplitudes as well as waveforms.

Model D is constructed from model C, with first-order discontinuities at 425 and 675 km, but lacking in the discontinuity at 500 km. The differences in waveforms for models C and D are negligible as shown in Figure 6.29, however, the error time series show that there are important differences in amplitudes.

HelMBERGER and Engen (1974) explained very large amplitudes in the shear wave data near 20° as the interference of reflections from the "425-km" and "675-km" discontinuities, as well as a small triplication formed by a velocity jump near 500 km. Burdick and HelMBERGER (1978) used SP data to examine this feature, but were very doubtful of including the discontinuity in the final model on account of amplitude data alone. This suspicion should be passed over as well to LP data. As an example, amplitudes on the NORSAR LP records can vary by up to 20% across the array for a single event. For a regional network such as WWSSN as used by HelMBERGER and Engen, control on absolute amplitudes will not be very satisfactory. It would appear then that any analysis of LP data by seeking the simplest permissible structure would not include small discontinuities.

The preliminary analysis of the processed NORSAR data in Section 5.6 indicated the presence of a small discontinuity between the major discontinuities near 400 and 650 km, presumably the "500-km" discontinuity. The arrivals on the C branch are very small, and not obvious on the raw and

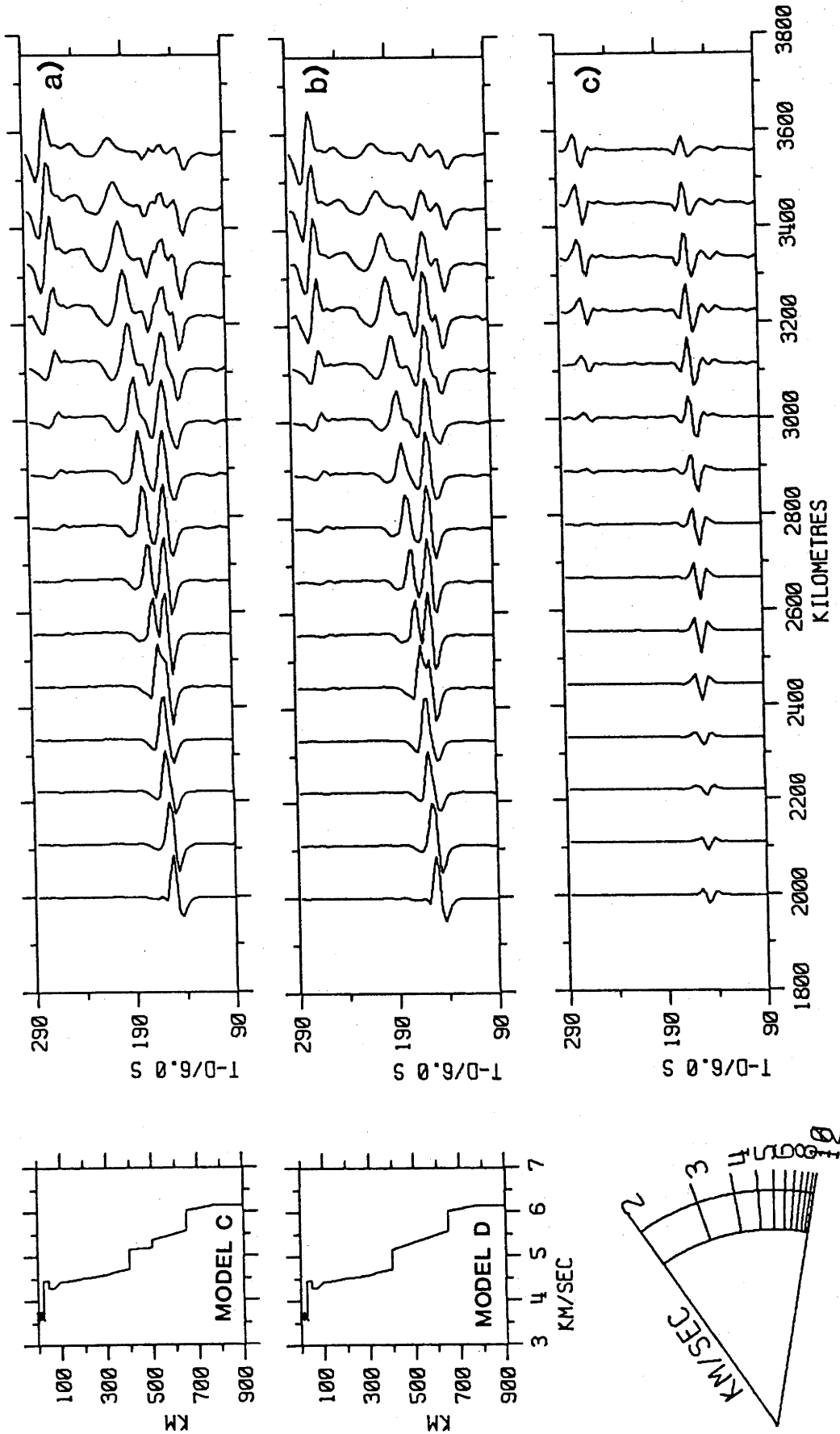


Figure 6.29: Synthetic SH seismograms for a) MODEL C and b) MODEL D. MODEL C has first-order discontinuities at 400, 530 and 650 km, and MODEL D has first-order discontinuities at 400 and 650 km. Panel c) represents the differences of the traces in a) and b), with amplitudes plotted relative to the trace amplitudes in a).

deconvolved data, however, iterative least-squares decomposition has enhanced arrivals on this branch. It is anticipated in this study that by using processed data, the presence of small discontinuities will be detected and delineated within the limitations imposed by the bandwidth of the deconvolved data. Indeed, because the smoothing effect of the instrument is the most degrading factor in obscuring small amplitude arrivals, Helmberger and Engen (1974), Burdick and Helmberger (1978), Given and Helmberger (1980), Burdick (1981) and Grand and Helmberger (1983) among others, may have resolved finer details in the velocity structure by removing instrumental effects from the data rather than convolving the instrument response with the synthetics.

6.4.3 THE MODELLING OF LOW-VELOCITY ZONES

In addition to the widely-observed low-velocity zone lying between 100 and 200 km, small "knee-like" structures, i.e., zones of high dv/dz underlain by a zone with a large negative gradient, have been suggested by Ram Datt (1977), Hales et al. (1980a), Leven (1980) and Hendrajaya (1981). With the exception of Leven, all these studies were of travel times and slowness. This feature was invoked to satisfy data that have very large amplitudes on the forward branch (understood to be rays bottoming in the region of high dv/dz) that decrease very rapidly with increasing epicentral distance (interpreted as the effect of the negative velocity gradient). The velocity contrast at the discontinuity below this feature must necessarily increase because of the negative velocity gradient, thus having the effect of shifting the apparent energy distribution on the retrograde branch to greater epicentral distances. Leven (1980) used Full Wave theory to model this structure, and found that synthetic SP seismograms are very sensitive to this type of structure. In addition, by carefully reinterpreting the data of Hales et al. (1980a) using synthetic seismograms, Leven (1980) eliminated the LVZ near 530 km in the CAP8 model, replacing it with a region of constant velocity gradients, and placed a small LVZ immediately below the "200-km" discontinuity.

It is therefore of interest to examine the effect of such features in velocity-depth profiles on LP synthetic seismograms. For this purpose, model E replaces the constant velocity gradient above the discontinuity at

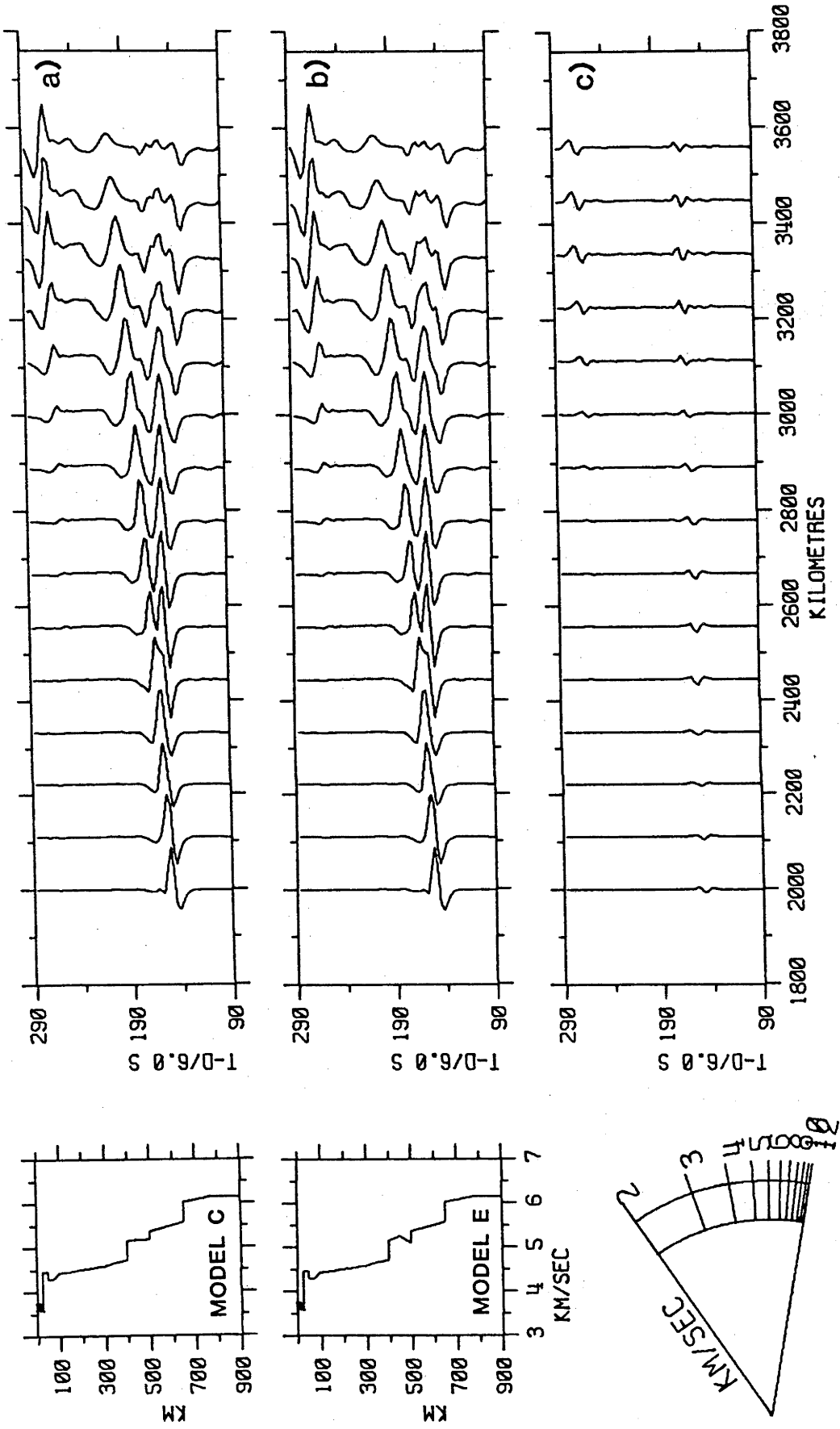


Figure 6.30: Synthetic SH seismograms for a) MODEL C and b) MODEL E. MODEL C has first-order discontinuities at 400, 530 and 650 km, and MODEL E has first-order discontinuities at 400 and 650 km, with a LVZ between them. Panel c) represents the differences of the traces in a) and b), with amplitudes plotted relative to the trace amplitudes in a).

500 km in model C with a "knee-like" structure, preserving the average velocity between the "425-km" and "500-km" discontinuities so as not to change the travel times. The synthetic seismogram (Figure 6.30) for models C and E show that the differences in waveform are not great, and that amplitudes on the error time series are small. This result is not unexpected for at the wavelengths under consideration, such features may not be "seen" by LP waves, and verifies in part an earlier proposition that the region lying between velocity discontinuities should be characterized by a constant or near-constant velocity gradient.

6.5 CONCLUSIONS

It is naive to expect any of the models under consideration to exactly represent the data. The reasons for this are clear: previous studies were either surface-wave or first- and second-arrival body-wave studies, whether timing or amplitude constrained. There has never before been any attempt to examine the entire body-wave train at these periods, even for SH. The data appear very complex, probably due to near-source structure and lateral heterogeneity. It is important to note that for models based on the same data set (e.g., IN and US26), observer bias markedly alters the character of the synthetic wave trains. In this and many other cases, travel time and slowness data of first arrivals do not constitute sufficient constraints for the purpose of generating reliable models. The clear identification of multiple reflections such as 2S400 enables much better constraints to be placed on the velocity contrasts and depth of the major mantle discontinuities.

The models and their corresponding synthetic seismograms fall into four categories:

- (1) Simple: JB, STAN 3, REDDOG-C, B1, MODEL 7, CNNS, EKW, NAT.
- (2) Intermediate: B1066, SHR14, PEM-C, PREM, S8, K8.
- (3) Complex: IN, US26, IN2, SHMEE, MA, KCA.
- (4) Very complex: SW-E, S2.

It appears that the complexity of the seismograms is proportional to the structure in the velocity-depth model. The data are apparently best modelled by the intermediate and complex structures, but considerable refinement is required before a realistic model can be presented. It is

important to recognize that small features in the velocity-depth models such as small velocity discontinuities and LVZ's will go unresolved in studies of LP waveforms. If however, the presence of such features can be ascertained by other methods such as data processing, small structures should be included in the final model. The final model should consist of first-order discontinuities, separated by regions of constant velocity gradients.

Although producing comparatively simple synthetics, the models SHR14 and PREM do constitute promising candidates for model refinement. Of course, some features from models considered as being complex must be incorporated into SHR14 and PREM so as to account for the C branch and make the structure of the later arrivals more realistic. It appears however, that with revision of the "435-km" and "600-km" discontinuities, the model SHMEE may represent the best starting model. Using these models as starting points, an S-wave model consistent with the data will be derived in Chapter 7.

CHAPTER 7

THE APPLICATION OF SYNTHETIC SEISMOGRAMS
TO THE INTERPRETATION OF LONG-PERIOD SH

7.1 INTRODUCTION

The previous chapter showed that there are serious inadequacies in using travel times and waveform analysis of LP first arrivals. Such studies smear fine details in the data, and may lead the interpreter to claim that fine structure does not exist because of the apparent absence of supportive data.

This situation can be improved by combining complete synthetic seismogram analysis with data processing such as deconvolution and iterative least-squares decomposition. Such processing will enhance interpretational subtlety of the entire body-wave train. The result is a velocity-depth model that is more complex than any model previously derived from LP data.

7.2 COMPLETE WAVEFORM MODELLING

For the purpose of this study, Chapter 6 suggested that with suitable modification, SHMEE would make an excellent starting model for further refinement.

As a first step to improving the model SHMEE, the suggestion of Chapter 6 regarding the positions and size of the "435-km" and "600-km" are considered. In order to improve the match between the apparent phase velocities of the S435 and D branch, and also to decrease the relatively large amplitudes on S435 at large distances, the "435-km" discontinuity was

raised to 400 km. This had the beneficial effect of decreasing the travel times and increasing the amplitudes of 2S400 (i.e., moving the critical-distance cusp, associated with large amplitude reflections, to smaller distances). Because this series of multiples have some of the largest relative amplitudes in the data, it was important to model them accurately at the expense of modelling multiples from shallow structure for which positive identification has not been obtained. 2S435 arrives about 140s after S on the synthetics for SHMEE (Figure 6.19). Raising the discontinuity changed the 2S400-S differential travel time to about 120s. This is an indication of the relative sensitivity of timing and amplitude of the multiples to changes in the model parameters.

The very large amplitudes about 50s after S between 2700 km (24.3°) and 3000 km (27°) for model SHMEE are due to constructive interference of S340 and S435. This interference has the effect of increasing the apparent period on these arrivals relative to the earlier arrivals. Raising the smaller discontinuity to 300 km moved the large amplitudes associated with the backward cusp to smaller distances. Increasing the depth of the lower-most discontinuity to 670 km shifted the cross-over from near 2280 km (20.5°) in SHMEE to near 2510 km (22.6°) with the consequence of increasing the travel time of the first arrivals beyond the cross-over. Unfortunately, amplitudes on the S670 branch increased relative to the low amplitude B branch arrivals, and resulted in a much higher apparent phase velocity. An important aspect of modelling this discontinuity was to ensure that the amplitudes on the S670 branch became negligible at distances beyond 3300 km (29.7°). Increasing the velocity gradient (dv/dz) above the "670-km" discontinuity decreased the velocity contrast across this feature, thus producing an acceptable match between the B and S670 branches for the distance range 2000 km to 3400 km (18° to 30.6°). The small amplitude second arrival at 2100 km (18.9°) was initially identified as the backward cusp of S670.

Synthetics for SHMEE in Chapters 2 and 6 show that the S530 branch extends with appreciable amplitude to distances beyond the 30° window. The apparent horizontal phase velocities for C and S530 agree. Decreasing the velocity contrast from 7% to 2% satisfies the amplitude constraint without imposing significant departure in the apparent phase velocity indicated by the spikogram travel times of the C branch. It must be emphasized that because there is no direct amplitude evidence for the "530-km" discontinuity at large distances, the structure being determined is the

largest that is consistent with the data.

Amplitudes on the S400 branch appear much larger near the end of the distance window than on the D branch. Decreasing the velocity contrast across the "400-km" discontinuity improved the fit with the D branch, but increased amplitudes on S530. To reduce these amplitudes, this discontinuity was raised to 500 km and the negative dv/dz immediately above it replaced with a positive dv/dz .

Due to the relative sensitivity of the multiple travel times to structure, positioning large amplitudes associated with the backward cusp of 2S300 and 2S400 was easy to achieve by slightly altering dv/dz and velocity contrast across the discontinuities, and so matching quite well the character of the arrivals in the vicinity of the G branch for distances beyond 2900 km (26°). Such small changes have little effect on the direct arrivals. It must be remarked that the largest multiples encountered in the synthetics are the 2S300 branch. These multiples are perhaps the most direct evidence for the "300-km" discontinuity and illustrate further the importance of identifying and using large amplitudes associated with critical (and sub-critical) distance multiple reflections. Increasing the depth to the lowermost discontinuity moved the critical cusp of 2S670 to several degrees beyond the data window, and so multiples from this discontinuity are not apparent in the synthetics.

The final task lies in modelling shallow structure, namely, the "200-km" discontinuity. At first, the relatively large amplitudes on the F branch from 2000 km to 2600 km (18° to 23.4°) were presumed to be multiple reflections from a discontinuity near a depth of 200 km. This would, however, imply that the backward cusp of S200 would lie near 900 km (8°) which seems too small. Furthermore, it is interesting to note that none of the synthetics presented in Chapter 6 (and Appendix 4) exhibit such a clear arrival. Without data at smaller distances, the exact nature of the Lehmann discontinuity and the F branch arrivals go unresolved in this study. Nevertheless, this structure has been retained because its presence has been inferred from P- and S-wave data in various parts of the world. Minor corrections were made to this discontinuity and dv/dz beneath it until a good match with the data at small distances was obtained.

The final model, SHME, is given in Table 7.1 and Figure 7.1. Synthetic SH seismograms spanning the distance range 2000 to 3600 km are presented in Figure 7.2, along with the corresponding geometrical ray travel times. The overall appearance of the synthetics now exhibits a complexity consistent

Table 7.1 SHME Velocity Model

Depth (km)	Velocity (km/s)
0	3.69
40	3.69
40	4.35
200	4.22
200	4.56
300	4.47
300	4.75
400	4.45
400	4.95
500	4.95
500	5.05
670	5.45
670	5.90
750	6.10
(750)	(6.30)

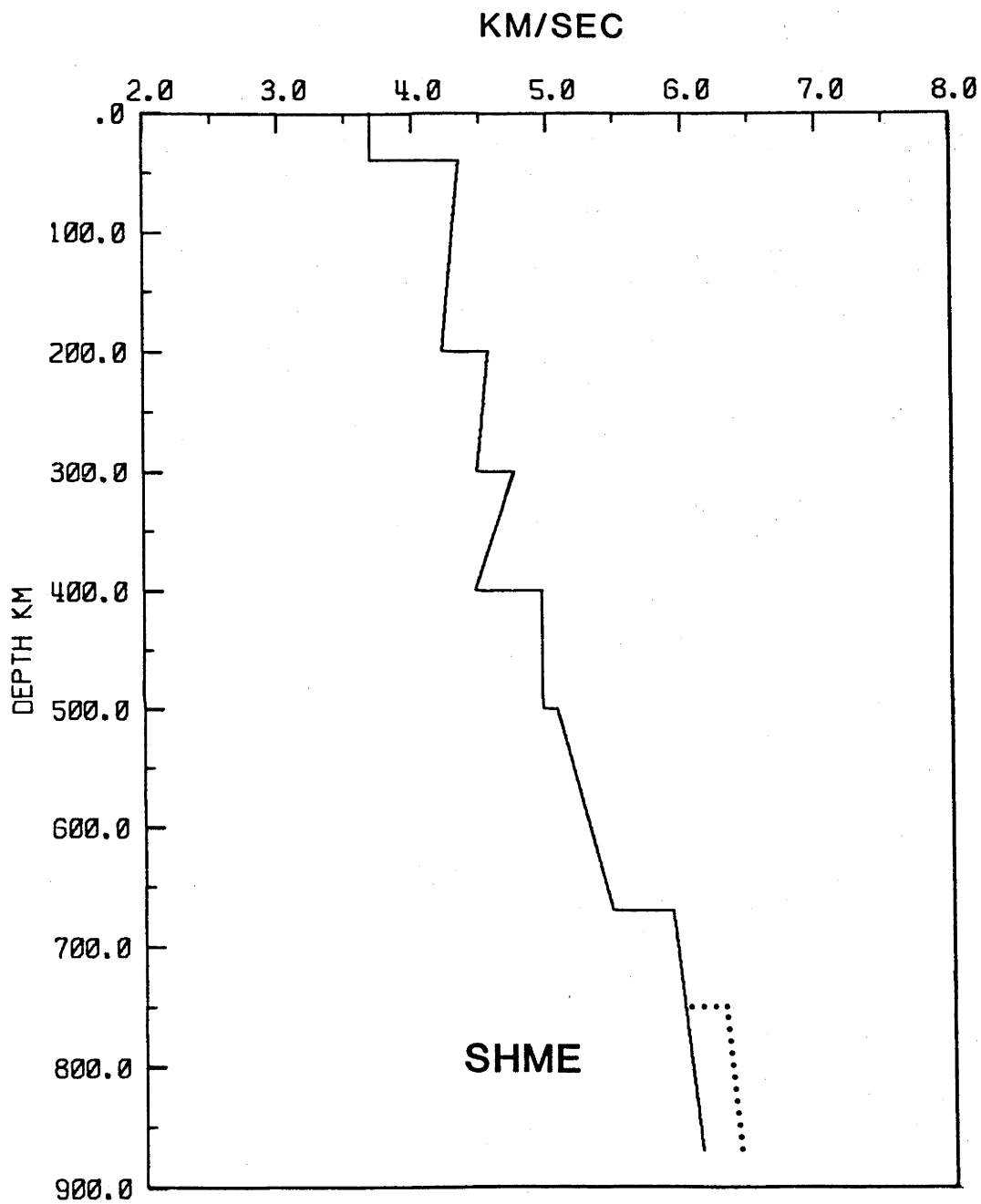


Figure 7.1: The SHME shear-wave velocity-depth model. Dotted curve indicates possible structure near 750 km.

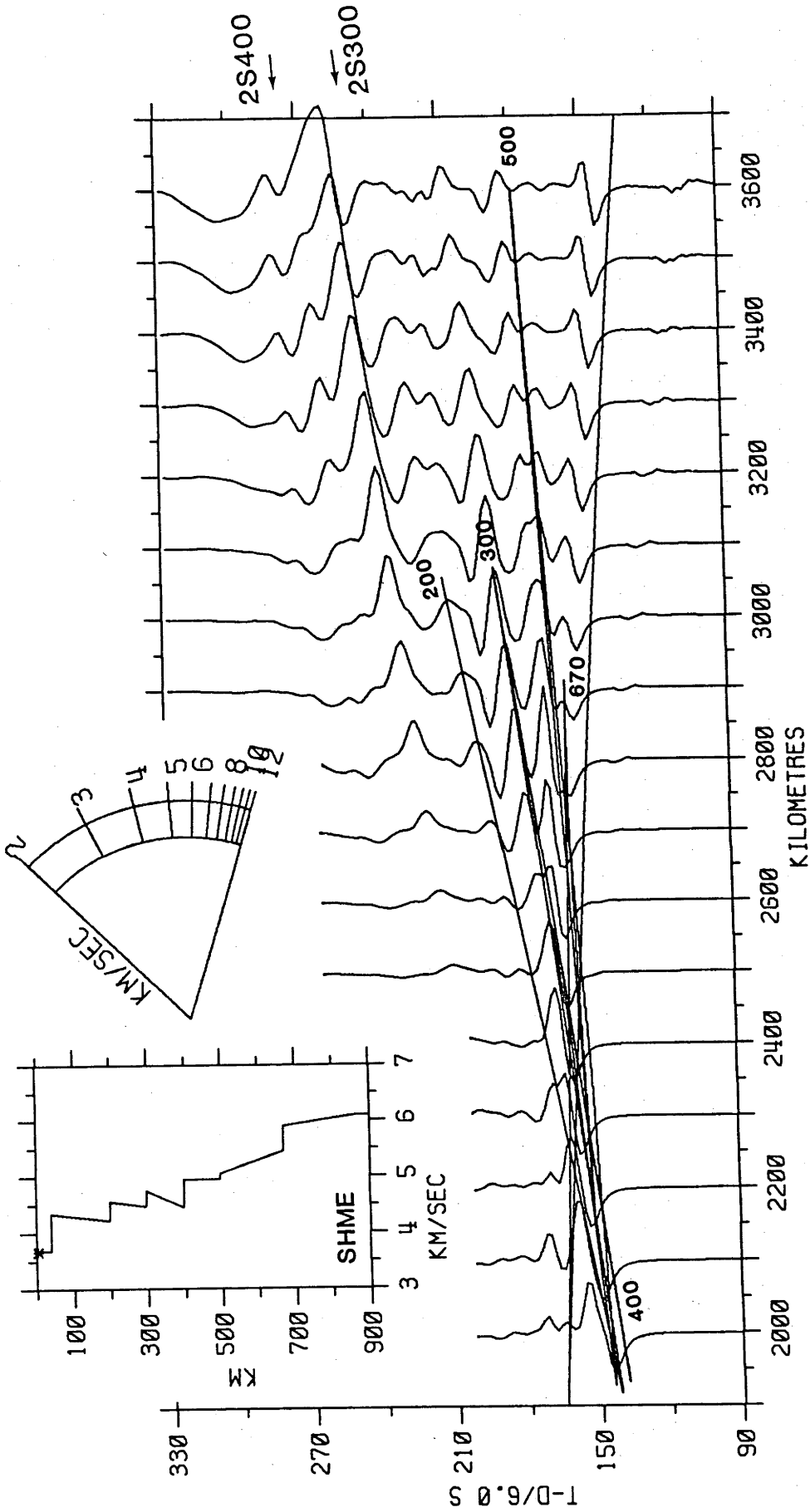


Figure 7.2: Synthetic SH seismograms for the SHME model. Caption as given by Figure 6.2. This figure should be compared with Figure 5.9. A transparency of this figure is provided in a pocket at the rear of this thesis.

with the data. With the transparent overlay supplied at the end of this thesis, the trace for trace fit of synthetics with data is surprisingly good considering the degree of scatter in the data.

To counter any suggestions that the choice of starting model (SHMEE) determined the form of the final model SHME, other starting models were used. Chapter 6 indicated that SHR14 and PREM would constitute reasonable starting points for independent refinement. Section 6.4.1 showed that the sharp transitional velocity zones in SHR14 could be replaced by first-order velocity discontinuities. Using both Model C and PREM, the first step lay in modelling the D branch. It quickly became apparent that a negative velocity gradient above a discontinuity with large velocity contrast placed near 400 km depth was the simplest structure consistent with the general character of the D branch. To further improve the fit with the D branch, and more importantly, to simulate the appearance of the multiples near the G branch, an additional discontinuity had to be placed near a depth of 300 km. To satisfy the appearance of the C branch in the spikograms, a discontinuity had to be placed near a depth of 490 km in the PREM model. Final alterations to velocity gradients and discontinuity contrasts and depths in order to match apparent phase velocities and amplitudes of the presumed branches ultimately led to a model almost indistinguishable from SHME. Thus, a considerable degree of confidence may be placed in the structure SHME.

7.3 INTERPRETATION

7.3.1 THE "200-KM" DISCONTINUITY

The structure above 200 km has been inferred from PREM, a globally averaged model. However, different refraction studies have indicated substantially differing depths for the Lehmann discontinuity (Simpson, 1973). Hales (1976) and Anderson (1979a,b) have suggested that this feature represents a zone of decoupling between the lithosphere and the underlying mantle based on the association of LVZ's in the depth range 100 to 200 km with tectonically active regions. However, any significant topography on the Lehmann discontinuity would be expected to impede possible plate motions. Further studies of the regional variations in the depth of this

discontinuity are needed to clarify this point, as the existence of topographic coupling would suggest that the mantle material below this discontinuity must convect at a rate similar to that of the lithospheric plates.

The low-shear velocity zone is believed to be caused by partial melting along the grain boundaries (Anderson and Sammis, 1970), although Goetz (1977) noted critical petrological experiments to verify this idea have yet to be performed, and that other mechanisms may well play an important role. The apparently abrupt onset of the LVZ observed in many studies of short-period data (e.g., Wiggins and HelMBERGER, 1973; Hales et al., 1980a) is difficult to explain in terms of partial melting, which one would intuitively expect to have a more gradual onset. Other variations in physical properties in this region such as transverse anisotropy (Dziewonski and Anderson, 1981) are probably the result of chemical zonation and/or mineralogical transformation and alignment. Ringwood (1975) argues that no phase transformations in the constituent minerals of the pyrolite model have been observed in the pressure range appropriate to depths between 150 and 330 km, preferring a chemical change from a peridotitic composition depleted in its low-melting point components to a primitive pyrolite composition. Liu (1980a) explains this structure as the lower pressure boundary of the transition between pyroxene and garnet (solid-solution) components of a pyrolite model. However, Liu's phase change at this depth requires a temperature of 1600°C - significantly higher than the 1300°C current thermal models would indicate (Graham and Dobrzykowski, 1976; Stacey, 1977) and higher than the estimated solidus of pyrolite at this depth (Ringwood, 1975). Anderson (1979a) ascribes the Lehmann discontinuity to the compositional change from peridotite to eclogite. Proposals for phase and chemical transformations have been criticized by Leven et al. (1981), who claim that the ensuing velocity contrast is not sufficient to satisfy the observed discontinuity. They suggest that this feature may be explained in terms of seismic velocity anisotropy associated with deformation induced preferred orientation of olivine (and possibly pyroxene) crystals, and is responsible for decoupling of the continental lithosphere from the underlying mantle. In a series of north-south and east-west experiments, Hendrajaya (1981) concluded that seismic anisotropy is not appropriate to explain the seismic velocities at a depth of about 200 km under the Australian continent. Clearly, the reason for the existence of this discontinuity has not yet been established

with certainty. Although the distance range of events in this study contained no amplitude evidence for the "200-km" discontinuity, it is envisaged that the strategy as used in this thesis employed at distances appropriate to the critical-distance cusps of the multiples from shallow structure would be of considerable importance due to the relative sensitivity of the multiples to changes in structure.

7.3.2 THE "300-KM" DISCONTINUITY

The "300-km" discontinuity poses some difficulties in its seismological interpretations. For shear-wave travel-time studies in the distance range 20° to 22° , the prograde S-refraction branch corresponding to the "300-km" discontinuity should constitute the first arrivals for considerably larger observational distances than the corresponding P travel-time branches (Hendrajaya, 1981), so it is surprising that this structure has not often appeared in previous short-period S-wave studies. A possible explanation for the transitional nature of the observations of these refraction branches is that a small amount of topographic relief on the discontinuity scatters the refracted energy of the corresponding branches, and this scattered energy may or may not be observed.

The "300-km" discontinuity is not a minor structure, entailing a velocity contrast of 6% in SHME which is similar to a value of 7% as determined by Hendrajaya (1981).

Ringwood (1975) explained that this structure marks the transformation of an Al-rich pyroxene to garnet. Akaogi and Akimoto (1977) found that the rapid increase in density of this phase transformation occurs near 17 GPa (170 kbars), and therefore would be associated with a discontinuity nearer 500 km depth.

7.3.3 THE "400-KM" DISCONTINUITY

Adherents of the pyrolite model interpret the "400-km" discontinuity as the transformation of olivine (α) to the beta structure (β). Akaogi and Akimoto (1979) suggest that the transformation $\alpha + \text{spinel}(\gamma) \rightarrow \beta$ through $\alpha + \beta$

stages along a geotherm of $1^{\circ}\text{C}/\text{km}$ would span the depth range 380 to 410 km. Of course, any study of LP data would be unable to determine the depth range over which the transition takes place. By increasing the amount of magnesium, it is possible that α may transform directly to β without the intermediate $\alpha+\gamma$ stage, the reaction taking place some 10 to 20 km deeper, and the total transition interval would be quite small - perhaps about 10 km (Ringwood, 1975). In terms of the present eclogite model (Anderson, 1979b), the "400-km" discontinuity represents the high pressure boundary of pyroxene and garnet solid-solutions transforming to a single phase garnet solid-solution. Liu (1979a, 1980b) has shown that this reaction is smeared out over 10 to 17 GPa (100 to 170 kbars) and that the transformation effectively occurs at depths of about 570 km. Furthermore, Liu showed that the zero-phase density change for this reaction is only 3 to 4% in the pressure range 14 to 17 GPa (140 to 170 kbars), which is too small to explain the observed changes in density (about 11% for SHME). Furthermore, the velocity increase of 0.5 km/s is considerably larger than the predicted value for the olivine \rightarrow γ -phase \rightarrow β -phase reaction which is about 0.28 km/s for the S-wave velocity (Ringwood, 1975).

The extraordinary size of the "400-km" discontinuity and efficiency with which energy propagates along the retrograde branch argues against significant scattering at this depth. However, it is difficult to reconcile having topographic relief on the "300-km" discontinuity, without postulating some corresponding relief as the "400-km" discontinuity, if the topography is the result of convection. If the "300-km" discontinuity is due to the pyroxene to garnet transformation, local variations of Al content at this depth could be responsible for topography on this discontinuity, whereas this would not effect the olivine to β structure transformation associated with the "400-km" discontinuity.

7.3.4 THE "500-KM" DISCONTINUITY

In terms of a pyrolitic mantle, the "500-km" discontinuity may be characterized by the β to γ phase transformation. Ringwood (1975) estimates that this transformation is accompanied by a density increase of 2%, and in view of the relative pressure insensitivity of shear velocity compared with compressional velocity in the spinel structure (Burdick and

Anderson, 1975), this structure could be transparent to shear waves, thereby generating serious doubts as to whether this could be seismically observed as a discontinuity by a study of shear waves. Furthermore, Akaogi and Akimoto (1979) show that due to uncertainties in the partitioning of Fe^{2+} - Mg^{2+} , this reaction may lie anywhere between 500 and 600 km. Yet this discontinuity has been clearly observed by this study and the shear-wave study of Hendrajaya (1981). Ringwood (1975) proposes the additional minor reactions of a Ca-rich garnet to perovskite, and diopside to perovskite, which accounts for a shear-wave velocity increase of about 0.06 km/s. In addition to the $\beta \rightarrow \gamma$ transformations, Akaogi and Akimoto (1977) and Liu (1977b) suggest that this discontinuity is the high-pressure boundary of the pyroxene to garnet transformation but that this boundary is relatively gradual, being achieved over a pressure interval of 7 GPa (70 kbars). This may explain why this transformation is not clearly observed in the seismic sections. Anderson (1979b) has recently proposed for the eclogite model a garnet to ilmenite transformation at this depth. Liu (1980b) claims that the zero-phase density change for this reaction is 7%, which is greater than current seismic models and this study indicate. Given the petrological input, it is difficult to say which transition (one, both, or all three) is responsible for the discontinuity feature at a depth near 500 km.

7.3.5 THE "670-KM" DISCONTINUITY

Ringwood (1975) interpreted this structure in terms of phase transitions of γ to stishovite, and components of a complex garnet solid-solution to ilmenite plus perovskite. Liu (1977b) explained this feature as a superposition of the decomposition of γ to perovskite plus rock salt and the transformation of garnet to ilmenite. Alternatively, Anderson (1979b) suggested that this discontinuity is the lowermost termination of the proposed eclogite mantle which commenced at the "200-km" discontinuity and terminated by the broad stability field of garnet. However, Liu (1979b) stated that the "670-km" discontinuity is not related to any of the equilibrium phase boundaries observed in olivine, pyroxene and garnet. Instead, Liu suggested a chemical transition from olivine (\pm garnet) above the boundary to a denser perovskite (\pm garnet) mantle below, basing his argument on the broad pressure-temperature fields that these

phase transformations occupy, and the gravitational instability of the decomposition products of γ , claiming that the denser perovskite will tend to sink and stay in the deeper part of the mantle.

It is unlikely that the phase transformations will occur at the same depth, and there is evidence to support that the "670-km" discontinuity is in fact a series of structures distributed over a depth range of up to 35 km (Hales et al., 1980a; Leven, 1980). LP waves will not be able to discriminate between this complex feature and a simple first-order discontinuity. On the other hand, if the "670-km" discontinuity represents a chemical change, then it may also represent a barrier to mantle convection, implying the need for at least a two cell structure in mantle convection models. For such a system, the region immediately above the "670-km" discontinuity will have a high thermal gradient thus causing a decrease in the elastic moduli. On the other hand, the geopressure condition requires that for stability, density increases with increasing depth. As a result, the seismic velocities above this discontinuity will have a negative gradient. The effect of this will be to produce large amplitudes on the retrograde branch, and the forward cusp will extend to large distances. This is clearly not the case with the data, where the amplitudes on the S670 branch are seen to terminate near 3200 km (28.8°). Yet some studies (Hendrajaya, 1981) claim extensions of this branch up to 42°. The exact nature of this discontinuity is therefore in question, although there can be little doubt of its existence due to the manner in which it manifests itself in many independent data suites.

7.3.6 STRUCTURE BELOW THE "670-KM" DISCONTINUITY

The present data provide no control over the form of the velocity profile below 670 km, apart from the fact that a near constant gradient is suggested in order to explain the small amplitudes on the prograde "670-km" branch. The sudden increase in relative amplitude of the first arrivals near 3400 km (30.6°) may indicate the presence of a cusp arising from a discontinuity below the "670-km" discontinuity. As with the "200-km" discontinuity, structure deeper than the "670-km" discontinuity is not constrained by comparison of the synthetic seismograms with the data, and a velocity increase may be arbitrarily located near 750 km. The "750-km"

discontinuity has been observed in previous studies, notably Hales et al. (1980a), Leven (1980) and Hendrajaya (1981). Ram Datt and Muirhead (1977), using the Warramunga Seismic Array, have also found evidence for this discontinuity, although they have modelled it at greater depth.

Liu (1977b, 1980a) has suggested for this discontinuity the transformation of Al-rich ilmenite-type solid-solution to orthorhombic perovskite structure, although this interpretation implies that the "670-km" discontinuity is not a chemical change. Alternatively, if the "670-km" discontinuity represents a chemical change with spinel (\pm garnet) above and rock salt below, then the "750-km" discontinuity may be a chemical change from rock salt to perovskite. Yet another explanation is that the region between the "670-km" and "750-km" features is a zone of mixing between the spinel and perovskite mineralogies. Clearly, as the geophysical and geochemical constraints of any feature become less restrictive with increasing depth, the number of possible explanations of any feature grows.

7.4 DISCUSSION

7.4.1 THE MODEL SHME

The outstanding anomaly with SHME are the uniformly low mantle velocities. The S-wave velocities of SHME are up to 5% slower than equivalent models (c.f. Figure 2.5). This arises from assuming that the data have JB travel times. A comparison of the JB and SHME mantle velocities show that they have similar average velocities. Altering the velocities by a constant percentage has the effect of rotating the travel-time curves. To see if this has any effect on the waveforms and amplitudes, the mantle velocities of SHME were increased by 5% to generate model SHME'. Comparing the data and synthetics for SHME with the synthetics for SHME' in Figure 7.3 show that negligible changes in waveform and amplitudes have occurred. This implies that this study has no control over absolute velocities, but that location and relative size of the discontinuities, and dv/dz between the discontinuities are well-constrained by the data. It is thus possible to require the S-wave travel times of the events to lie on some arbitrarily faster travel-time curve such as CNNS,

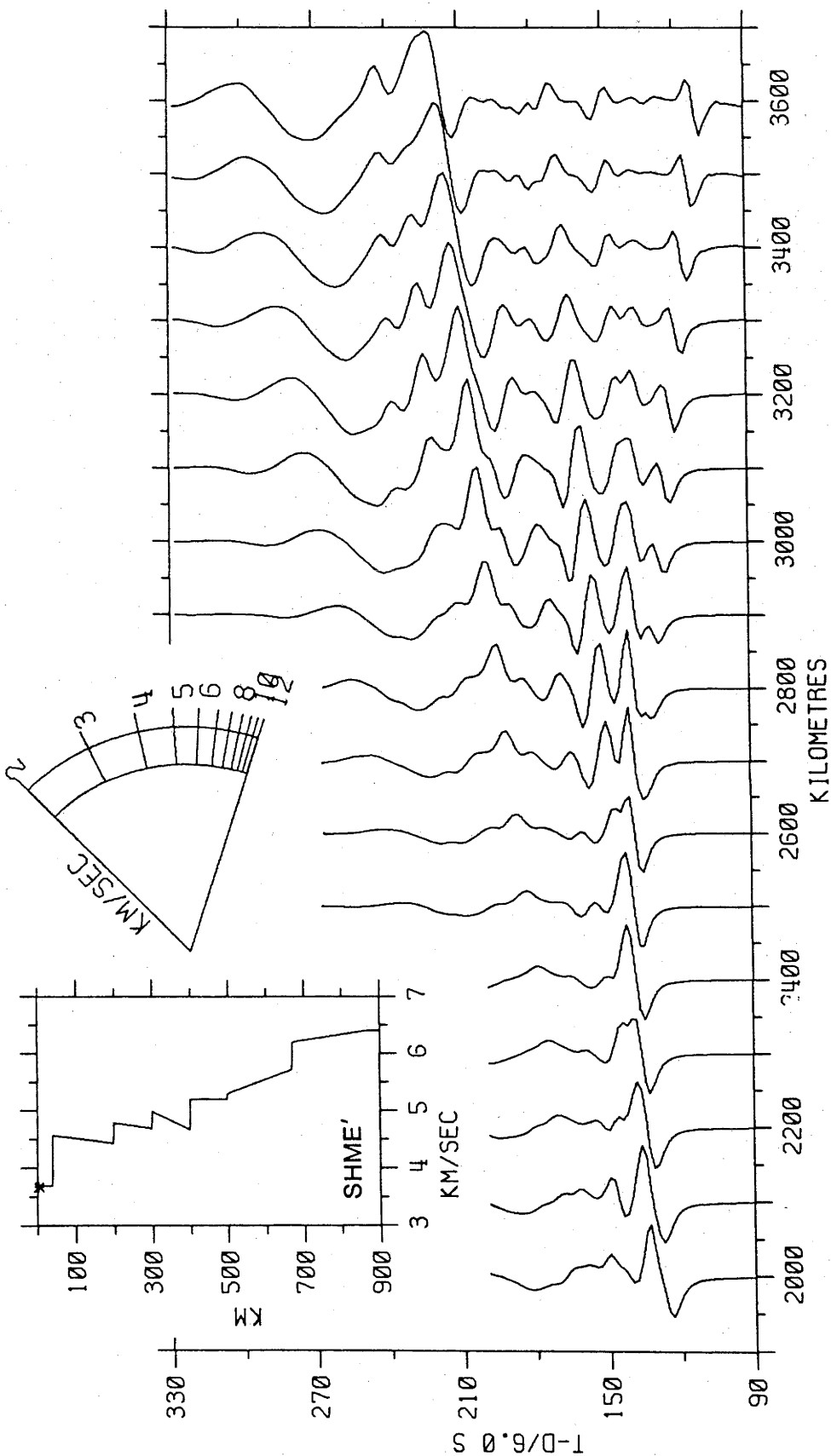


Figure 7.3: Synthetic SH seismograms for the SHME' model. Caption as given by Figure 6.2. Increasing the velocities of SHME by 5% has rotated clockwise the travel times of the synthetics for SHME' relative to the synthetics of SHME (Figure 7.2).

and the average velocity of SHME may then be accordingly increased and still maintain a close fit between synthetics and data.

It is stressed that throughout this study, absolute travel times could not be used on account of source mislocation errors. Travel time is a broad integral property of a model, while the theoretical waveforms of synthetics for a particular model depend more strongly on its fine structure. This is particularly true with regard to the uppermost 250 km - where structural variations can impart considerable differences in first arrival travel times between synthetics for the model under consideration and a reference model. Since epicentre location and origin time of the Mediterranean and North Atlantic events were based on JB travel times, the absolute travel times may have systematic errors of several seconds, and thus cannot be controlled in this study.

7.4.2 WAVEFORM INVERSION

A formal inversion scheme is not applicable in this study because the necessary quantity of quality travel-time and slowness data are not available from the limited set of LP data used in this study. In addition, formal inversion schemes do not give an appreciation of how structure manifests itself in seismic data, and requires an initial starting model which may or may not converge to a solution. Mellman (1980) used an iterative inversion method to determine velocities as a function of depth using waveforms of far-field body-wave seismograms. Mellman's method, however, makes use of the first arriving reflected and refracted arrivals as calculated by the Modified First Motion method of Mellman and Helmberger (1978). The inversion is accomplished by minimising an error function that expresses the difference between data and synthetic seismograms. This error function is constructed to be insensitive to absolute amplitude and travel times, and is thus a measure of waveform error only. As such, and because an initial starting model must be specified for the inversion, this method is not a significant improvement on trial-and-error waveform modelling. The extension of this technique of waveform inversion using the entire wave train and eliminating the need for a starting model (i.e., finding a solution directly rather than iteratively as advocated by Ingate, 1983, Appendix 3) is beyond currently available numerical techniques.

The remainder of this section will discuss the application and results of alternative data analysis strategies.

7.4.3 ALTERNATIVE MODELS

To compare the results of the analysis strategy proposed in this thesis with other methods of LP data analysis, velocity-depth models were derived from travel-time data alone and a combination of travel times and first-arrival waveforms. The latter strategies have been widely used in the literature, and the results from some studies have been described in Chapter 6.

In the first case, the relative travel times corresponding to the arrivals on the A, B and D branches were estimated from the deconvolved data. The spikogram data was not used because such processing is not consistent with the approach taken by earlier studies such as Ibrahim and Nuttli (1967). Geometrical ray theory was used to determine travel-time branches that approximated the estimated arrival times. The final model (Table 7.2, Figure 7.4) has first-order discontinuities at depths of 400 and 690 km. The structure above 220 km is a synthesis of PREM and the crustal model given in Chapter 1. The travel times (Figure 7.5) appear to satisfy the location of the D cusp beyond 3400 km (30.6°), and the B cusp near 3200 km (28.8°). The synthetic seismograms have been superimposed on the travel-time branches, and show that the travel-time study has underestimated the distances to the forward cusps (associated with relatively low amplitudes) predicted by the synthetics.

The second step in this comparison used waveforms of first arrivals. In order to satisfy the complex interaction near 24° , the lowermost discontinuity had to be placed at a depth of 650 km. The need to alter the depth to this discontinuity by 40 km bears upon the problem of estimating travel times from LP data. Such estimates may be in error by up to 2s, with consequential errors in location of the cross-over near 24° . Estimates of onset times of second arrivals will be even less reliable because of the disturbance caused by the first arrival.

Another important difference between the models obtained by these two methods is that for structure below 220 km, the average mantle velocity of the second model is 4% less than the first model. To complement this

Table 7.2 Velocity models derived from travel times and waveforms of first arrivals

Model 1 [*]		Model 2 ⁺	
Depth (km)	Velocity (km/s)	Depth (km)	Velocity (km/s)
0	3.69	0	3.69
40	3.69	40	3.69
40	4.67	40	4.50
220	4.35	220	4.35
220	4.78	220	4.50
400	4.83	400	4.60
400	5.10	400	4.90
690	5.50	650	5.40
690	6.20	650	6.00
870	6.31	870	6.10

* Derived from travel times of first arrivals alone.

+ Derived from travel times and waveforms of first arrivals.

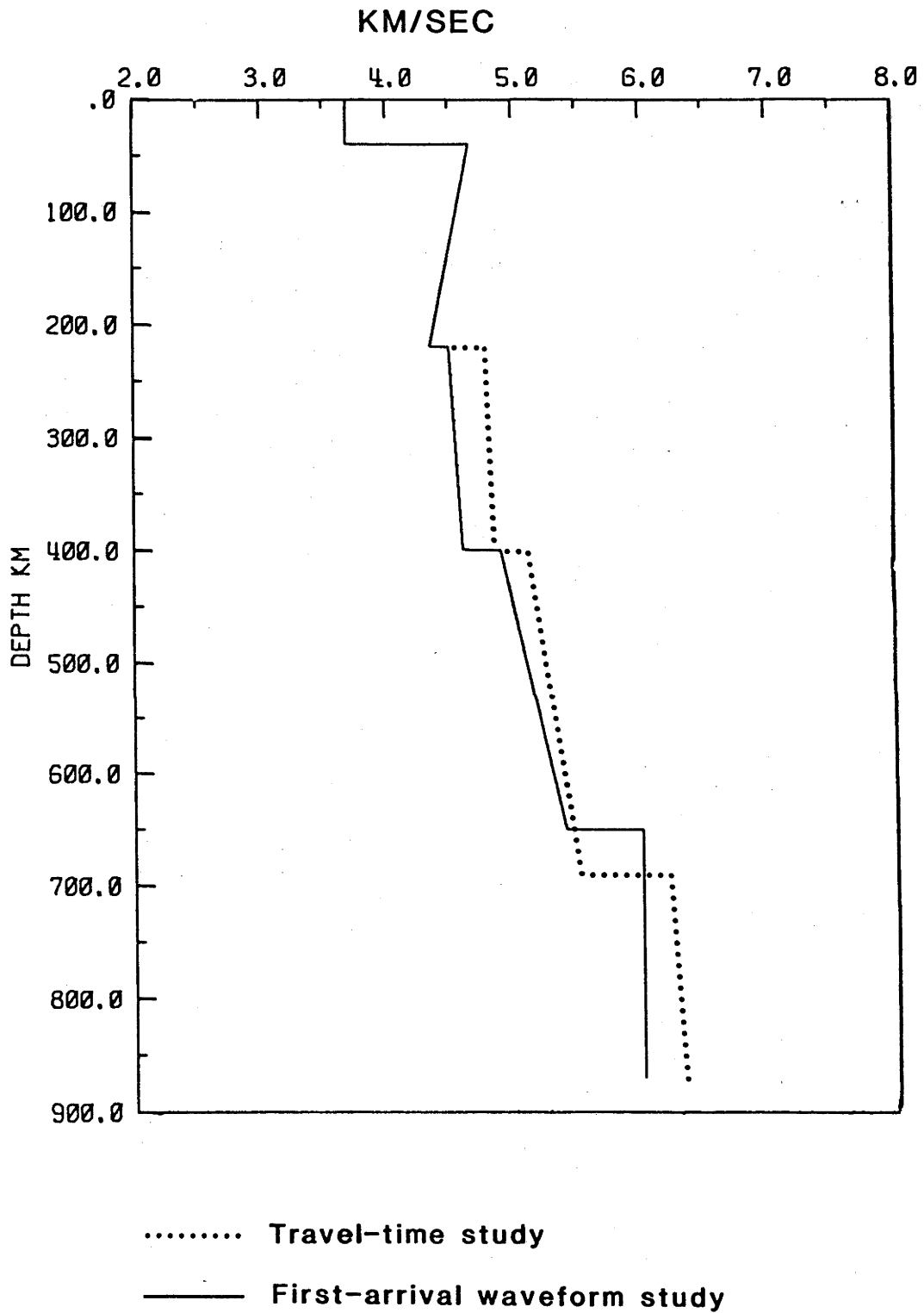


Figure 7.4: Shear-wave velocity-depth models determined using travel-time data alone (dotted line) and first-arrival waveform data (solid line).

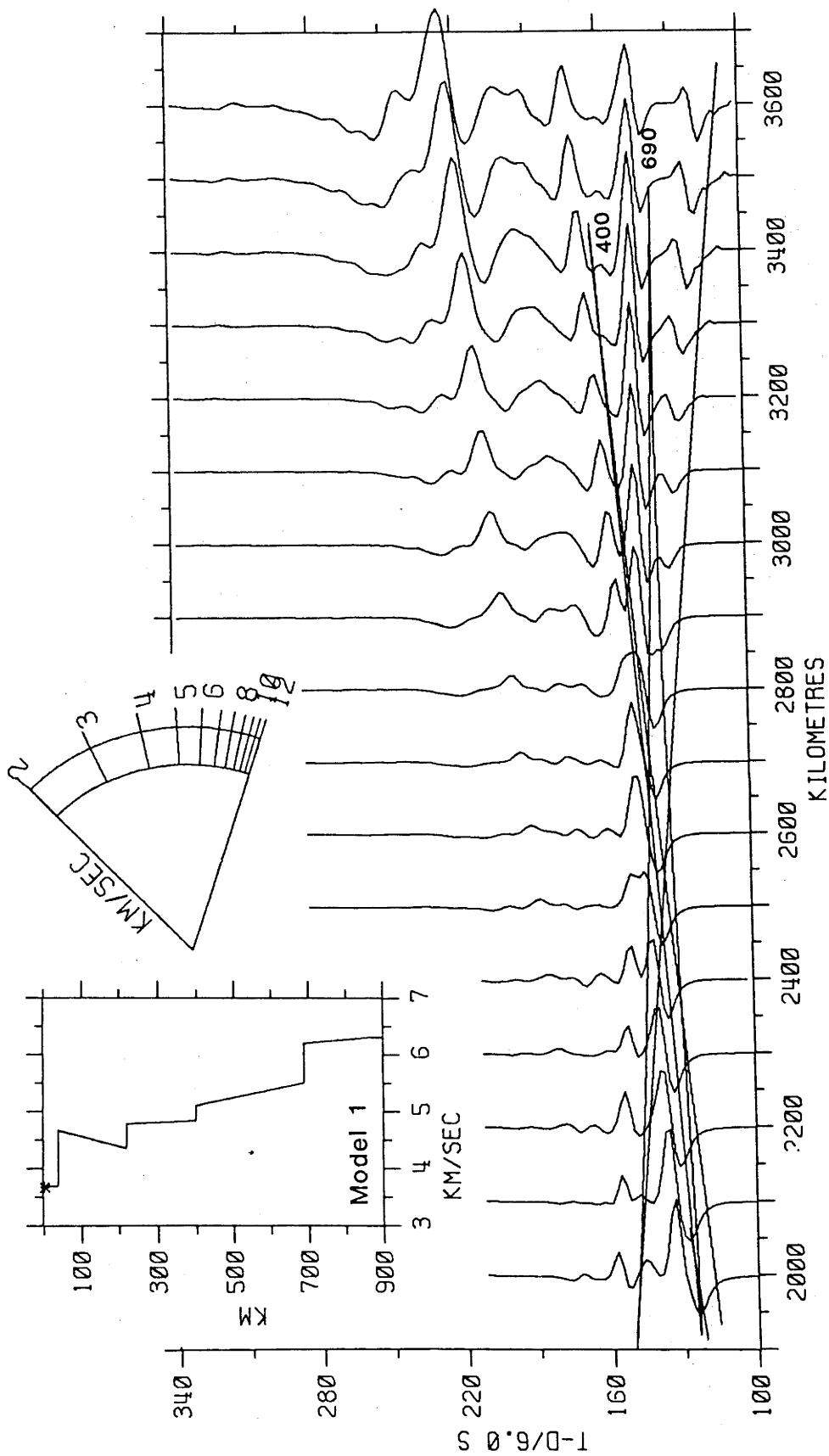


Figure 7.5: Synthetic SH seismograms for the shear-wave-velocity model derived from the travel-time data alone. Caption as given by Figure 6.2.

decrease in average velocity, the velocity contrast at the Moho of the second model was decreased by 4%. The reason for the apparently slow mantle velocities has already been covered. The final model is given in Table 7.2 and Figure 7.4. A direct comparison of the first 60s of the synthetics with the data are given in Figure 7.6. The fit is at least as good as has been obtained in previous waveform studies such as given by Given and Helmberger (1980), Figure 7 (c.f. Helmberger and Engen, 1974; Burdick and Helmberger, 1978; Burdick, 1981). Some discrepancies in waveform are apparent, although an equivalent study would probably attribute these to source estimation problems and scatter in the data rather than the assumption of an oversimplified model. As such, a similar degree of confidence can be placed in this second model as in the models SHR14, K8 and S8. However, the 60s window seems unnecessarily narrow and would exclude secondary arrivals except in the vicinity of a cross-over. An essential difference between this study and previous waveform studies lies in the use of deconvolved data. The expansion of bandwidth has made the modelling more difficult because subtle features of both synthetic and recorded data will not be smeared by the instrument response.

The complete synthetic seismograms and travel times for the second model are given in Figure 7.7. As expected, the character of the synthetics are remarkably simple, like that of Figure 7.5 and do not describe the data nearly as well as the synthetics for SHME (Figure 7.2). Clearly, simple models are derived from simplistic studies, and inadequately describe the S-wave velocity structure in Europe.

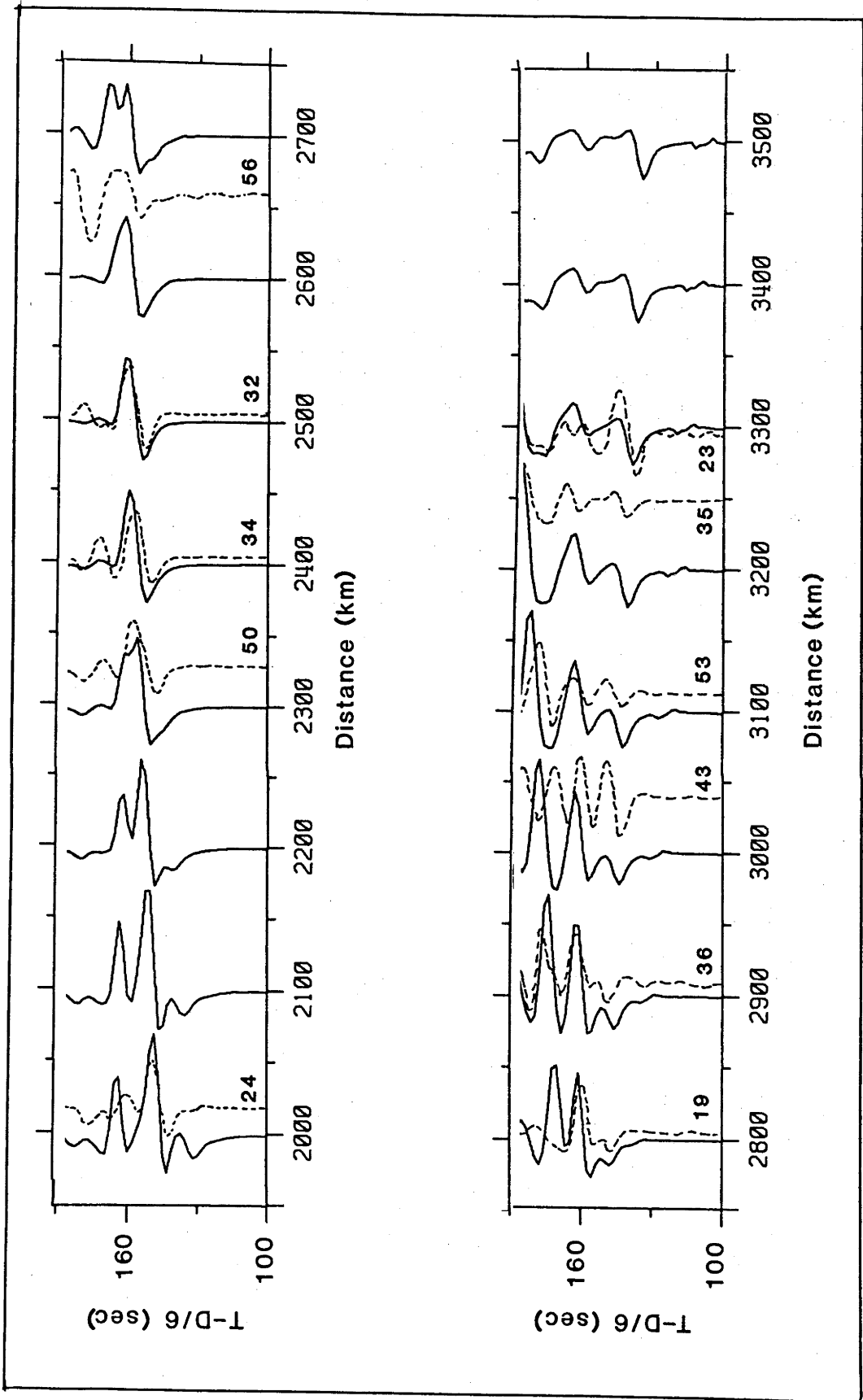


Figure 7.6: Comparison of first 60s of select deconvolved and stacked data traces (dashed lines) with strike-slip surface-focus synthetic SH seismograms for the model derived from first arrivals alone. Traces are normalized to peak amplitude.

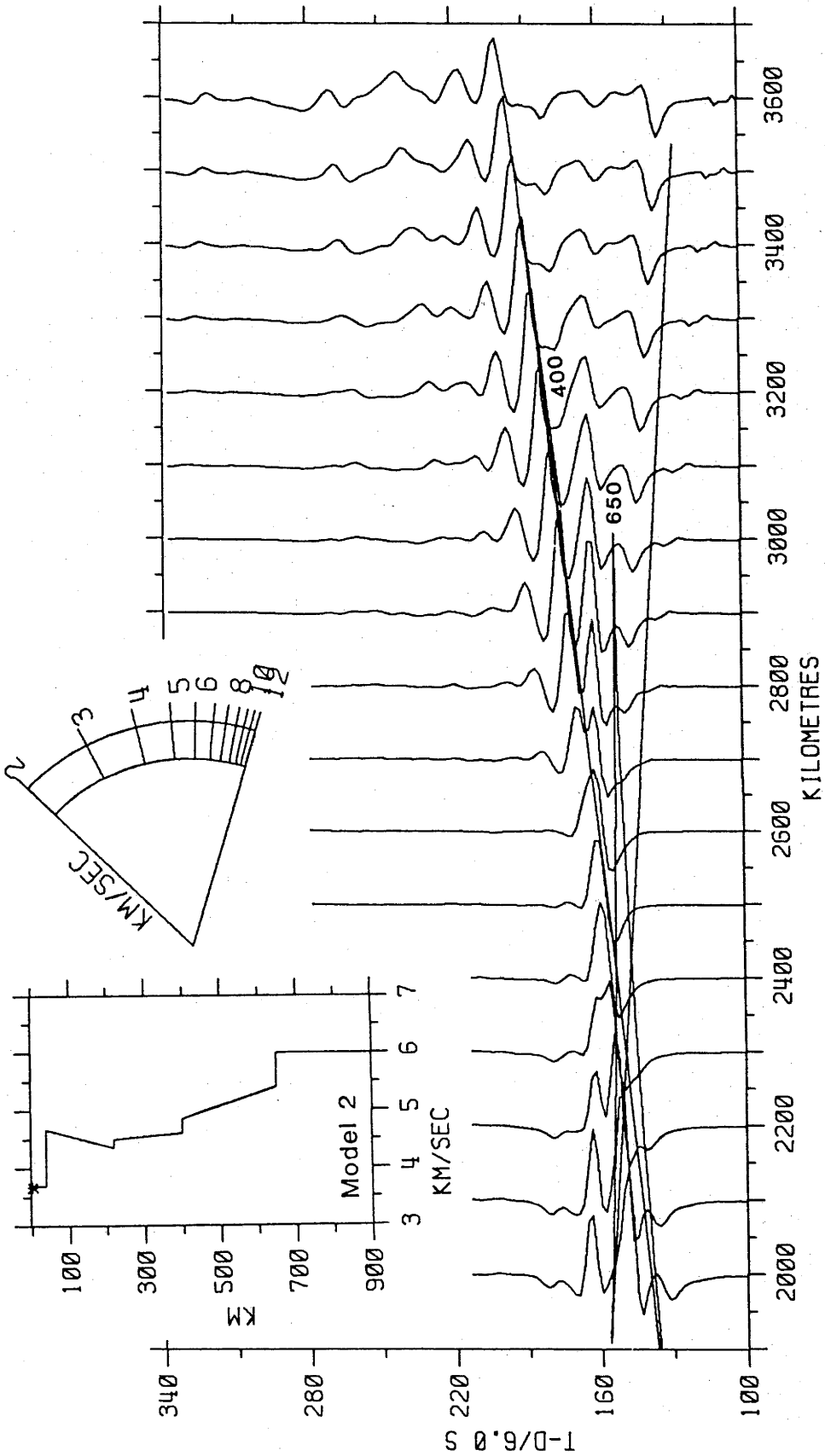


Figure 7.7: Synthetic SH seismograms for the shear-wave-velocity model derived from waveforms of first arrivals alone. Caption as given by Figure 6.2.

7.5 CONCLUSIONS

The data analysis strategy proposed in Chapter 1 has been successfully utilized in the construction of a well-constrained SH velocity-depth model of western Europe. Careful modelling of processed LP data with complete synthetic seismograms has resulted in the model SHME, with discontinuities in velocity at depths of 300, 400, 500 and 670 km, representing velocity contrasts of 6%, 11%, 2% and 8% respectively. A model without the "500-km" discontinuity would satisfy the deconvolved waveform data, but not the spikograms. The narrow data window from 18° to 30° does not constrain structure above 200 km or below 670 km. The "200-km" discontinuity in SHME has been inferred from other models, and the presence of the discontinuity near 750 km was inferred from two oceanic events near the edge of the data window. Three independent starting models were used in the trial-and-error inversion, SHR14, PREM and SHMEE, yet all three inversions led ultimately to one model. The importance of the analysis strategy is stressed and has been vindicated by way of example. Data should be first deconvolved and some technique such as iterative least-squares decomposition be applied to indicate the arrival times of the larger amplitude component wavelets. It is not possible to obtain a realistic model from travel-time data alone or waveform data of the first few cycles of LP data. The model SHME is more complex than any model previously derived from LP data with the exception of SHMEE, and approaches the complexity of models derived from recent studies of high quality SP data.

CHAPTER 8

FUTURE RESEARCH

Current research in Earth structure seismology is admitting to seismic-wave velocity models of the upper mantle an ever increasing degree of complexity, reflecting increasing sophistication in data collation, processing and interpretation. The strategy proposed in this thesis, that of utilizing the entire wave train, is part of that trend, and may be expected to become an important methodology in forthcoming seismological studies.

For the future success of this strategy in studies of body waves, the data window should be extended to encompass the critical distances for multiples reflected from regions of rapidly varying velocity to depths of at least 1000 km. In order to circumvent the problems of using only one station (in this study, NORSAR effectively acted as a single station), several events should be recorded by a large array such as the SRO/ASRO network of digitally recording stations. However, regional networks imply sparse spatial sampling and source-receiver wave paths that may traverse a wide variety of tectonic provinces. The Canadian National Network of twenty five digital broad-band stations is expected to be fully operational by 1984, providing denser regional coverage than the SRO/ASRO network. Most of the Canadian network is favourably sited on the relatively stable Canadian Shield, with the Aleutian Islands and western Pacific providing rich source regions. This situation would be considerably improved if long lines of instruments could be used such as the Central Australia Project (Hales et al., 1980a) and the recently deployed Network of Automatically Registering Seismographs (NARS) on the West European Platform (Nolet and Vlaar, 1982). Australia is particularly fortunate to be located between 10° and 50° of the Banda Sea-Taiwan trend, a source region of deep events. Deep events reduce the uncertainty of the velocity distribution at the source depth provided, of course, that the focal depth can be reliably

determined. The NARS line is not so fortuitously placed, with only the shallow south Atlantic/Caribbean and Arctic source regions lying along the axis of the line. The arrays are equipped with broad-band sensors, which may enable the identification of energy arising from sub-critical reflections, constraining further the exact nature of velocity discontinuities. Ultimately, this strategy will be extended to include P and SV data.

Synthetic seismogram modelling is expensive in terms of time and often money even for relatively simple models of isotropic and laterally homogeneous models. This is particularly the case with Reflectivity method based programmes which are so well suited to studies of radial variations in velocity. Advances in software and hardware aside, a future direction the Reflectivity method may take is the elimination of the thin-layer approximation, so that regions of constant change of material parameters can be dealt with by one expression in the propagator matrices. Applications of this approach have already been suggested by Woodhouse (1978), but the method has yet to be developed for regions of rapid velocity variation with depth. Furthermore, to circumvent the task of iteratively correcting trial models by comparing the synthetic seismograms with the data, some method of directly and automatically inverting all the waveform data for velocity as a function of depth may be developed. The effectiveness of such a method is limited by the degree of heterogeneity in the real Earth.

Clearly, the realistic goal of establishing reliable upper mantle velocity models, *inter alia*, will lead to a better understanding of the geodynamic processes as manifest in the physical and chemical properties of the Earth.

BIBLIOGRAPHY

- ABO-ZENA, A., 1979. Dispersion function computations for unlimited frequency values. *Geophys.J.*, 58, 91-105.
- AKAIKE, H., 1969. Fitting autoregressive models for prediction. *Ann.Inst.Statist.Math.*, 21, 243-247.
- AKAOGI, M. and AKOMOTO S., 1977. Pyroxene-garnet solid-solution equilibria in the systems $Mg_4Si_4O_{12}$ - $Mg_3Al_2Si_3O_{12}$ and $Fe_4Si_4O_{12}$ - $Fe_3Al_2Si_3O_{12}$ at high pressures and temperatures. *Phys.Earth Planet.Inter.*, 15, 90-106.
- AKAOGI, M. and AKIMOTO, S., 1979. High pressure phase equilibria in a garnet lherzolite, with special reference to Mg^{2+} - Fe^{2+} partitioning among constituent minerals. *Phys.Earth Planet.Inter.*, 19, 31-51.
- AKI, K. and RICHARDS, P.G., 1980. Quantitative Seismology, Volume I and II. W.H.Freeman and Company, 931 pp.
- ANDERSON, D.L., 1979a. The deep structure of continents. *J.Geophys.Res.*, 84, 7555-7560.
- ANDERSON, D.L., 1979b. The upper mantle transition region: Eclogite? *Geophys.Res.Lett.*, 6, 433-436.
- ANDERSON, D.L. and TOKSÖZ, M.N., 1963. Surface waves on a spherical Earth, 1. Upper mantle structure from Love waves. *J.Geophys.Res.*, 68, 3483-3500.
- ANDERSON, D.L., BEN-MENAHEN, A. and ARCHAMBEAU, C.B., 1965. Attenuation of seismic energy in the upper mantle. *J.Geophys.Res.*, 70, 1441-1447.
- ANDERSON, D.L. and JULIAN, B.R., 1969. Shear velocities and elastic parameters of the mantle. *J.Geophys.Res.*, 74 3281-3286.
- ANDERSON, D.L. and HART, R.S., 1978. Attenuation models for the Earth. *Phys.Earth.Planet.Inter.*, 16, 289-306.
- ANDERSON, D.L. and SAMMIS, C., 1970. Partial melting in the upper mantle. *Phys.Earth Planet.Inter.*, 3, 41-50.
- ANDRIANOVA, Z.S., KEILIS-BOROK, V.I., LEVSHIN, A.L. and NEIGANZ, M.G., 1967. Seismic Love Waves. New York: Consultants Bureau.
- BACKUS, G.E. and GILBERT, J.F., 1967. Numerical application of a formalism for geophysical inverse problems. *Geophys.J.R.astr.Soc.*, 13, 247-276.
- BACKUS, G.E. and GILBERT, J.F., 1968. The resolving power of gross Earth data. *Geophys.J.R.astr.Soc.*, 16, 169-205.
- BACKUS, G.E. and GILBERT, J.F., 1970. Uniqueness in the inversion of

- inaccurate gross Earth data. *Phil.Trans.R.Soc., Series A.*, 266, 123-192.
- BAKER, M.R., 1979. Application of time series analysis to the enhancement of seismic refraction data interpretation. M.Sc Thesis, Purdue University, 73 pp.
- BERTEUSSEN, K.A., 1976. The origin of slowness and azimuth anomalies at large arrays. *Bull.Seism.Soc.Am.*, 66, 719-741.
- BIRCH, F., 1961. Composition of the Earth's mantle. *Geophys.J.R.astr.Soc.*, 4, 295-311.
- BRUNE, J.N., 1970. Tectonic stress and the spectra of seismic waves from earthquakes. *J.Geophys.Res.*, 75, 4997-5009.
- BULLEN, K.E., 1963. An Introduction to the Theory of Seismology. Cambridge University Press, 381 pp.
- BUNGUM, H., HUSEBYE, E.S. and FINGDAL, F., 1971. The NORSAR array and preliminary results of data analysis. *Geophys.J.R.astr.Soc.*, 25, 115-126.
- BURDICK, L.J., 1981. A comparison of upper mantle structure beneath North America and Europe. *J.Geophys.Res.*, 86, 5926-5936.
- BURDICK, L.J. and ANDERSON, D.L., 1975. Interpretation of velocity profiles in the mantle. *J.Geophys.Res.*, 80, 1070-1074.
- BURDICK, L.J. and HELMBERGER, D.V., 1978. The upper mantle P-velocity structure of the western United States. *J.Geophys.Res.*, 83, 1699-1712.
- BURDICK, L.J. and ORCUTT, J.A., 1979. A comparison of the generalized ray and reflectivity methods of waveform synthesis. *Geophys.J.R.astr.Soc.*, 58, 261-278.
- BUTTKUS, B., 1975. Homomorphic filtering - theory and practice. *Geophys.Prosp.*, 23, 712-748.
- CAGNETTI, V., PASQUALE, V. and POLINARI, S., 1978. Fault-plane solutions and stress regimes in Italy and adjacent regions. *Tectonophysics*, 46, 239-250.
- CALCAGNILE, G., PANZA, G.F. and KNOPOFF, L., 1979. Upper mantle structure of north-central Italy from the dispersion of Rayleigh waves. *Tectonophysics*, 56, 51-63.
- CAPUTO, M., KNOPOFF, L., MANTOVANI, R., MUELLER, S. and PANZA, G.F., 1976. Rayleigh wave phase velocities and upper mantle structure in the Apennines. *Ann.Geofis.*, 29, 199-214.
- CAREY, S.W., 1955. The orocline concept in geotectonics. *Proc.Roy.Soc.Tasmania*, 89, 255-288.

- CARA, M., NERCESSIAN, A. and NOLET, G., 1980. New inferences from higher mode data in western Europe and northern Eurasia. *Geophys.J.R.astr.Soc.*, 61, 459-478.
- CARPENTER, E.W., 1966. Absorption of elastic waves - an operator for a constant Q mechanism. Atomic Weapons Research Establishment (AWRE) Report O-43/66.
- CHANDER, R., ALSOP, L.E. and OLIVER, J., 1968. On the synthesis of shear-coupled PL waves. *Bull.Seism.Soc.Am.*, 58, 1849-1877.
- CHAPMAN, C.H., 1978. A new method for computing synthetic seismograms. *Geophys.J.R.astr.Soc.*, 54, 481-518.
- CHOY, G.L. and RICHARDS, P.G., 1975. Phase distortion and Hilbert transformation in multiply reflected and refracted body waves. *Bull.Seism.Soc.Am.*, 65, 55-70.
- CHOY, G.L., CORMIER, V.F., KIND, R., MÜLLER, G. and RICHARDS, P.G., 1980. A comparison of synthetic seismograms of core phases generated by the full wave theory and the reflectivity method. *Geophys.J.R.astr.Soc.*, 61, 21-39.
- CLAERBOUT, J.F., 1976. *Fundamentals of Geophysical Data Processing*. McGraw Hill Inc., 274 pp.
- CLAERBOUT, J.F., 1977. Parsimonious deconvolution. Stanford Exploration Project, Report No. 13, 1-32.
- CLAYTON, R.W. and WIGGINS, R.A., 1976. Source shape estimation and deconvolution of teleseismic body waves. *Geophys.J.R.astr.Soc.*, 47, 151-177.
- CLEARY, J.R., 1975. Decomposition of SH wave trains. Australian National University, Research School of Earth Sciences Annual Report, 105 pp.
- CLEARY, J.R. and ANDERSSON, R., 1979. Seismology and the internal structure of the Earth. In: *The Earth: Its Origin, Structure and Evolution*. M.W. McElhinny (ed.) Academic Press, New York, 597 pp.
- CLEARY, J.R. and HALES, A.L., 1966. An analysis of the travel times of P waves to North American stations in the distance range 32° to 100° . *Bull.Seism.Soc.Am.*, 56, 467-489.
- CLEARY, J.R., INGATE, S.F., KING, D.W. and WANG, C., 1982. Upper mantle modelling using long-period SH body-wave trains. *Phys.Earth Planet.Inter.*, 30, 36-48.
- CORMIER, V.F. and RICHARDS, P.G., 1977. Full wave theory applied to a discontinuous velocity increase: the inner core boundary. *J.Geophys.*, 43, 3-31.

- CRAMPIN, S. and KING, D.W., 1977. Evidence for anisotropy in the upper mantle beneath Eurasia from the polarization of higher mode seismic surface waves. *Geophys.J.R.astr.Soc.*, 49, 59-85.
- DALEY, P.F. and HRON, F., 1982. Ray-reflectivity method for SH waves in stacks of thin and thick layers. *Geophys.J.R.astr.Soc.*, 69, 527-535.
- DAVIES, E.B. and MERCADO, E.J., 1968. Multichannel deconvolution filtering of field recorded data. *Geophysics*, 33, 711-722.
- DER, Z.A. and LANDISMAN, M., 1972. Theory of errors, resolution, and separation of unknown variables in inverse problems, with application to the mantle and the crust in southern Africa and Scandinavia. *Geophys.J.R.astr.Soc.*, 27, 137-178.
- DE VOOGD, N., 1974. Wavelet shaping and noise reduction. *Geophys.Prosp.*, 22, 354-369.
- DEWEY, J.F., PITMAN, W.C. III, RYAN, W.B.F. and BONNIN, J., 1973. Plate tectonics and the evolution of the Alpine system. *Geol.Soc.Am.Bull.*, 84, 3137-3180.
- DEY-SARKAR, S.K., 1974. Upper mantle P-wave velocity distributions beneath western Canada. Ph.D Thesis, University of Toronto, Canada, 128 pp.
- DEY-SARKAR, S.K. and WIGGINS, R.A., 1976. Source deconvolution of teleseismic P-wave arrivals between 14° and 40° . *J.Geophys.Res.*, 81, 3633-3641.
- DUNKIN, J.W., 1965. Computation of model solutions in layered, elastic media at high frequencies. *Bull.Seism.Soc.Am.*, 55, 335-358.
- DZIEWONSKI, A.M., 1970. Correlation properties of free period partial derivations and their relation to the resolution of gross Earth data. *Bull.Seism.Soc.Am.*, 60, 741-768.
- DZIEWONSKI, A.M., 1971. Upper mantle models from "pure path" dispersion data. *J.Geophys.Res.*, 76, 2587-2601.
- DZIEWONSKI, A.M., HALES, A.L. and LAPWOOD, E.R., 1975. Parametrically simple Earth models consistent with geophysical data. *Phys.Earth Planet.Inter.*, 10, 12-48.
- DZIEWONSKI, A.M. and ANDERSON, D.L., 1981. Preliminary reference Earth model. *Phys.Earth Planet.Inter.*, 25, 297-356.
- DZIEWONSKI, A.M., CHOU, T.-A. and WOODHOUSE, J.H., 1981. Determination of earthquake source parameters from wave-form data for studies of global and regional seismicity. In: *Identification of Seismic Sources - Earthquakes or Underground Explosions*, 233-254, E.S. Husebye and S. Mykkeltveit (eds), Reidl Publishing Co.; and, *J.Geophys.Res.*, 86,

2825-2852.

- ENGDahl, E.R., TAGGERT, J., LOBDELL, J.L., ARNOLD, E.P. and CLAWSON, G.E., 1968. Computational methods. *Bull.Seism.Soc.Am.*, 58, 1339-1344.
- ENGLAND, P.C., WORTHINGTON, M.H. and KING, D.W., 1977. Lateral variation in the structure of the upper mantle beneath Eurasia. *Geophys.J.R.astr.Soc.*, 48, 71-79.
- ENGLAND, P.C., KENNET, B.L.N. and WORTHINGTON, M.H., 1978. A comparison of the upper mantle structure beneath Eurasia and the North Atlantic and Arctic Oceans. *Geophys.J.R.astr.Soc.*, 54, 575-585.
- EWING, W.M., JARDETZKY, W.S. and PRESS, F., 1957. *Elastic Waves in Layered Media*. McGraw-Hill, New York, 380 pp.
- FUCHS, K., 1968. Das Reflexions- und Transmissionsvermögen eines geschichteten Mediums mit beliebiger Tiefen-Verteilung der elastischen modulen und der Dichte für schragen Einfall ebener wellen. *Z.F.Geophys.*, 34, 389-413.
- FUCHS, K., 1980. Calculation of synthetic seismograms by the reflectivity method. *B.M.R. Record* 1980/64.
- FUCHS, K. and MÜLLER, G., 1971. Computation of synthetic seismograms with the reflectivity method and comparison with observations. *Geophys.J.R.astr.Soc.*, 23, 417-433.
- GILBERT, F. and HELMBERGER, D.V., 1972. Generalized ray theory for a layered sphere. *Geophys.J.R.astr.Soc.*, 27, 57-80.
- GILBERT, F. and DZIEWONSKI, A.M., 1975. An application of normal mode theory to the retrieval of structural parameters and source mechanisms from seismic spectra. *Phil.Trans.R.Soc.*, 278, 187-269.
- GIVEN, J.W. and HELMBERGER, D.V., 1980. Upper mantle structure of northwestern Eurasia. *J.Geophys.Res.*, 85, 7183-7194.
- GOETZE, C., 1977. A brief summary of our present day understanding of the effect of volatiles and partial melting on the mechanical properties of the upper mantle. In *High Pressure Research, Application in Geophysics*, Manghni and Atimoto (eds), Academic Press, New York.
- GRAHAM, E.K. and DOBRZYROWSKI, D., 1976. Temperatures in the mantle as inferred from simple compositional models. *American Mineralogist*, 61, 549-554.
- GRAND, S.P. and HELMBERGER, D.V., 1983. Upper mantle shear structure of North America. Pre-print.
- GREEN, R.W. and HALES, A.L., 1968. The travel times of P waves to 30° in the central United States and upper mantle structure.

- Bull.Seism.Soc.Am., 58, 267-289.
- GREGERSEN, S., 1977. P-wave travel-time residuals caused by a dipping plate in the Aegean Arc in Greece. *Tectonophysics*, 37, 88-93.
- GRIFFITHS, L.J., SMOLKA, F.R. and TREMBLY, L.D., 1977. Adaptive deconvolution: A new technique for processing time-varying seismic data. *Geophysics*, 42, 742-759.
- GUPTA, H.K. and NARAIN, H., 1967. Crustal structure in the Himalayan and Tibet Plateau region from surface wave dispersion. *Bull.Seism.Soc.Am.*, 57, 235-248.
- HADDON, R.A. and HUSEBYE, E.S., 1978. Joint interpretation of P-wave time and amplitude anomalies in terms of lithospheric heterogeneities. *Geophys.J.R.astr.Soc.*, 55, 19-43.
- HALES, A.L., 1976. ScS travel-time residuals and the differences between continents and oceans. *Earth.Planet Sci.Lett.*, 33, 249-254.
- HALES, A.L., HELSLEY, C.E. and NATION, J.B., 1970. P travel times for an oceanic path. *J.Geophys.Res.*, 75, 7362-7381.
- HALES, A.L., MUIRHEAD, K.J. and RYNN, J.M.W., 1980a. A compressional velocity distribution for the upper mantle. *Tectonophysics*, 63, 309-348.
- HALES, A.L., MUIRHEAD, K.J. and RYNN, J.M.W., 1980b. Crust and upper mantle shear velocities from controlled sources. *Geophys.J.R.astr.Soc.*, 63, 659-670.
- HARKRIDER, D.G., 1964. Surface waves in multilayered elastic media. I. Rayleigh and Love waves from buried sources in a multi-layered elastic half-space. *Bull.Seism.Soc.Am.*, 54, 627-679.
- HARKRIDER, D.G., 1976. Potentials and displacements for two theoretical seismic sources. *Geophys.J.R.astr.Soc.*, 47, 97-133.
- HASKELL, N.A., 1953. The dispersion of surface waves in multi-layered media. *Bull.Seism.Soc.Am.*, 43, 17-34.
- HASKELL, N.A., 1960. Crustal reflection of plane SH waves. *J.Geophys.Res.*, 65, 4147-4150.
- HASKELL, N.A., 1963. Radiation pattern of Rayleigh waves from a fault of arbitrary dip and direction of motion in a homogeneous medium. *Bull.Seism.Soc.Am.*, 53, 619-642.
- HELMBERGER, D.W., 1973. Numerical seismograms of long-period body waves from seventeen to forty degrees. *Bull.Seism.Soc.Am.*, 63, 633-646.
- HELMBERGER, D.V., 1974. Generalized ray theory for shear dislocations. *Bull.Seism.Soc.Am.*, 64, 45-64.

- HELMBERGER, D.V. and WIGGINS, R.A., 1971. Upper mantle structure of midwestern United States. *J.Geophys.Res.*, 76, 3229-3245.
- HELMBERGER, D.V. and ENGEN, G.R., 1974. Upper mantle shear structure. *J.Geophys.Res.*, 79, 4017-4078.
- HENDRAJAYA, L., 1981. The shear-wave velocity structure in the mantle to 1100 km depth, determined using the Warramunga seismic array. Ph.D Thesis, Australian National University, Canberra, 295 pp.
- HILL, D.P., 1974. Phase shift and pulse distortion in body waves due to internal caustics. *Bull.Seism.Soc.Am.*, 64, 1733-1742.
- HIRN, A., STEINMETZ, L., KIND, R. and FUCHS, K., 1973. Long range profiles in western Europe: II. Fine structure of the lower lithosphere in France (Southern Bretagne). *Z.Geophys.*, 39, 363-384.
- HIRN, A., HAESSLER, H., TRONG, P.H., WITTLINGER, G. and MENDES VICTOR, L.A., 1980. Aftershock sequence of the January 1st, 1980, earthquake and present-day tectonics in the Azores. *Geophys.Res.Lett.*, 7, 501-504.
- HOVLAND, J., GUBBINS, D. and HUSEBYE, E.S., 1981. Upper mantle heterogeneities beneath central Europe. *Geophys.J.R.astr.Soc.*, 66, 261-284.
- IBRAHIM, A.K. and NUTTLI, O.W., 1967. Travel-time curves and upper mantle structure from long-period S waves. *Bull.Seism.Soc.Am.*, 57, 1063-1092.
- INGATE, S.F., 1983. An alternative method for focal-plane solutions from a single station. *Geophys.Res.Lett.*, (in press).
- INGATE, S.F., KIND, R. and BOCK, G., 1983. Synthesis of complete SH seismograms. *Geophys.J.R.astr.Soc.*, (in press).
- INGATE, S.F. and MUIRHEAD, K.J., Exact deconvolution, (in prep.).
- JORDAN, T.H., 1975. The continental tectosphere. *Rev.Geophys.Space Phys.*, 13, 1-12.
- JORDAN, T.H. and ANDERSON, D.L., 1974. Earth structure from free oscillations and travel times. *Geophys.J.R.astr.Soc.*, 36, 411-459.
- KANAMORI, H. and STEWART, G.S., 1978. Seismological aspects of the Guatemala earthquake. *J.Geophys.Res.*, 83, 3427-3434.
- KAUSEL, E. and SCHWAB, F., 1973. Contributions to Love-wave transformation theory: Earth-flattening transformation for Love waves from a point source to a sphere. *Bull.Seism.Soc.Am.*, 63, 983-993.
- KAUSEL, E.G., SCHWAB, F. and MANTOVANI, E., 1977. Oceanic Sa. *Geophys.J.R.astr.Soc.*, 50, 407-440.
- KENNETT, B.L.N., 1975a. The effects of attenuation on seismograms. *Bull.Seism.Soc.Am.*, 65, 1643-1651.

- KENNETT, B.L.N., 1975b. Theoretical seismogram calculation for laterally varying crustal structures. *Geophys.J.R.astr.Soc.*, 42, 579-589.
- KENNETT, B.L.N., 1980. Seismic waves in a stratified half-space - II. Theoretical seismograms. *Geophys.J.R.astr.Soc.*, 61, 1-10.
- KIKUCHI, M. and KANAMORI, H., 1982. Inversion of complex body waves. *Bull.Seism.Soc.Am.*, 72, 491-506.
- KIND, R., 1976. Computation of reflection coefficients for layered media. *J.Geophys.*, 42, 191-200.
- KIND, R., 1978. The reflectivity method for a buried source. *J.Geophys.*, 44, 603-612.
- KIND, R., 1979. Extensions of the reflectivity method. *J.Geophys.* 45, 373-380.
- KIND, R. and MÜLLER, G., 1975. Computations of SV waves in realistic earth models. *J.Geophys.*, 41, 149-172.
- KIND, R. and SEIDL, D., 1982. Analysis of broadband seismograms from the Orile Area. *Bull.Seism.Soc.Am.*, 72, 2131-2146.
- KING, D.W. and CALCAGNILE, G., 1976. P-wave velocities in the upper mantle beneath Fennoscandia and Western Russia. *Geophys.J.R.astr.Soc.*, 46, 407-432.
- KNOPOFF, L., 1964. A matrix method for elastic wave problems. *Bull.Seism.Soc.Am.*, 54, 431-438.
- KOSMINSKAYA, I.P., MIKHOTA, G.G. and TULINA, Y.V., 1958. Crustal structure of the Pamir-Alai zone from seismic depth sounding data. *Izvestiya Acad.Soc.USSR., Geophys.Ser.*, 673-683, English translation.
- KOVACH, R.L. and ROBINSON, R., 1969. Upper mantle structure in the Basin and Range Province, western North America, from the apparent velocities of S waves. *Bull.Seism.Soc.Am.*, 59, 1653-1665.
- LANGSTON, C.A., 1982. Single-station fault-plane solutions. *Bull.Seism.Soc.Am.*, 72, 729-744.
- LANGSTON, C.A. and HELMBERGER, D.V., 1975. A procedure for modelling shallow dislocation sources. *Geophys.J.R.astr.Soc.*, 42, 117-130.
- LEHMANN, I., 1959. Velocities of longitudinal waves in the upper part of the earth's mantle. *Ann.Geophys.*, 15, 93-118.
- LEHMANN, I., 1962. The travel times of the longitudinal waves of the Logan and Blanca atomic explosions, and their velocities in the upper mantle. *Bull.Seism.Soc.Am.*, 52, 519-526.
- LEHMANN, I., 1967. Low velocity layers. In: *The Earth's Mantle*, T.F. Gaskell (ed.), Academic Press, London, 509 pp.

- LE PICHON, X., 1968. Sea-floor spreading and continental drift. *J.Geophys.Res.*, 73, 3661-3697.
- LEVEN, J.H., 1980. The application of synthetic seismograms. Ph.D Thesis, Australian National University, Canberra, 234 pp.
- LEVEN, J.H., JACKSON, I. and RINGWOOD, A.E., 1981. Upper mantle anisotropy and lithospheric decoupling. *Nature*, 289, 234-239.
- LEVINSON, N., 1947. The Weiner RMS (root-mean-square) error criterion in filter design and prediction. Appendix B In: *Extrapolation, Interpolation and Smoothing of Stationary Time Series*, N. Wiener, M.I.T. Press, Massachusetts, 163 pp.
- LEVY, S. and OLDENBURG, D.W., 1982. The deconvolution of phase shifted wavelets. *Geophysics*, 47, 1285-1294.
- LIAO, A.H., SCHWAB, F. and MANTOVANI, E., 1978. Computation of complete theoretical seismograms for torsional waves. *Bull.Seism.Soc.Am.*, 68, 317-324.
- LINES, L.R. and ULRYCH, T.J., 1977. The old and the new in seismic deconvolution and wavelet estimation. *Geophys.Prosp.*, 25, 512-540.
- LIU, L., 1977a. Mineralogy and chemistry of the mantle above 1000 km. *Geophys.J.*, 48, 53-62.
- LIU, L., 1977b. The system enstatite-pyrope at high pressures and temperatures and the mineralogy of the Earth's mantle. *Earth Planet.Sci.Lett.*, 36, 237-245.
- LIU, L., 1979a. Phase transformations and the constitution of the deep mantle. In: *The Earth: It's Origin, Structure and Evolution*. M.W. McElhinny (ed.) Academic Press, New York, 597 pp..
- LIU, L., 1979b. On the 650-km seismic discontinuity. *Earth Planet.Sci.Lett.*, 42, 202-208.
- LIU, L., 1980a. The pyroxene-garnet transformation and it's implication for the 200-km discontinuity. *Phys.Earth Planet.Inter.*, 23, 286-299.
- LIU, L., 1980b. The mineralogy of an eclogite Earth mantle. *Phys.Earth Planet.Inter.*, 23, 265-267.
- LYSMER, J. and DRAKE, L.A., 1972. A finite element method for seismology. In: *Methods in Computational Physics*, Vol. II, B.A. Bolt (ed.).
- MCKENZIE, D., 1972. Active tectonics of the Mediterranean region. *Geophys.J.R.astr.Soc.*, 30, 109-185.
- MACK, H., 1969. Nature of short-period signal variations of LASA. *J.Geophys.Res.*, 74, 3161-3170.
- MASSÉ, R.P., 1973. Compressional velocity distribution beneath

- central and eastern North America. *Bull.Seism.Soc.Am.*, 63, 911-935.
- MASSÉ, R.P. and ALEXANDER, S.S., 1974. Compressional velocity distribution beneath Scandinavia and Western Russia. *Geophys.J.R.astr.Soc.*, 39, 587-602.
- MAYER-ROSA, D. and MUELLER, S., 1973. The gross velocity depth distribution of P and S waves in the upper mantle of Europe from earthquake observations. *Z.Geophys.*, 23, 435-449.
- MELLMAN, G.R., 1980. A method of body-wave waveform inversion for the determination of Earth structure. *Geophys.J.R.astr.Soc.*, 62, 481-504.
- MELLMAN, G.R. and HELMBERGER, D.V., 1978. A modified first motion approximation for the synthesis of body-wave seismograms. *Geophys.J.R.astr.Soc.*, 54, 129-140.
- MEREU, R.F., 1976. Exact wave-shaping with a time-domain digital filter of finite length. *Geophysics*, 41, 659-672.
- MEREU, R.F. and HUNTER, J.A., 1969. Crustal and upper mantle structure under the Canadian shield from Project Early Rise data. *Bull.Seism.Soc.Am.*, 59, 147-165.
- MUIRHEAD, K.J., CLEARY, J.R. and FINLAYSON, D.M., 1977. A long range seismic profile in south-eastern Australia. *Geophys.J.R.astr.Soc.*, 48, 509-519.
- MÜLLER, G., 1977. Earth-flattening approximation for body waves derived from geometric ray theory - improvements, corrections and range of applicability. *J.Geophys.*, 42, 429-436.
- MÜLLER, G. and SCHOTT, W., 1981. Some recent extensions of the reflectivity method. In: *Identification of Seismic Sources - Earthquake or Underground Explosion*, 347-371, E.S. Husebye and S. Mykkeltveit, (eds) Reidel Publishing Co.
- NOLET, G., 1977. The upper mantle under western Europe inferred from the dispersion of Rayleigh modes. *J.Geophys.*, 43, 265-285.
- NOLET, G. and VLAAR, N.J., 1982. The NARS project. *J.Eur.U.Geosc.*, 2, 17-25.
- NORTH, R.G., 1977. Seismic moment, source dimensions, and stresses associated with earthquakes in the Mediterranean and Middle East. *Geophys.J.R.astr.Soc.*, 48, 137-161.
- NUTTLI, O.W., 1969. Travel times and amplitudes of S waves from nuclear explosions in Nevada. *Bull.Seism.Soc.Am.*, 59, 385-398.
- O'BRIEN, P.S., 1969. Some experiments concerning the primary seismic pulse. *Geophys.Prosp.*, 17, 511-547.

- OKAL, E.A. and ANDERSON, D.L., 1975. A study of lateral inhomogeneities in the upper mantle by multiple ScS travel-time residuals. *Geophys.Res.Lett.*, 2, 313-316.
- OOE, M. and ULRYCH, T.J., 1979. Minimum entropy deconvolution with an exponential transformation. *Geophys.Prospect.*, 27, 458-473.
- OPPENHEIM, A.V., 1965. Superposition in a class of non-linear systems. Technical Report No. 432, Research Laboratory of Electronics, M.I.T., Cambridge, Mass.
- OPPENHEIM, A.V., SCHAFER, R.W., STOCKHAM, T.G., 1968. Nonlinear filtering of multiplied and convolved signals. *Proc.I.E.E.E.*, 65, 1264-1291.
- PANZA, G.F., 1979. The crust and upper mantle in southern Italy from geophysical data. *Riv.Ital.Geofis.Sei.Affini.*, 5, 17-22.
- PANZA, G.F. and MUELLER, S., 1979. The plate boundary between Eurasia and Africa in the Alpine area. *Mem.Sci.Geol.*, 33, 43-50.
- PEACOCK, K.L. and TRIETEL, S., 1969. Predictive deconvolution: Theory and practice. *Geophysics*, 34, 155-169.
- PHINNEY, R.A., 1961. Propagation of leaking interference waves. *Bull.Seism.Soc.Am.*, 51, 527-555.
- PILANT, W.L., 1979. *Elastic Waves in the Earth*. Elsevier, 493 pp.
- PITMAN III, W.C. and TALWANI, M., 1972. Sea-floor spreading in the North Atlantic. *Geol.Soc.Am.Bull.*, 83, 619-646.
- RAM DATT, 1977. A P-wave velocity structure for upper mantle and transition zone using the WRA seismic array. Ph.D Thesis, Australian National University, Canberra, 223 pp.
- RAM DATT and MUIRHEAD, K.J., 1976. Evidence for a sharp velocity increase near 770 km depth. *Phys.Earth Planet.Inter.*, 13, 37-46.
- RAM DATT and MUIRHEAD, K.J., 1977. Evidence of multiplicity in the P-travel-time curve beyond 30 degrees. *Phys.Earth Planet.Inter.*, 15, 28-38.
- RICE, R.B., 1962. Inverse convolution filters. *Geophysics*, 27, 4-18.
- RICHARDS, P.G., 1976. On the adequacy of plane-wave reflection-transmission coefficients in the analysis of seismic body waves. *Bull.Seism.Soc.Am.*, 66, 701-717.
- RINGWOOD, A.E., 1975. *Composition and Petrology of the Earth's Mantle*. McGraw HillBook Co., New York.
- RINGWOOD, A.E. and MAJOR, A., 1967. Some high pressure transformations of geophysical interest. *Earth Planet.Sci.Lett.*, 2, 106-110.
- ROBINSON, E.A., 1957. Predictive decomposition of seismic traces.

- Geophysics, 22, 767-778.
- ROBINSON, E.A., 1967. Multichannel Time Series Analysis with Digital Computer Programs. Holden Day, San Francisco.
- ROBINSON, E.A., and TREITEL, S., 1967. Principles of digital Weiner filtering. Geophys.Prosp., 15, 311-333.
- ROBINSON, R. and KOVACH, R.L., 1972. Shear-wave velocities in the Earth's mantle. Phys.Earth Planet.Inter., 5, 30-44.
- ROMANOWICZ, B.A., 1980. A study of large-scale lateral variations of P velocity in the upper mantle beneath Western Europe. Geophys.J.R.astr.Soc., 63, 217-232.
- ROTSTEIN, Y., and KAFKA, A.L., 1982. Seismotectonics of the southern boundary of Anatolia, eastern Mediterranean regions: subduction, collision and arc jumping. J.Geophys.Res., 87, 7694-7706.
- SATÔ, Y., 1954. Study on surface waves X. Equivalency of SH waves and sound waves in a liquid. Bull.Earthquake Res.Inst., 32, 7-16.
- SAVAGE, J.C., 1966. Radiation from a realistic model of faulting. Bull.Seism.Soc.Am., 56, 577-592.
- SCHOTT, W., 1979. Die Reflectivitätsmethode für SH-Wellen in Theorie und Anwendung. Diploma Thesis, University of Karlsruhe, G.D.R., 97 pp.
- SCHWAB, F. and KNOPOFF, L., 1973. Long waves and the torsional free modes of a multilayered anelastic sphere. Bull.Seism.Soc.Am., 63, 1107-1117.
- SHERIFF, R.E., 1977. Limitations on resolution of seismic reflections and geologic detail derivable from them. Amer.Assoc.Pet.Geol., Memoir 26, 3-15.
- SIMPSON, D.W., 1973. P-wave velocity structure of the upper mantle in the Australian region. Ph.D Thesis, Australian National University, Canberra, 212 pp.
- SIPKIN, S.A. and JORDAN, T.H., 1975. Lateral heterogeneity of the upper mantle determined from the travel-times of ScS. J.Geophys.Res., 80, 1474-1484.
- SOLOMON, S.C., 1973. Shear wave attenuation and melting beneath the mid-Atlantic ridge. J.Geophys.Res., 78, 6044-6059.
- STACEY, F.D., 1977. Physics of the Earth. 2nd ed. John Wiley and Sons, New York, 414 pp.
- STEINMETZ, L., HIRN, A. and PERRIER, G., 1974. Reflexions sismiques a la base de l'asténosphère. Ann.Geophys., 30, 173-180.
- SU, S.S., and DORMAN, J., 1965. The use of leaking modes in seismogram interpretation and in studies of crust-mantle structure.

- Bull.Seism.Soc.Am., 55, 989-1021.
- SYKES, L.R., 1967. Mechanisms of earthquakes and nature of faulting on the mid-ocean ridges. J.Geophys.Res., 72, 2131-2153.
- TREITEL, S. and ROBINSON, E.A., 1966. The design of high resolution digital filters. I.E.E.E. Trans.Geosci.Electronics GE-4, 25-38.
- TREITEL, S. and WANG, R.J., 1976. The determination of digital Weiner filters from an ill-conditioned system of normal equations. Geophys.Prosp., 24, 317-327.
- TRIBOLET, J.M., 1977. A new phase unwrapping algorithm. I.E.E.E. Trans Acoustics, Speech and Signal Processing, 25, 170-177.
- TRIBOLET, J.M., 1979. Seismic Applications of Homomorphic Signal Processing. Prentice-Hall, New Jersey, 195 pp.
- ULRYCH, T.J., 1971. Application of homomorphic deconvolution to seismology. Geophysics, 36, 650-660.
- ULRYCH, T.J., JENSEN, O.J., ELLIS, R.M. and SOMERVILLE, P.G., 1972. Homomorphic deconvolution of some teleseismic events. Bull.Seism.Soc.Am., 62, 1269-1281.
- VAISNYS, J.R., 1967. Dislocation velocities and deformation in the mantle. Geophys.J.R.astr.Soc., 14, 67-72.
- WANG, C.Y. and HERRMANN, R.B., 1980. A numerical study of P-, SV- and SH-wave generation in a plane layered medium. Bull.Seism.Soc.Am., 70, 1015-1036.
- WANG, R., 1969. The determination of optimum gate lengths for time-varying Weiner filtering. Geophysics, 34, 633-695.
- WEIDNER, D.J. and AKI, K., 1973. Focal depth and mechanism of mid-ocean ridge earthquakes. J.Geophys.Res., 78, 1818-1831.
- WHITCOMB, J.H. and ANDERSON, D.L., 1970. Reflection of P'P' seismic waves from discontinuities in the mantle. J.Geophys.Res., 75, 5713-5728.
- WIDROW, B. and HOFF, M.E., 1960. Adaptive switching circuits. I.R.E. W.E.C.O.N. Conven.Rec., part 4, 96-104.
- WIGGINS, R.A., 1978. Minimum entropy deconvolution. Geoexploration, 16, 21-35.
- WIGGINS, R.A. and HELMBERGER, D.V., 1973. Upper mantle structure of western United States. J.Geophys.Res., 78, 1870-1880.
- WIGGINS, R.A. and ROBINSON, E.A., 1965. Recursive solution to the multi-channel filtering problem. J.Geophys.Res., 70, 1885-1891.
- WOODHOUSE, J.H., 1978. Asymptotic results for elastodynamic propagator matrices in plane stratified and spherically stratified Earth models. Geophys.J.R.astr.Soc., 54, 263-280.

APPENDIX 1

Cleary, J.R., Ingate, S.F., King, D.W. and Wang, C., 1982. Upper mantle modelling using long-period SH body-wave trains. *Phys.Earth Planet.Inter.*, 30, 36-48.

Upper mantle modelling using long-period SH body-wave trains

J.R. Cleary^{1,*}, S.F. Ingate¹, D.W. King² and C. Wang³

¹ *Research School of Earth Sciences, Australian National University, Canberra, A.C.T. (Australia)*

² *Offshore Oil NL, GPO Box 4246, Sydney, N.S.W. (Australia)*

³ *Institute of Earth Sciences, Academia Sinica, Taipei (Taiwan)*

(Received February 16, 1982; revision accepted May 7, 1982)

Cleary, J.R., Ingate, S.F., King, D.W. and Wang, C., 1982. Upper mantle modelling using long-period SH body-wave trains. *Phys. Earth Planet. Inter.*, 30: 36–48.

The resolution of fine shear-velocity structure in the upper mantle is difficult because of the low signal-to-noise conditions in most recordings of short-period S waves, and the poor resolving power of long-period S data. The resolution obtainable from the latter could be improved if a greater proportion of the SH body-wave train at distances less than about 40°, presumably comprised of arrivals from a variety of multiple paths through the upper mantle, could be separated into its component signals. Attempts at deconvolving these wave trains by standard techniques, however, usually result in "noisy" spike sequences which are extremely difficult to interpret.

The authors have devised an empirical method of decomposing an SH body-wave train into its component arrivals, based on sequential removal of the response wavelets from the train. Although the method is approximate in that it assumes the absence of phase distortion, it provides clear spike sequences which can be used to derive a starting model for the application of refinement techniques. Application of the method to SH wave trains recorded at NORSAR from Mediterranean earthquakes has enabled the construction of an SH-velocity model for the upper mantle beneath eastern Europe in which the discontinuity profile is strikingly similar to those of recent detailed P-velocity models for the upper mantle beneath central Australia.

1. Introduction

Array studies of the P-wave velocity distribution in the upper mantle have in recent years enabled the resolution of fine structure both radially and laterally (e.g. King and Calcagnile, 1976; England et al., 1977; Ram Datt and Muirhead, 1976, 1977; Ram and Mereu, 1977). Similar resolution of fine structure in the upper mantle shear velocity distribution is, however, less readily achieved, because of the difficulty of recording short-period S waves at sufficiently high signal-to-noise ratios. Radial and lateral variations of shear wave velocities have been inferred from long-period body waves (e.g. Ibrahim and Nuttli, 1967; Nuttli,

1969; Robinson and Kovach, 1972) and surface waves (e.g. Knopoff, 1972; Goncz and Cleary, 1976) but with poor resolution, imposed mainly by the spectral content of the observational data. Helmberger and Engen (1974) demonstrated, using synthetic seismograms, that many details of published shear velocity models were inconsistent with SH waveforms observed at LRSM and WWSSN stations in North America. Synthetic seismograms offer significant improvements in model resolution (see also Kind and Muller, 1975; Choy, 1977; Kind, 1978) when source effects can be reliably modelled.

An alternative means of improving model resolution is to attempt direct decomposition (deconvolution) of observed S-wave trains into their component body-wave arrivals. In the present paper

* Deceased, December 25, 1981.

the authors describe and apply an empirical method for the sequential decomposition of SH wave trains; the method appears to provide results that are more readily interpretable than those obtained by automatic least-squares inverse filtering (Robinson, 1967). The difficulties associated with the interpretation of automatically deconvolved seismograms may be mitigated by procedures based on some criterion of simplicity, such as in Minimum Entropy Deconvolution (Wiggins, 1977). In the present context, however, the development of processing methodologies needs to be rationalized with regard to *problem solving*. The decomposition strategy described in the present paper is in the spirit of exploratory data analysis advocated by Tukey (1977) and indirectly by Keilis-Borok (1964, 1972). Briefly, Tukey contends that most data analysis should be investigative, because "it is important to understand what you CAN DO before you learn to measure how WELL you seem to have DONE it".

Sequential decomposition of a suite of events from southern Europe recorded at the NORSAR array has produced an interpretable sequence of secondary arrivals in the interval of several minutes between the S and fundamental Love mode arrivals. SH body wave trains have not to the authors' knowledge been previously exploited in their entirety. Interpretation of the latter parts of the trains as a series of multiple arrivals has resulted in a solution for S-velocity structure in the upper mantle beneath eastern Europe which should constitute an acceptable starting model for more detailed investigation.

2. Observational data

The NORSAR array and its associated data processing centre (DPC) have been described in detail by Bungum et al. (1971). Prior to 1977, the so-called long period (LP) array at NORSAR comprised 22 matched three-component sets of Geotech 8700C and 7505B seismometers distributed over an aperture of 110 km. The entire output of the array, sampled once each second almost continuously during the 6 y 1971–1976, is available on digital magnetic tape at the NORSAR DPC. European seismicity is such that the data archive is not well endowed with events of magnitude 5 and over at distances appropriate to upper mantle investigations, i.e. $\Delta < 40^\circ$. However, a number of events from southerly azimuths in the distance range 20–28° have been well recorded at NORSAR; these events (Table I, Fig. 1) sample the upper mantle beneath eastern Europe.

In the present study, attention is confined to horizontal transverse (HT) components of LP shear waves, which can be readily obtained from digital data by combination of N–S and E–W component recordings. HT components are significantly simpler than corresponding recordings of vertical (V) and horizontal radial (HR) components; the relative complexity of V and HR components can be attributed to contamination by shear-coupled PL waves and other P–SV interactions (cf. Helmberger and Engen, 1974). HT components of LP body wave recordings generally exhibit high coherence across the array aperture, being much less affected by irregularities in local structure

TABLE I
NEIS data for events used

Region	Date	Lat. (°N)	Long. (°E)	Origin time			Depth (km)	m_b	Azimuth (deg.)
				(h)	m	s)			
Albania	Sept. 16, 1972	40.3	19.7	03	53	26.5	15	5.1	161
Greece–Albania	Nov. 24, 1972	39.5	20.3	03	48	35.1	11	5.3	160
Greece	Sept. 13, 1972	37.9	22.4	04	13	20.5	83	6.0	157
Turkey	May 25, 1971	39.0	29.7	05	43	27.0	24	5.8	143
Crete	Nov. 29, 1973	35.2	23.8	10	57	42.7	26	5.7	156

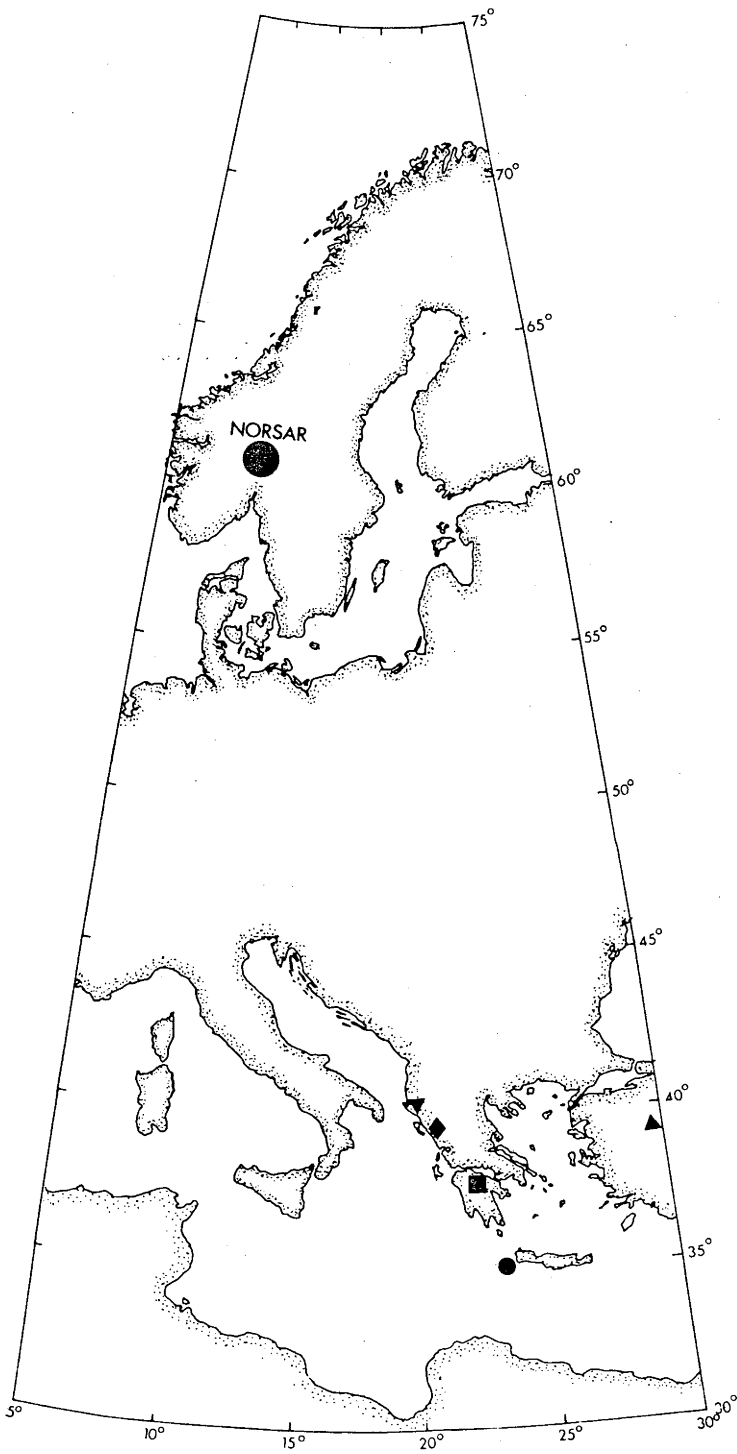


Fig. 1. Earthquakes used in this study (Table I) in relation to the NORSAR array. ▽, Albania; ◆, Greece-Albania; ■, Greece; ▲, Turkey; ●, Crete.

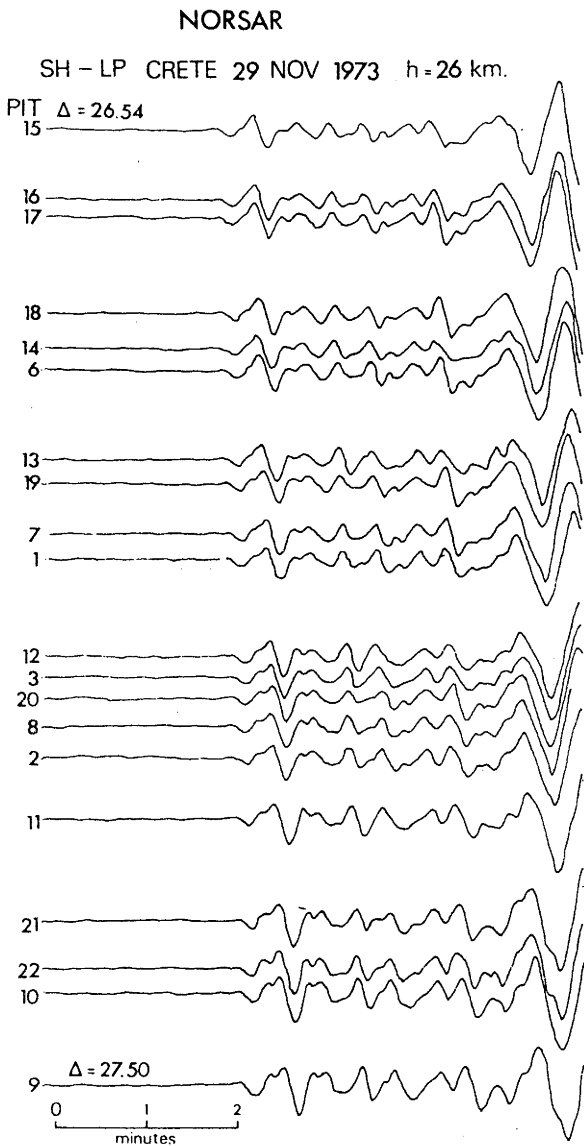


Fig. 2. SH wave trains from an earthquake in Crete, recorded at NORSAR LP sites. Note the coherence of the entire train across the array.

than the corresponding short-period recordings (cf. Bertuessen, 1976). A representative example of the data used in the present study is shown in Fig. 2, where the HT recordings at NORSAR LP sites of an SH train from an earthquake near Crete are displayed in the form of a record section. The high coherence of the signals across the entire train of

arrivals is evident. Progressive changes in the wave forms with distance are also apparent; such changes are caused by the relative "move-out" of waves with slightly different apparent velocities which have travelled by different paths through the upper mantle. In the following section a simple empirical technique for the resolution of the interfering components of the recorded wave trains is described.

3. Sequential decomposition

A simple procedure for the decomposition of a long-period SH wave train into its component body wave arrivals is illustrated in Fig. 3, using the Crete SH train from NORSAR site 15 shown in Fig. 1 (the site numbering used in this paper is that of Bertuessen (1976), Fig. 1). In essence, the method consists of sequential removal of the response wavelets from the train, beginning with the first-arriving wavelet, as described by King et al. (1978). The seismic trace then, after subtraction of the suitably scaled wavelet, represents a difference error which is subjectively minimized, and shown in Fig. 3. The dispersed Love wave is clearly seen near the end of the error train. The response wavelet used in this instance was based on the response of a NORSAR-type period horizontal seismometer system to an SH signal from a near-surface strike-slip source, as calculated by Helmberger and Engen (1974), modified slightly to improve the fit to the observed arrivals in the sense of subjectively minimizing the difference error. The times and magnitudes of the component wavelets can be represented by an equivalent spike sequence, as shown at the bottom of the figure.

The solution can be checked by convolving the response wavelet with the derived spike sequence to form a reconstructed wave train, as shown in Fig. 4. The beginning of the inferred Love wave train has been "patched in" at the end of the reconstructed seismogram to complete the picture. Also shown for comparison in Fig. 4 are automatic deconvolutions of the reconstructed and recorded wave trains using an inverse filter derived from the assumed wavelet using programs published by Robinson (1967). An independent automatic de-

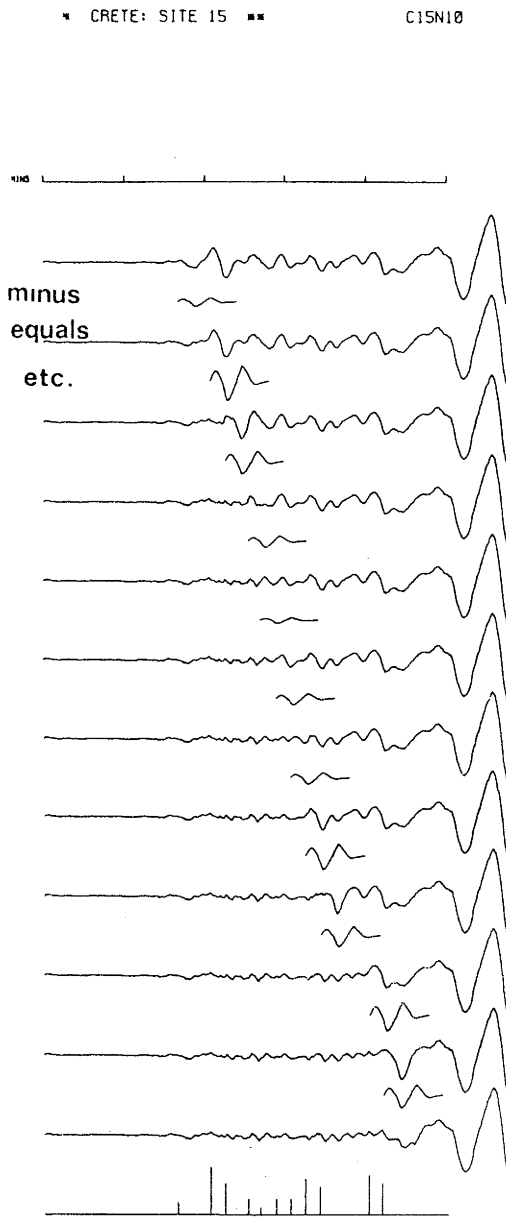


Fig. 3. An illustration of the method of sequential decomposition, as applied to the SH wave train recorded from the Crete earthquake at NORSAR site 15. The same wavelet (with only the amplitude changed) is subtracted sequentially from the train up to the arrival of the Love wave. The difference error formed by subtraction is demonstrably small. The times and amplitudes of the component wavelets are represented by the spike sequence at the bottom of the figure.

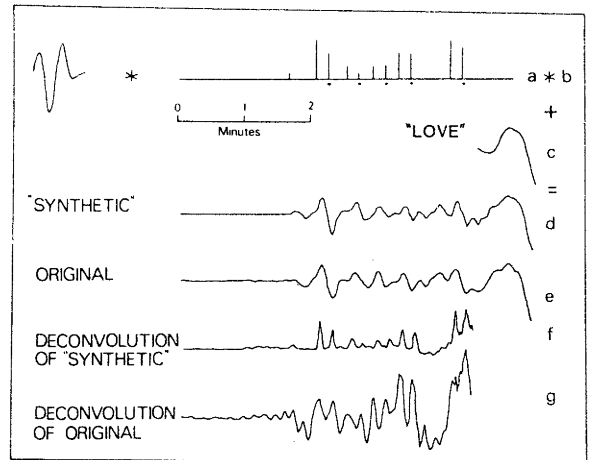


Fig. 4. Convolution of the wavelet (a) with the spike sequence (b) of Fig. 3, with the addition of an inferred Love wave arrival (c), results in a "synthetic" SH train (d) which is compared with the original record (e). When the synthetic (d) is automatically deconvolved using an inverse filter derived from wavelet (a), the resulting spike sequence (f) is similar to that of (b). If, however, the same technique is applied to the original record (e) using the same wavelet, the complex deconvolved record (g) results, illustrating the limitations inherent in deconvolving such trains by standard techniques. The asterisks at the bottom of the spike sequence indicate arrivals of probable "sS" type.

convolution using a program written by J. Claerbout, in which 5% white noise is added to the diagonal element of the autocorrelation matrix, was for the present purposes indistinguishable from that shown.

4. Discussion of method

The remarkable similarity between the recorded and reconstructed wave trains in Fig. 4 appears to vindicate the fundamental assumption underlying sequential decomposition, namely that the recorded SH train can be represented by a wavelet and a spike sequence. Of particular interest in the spike sequence of Fig. 4 is the succession of paired spikes, suggesting a series of phases accompanied by their near-surface-reflected counterparts. The time separation within each pair is 10–11 s, corresponding to a focal depth of 22–24 km; a focal depth of 26 km was reported for the event by NEIS (ISC gives 37 km). The reflection coefficient for SH waves incident upon a free surface is

always real and unity, meaning that there can be no phase shift and partitioning of energy, i.e. the polarity of the reflected phase is determined solely by the orientation of the source. The absence of polarity reversals between phase pairs indicates that the source mechanism was predominantly strike-slip (Helmberger, 1974), which is not unreasonable on tectonic grounds (McKenzie, 1972), and is consistent with the configuration of the response wavelet.

It is apparent from Fig. 4 that the empirical procedure improves resolution dramatically, albeit subjectively. The automatic procedure, on the other hand, improves resolution less dramatically and at the expense of a signal-to-noise degradation. The quality of automatic deconvolution is limited, *inter alia*, by the fidelity of the wavelet used for filter synthesis. The authors remark that the non-white nature of the putative spike sequence and the unknown phase properties of the effective source wavelet preclude the possibility of determining the wavelet directly from the trace autocorrelation (e.g. Dey-Sarkar and Wiggins, 1976). The empirical method seeks the least number of spikes that is consistent with the data, and differs fundamentally from the least-squares method (Robinson 1967). The method appears to be conceptually similar to the Minimum Entropy Deconvolution technique introduced by Wiggins (1977), although it does not use multiple traces except to extend the distance range of the observations. Formal development of an optimum processing strategy is beyond the scope of the present paper, but is currently under investigation. The method presented here is approximate in that it assumes the absence of phase distortion (although it allows for the possibility of phase inversion), however, the assumption of a stationary wavelet is implicit in many seismic data analysis strategies (Helmberger and Engen, 1974; Dey-Sarkar and Wiggins, 1976; Burdick, 1981). In general the effect of moderate phase distortion is to produce a small shift in the apparent arrival time of the phase. The method should therefore be considered as providing a first approximation solution which can then be used as a starting model for the application of refinement techniques. As will be argued in the next section, it seems that the phase distortion present in the

detected arrivals is usually small.

In the following section the extended sequence of arrivals found by the above method for the entire data set of Table I is interpreted in terms of singly- and multiply-reflected/refracted SH phases in a layered upper mantle.

5. Results and interpretation

For each of the five events listed in Table I, HT seismograms from the extreme sites of the NORSAR array were decomposed into their component wavelets according to the technique described earlier. Original, decomposed and reconstructed seismograms from each event are shown

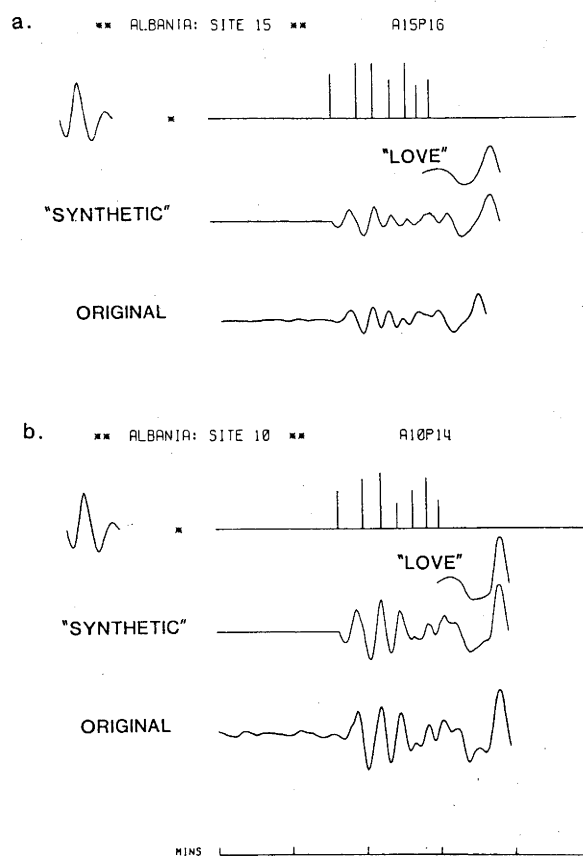


Fig. 5. Reconstructions of wave trains from spike sequences derived from sequential decomposition of SH trains from Albania earthquake recorded at NORSAR sites (a) 15 and (b) 10, compared with the original records (cf. Tables I and II).

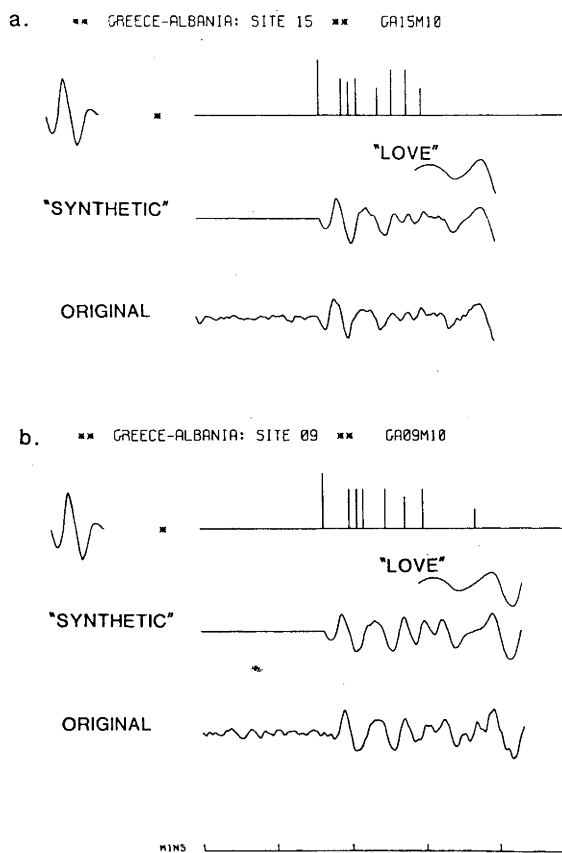


Fig. 6. Same as Fig. 5, for Greece-Albania earthquake recorded at sites (a) 15 and (b) 9.

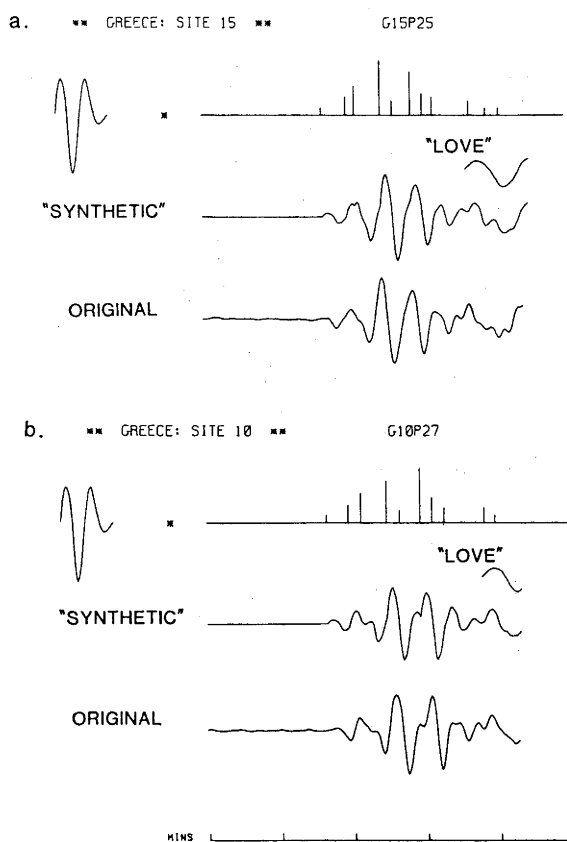


Fig. 7. Same as Fig. 5, for Greece earthquake recorded at sites (a) 15 and (b) 10.

in Figs. 5–9. The times and distances were calculated from NEIS locations, with corrections for focal depth applied (Table II). NEIS data were used because when the records were processed at NORSAR the ISC determinations were not available; the effect of small errors in location would, however, be minimal.

Throughout this part of the study, the modelling strategy was to match wave shapes, times and amplitudes, in order to obtain the best possible approximations to the original records. This was most successful for the Crete event (Fig. 9), where the noise level was very low, and perhaps least successful for Greece-Albania (Fig. 6), where the noise level was high. Some obvious departures in the modelling are at the beginning of the records, where it seemed necessary to make the amplitude

of the first arrival too large in order to match the shape of the succeeding peak. This could be an effect of phase distortion in the second arrival (since the direct first arrival is not distorted); alternatively, it may indicate the presence of an arrival intermediate between those modelled by the first and second spikes. This will be further discussed below. It is not apparent in the Turkey records shown here (Fig. 8) that the trains commence with a trough, as shown in the modelling, but arrivals at other array sites show that a trough is present. Difficulties in modelling also occurred in the parts of the records where the Love waves began to arrive, and the spike sequences in these regions have no claim to high accuracy.

Apart from Crete, the only event for which presumed "sS"-type reflections were found was

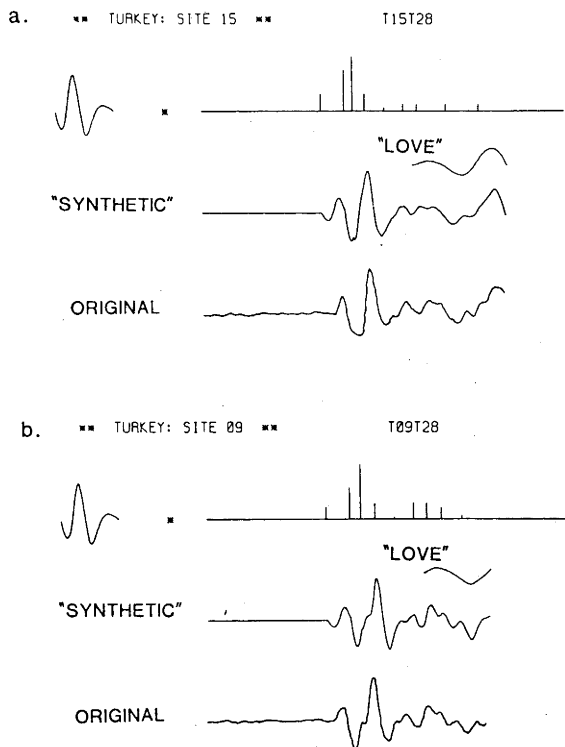


Fig. 8. Same as Fig. 5, for Turkey earthquake recorded at sites (a) 15 and (b) 9.

Greece, with an apparent "sS-S" separation of 27–28 s, corresponding to a focal depth of 65–70 km. The NEIS focal depth determination was 83 km, compared to a calculation of 75 km by ISC. The other events were apparently shallow, with depths of 15, 11 and 24 km from NEIS, and 15, 11 and 16 km from ISC, for Albania, Greece–Albania and Turkey, respectively. It is therefore probable that the wavelets derived for these events were a combination of the direct wave and the near-surface reflection.

It is noteworthy that no arrival having a reversed phase was detected on any of the records. It can be shown from eq. 12-25 of Pilant (1979) that the phase shift of an SH wave totally reflected at a plane interface between two elastic media varies from zero at the critical angle to π at grazing incidence. Under these conditions, the effect of geometrical spreading is such that the amplitude of the wave is large in the vicinity of the critical

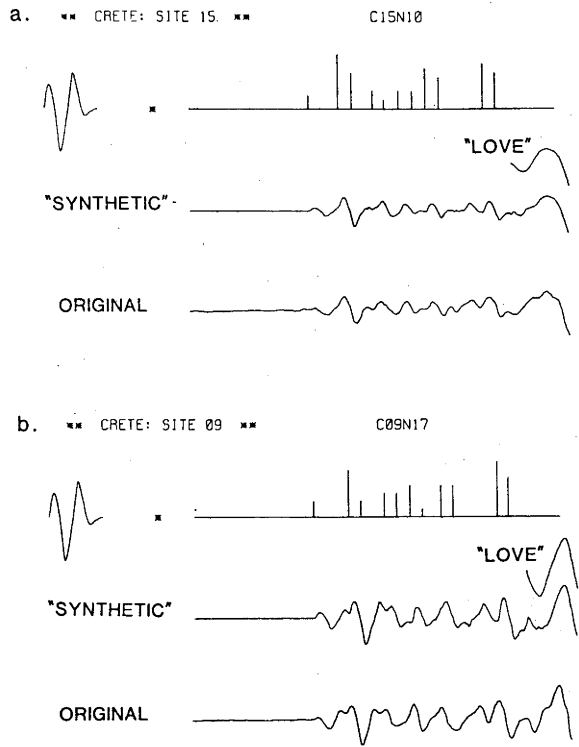


Fig. 9. Same as Fig. 5, for Crete earthquake recorded at sites (a) 15 and (b) 9.

angle, but decreases fairly rapidly as the angle of incidence increases, i.e. as the phase shift increases. This is illustrated in Fig. 10. When total reflection occurs within a transition zone, on the other hand, the wave energy tends to be distributed more evenly along the retrograde branch. The absence of detected phase reversals may indicate, therefore, that velocity changes in the upper mantle take place over depth intervals which are small compared with the wavelengths (~ 100 km) of the signals recorded by the NORSAR LP instruments, so that reflected phases with large phase shifts are sufficiently small to be masked by other arrivals. As Fig. 11 of Choy and Richards (1975) indicates, the amount of distortion in the wave form is small for phase shifts up to at least 30° , so the presence of phase shifts of this order will not

TABLE II

Spike sequence data used in Fig. 11

Event	Albania		Greece-Albania		Greece		Turkey		Crete	
	Site Code	Site Code	Site Code	Site Code	Site Code	Site Code	Site Code	Site Code	Site Code	Site Code
Δ , deg	20.84	21.70	21.73	22.68	23.63	24.50	24.35	25.30	26.56	27.52
δ , deg	0.09	0.09	0.06	0.06	0.58	0.58	0.14	0.14	0.15	0.15
Δ_c , deg	20.93	21.79	21.79	22.74	24.21	25.08	24.49	25.44	26.71	27.67
t , s	516.5	531.5	534.9	554.9	548.0	563.0	572.0	587.0	608.3	623.3
t_r , s	4.9	4.9	3.6	3.6	25.8	25.8	7.8	7.8	8.4	8.4
t_c , s	521.4	536.4	538.5	558.5	573.8	588.8	579.8	594.8	616.7	631.7
t_r , s	21.2	15.6	17.7	15.0	-4.8	-10.6	-5.5	-13.2	-21.7	-29.6
Spike sequence	0	0	0	0	0	0	0	0	0	0
s	21	20	18	21	20	18	19	19	24	28
	34	35	24	27	27 *	28 *	26	28	35 *	38 *
	49	48	30	32	48 *	49 *	37	39	52	57
	61	62	47	50	58	60	53	56	61 *	67 *
	77	73	59	66	73 *	77 *	69	72	73	78
	115	82	71	81	83 *	87 *	80	83	84 *	88 *
		116	83	124	91	97	104	95	95	103
					119 *	129 *	132	110	106 *	113 *
					128	138			142	149
					137	147			152 *	158 *
					147	157				

Notes: Site is the NORSAR site number taken from Fig. 1 of Bertuessen (1976).

Code is an event/site code used in Fig. 10.

 Δ is epicentral distance calculated from the NEIS location (Table I). δ is a distance correction calculated from the NEIS focal depth. Δ_c is corrected epicentral distance, used in Fig. 10. t is travel time calculated from observed S arrival time and NEIS origin time. t_r is a time correction calculated from the NEIS focal depth. t_c is corrected travel time. t_r is reduced time $t_c - \Delta_c \times 23.9$.Spike sequence times should be added to t_r to give the times in Fig. 10.

* Spike sequence times interpreted as arrivals of "sS" type.

invalidate the technique. They do, however, produce a time change of ϕ/ω , where ϕ is the phase shift and ω the wave frequency (Ewing et al., 1957, p. 90). The effect is relatively small; for a phase shift of 30° in a wave of period 20 s, the equivalent time change is 1.7 s.

It may also be noted that reflection of SH waves at a free surface is not accompanied by a phase shift (Pilant, 1979, p. 89), so phases of "SS" type would be consistent with the observations in this respect.

The times of all the inferred arrivals (corresponding to the spike sequences of Table II and

Figs. 5-9) have been summarized on a reduced time plot in Fig. 11. Although this aggregation of the data—especially for the later-arriving phases—is somewhat bewildering at first, certain aspects of the figure give cause for encouragement. There is, for example, excellent agreement between the sequences A10 and GA15, for which the corrected distances were virtually identical. Again, although the scatter of the data undoubtedly inhibits the recognition of distance-related trends in the sequences of arrivals, some trends are visible on close inspection. In general, the scatter is worst where small arrivals have been picked towards the

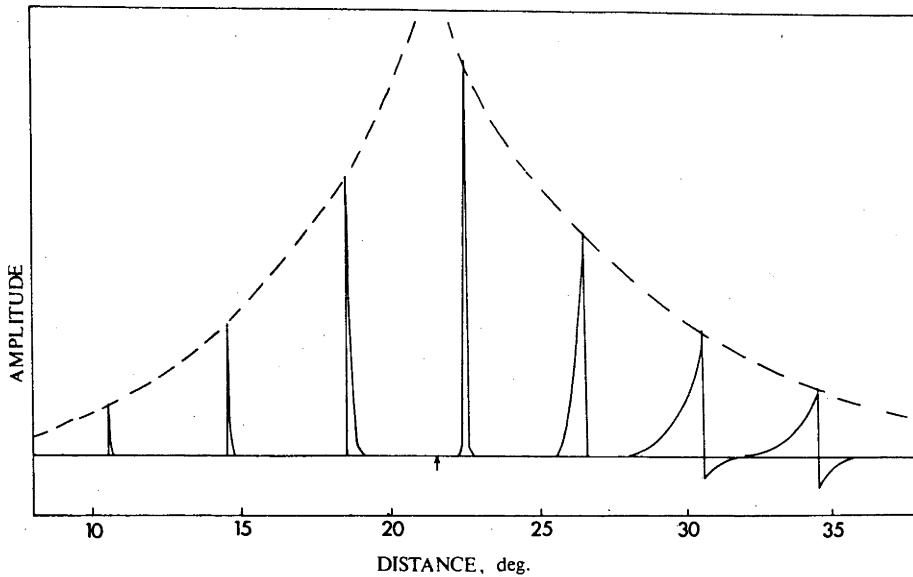


Fig. 10. Cartoon based on synthetic data, showing the variation in amplitude and shape of a pulse as it passes along a reflection branch. The arrow marks the position of the critically-reflected arrival. Note how degradation of the signal is accompanied by decrease in amplitude as the angle of incidence increases beyond the critical angle.

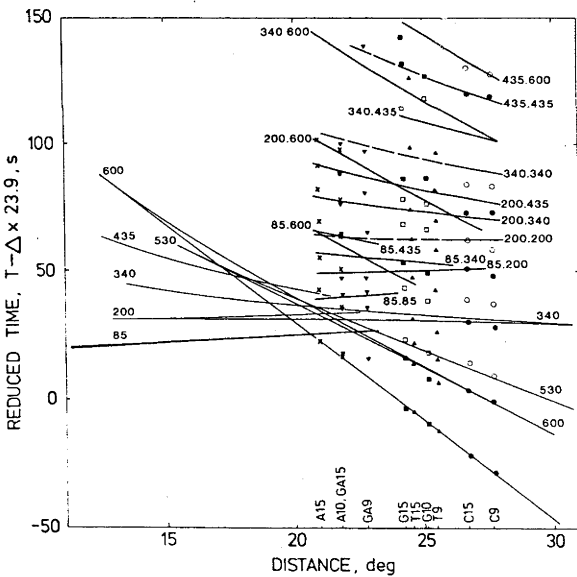


Fig. 11. Reduced travel-time/distance plot for the spike sequences listed in Table II. The open symbols \square , \circ represent probable surface-reflected phases of "sS" type. Also shown are (i) a branched travel-time curve derived from the S-velocity distribution of Table III, with cusps labelled according to the bottoming depths of the associated rays; and (ii) a series of multiple branches of "SS" type (where x, y are the bottoming depths of the two legs of the phase x, y), labelled as x, y .

end of a sequence, where the record is disturbed by the presence of a Love wave. Scatter may also have been produced by factors such as phase distortion and structural variations along the path. Perhaps most importantly, phases arriving within about a quarter-wavelength of each other are very difficult to separate, and may be interpreted as a single phase.

Single ray paths in plausible upper mantle models can only account for the first few arrivals of the sequences in Fig. 11. It was therefore necessary to consider multiples incorporating a free-surface reflection, both symmetric (of $2S_x$ type) and asymmetric (of $S_x S_y$ type; where x and y are the depths of reflecting/refracting horizons). It quickly became apparent that, in addition to the well-known discontinuities near 400 and 600 km (and possibly also near 500 km), additional discontinuities had to be postulated above these levels. From a model with discontinuities at 85, 200 and 340 km, reasonable approximations to the slowness vector estimates of the spike sequences were obtained with the multiples $2S_{85}$, S_{85} , S_{200} , $S_{85}S_{200}$, $2S_{200}$, $2S_{340}$, $S_{200}S_{435}$, $S_{340}S_{435}$ and $2S_{435}$ as computed by geometrical ray theory. Asymmetric multiples in-

volving more widely separated combinations of these presumed discontinuities (e.g. $S_{85}S_{435}$, $S_{85}S_{600}$, $S_{200}S_{600}$ and $S_{340}S_{600}$) would also occur, and have been included in Fig. 11 (multiples involving a discontinuity at 530 km have not been included because its existence has been inferred from only one pair of points). Although these additional multiples may well contribute to the scatter in the observations, they will in general be of low amplitude, since they will normally include a reflection (from the shallower of the discontinuity pair) having an angle of incidence much smaller than the critical angle. They nevertheless indicate the potential complexity of the SH train, and the need to refine the model by the use of complete synthetic seismograms.

Details of the derived S velocity model are provided in Table III. The 435 and 600 km discontinuities are well known in the literature; so, to a lesser extent, is the 530 km discontinuity (see for example Jordan and Anderson, 1974; Helmberger and Engen, 1974). As noted above, the presence of a discontinuity at 530 km has been inferred here only from arrivals associated with the Turkey event, although similar phases could have been obscured in the Greece and Crete records by "sS"-type arrivals at about the same times (cf. Fig. 11). It

TABLE III

S-velocity model for the upper mantle beneath eastern Europe

Depth (km)	Velocity (km s ⁻¹)
0	3.67
40	3.67
40	4.50
85	4.48
85	4.53
200	4.25
200	4.50
340	4.50
340	4.80
435	4.35
435	5.15
530	5.05
530	5.38
600	5.40
600	6.17
700	6.17

may be remarked also that the separation between the direct and 600 km branches in Fig. 11 is much greater in this distance range than that given by Helmberger and Engen's (1974) model. In fact the Helmberger and Engen study included few observations in this range, and the position of the 600 km branch was inferred by them from other data rather than directly observed. The 600 km branch arrivals are the clearest and largest of all on the authors' records. It is possible, however, that intermediate arrivals (corresponding, say, to a discontinuity at about 650 km) are also present, but because of low amplitudes were not separable. This could be the reason for the difficulty in matching the amplitudes of the first arrivals, and may also explain the late "first" arrival on GA9 (see Fig. 11).

Although the model as a whole is more complicated than many published upper mantle models—including a P-velocity model by Burdick and Helmberger (1978)—there are many indications that the upper mantle is more complex than previously supposed. The presence of small discontinuities near 100 and 200 km has been inferred from P-wave data in various parts of the world (see

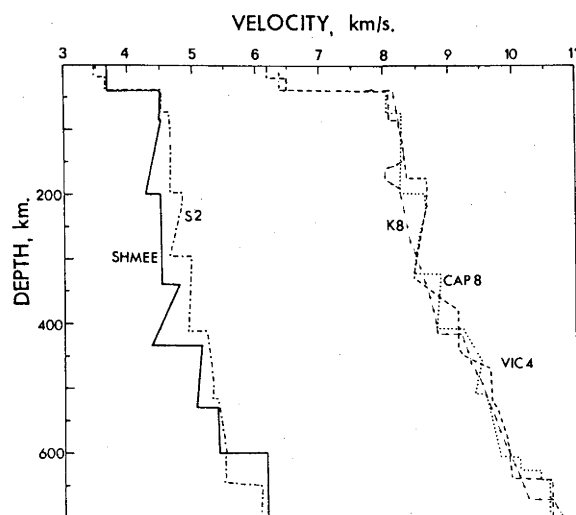


Fig. 12. The S-velocity distribution of Table III (SHMEE), compared with an S-velocity distribution (S2) by Hendrajaya (1981) and P-velocity distributions (K8, CAP8, VIC4) by Given and Helmberger (1980), Hales et al. (1980) and McMechan (1979).

Green and Hales, 1968; Mereu and Hunter, 1969; Hirn et al., 1973; Muirhead et al., 1977 for the former; and Lehmann, 1959, 1962; Hales et al., 1970; 1980; Steinmetz et al., 1974; Ram Datt and Muirhead, 1976; Muirhead et al., 1977 for the latter). Indeed Anderson (1979) has named the feature at 200 km the Lehmann discontinuity because of its global significance. In Fig. 12, the present S-velocity model (SHMEE) is compared with a recent complex shear velocity model of the upper mantle beneath central Australia, S2, obtained from an array analysis by Hendrajaya (1981). In addition, some recent complex compressional velocity models of the upper mantle beneath central Australia (CAP8: traverse experiment by Hales et al., (1980)), northwestern Eurasia (K8: slowness estimates and synthetic seismogram analysis by Given and Helmberger (1980)) and eastern United States (VIC4: amplitude constrained data analysis by McMechan (1979)) are also presented. Although the P and S data sets are from different regions, the resemblance between the P and S models are striking.

6. Conclusions

The further progress of observational seismology depends to a large extent on the utilization of as much of the seismic record as possible, rather than just the more readily identifiable phases. In recent years, considerable advances have been made in this direction by the use of synthetic seismograms in modelling. Until now, however, attention has been largely restricted to the successful modelling of the first few cycles of the train (see for example Helmberger and Engen, 1974). An attempt has been made here to model the entire SH train. It has been shown that the entire SH-wave train before the Love wave onset can be modelled by a sequence of stationary phase wavelets and that this sequence can be interpreted in terms of refracted arrivals together with multiples incorporating free surface reflections for a somewhat complex upper mantle model. Although the approach has been an empirical one and neither the wavelet sequence nor the interpretation in terms of refractions and multiple reflections is

likely to be unique, a model having a sufficiently close approximation to the real Earth to be capable of realistic refinement using synthetic seismogram techniques has been generated.

It is stressed again, therefore, that the model presented here must be viewed as a starting model for a further stage in the investigation. The solution obtained is undoubtedly non-unique, not only on account of the well-known trade-off between the positions of the interfaces and the velocity gradients between them, but also because the aim of obtaining the simplest model consistent with the data has almost certainly resulted in an oversimplified series of spike sequences. It is hoped that when complete synthetic seismograms are derived from the model, the discrepancies in amplitude (and wave shape) thus revealed will enable the velocity structure to be refined to the extent that a close approximation to uniqueness will be achieved.

Acknowledgements

The data used in this study were processed, and the work commenced, while two of us (JRC, DWK) were in receipt of NTNF Fellowships at NORSAR. Another of us (SFI) has since spent time at NORSAR collecting additional data for a continuation of the study.

References

- Anderson, D.L., 1979. The deep structure of continents. *J. Geophys. Res.*, 84: 7555-7560.
- Bertuessen, K.A., 1976. The origin of slowness and azimuth anomalies at large arrays. *Bull. Seismol. Soc. Am.*, 66: 719-741.
- Bungum, H., Husebye, E.S. and Ringdal, F., 1971. The NORSAR array and preliminary results of data analysis. *Geophys. J. R. Astron. Soc.*, 25: 115-126.
- Burdick, L.J., 1981. A comparison of upper mantle structure beneath North America and Europe. *J. Geophys. Res.*, 86: 5926-5936.
- Burdick, L.J. and Helmberger, D.V., 1978. The upper mantle P velocity structure of the western United States. *J. Geophys. Res.*, 83: 1699-1712.
- Choy, G.L., 1977. Theoretical seismograms of core phases calculated by frequency dependent full wave theory, and their interpretation. *Geophys. J.R. Astron. Soc.*, 51: 275-311.

- Choy, G.L. and Richards, P.G., 1975. Pulse distortion and Hilbert transformation in multiply reflected and refracted body waves. *Bull. Seismol. Soc. Am.*, 65: 55-70.
- Dey-Sarkar, S.K. and Wiggins, R.A., 1976. Source deconvolution of teleseismic P wave arrivals between 14° and 40°. *J. Geophys. Res.*, 81: 3633-3641.
- England, P.C., Worthington, M.H. and King, D.W., 1977. Lateral variation in the structure of the upper mantle beneath Eurasia. *Geophys. J.R. Astron. Soc.*, 48: 71-79.
- Ewing, W.M., Jardetzky, W.S. and Press, F., 1957. *Elastic Waves in Layered Media*. McGraw-Hill, New York, 380 pp.
- Given, J.W. and HelMBERGER, D.V., 1980. Upper mantle structure of northwestern Eurasia. *J. Geophys. Res.*, 85: 7183-7194.
- Goncz, J.H. and Cleary, J.R., 1976. Variations in the structure of the upper mantle beneath Australia, from Rayleigh wave observations. *Geophys. J. R. Astron. Soc.*, 44: 507-516.
- Green, R.W.E. and Hales, A.L., 1968. The travel times of P waves to 30° in the central United States and upper mantle structure. *Bull. Seismol. Soc. Am.*, 58: 267-289.
- Hales, A.L., Hellsley, C.E. and Nation, J.B., 1970. P travel times for an oceanic path. *J. Geophys. Res.*, 75: 7362-7381.
- Hales, A.L., Muirhead, K.J. and Rynn, J.M.W., 1980. A compressional velocity model for the upper mantle. *Tectonophysics*, 63: 309-348.
- HelMBERGER, D.V., 1974. Generalised ray theory for shear dislocations. *Bull. Seismol. Soc. Am.*, 64: 45-64.
- HelMBERGER, D.V. and Engen, G.R., 1974. Upper mantle shear structure. *J. Geophys. Res.*, 79: 4017-4078.
- Hendrajaya, L., 1981. The shear-wave velocity structure in the mantle to 1100 km depth, determined using the Warramunga seismic array. Ph.D. Thesis, Australian National University, Canberra, unpublished.
- Hirn, A., Steinmetz, L., Kind, R. and Fuchs, K., 1973. Long range profiles in western Europe. II. Fine structure of the Lower lithosphere in France (Southern Bretagne). *Z.f. Geophys.*, 39: 363-384.
- Ibrahim, A.K. and Nuttli, O.W., 1967. Travel-time curves and upper mantle structure from long-period S waves. *Bull. Seismol. Soc. Am.*, 57: 1063-1092.
- Jordan, T.H. and Anderson, D.L., 1974. Earth structure from free oscillations and travel-times. *Geophys. J.R. Astron. Soc.*, 36: 411-459.
- Keilis-Borok, V.I., 1964. Seismology and logic. In: H. Odishaw (Editor), *Research in Geophysics*, Vol 2. MIT Press, Cambridge, MA.
- Keilis-Borok, V.I. (Editor), 1972. *Computational Seismology*. Consultants Bureau, London.
- Kind, R., 1978. The Reflectivity method for a buried source. *J. Geophys.*, 44: 603-612.
- Kind, R. and Muller, G., 1975. Computations of SV waves in realistic earth models. *Z.f. Geophys.*, 41: 149-172.
- King, D.W. and Calcagnile, G., 1976. P-wave velocities in the upper mantle beneath Fennoscandia and western Russia. *Geophys. J.R. Astron. Soc.*, 46: 407-432.
- King, D.W., Cleary, J.R. and Wang, C. Upper mantle modelling using long-period SH wave trains. (abstract), *EOS*. 59: 1141.
- Knopoff, L., 1972. Observation and inversion of surface-wave dispersion. *Tectonophysics*, 13: 497-519.
- Lehmann, I., 1959. Velocities of longitudinal waves in the upper part of the earth's mantle. *Ann. Géophys.*, 15: 93-118.
- Lehmann, I., 1962. The travel times of the longitudinal waves of the Logan and Blanca atomic explosions, and their velocities in the upper mantle. *Bull. Seismol. Soc. Am.*, 52: 519-526.
- McKenzie, D., 1972. Active tectonics of the Mediterranean region. *Geophys. J.R. Astron. Soc.*, 30: 109-185.
- McMechan, G.A., 1979. An amplitude constrained P-wave velocity profile for the upper mantle beneath the eastern United States. *Bull. Seismol. Soc. Am.*, 69: 1733-1744.
- Mereu, R.F. and Hunter, J.A., 1969. Crustal and upper mantle structure under the Canadian shield from Project Early Rise data. *Bull. Seismol. Soc. Am.*, 59: 147-165.
- Muirhead, K.J., Cleary, J.R. and Finlayson, D.M., 1977. A long-range seismic profile in south-eastern Australia. *Geophys. J.R. Astron. Soc.*, 48: 509-519.
- Nuttli, O.W., 1969. Travel-times and amplitudes of S waves from nuclear explosions in Nevada. *Bull. Seismol. Soc. Am.*, 59: 385-398.
- Pilant, W.L., 1979. *Elastic Waves in the Earth*. Elsevier, Amsterdam, 493 pp.
- Ram, A. and Mereu, R.F., 1977. Lateral variations in the upper-mantle structure around India as obtained from Guaribidanur seismic array data. *Geophys. J.R. Astron. Soc.*, 49: 87-114.
- Ram Datt and Muirhead, K.J., 1976. Evidence for a sharp velocity increase near 770 km depth. *Phys. Earth Planet. Inter.*, 13: 37-46.
- Ram Datt and Muirhead, K.J., 1977. Evidence of multiplicity in the P travel-time curve beyond 30 degrees. *Phys. Earth Planet. Inter.*, 15: 28-38.
- Robinson, E.C., 1967. *Multichannel Time Series Analysis with Digital Computer Programs*. Holden-Day, San Francisco, CA.
- Robinson, R. and Kovach, R.L., 1972. Shear wave velocities in the Earth's mantle. *Phys. Earth Planet. Inter.*, 5: 30-44.
- Steinmetz, L., Hirn, A. and Perrier, G., 1974. Reflexions sismiques a la base de l'asthenosphere. *Ann Géophys.*, 30: 173-180.
- Tukey, J.W., 1977. *Exploratory Data Analysis*. Addison-Wesley, Reading, MA.
- Wiggins, R.A., 1977. Minimum entropy deconvolution. Proceedings of the International Symposium on Computer Aided Seismic Analysis and Discrimination. June 9 and 16, 1977. Falmouth, MA. I.E.E.E. Computer Society, pp. 7-14.

APPENDIX 2

THE CALCULATION OF $\dot{v}(0)/c$

THE CALCULATION OF $\dot{v}(0)/c$.

The analytical derivation of the tangential surface displacements for the case of a general point source at depth $z=s$ in a layered medium may be written as

$$\begin{bmatrix} V_\ell \\ T_\ell \end{bmatrix} = \begin{bmatrix} \frac{\dot{v}_\ell(0)}{c} \\ 0 \end{bmatrix} + A_s^{-1} \begin{bmatrix} \Delta_{\ell 1} \\ \Delta_{\ell 2} \end{bmatrix} \quad \text{A2.1}$$

(Harkrider, 1964, equation 119). Here, $(\Delta_{\ell 1}, \Delta_{\ell 2})$ is the discontinuous displacement-stress vector defined in equations (4.9) and (4.20), and A_s is the product of the layer matrices above the source, including that part of the homogeneous source layer above the source, i.e.,

$$A_s = a_s a_{s-1} \cdots a_1$$

where the a_m are the layer matrix for the m th layer, and is given by

$$a_m = \begin{bmatrix} \cos Q_m & \frac{i \sin Q_m}{\mu_m r_{\beta m}} \\ i \sin Q_m \mu_m r_{\beta m} & \cos Q_m \end{bmatrix}$$

with $Q_m = kr_{\beta_m} d_m$, $k = \omega/c$, $d_m = z_m - z_{m-1}$, $\mu_m = \beta_m^2 \rho_m$,

$$r_{\beta_m} = \frac{c^2}{\beta_m^2} - 1 \quad c > \beta_m$$

$$r_{\beta_m} = -i \left(1 - \frac{c^2}{\beta_m^2} \right) \quad c \leq \beta_m$$

A2.2

c = phase velocity, β_m = shear velocity, ρ_m = density.

Writing the inverse of A_s as

$$(A_s)^{-1} = \begin{bmatrix} (A_s)_{22} & -(A_s)_{12} \\ -(A_s)_{21} & (A_s)_{11} \end{bmatrix}$$

Equation A2.1 may be rewritten as

$$\frac{\dot{v}_\ell(0)}{c} = V_\ell - (A_s)_{22} \Delta_{\ell 1} + (A_s)_{12} \Delta_{\ell 2}$$

$$T_\ell = -(A_s)_{21} \Delta_{\ell 1} + (A_s)_{11} \Delta_{\ell 2}$$

with

$$V_\ell = - \left[\frac{J_{12} - J_{22}}{J_{11} - J_{21}} \right] T_\ell$$

The J matrix is also a Haskell matrix, and is the product of the half-space

($m=n$) matrix (E^{-1}) and the layer matrix product for the whole space (A).
i.e.,

$$J = E^{-1}A$$

where

$$E^{-1} = \begin{bmatrix} (ik)^{-1} & 0 \\ 0 & -(ik \mu_n r_{\beta n})^{-1} \end{bmatrix}$$

$$A = a_{n-1} a_{n-2} \dots a_s \dots a_1 = a_{n-1} \dots a_{s+1} A_s$$

Using (A2.1), (4.9) and (4.20), the horizontal point force ($\ell = 1$) is given by

$$\frac{\dot{v}(0)}{c} = \left[\begin{array}{c} (A_s)_{12} - \frac{J_{12} - J_{22}}{J_{11} - J_{21}} (A_s)_{11} \end{array} \right] \frac{-kL(\omega)}{2\pi} \quad \text{A2.3}$$

and for the shear dislocation source ($\ell = 1, 2$).

$$\frac{\dot{v}_1(0)}{c} = 2ik^2 k_{\beta}^2 R \left[\frac{J_{12} - J_{22}}{J_{11} - J_{21}} (A_s)_{21} - (A_s)_{22} \right] \quad \text{A2.4}$$

$$\frac{\dot{v}_2(0)}{c} = -k^2 k_{\beta}^2 \mu R \left[\frac{J_{12} - J_{22}}{J_{11} - J_{21}} (A_s)_{11} + (A_s)_{12} \right]$$

APPENDIX 3

Ingate, S.F., 1983. An alternative method for fault-plane solutions from a single station. *Geophys.Res.Lett.*, (in press).

Abstract. An alternative to the method of Langston (1982) for determining fault-plane solutions from a single 3-component seismic station is proposed. The method calculates synthetic P and SH seismograms for three basic orientations of a shear dislocation embedded in a plane layered Earth model, and uses least-squares to minimise the error between the observed data and a linear sum of the synthetic seismograms. The result is five trigonometric functions of fault strike θ , fault dip δ , and rake of the slip vector λ . When applied to the Borrego Mountain event of 9 April 1968, the method provides a solution which is in close agreement with well-constrained studies of the main shock.

Introduction

Several situations arise where it is necessary to determine fault-plane solutions from a single station. In many parts of the world the distribution of seismic stations is inadequate to constrain both the nodal planes from first motion data. In other situations a solution may be required before the first motion data becomes available from the global network. Most important is that studies of historical earthquakes often have to rely on very few station records. Langston (1982) has presented a method to determine meaningful source orientation parameters from the analysis of long-period body-wave data obtained from a single three-component station. Langston's method employs a systematic trial-and-error technique of cycling through all combinations of strike, rake and dip of a fault plane, computing synthetic seismograms for P (dilatational waves) and SH (horizontally polarised rotational waves) and minimising some objective (albeit with subjective limits) difference function between the observed and synthetic seismograms. In all, 11,000 synthetic seismograms need to be calculated. This appears to be an unnecessary task. The least-squares technique presented here finds a solution directly, is numerically simpler, and does not require the assignment of arbitrary limits to an error function.

Method

For a shear dislocation point source, only three quantities (strike θ , dip δ of fault and rake λ of the slip vector) are required to specify the orientation of a fault plane and the slip vector because the source theory

used requires the condition that the couples be orthogonal. Thus, displacement Green's functions for an arbitrarily oriented double-couple embedded within a plane layered Earth may be easily calculated using ray or layer matrix methods. Consideration of the radiation pattern aside, time functions for an arbitrarily oriented shear dislocation may be alternatively generated by appropriately multiplying the orthogonally placed Green's functions for vertical strike-slip, vertical dip-slip and 45° dip-slip (seen at an azimuth of 45°) displacements and summing. Thus, in cylindrical coordinates (r, z, θ) , the far-field vertical, w , and horizontal tangential displacements, v , may be written as (Langston, 1982)

$$w(t, r, z, \theta) = S(t) * \sum_{i=1}^3 H_i(t, r, z) A_i(\theta, \delta, \lambda)$$

1

$$v(t, r, z, \theta) = S(t) * \sum_{i=4}^5 H_i(t, r, z) A_i(\theta, \delta, \lambda)$$

where $S(t)$ represents the source-time function, attenuation operator, geometrical spreading and instrumental response; A_i are trigonometric functions of fault strike θ , dip δ and rake λ , which can be found in Langston and Helmberger (1975, equation 2), and H_i the P and SH displacement Green's functions for vertical strike-slip ($i=1,4$), vertical dip-slip ($i=2,5$) and 45° dip-slip seen at 45° azimuth ($i=3$).

To solve for the unknown A_i , least-squares is used to minimize the error between the observed and synthetic seismograms. In matrix notation

$$\left(\sum_{t=0}^n H_i(t) H_j(t) \right)_{ij} (A_i) = \begin{cases} \sum_{t=0}^n (w(t) H_i(t)) & i, j, = 1, 3 \\ \sum_{t=0}^n (v(t) H_i(t)) & i, j = 4, 5 \end{cases} \quad 2$$

or solving for A_i

$$\underline{A} = \underline{H}^{-1} \underline{W}$$

which necessitates inversion of a 5x5 symmetric matrix, and calculating the cross-correlation vector (of synthetics with observed data) \underline{W} . Note that $H_i H_j = 0$ for $i < 3$, $j = 4, 5$ and for $i \geq 4$, $j < 3$. Thus the H matrix may be partitioned into 3x3 and 2x2 non-zero sub-matrices. The Green's functions are dependent on the Earth model, epicentral depth and ray take-off angle, and thus need be calculated once for each solution. Other than the model parameters, the reliability of the solution will be highly dependent on the source-receiver azimuth. Thus, SH data are included to increase the chances of finding a reliable solution. SV (vertically polarized rotational waves) data are not included due to possible contamination by the P coda and converted phases. For real data the inversion will be most successful when the station is located near the P-T axes (for P). Of course, without recourse to body-wave data analysis from a widely distributed network of instruments, there is a degree of non-uniqueness in the solution. Nevertheless, such a first-order solution may be considered reliable within the framework of the model.

Example

As a test of the method, it has been applied to the Borrego Mountain event of 9 April 1968 from which Langston (1982) has obtained a single station fault-plane solution. As this event has been studied at length (Allen and Nordquist, 1972; Burdick and Mellman, 1976), a solution does exist against which our results can be checked. The data were digitized from photographically enlarged figures given by Langston loc.cit. and the surface displacements were calculated using the ray method of Langston and Helmlinger (1975). The solution may contain errors because of both the digitization method and because the surface displacements are calculated for a shear dislocation at a depth of 9 km in a half-space. Langston calculated the response for a layer over a half-space, and was careful to include all important reverberations. The Moho (depth = 30 km) reflections show up as fairly low-amplitude ripples in the tail of the observed and synthetic data, as indicated in Figure 1. The difference error between the digitized waveform and Langston's synthetic is seen to be greater than the error between the digitized waveform and synthetic as calculated by this study; it would therefore appear that the assumption of a shear dislocation in a half-space is reasonable, especially as the least-squares inversion is attempting to match the first large excursions in the P-wave data rather

than the small ripples in the tail. Nevertheless, it is straight forward to incorporate a layered crustal model into the synthetics.

The least-squares solution determines that the event was predominantly strike-slip ($A_1, A_4 = -1.0, 0.49$), but with small components of vertical and 45° dip-slip ($A_2, A_3, A_5 = -0.11, -0.07, -0.01$). The relative contributions of the basic synthetic seismograms to the "best-fit" synthetic P and SH seismograms are shown in Figure 2. Using the normalized A_1 to solve the trigonometric functions (Langston and Helmberger, 1975, equation 2) for θ , δ and λ will actually give four solutions: two fault-planes and their normals (the auxiliary planes). This is due to the indeterminacy in sign of the inverse trigonometric functions, arising from the fact that a shear dislocation cannot be uniquely represented by an arbitrary linear sum of the Green's functions. The choice between one orthogonal pair and the other can be made given a priori knowledge of the direction of faulting in the source region. This assumption must be made for any inversion that assumes a pure dislocation source (including Langston's method). Of course, this least-squares scheme can be used to directly solve for the moment tensor if the source time function for each tensor element is known, thus enabling a unique solution to be P-T axes to be found. This direct approach may differ from the methods of moment tensor inversion of, among others, Dziewonski et al (1981) and Langston (1981). In their methods it is necessary to assume an initial solution to the moment tensor and proceed by iterations that may or may not converge depending upon the 'nearness' of the initial guess. This paper however, is concerned with developing a numerically more efficient method than the trial-and-error approach of Langston (1982) for which a bare minimum of data are available. Solving the trigonometric functions relative to SCP at an azimuth of 65° , we find $\theta=213^\circ$, $\delta=83^\circ$, $\lambda=0^\circ$. Presumably, these values for θ , δ and λ define the auxiliary plane, and thus by using equations 4.126-4.130 of Ben-Menahem and Singh (1981), the normal plane is right-lateral ($\lambda=187^\circ$), striking -57° with 89° dip. This is similar to the solution obtained by Allan and Nordquist (1972) ($\theta, \delta, \lambda = -48^\circ, 83^\circ, 180^\circ$), and Burdick and Mellman (1976) ($\theta, \delta, \lambda = -45^\circ, 81^\circ, 178^\circ$). Inspection of Figure 1 shows that our synthetics (correlation coefficients for P and SH data are 0.92, 0.88 respectively) fit the data much more closely (excluding reverberations) than Langston's synthetics (correlation coefficients 0.82, 0.77). No claim to exactness of solutions to fault-plane mechanisms from single station data can be made as the procedure is highly non-unique. Yet, the solutions

are demonstrably similar to solutions obtained by previous workers. The results then represent workable first-order solutions.

Acknowledgements. I thank Anton Hales for his help and discussions in the early part of this work, Ken Muirhead and Gunter Bock for critically reading the manuscript, and Charles Langston for his helpful review.

References

- Allen, C.R. and J.M. Nordquist, Foreshock, main shock and larger aftershocks of the Borrego Mountain earthquake, U.S. Geol. Surv. Profess. Paper 787, 16-23, 1972.
- Ben-Menahem, A. and S.J. Singh, Seismic Waves and Sources, Springer Verlag, 1108 pp, 1981.
- Burdick, L.J. and G.R. Mellman, Inversion of the body waves from the Borrego Mountain earthquake to the source mechanism, Bull. Seism. Soc. Am., 66, 1485-1499, 1976.
- Dziewonski, A.M., T.-A. Chou and J.H. Woodhouse, Determination of earthquake source parameters from wave-form data for studies of global and regional seismicity, J. Geophys. Res., 86, 2825-2852, 1981.
- Langston, C.A., Source inversion of seismic waveforms: the Koyna, India, earthquakes of 13 September 1967, Bull. Seism. Soc. Am., 71, 1-24, 1981.
- Langston, C.A., Single-station fault plane solutions, Bull. Seism. Soc. Am., 72, 729-744, 1982.
- Langston, C.A. and D.V. Helmberger, A procedure for modelling shallow dislocation sources, Geophys. J. R. astr. Soc., 42, 117-130, 1975.

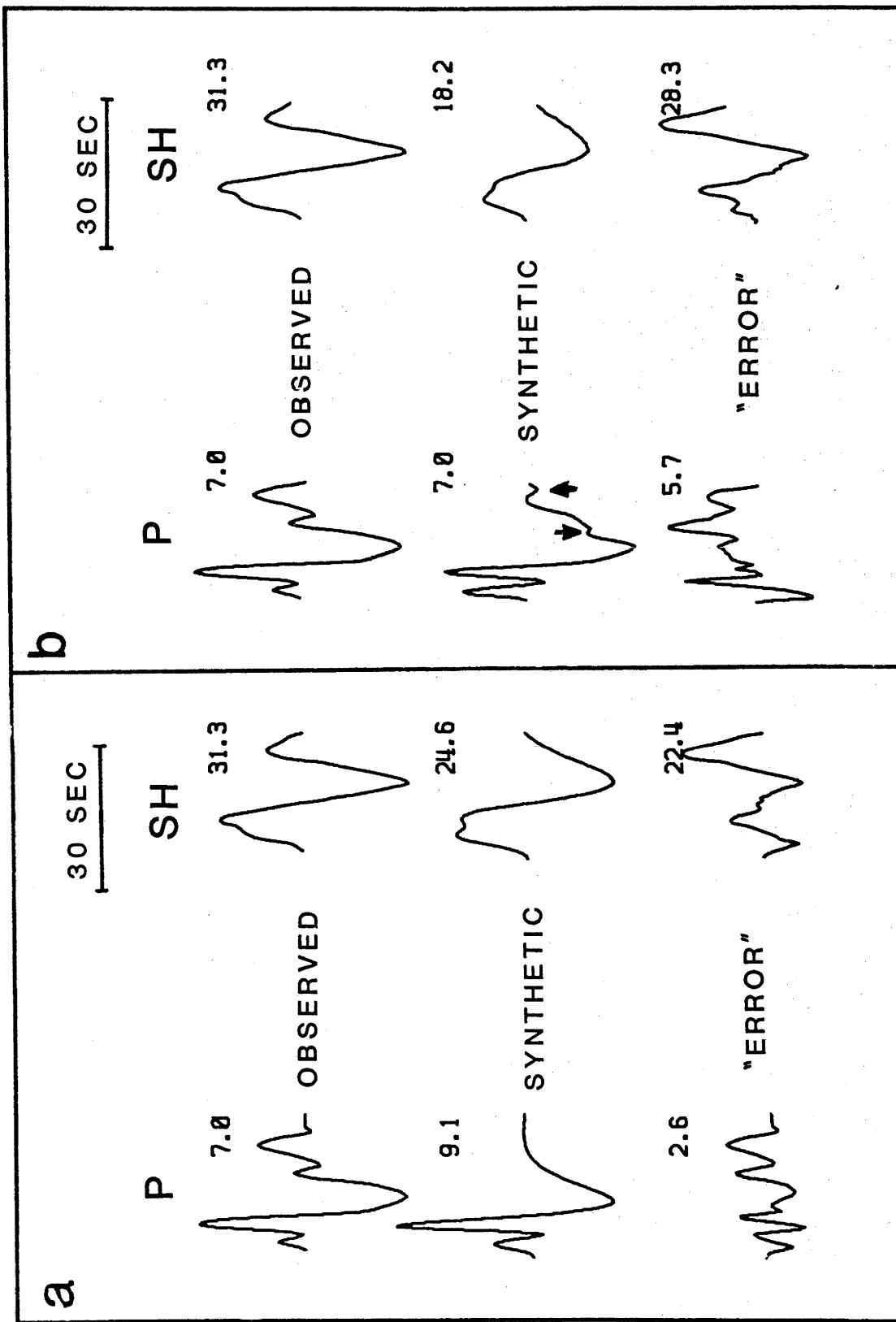


Figure 1: A comparison of the least-squares method (a) with the iterative method of Langston (b). The observed waveforms are of the Borrego Mountain earthquake recorded at SCP. The trace labelled error is the difference of observed and synthetic waveforms. The number to the right of each waveform is the amplitude in microns. The arrows indicate Moho reflection contributions included in

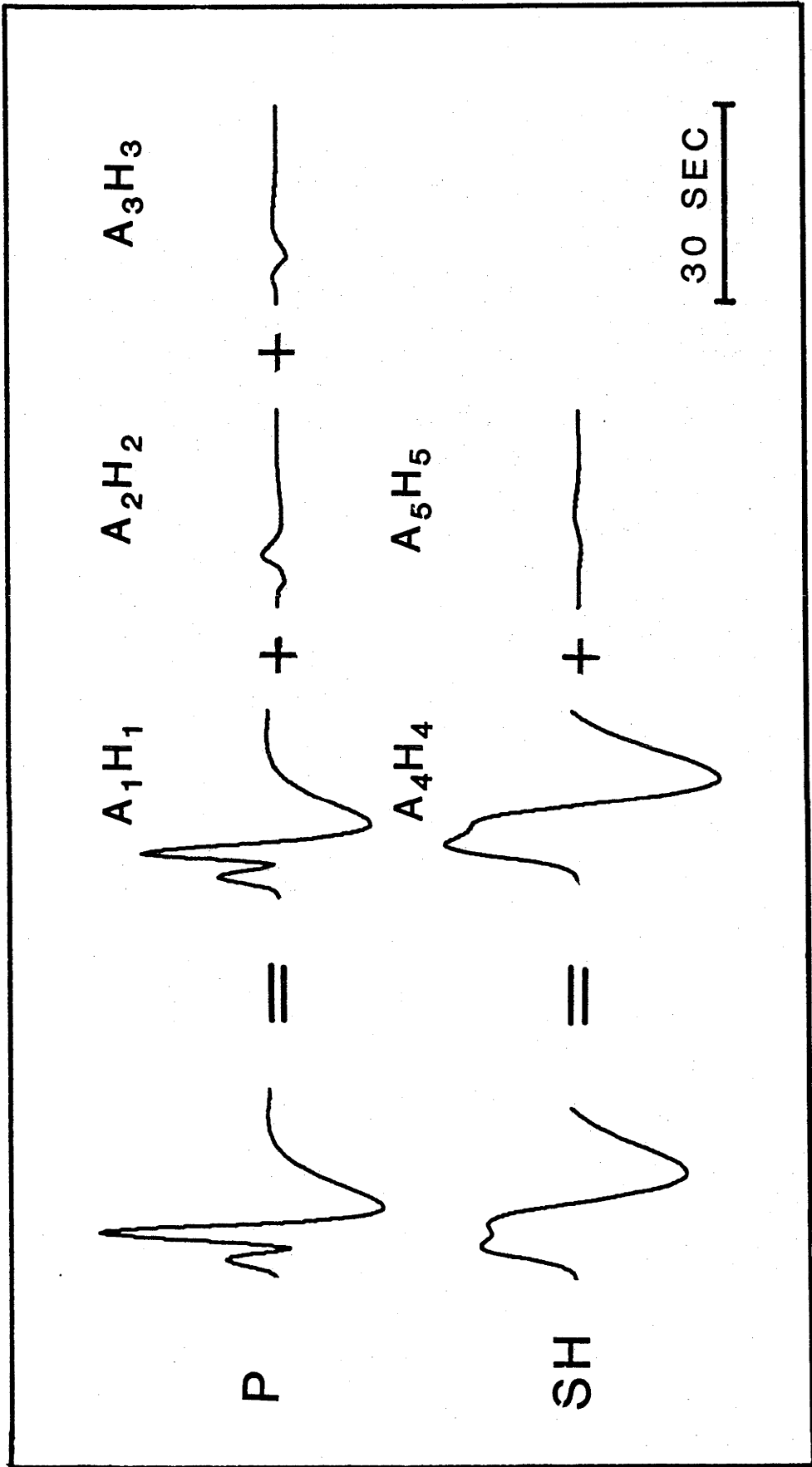


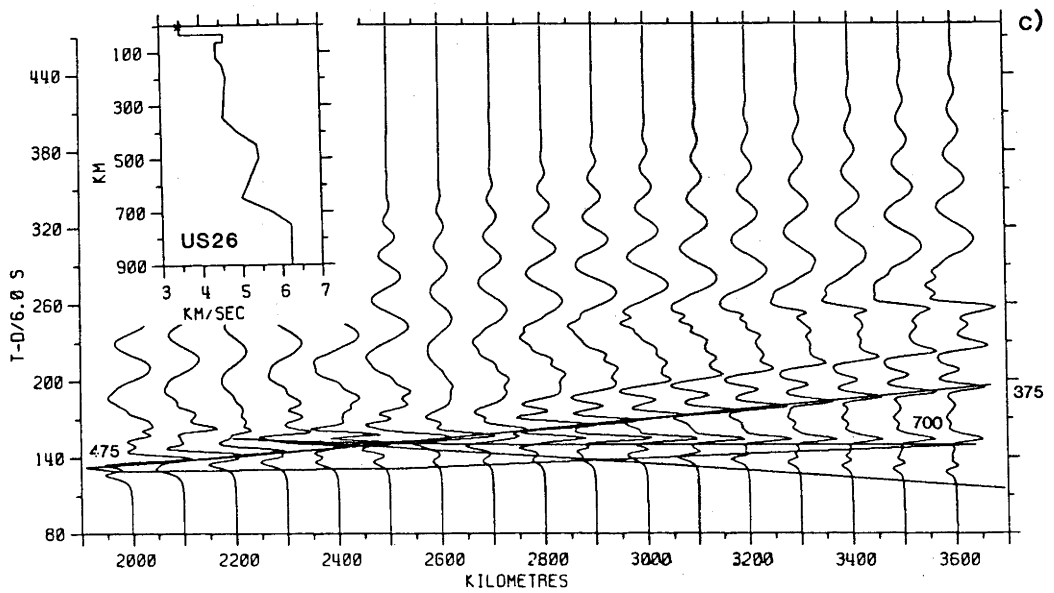
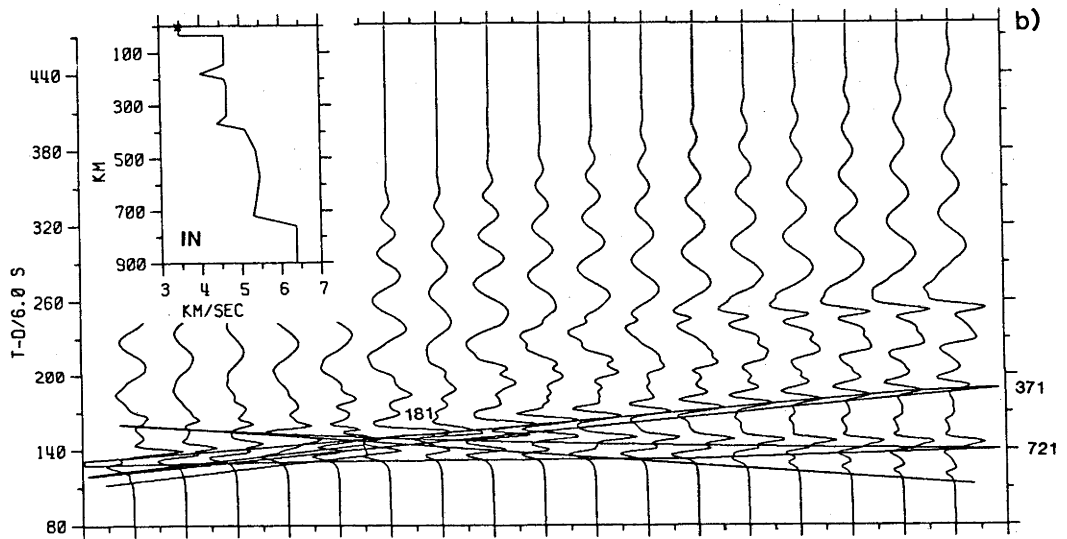
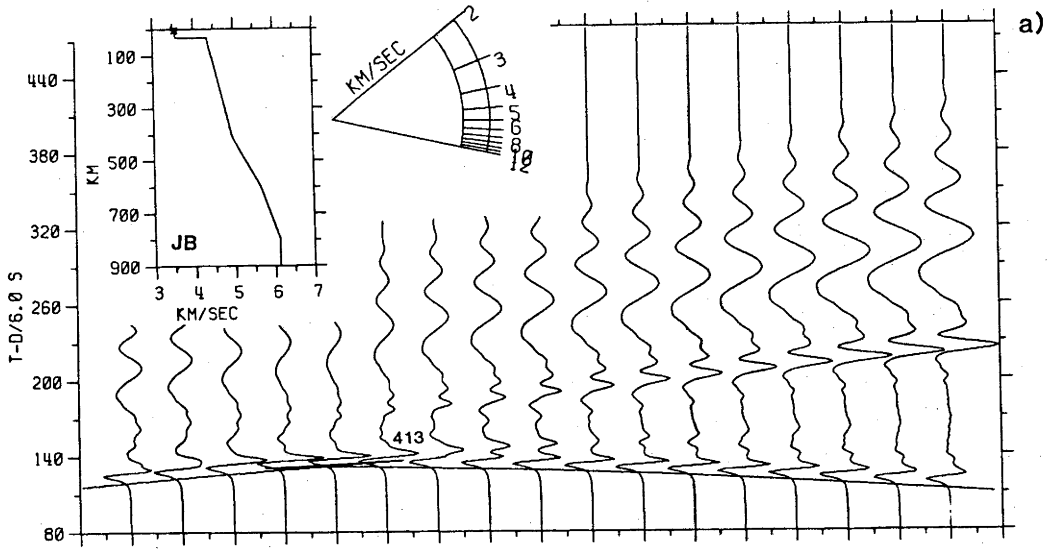
Figure 2: Relative contributions of the i th terms of Equation 1 to the synthetic P and SH seismograms of Figure 1a.

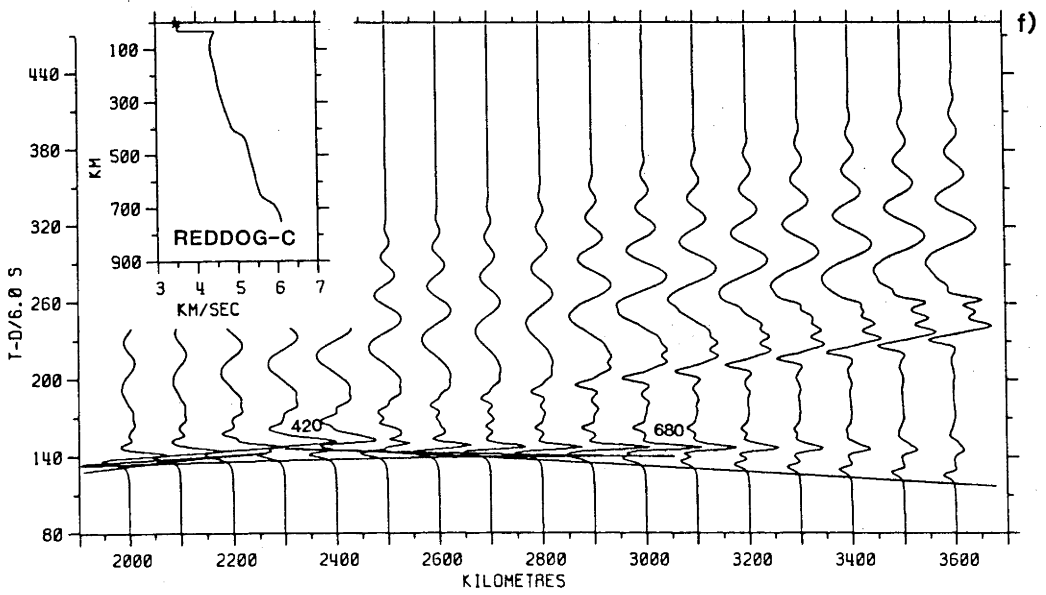
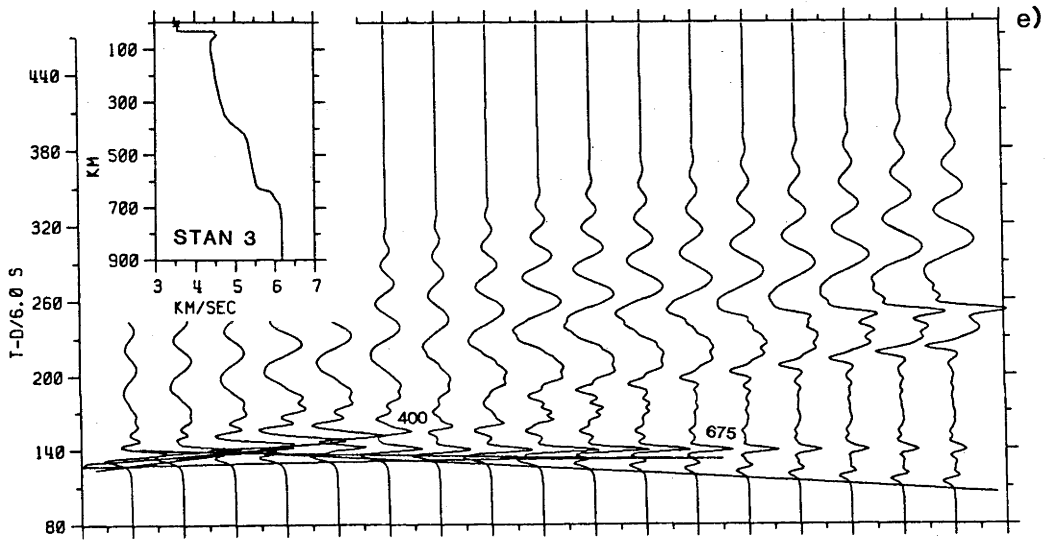
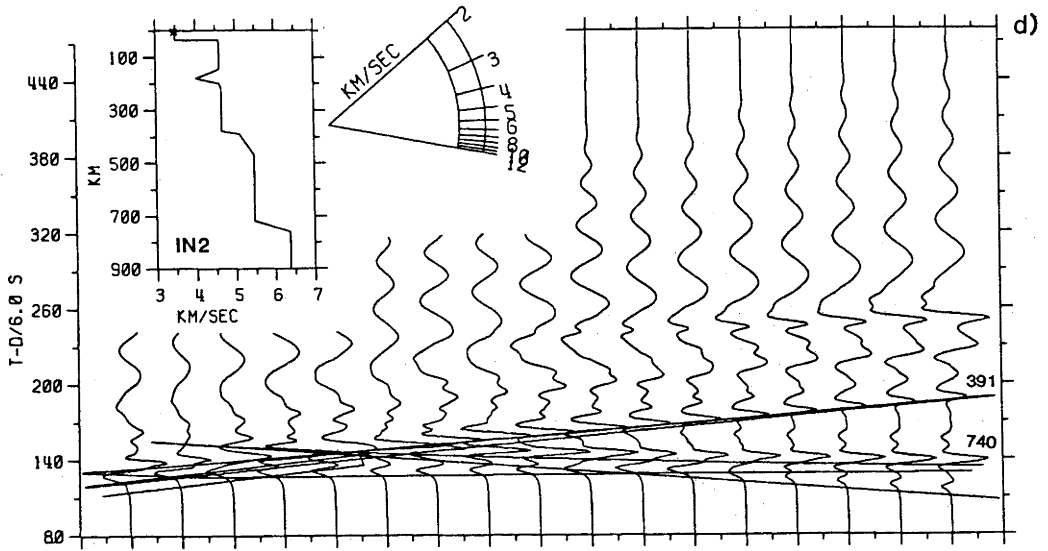
APPENDIX 4

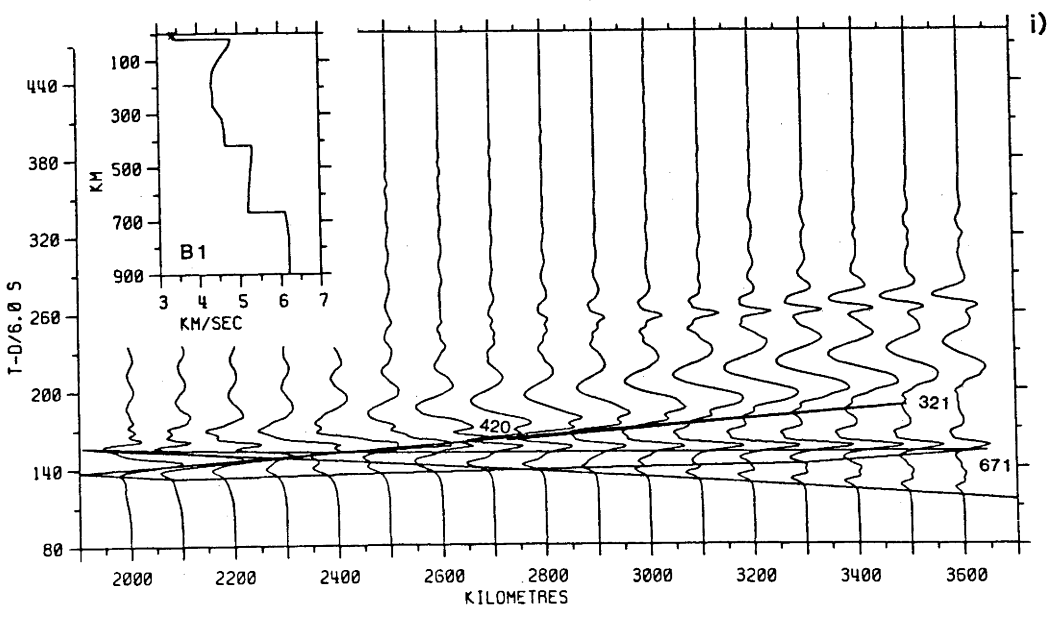
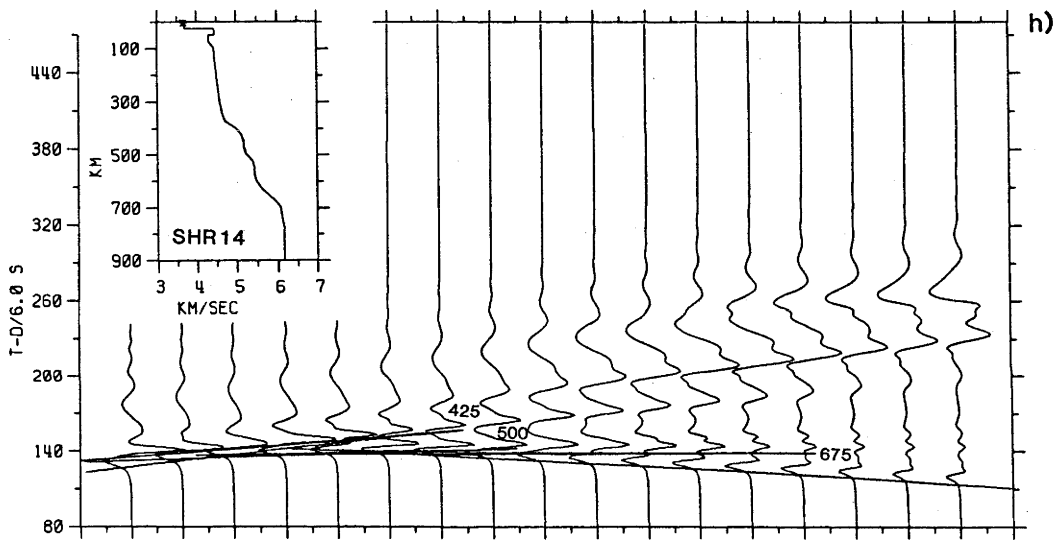
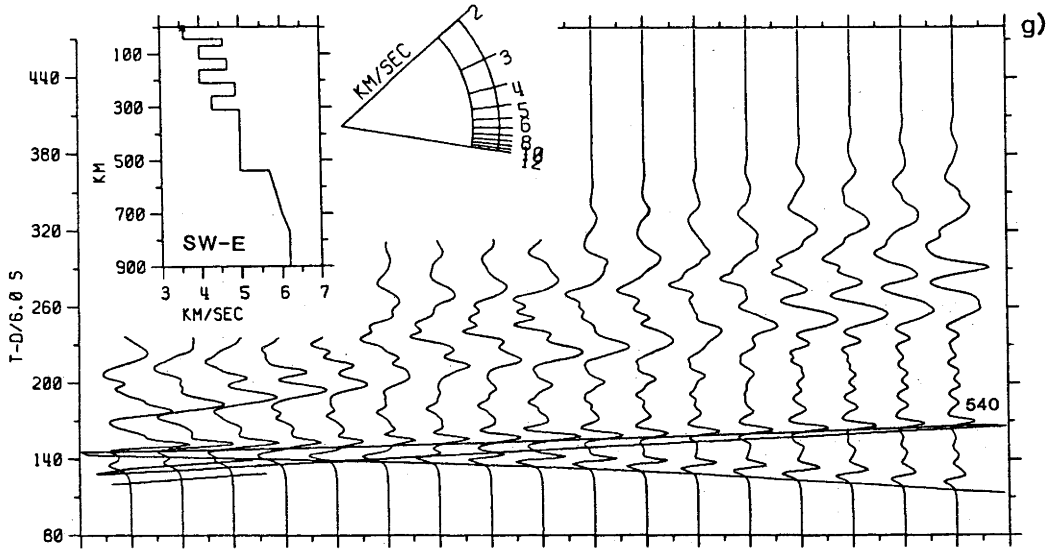
SYNTHETIC SH SEISMOGRAMS FOR A SUITE OF VELOCITY-DEPTH MODELS

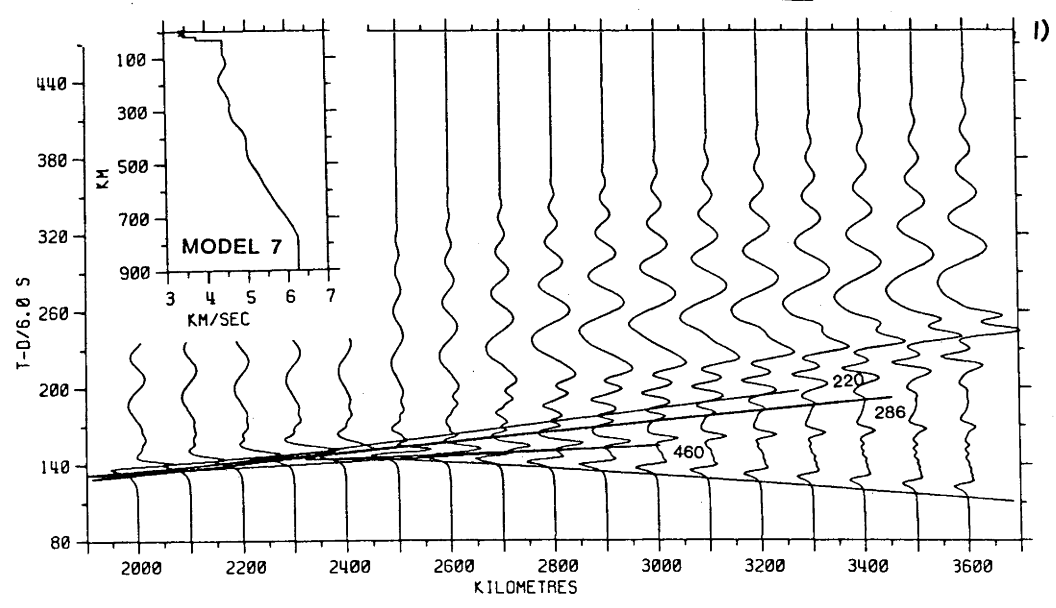
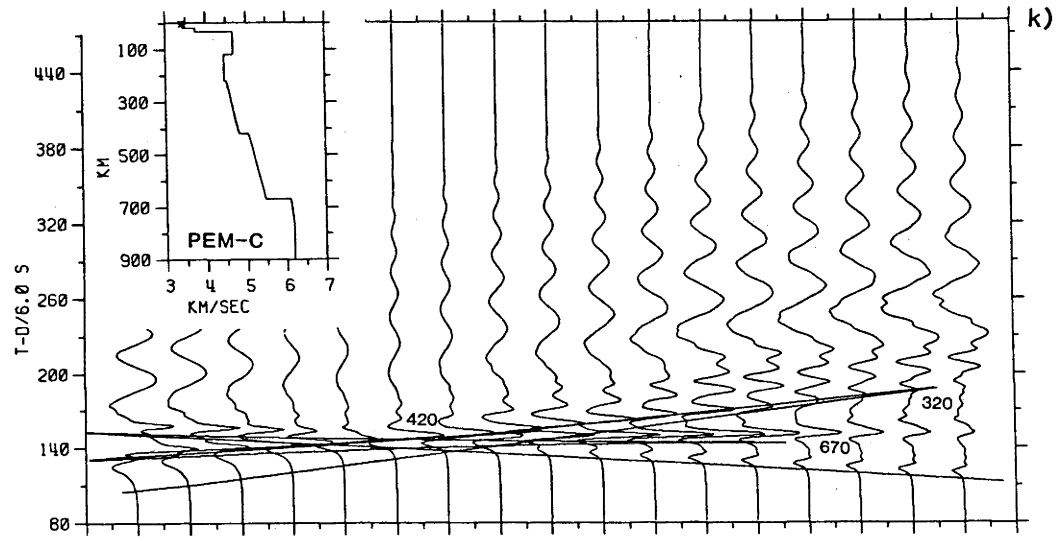
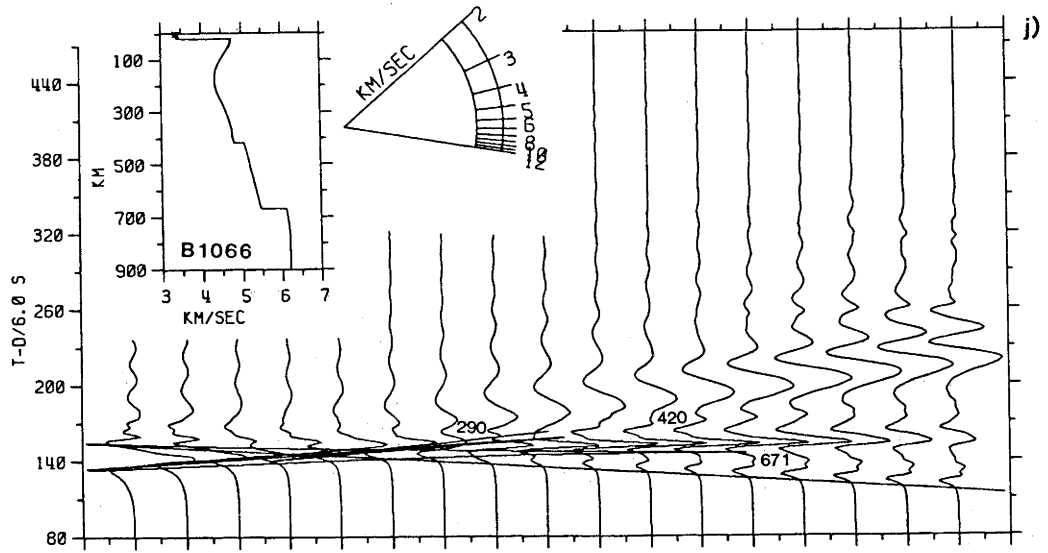
Synthetic seismograms have been calculated for a suite of shear-wave velocity-depth models, and for compressional-wave models after an appropriate conversion of velocities. The distance range extends from 2000 km (18°) to 3600 km (32.4°). The integration limits for phase velocity extend from 3 km/s to 22 km/s, and so include surface waves. Superimposed on the synthetics are branched travel times as calculated by geometrical ray theory, with cusps labelled according to the bottoming depths of the associated rays.

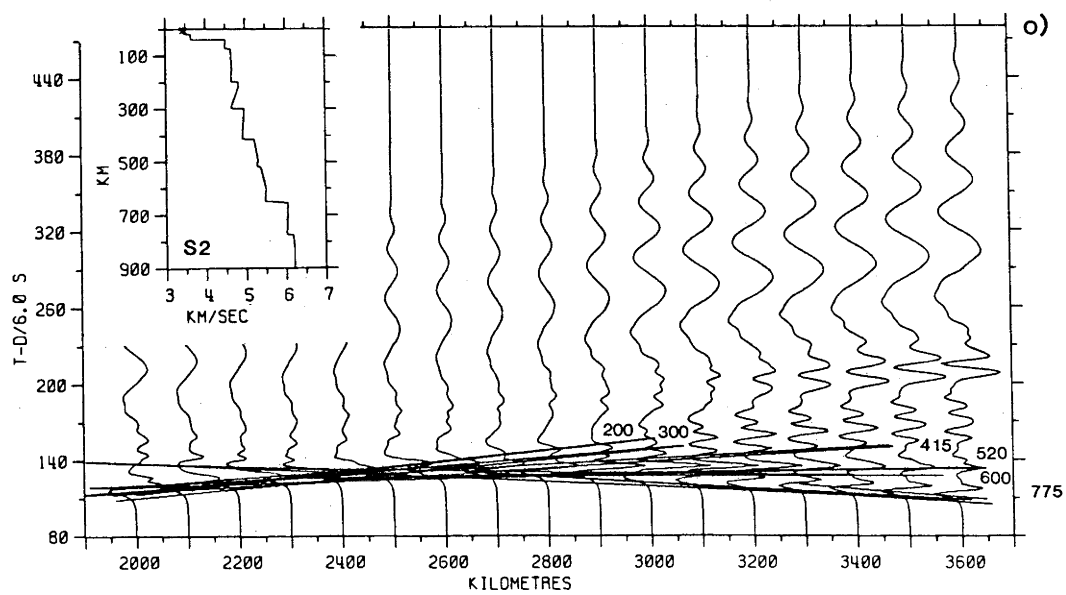
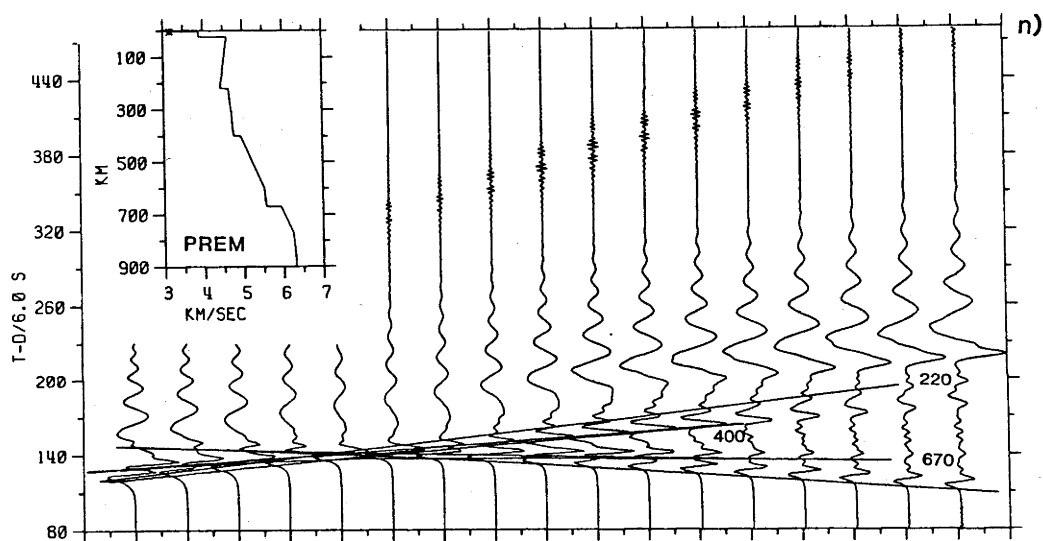
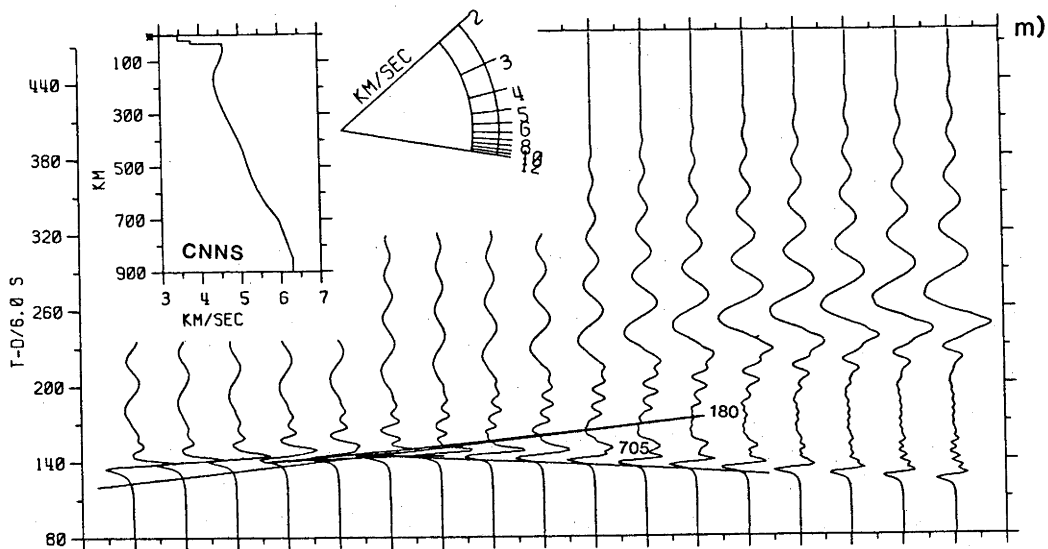
Figure A4.1: Synthetic SH seismograms for a suite of S- and P-(converted to S)wave models. Branched travel-time curves are plotted for the direct arrivals, and have cusps labelled according to the bottoming depths of the associated rays. Amplitudes are trace normalized. Velocity integration limits are 3.0 to 22 km/s, and so include surface waves. Successive panels are for the models: a) JB; b) IN; c) US26; d) IN2; e) STAN 3; f) REDDOG-C; g) SW-E; h) SHR14; i) B1; j) B1066; k) PEM-C; l) MODEL 7; m) CNNS; n) PREM; o) S2; p) SHMEE; q) MA; r) KCA; s) EKW; t) NAT; u) K8; v) S8.

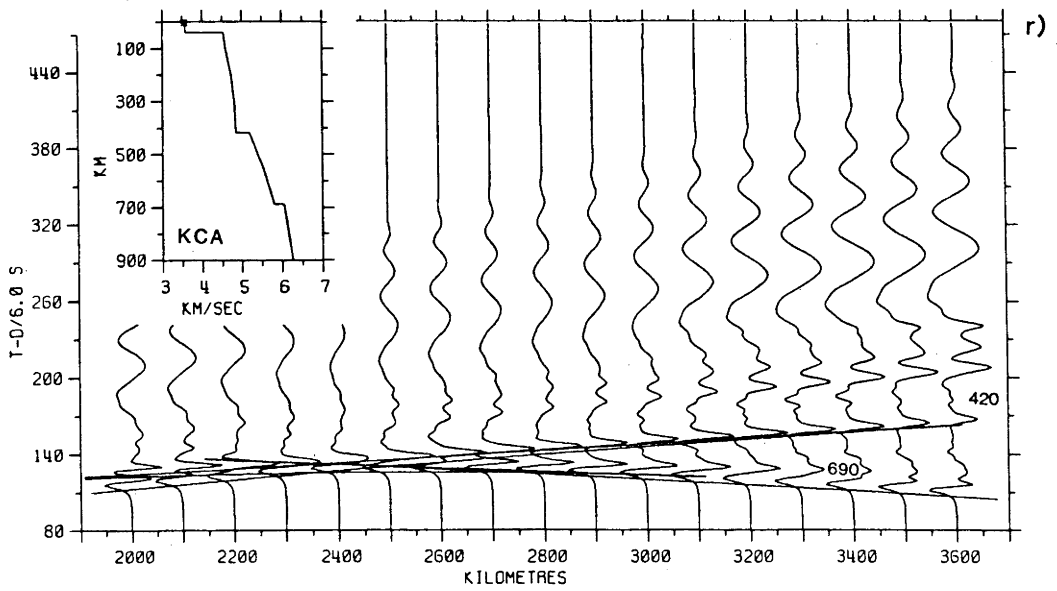
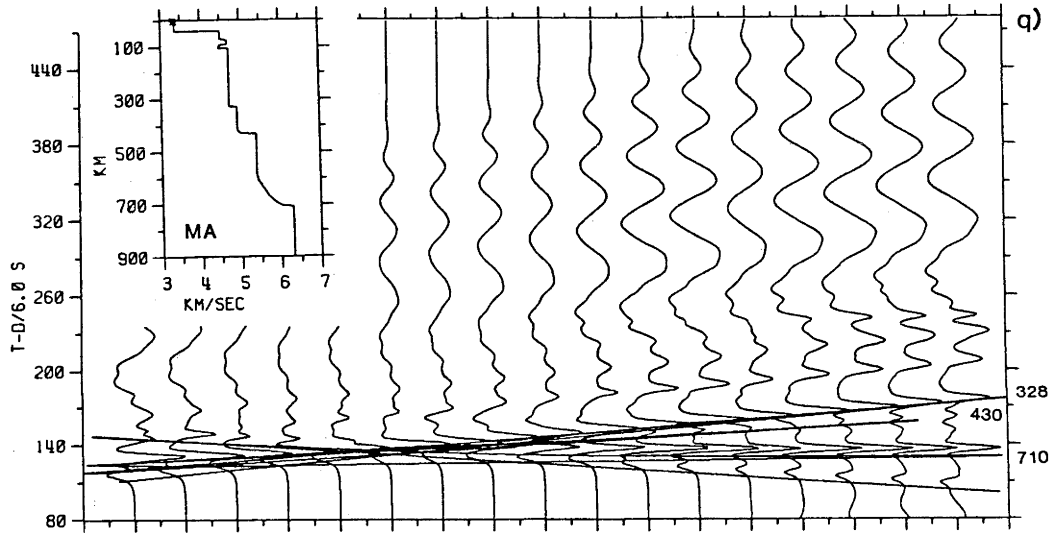
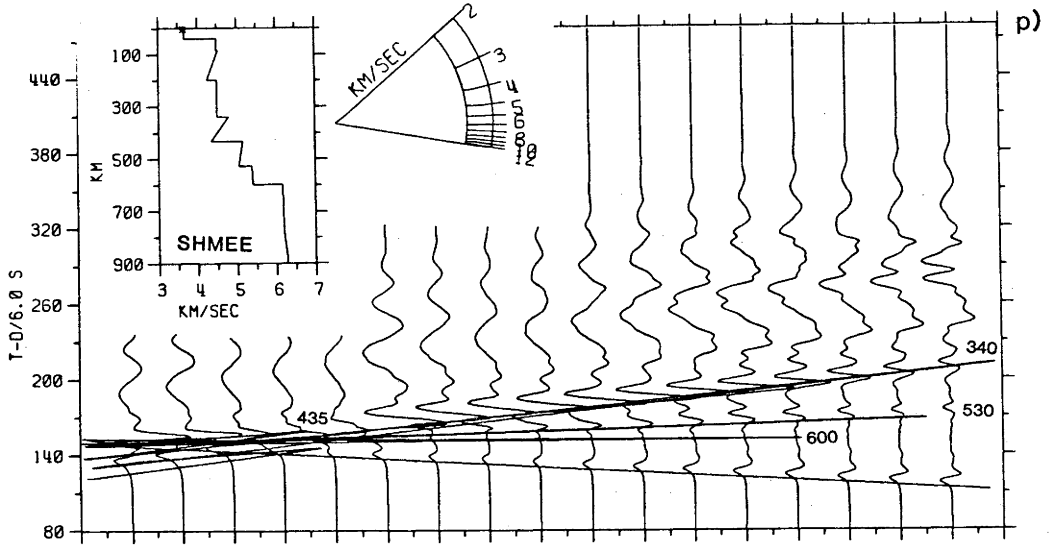


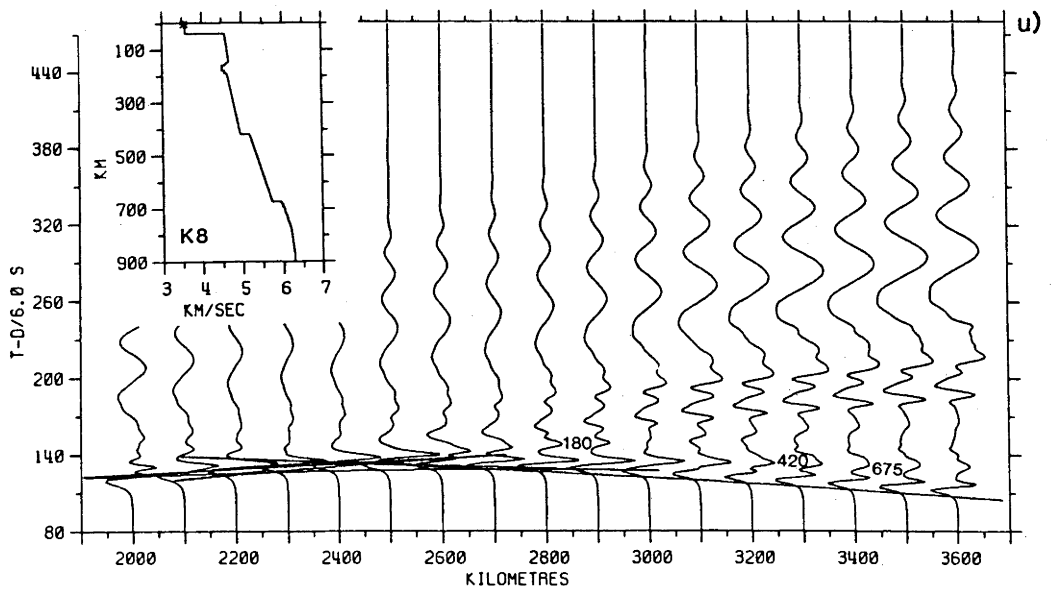
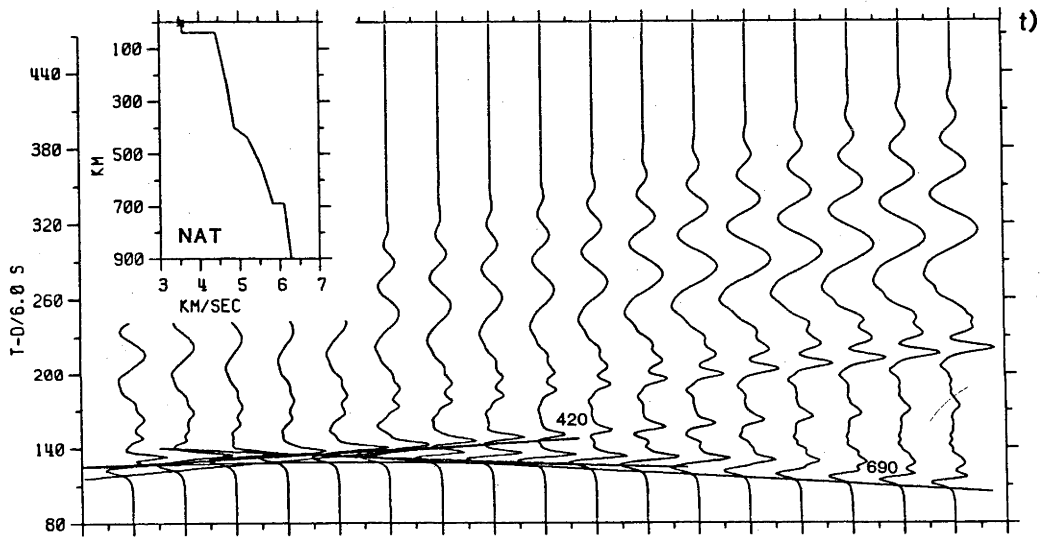
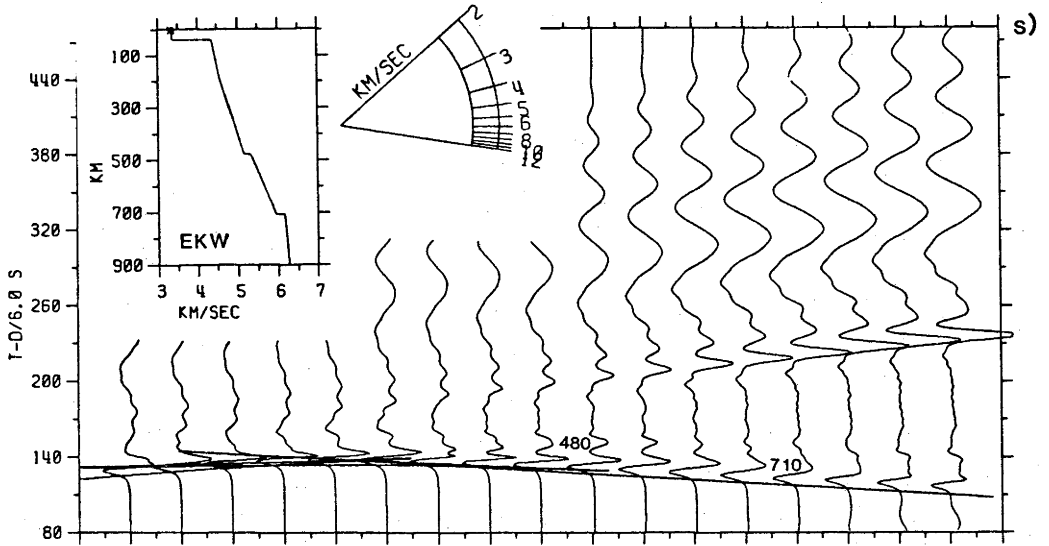


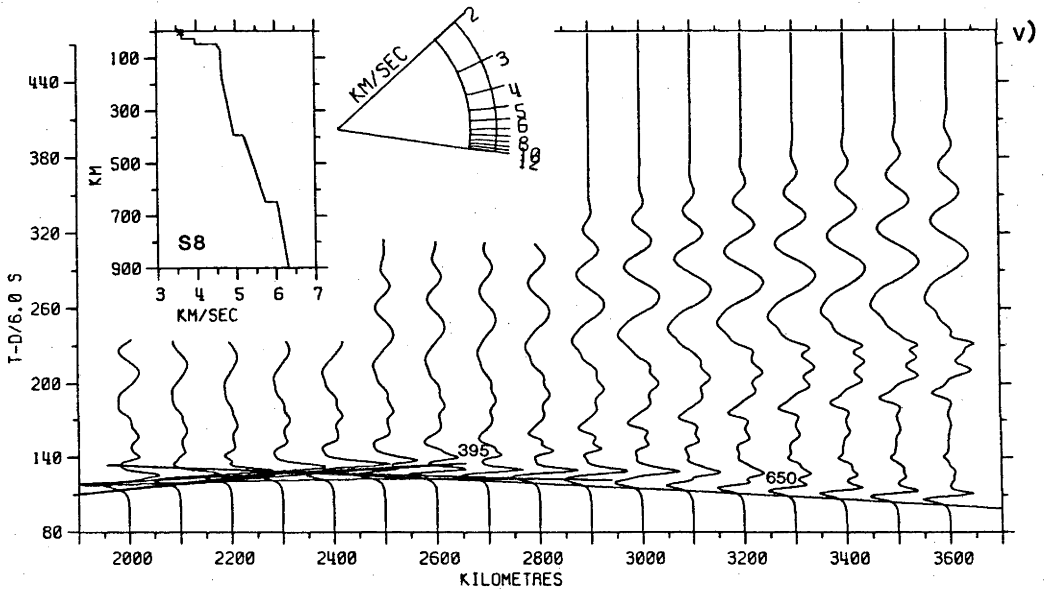












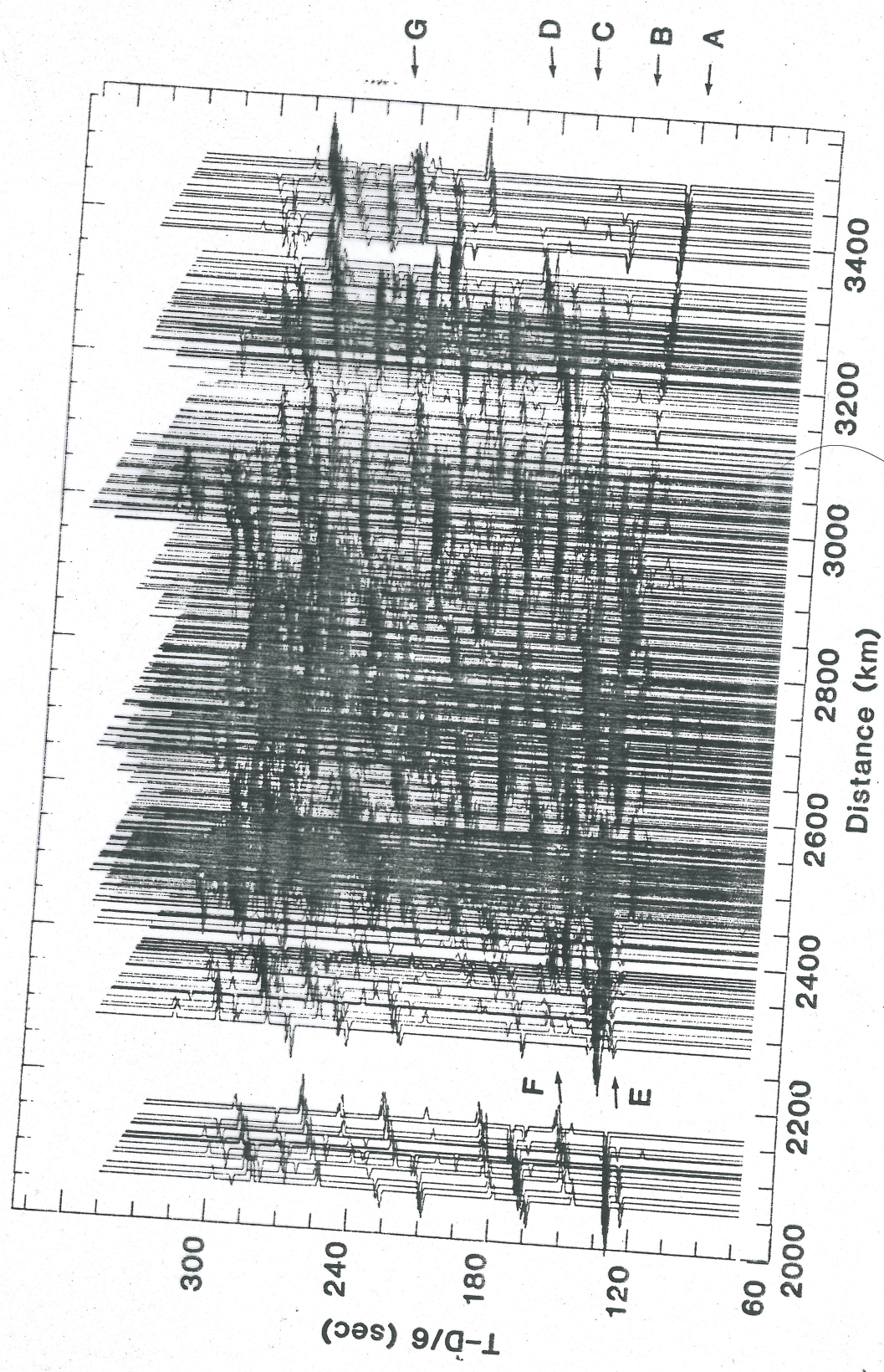


Figure 5.8: Iteratively decomposed traces of the data in Table 5.1. Nine iterations were used in the decomposition. Arrival times have been corrected to lie on the surface-focus Jeffreys-Bullen travel-time curve. Traces are normalized to peak amplitude. Interpreted travel-time branches are indicated. A transparency of this figure is provided in a pocket at the rear of this thesis.

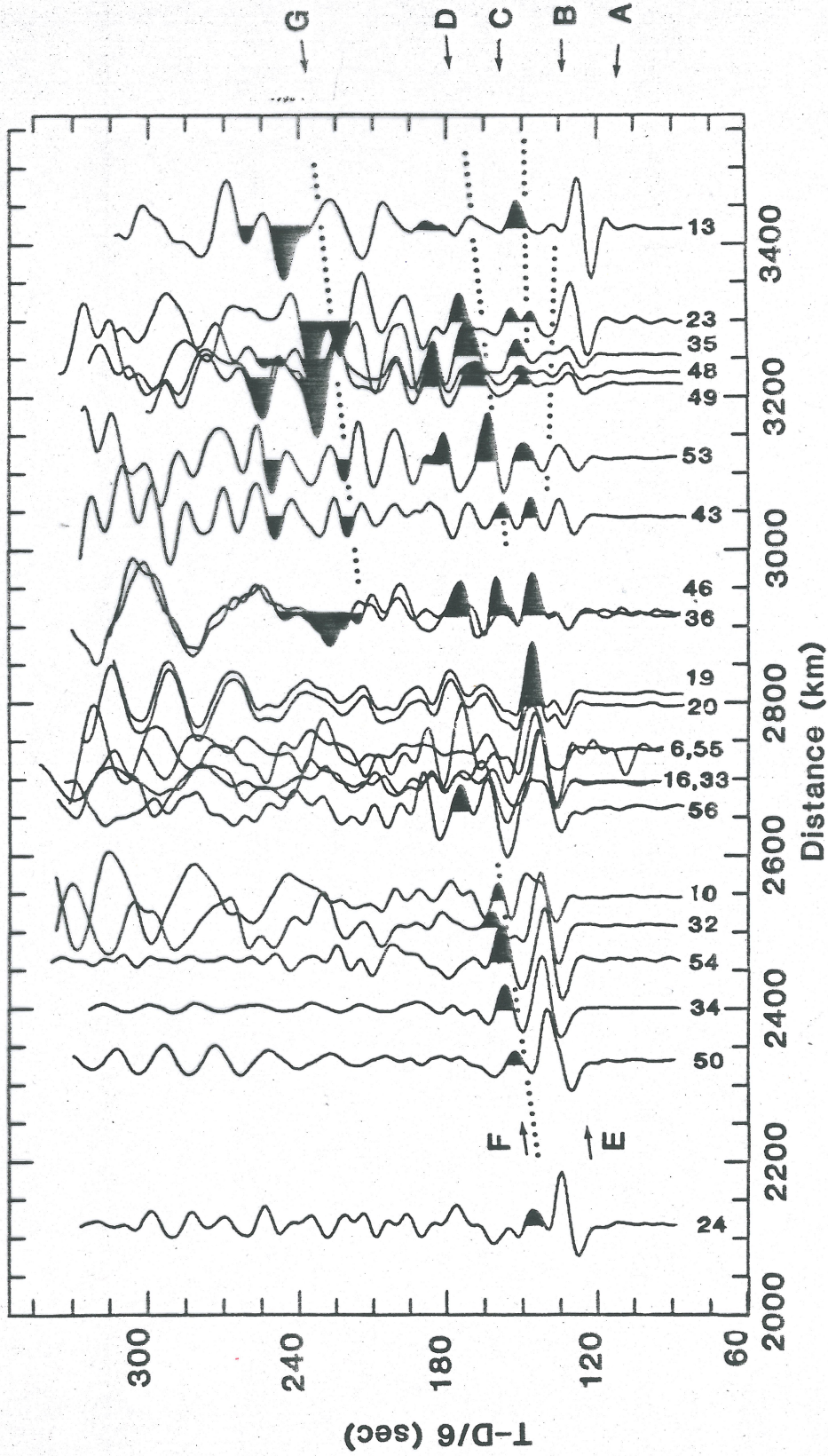


Figure 5.9: Repeat of Figure 5.7 with interpreted travel-time branches indicating identified arrivals in the data. Dotted lines indicate correlations of waveform peaks. A transparency of this figure is provided in a pocket at the rear of this thesis.

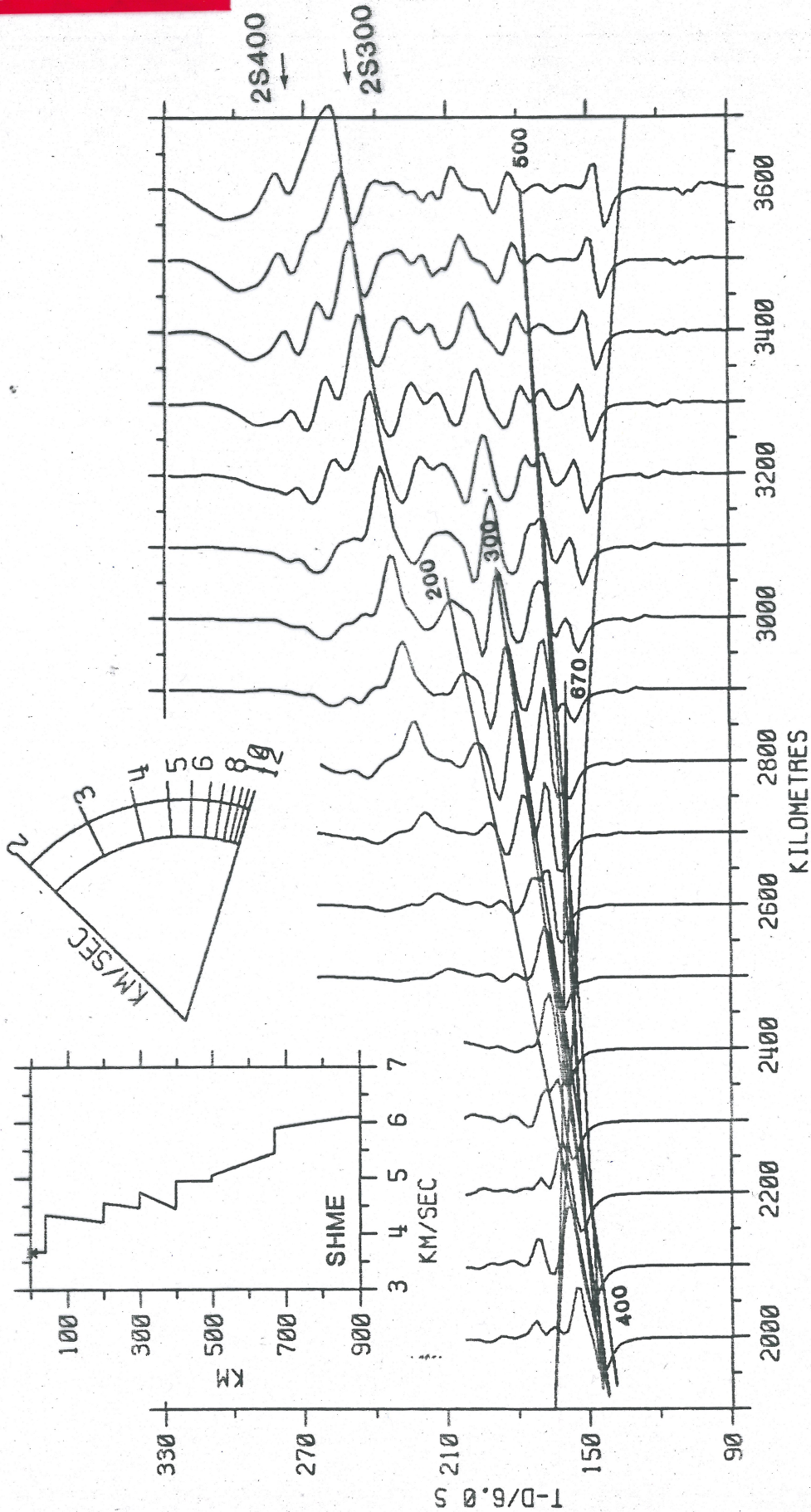


Figure 7.2: Synthetic SH seismograms for the SHME model. Caption as given by Figure 6.2. A transparency of this figure is provided in a pocket at the rear of this thesis.